

12

DNA-TR-81-78

# PROPAGATION OF WIDE BANDWIDTH SIGNALS THROUGH STRONGLY TURBULENT IONIZED MEDIA

AD A131355

Dennis L. Knepp  
Mission Research Corporation  
P.O. Drawer 719  
Santa Barbara, California 93102

15 March 1982

Technical Report

CONTRACT No. DNA 001-81-C-0081

APPROVED FOR PUBLIC RELEASE;  
DISTRIBUTION UNLIMITED.

THIS WORK WAS SPONSORED BY THE DEFENSE NUCLEAR AGENCY  
UNDER RDT&E RMSS CODE 8322081466 S99QAXHB00005 H2590D.

DTIC FILE COPY

Prepared for  
Director  
DEFENSE NUCLEAR AGENCY  
Washington, DC 20305

DTIC  
ELECTE  
AUG 11 1983  
B

83 08 11 00 3

Destroy this report when it is no longer needed. Do not return to sender.

PLEASE NOTIFY THE DEFENSE NUCLEAR AGENCY,  
ATTN: STTI, WASHINGTON, D.C. 20305, IF  
YOUR ADDRESS IS INCORRECT, IF YOU WISH TO  
BE DELETED FROM THE DISTRIBUTION LIST, OR  
IF THE ADDRESSEE IS NO LONGER EMPLOYED BY  
YOUR ORGANIZATION.



UNCLASSIFIED

SECURITY CLASSIFICATION OF THIS PAGE (When Data Entered)

REPORT DOCUMENTATION PAGE		READ INSTRUCTIONS BEFORE COMPLETING FORM
1 REPORT NUMBER DNA-TR-81-78	2 GOVT ACCESSION NO. AD-A131355	3 RECIPIENT'S CATALOG NUMBER
4 TITLE (and Subtitle) PROPAGATION OF WIDE BANDWIDTH SIGNALS THROUGH STRONGLY TURBULENT IONIZED MEDIA		5 TYPE OF REPORT & PERIOD COVERED Technical Report
7 AUTHOR(s) Dennis L. Knepp		6 PERFORMING ORG. REPORT NUMBER MRC-R-671
9 PERFORMING ORGANIZATION NAME AND ADDRESS Mission Research Corporation P.O. Drawer 719 Santa Barbara, California 93102		8 CONTRACT OR GRANT NUMBER(s) DNA 001-81-C-0081
11 CONTROLLING OFFICE NAME AND ADDRESS Director Defense Nuclear Agency Washington, D.C. 20305		10 PROGRAM ELEMENT PROJECT, TASK AREA & WORK UNIT NUMBERS Task S99QAXHB-00005
14 MONITORING AGENCY NAME & ADDRESS (if different from Controlling Office)		12 REPORT DATE 15 March 1982
		13 NUMBER OF PAGES 248
		15 SECURITY CLASS (of this report) UNCLASSIFIED
		15a DECLASSIFICATION DOWNGRADING SCHEDULE N/A since UNCLASSIFIED
16 DISTRIBUTION STATEMENT (of this Report)  Approved for public release; distribution unlimited.		
17 DISTRIBUTION STATEMENT (of the abstract entered in Block 20, if different from Report)		
18 SUPPLEMENTARY NOTES  This work was sponsored by the Defense Nuclear Agency under RDT&E RMSS Code B322081466 S99QAXHB00005 H2590D.		
19 KEY WORDS (Continue on reverse side if necessary and identify by block number) Satellite Communication Random Media Signal Scintillation Dispersive Media Ionospheric Propagation Wide Bandwidth Signals Frequency Selective Environment Pseudonoise Spread Spectrum		
20 ABSTRACT (Continue on reverse side if necessary and identify by block number)  Analytic and numerical techniques are presented which directly address the problem of propagation of wide bandwidth signals through random ionized media. This work is applicable to the problems of satel- lite communication and space based radar observation through a disturbed ionospheric propagation channel that would result from a high altitude chemical release or nuclear detonation.		

DD FORM 1 JAN 73 1473 EDITION OF 1 NOV 65 IS OBSOLETE

UNCLASSIFIED

SECURITY CLASSIFICATION OF THIS PAGE (When Data Entered)

## 20. ABSTRACT (continued)

An analytic solution is presented for the two-position, two-frequency mutual coherence function for spherical wave propagation in the strong scattering limit. This solution is used to derive simple expressions for the power impulse response function and to determine its relationship to the important parameters of decorrelation distance and coherence bandwidth which describe the disturbed propagation channel. Results for mean time delay and time delay jitter are presented and compared to direct simulation results and to other theoretical calculations.

A numerical/analytical solution to the parabolic wave equation is presented in the form of a multiple phase-screen (MPS) propagation simulation. In this very general solution technique, the random medium is divided into a finite number of layers. The field fluctuation through each layer is obtained by replacing the layer by a centrally located thin phase-screen, whose statistical properties are determined from the statistics of the electron-density irregularities. The waveform then propagates from phase-screen to phase-screen via an exact solution to the Fresnel-Kirchhoff equation. For wide bandwidth waveforms, numerical solutions are obtained at a number of discrete frequencies centered about the carrier and then time-domain solutions are obtained by Fourier transform techniques. Detailed results are presented for a number of interesting cases including propagation of a 20 MHz bandwidth signal through a finite barium cloud at a carrier frequency of 100 MHz.

One of the major uses of the MPS propagation simulation has been to provide realizations of the received signal after propagation through a disturbed channel. The MPS simulation obtains a general solution of the parabolic wave equation under both weak and strong scattering conditions. A second technique to directly obtain realizations of wide bandwidth waveforms is presented here. This technique is limited to the case of strong scattering but requires only a fraction of the computer resources needed for MPS signal generation. Detailed comparisons of the two signal generation techniques are presented.



## PREFACE

The author is indebted to Dr. Robert W. Stagat and Mr. Robert L. Bogusch of Mission Research Corporation and to Major Leon A. Wittwer of the Defense Nuclear Agency for their helpful discussions regarding this work.

**A**



## TABLE OF CONTENTS

<u>Section</u>	<u>Page</u>
PREFACE	1
LIST OF ILLUSTRATIONS	6
LIST OF TABLES	13
1 INTRODUCTION	15
1.1 BACKGROUND	15
1.2 MPS PROPAGATION SIMULATION	16
1.3 STATISTICAL SIGNAL GENERATION	19
1.4 SOLUTION FOR TWO-FREQUENCY MUTUAL COHERENCE FUNCTION	20
2 MPS NUMERICAL PROPAGATION SIMULATION	22
2.1 PHASE-SCREEN TECHNIQUES	22
2.2 FORMULATION	25
2.2.1 Phase Power Spectral Density	28
2.2.2 Power Law Phase PSD	31
2.2.3 Gaussian Phase PSD	32
2.2.4 Phase-Screen Generation	33
2.2.5 Criteria for MPS Application	36
2.3 APPLICATION TO A GAUSSIAN LENS	39
2.4 APPLICATION TO A RANDOM PHASE-SCREEN	41

## TABLE OF CONTENTS (Continued)

<u>Section</u>	<u>Page</u>
2.5 WIDE BANDWIDTH MPS CALCULATION	49
2.5.1 Time-Domain Propagation Through a Strong Gaussian Lens	50
2.5.2 Time-Domain Propagation Through a Striated Barium Cloud	65
2.6 HOMOGENEOUS FLUCTUATIONS - $r$ COMPARED TO THEORY	69
2.7 COMPARISON OF $\langle \tau \rangle$ AND $\sigma_\tau$ TO THEORY	81
3 STATISTICAL SIGNAL GENERATION	87
3.1 STATISTICAL SIGNAL REALIZATIONS	87
3.2 FORMULATION	88
3.2.1 Wide Bandwidth Signals	91
3.2.2 Total Phase Shift, Time Delay, and Doppler Frequency	95
3.2.3 Impulse Response Function	98
3.2.4 Statistics of a Realization	100
3.3 IMPULSE RESPONSE FUNCTION GENERATION	101
3.3.1 Realizations of the Parabolic Wave Equation Solution	102
3.3.2 Realizations of the Impulse Response Function	107
3.4 RAYLEIGH COMPONENT OF THE COMPOSITE SIGNAL	109
3.4.1 Rayleigh Signal Component for Elongated Irregularities	111
3.4.2 Rayleigh Signal Component for Isotropic Irregularities	120

## TABLE OF CONTENTS (Continued)

<u>Section</u>	<u>Page</u>
3.5 EXAMPLES OF STATISTICALLY GENERATED SIGNALS	121
3.5.1 Example 1: Diffraction Important	121
3.5.2 Example 2: Focusing Important	135
4 TWO-FREQUENCY MUTUAL COHERENCE FUNCTION	146
4.1 FORMULATION	147
4.1.1 Power Impulse Response Function	148
4.1.2 Two-Frequency Mutual Coherence Function	151
4.1.3 $A_0$ and $A_2$ Calculation	157
4.1.4 $\sigma_\phi^2$ Calculation	160
4.1.5 $\Gamma$ Solution	161
4.2 GENERALIZED POWER SPECTRUM	170
4.3 POWER IMPULSE RESPONSE FUNCTION SOLUTION	174
4.3.1 Limiting Values	175
4.4 MEAN TIME DELAY AND TIME DELAY JITTER	182
4.4.1 Mean Time Delay $\langle \tau \rangle$	183
4.4.2 $\langle \tau \rangle$ and $\sigma_\tau$ - Thin Phase-Screen Approximation	185
4.5 VALIDITY OF THE THIN PHASE-SCREEN APPROXIMATION	186
4.5.1 $S_h^2$ -Rytov Approximation	187
4.5.2 $S_h^2$ -Thin Phase-Screen Approximation	190
4.5.3 Comparison of Results	191
4.5.4 $\langle \tau \rangle$ and $\sigma_\tau$ - Thick Layer Versus Thin Screen	196

## TABLE OF CONTENTS (Concluded)

<u>Section</u>	<u>Page</u>
REFERENCES	209
APPENDIX A	215
A-1 EVALUATION OF THE GENERALIZED POWER SPECTRUM	215
A.1.1 Numerical Method	215
A.1.2 Examples of $S(k, \tau)$	219

## LIST OF ILLUSTRATIONS

<u>Figure</u>	<u>Page</u>
2-1. Propagation of signals through a disturbed transionospheric communications channel.	23
2-2. Multiple phase-screen representation of the geometry of Figure 2-1.	29
2-3. Diffraction pattern of a Gaussian lens.	42
2-4. Realization of phase for a Gaussian PSD.	44
2-5. Comparison of numerically generated phase PSD with desired Gaussian PSD.	46
2-6. Comparison of correlation function of numerically generated phase with desired analytic correlation function.	46
2-7. Realization of phase for a power law PSD.	47
2-8. Comparison of numerically generated phase PSD with desired power law PSD.	47
2-9. $S_4$ scintillation index for Gaussian spectrum.	48
2-10. Example of envelope of wideband signal after propagation through nonselective and frequency selective propagation channels.	54
2-11. Signal amplitude and phase at 100 MHz, 3 km from a strong Gaussian lens.	56
2-12. Signal amplitude and phase at 100 MHz, 5 km from a strong Gaussian lens.	57

## LIST OF ILLUSTRATIONS (Continued)

<u>Figure</u>	<u>Page</u>
2-13. Signal amplitude and phase at 100 MHz, 10 km from a strong Gaussian lens.	58
2-14. Signal amplitude and phase at 100 MHz, 50 km from a strong Gaussian lens.	59
2-15. Signal amplitude and phase at 100 MHz, 100 km from a strong Gaussian lens.	60
2-16. Envelope of time-domain waveform 3 km from a strong Gaussian lens.	62
2-17. Envelope of time-domain waveform 10 km from a strong Gaussian lens.	62
2-18. Envelope of time-domain waveform 50 km from a strong Gaussian lens.	63
2-19. Envelope of time-domain waveform 100 km from a strong Gaussian lens.	63
2-20. Envelope of time-domain waveform 100 km from a strong Gaussian lens.	64
2-21. Phase-screen realization as model of scattering properties of barium cloud Esther.	66
2-22. Envelope of time-domain signal after propagation through deterministic barium cloud.	68
2-23. Envelope of received time-domain signal after propagation through an ionized, striated barium cloud.	68
2-24. Close-up of central portion of Figure 2-23.	70
2-25. Received PN code correlator output, PLACES experiment, first beacon rocket.	70
2-26. Comparison of magnitude of $r$ , single MPS realization versus theory.	72
2-27. Comparison of phase of $r$ , single MPS realization versus theory, $\Delta x = 0$ .	72

## LIST OF ILLUSTRATIONS (Continued)

<u>Figure</u>	<u>Page</u>
2-28. Comparison of phase of $r$ , single MPS realization versus theory, $\Delta x = 0.61$ m.	73
2-29. Comparison of phase of $r$ , single MPS realization versus theory, $\Delta x = 1.22$ m.	73
2-30. Comparison of phase of $r$ , single MPS realization versus theory, $\Delta x = 1.83$ m.	74
2-31. Comparison of phase of $r$ , single statistical realization versus theory, $\Delta x = 2.44$ m.	74
2-32. Envelope of received time-domain waveform--first 101 x-values from MPS simulation.	76
2-33. Average received time-domain envelope--MPS signal realization.	76
2-34. Comparison of amplitude of $r$ , single MPS realization versus theory.	78
2-35. Comparison of amplitude of $r$ , single MPS realization versus theory.	78
2-36. Comparison of amplitude of $r$ , single MPS realization versus theory.	79
2-37. Comparison of amplitude of $r$ , single MPS realization versus theory.	79
2-38. Comparison of two-sided bandwidth, $f_r$ , many MPS calculations versus theory.	80
2-39. Comparison of mean time delay, $\langle t \rangle$ , many MPS realizations versus theory.	85
2-40. Comparison of time delay jitter, $\sigma_t$ , many MPS realizations versus theory.	85
3-1. Geometry of transionospheric satellite communications link through a thick scattering layer.	90



## LIST OF ILLUSTRATIONS (Continued)

<u>Figure</u>	<u>Page</u>
3-2. Rayleigh signal component outer scale versus $\sigma_\phi$ and $\sigma_{\phi R}$ , elongated irregularities.	115
3-3. Rayleigh signal component $\sigma_{\phi R}$ versus $\sigma_\phi$ , elongated irregularities.	115
3-4. Rayleigh signal component $\alpha_R$ versus $\sigma_\phi$ , elongated, irregularities, $L_R/l_R = 100$ .	118
3-5. Rayleigh signal component outer scale versus $\sigma_\phi$ and $\sigma_{\phi R}$ , isotropic irregularities.	118
3-6. Rayleigh signal component $\sigma_{\phi R}$ versus $\sigma_\phi$ , isotropic irregularities.	122
3-7. Rayleigh signal component $\alpha_R$ versus $\sigma_\phi$ , isotropic irregularities, $L_R/l_R = 100$ .	122
3-8. Normalized power impulse response function, $\alpha = 100$ .	124
3-9. Comparison of magnitude of $r$ , single statistical realization versus theory.	126
3-10. Comparison of phase of $r$ , single statistical realization versus theory, $\Delta x = 0$ .	126
3-11. Comparison of phase of $r$ , single statistical realization versus theory, $\Delta x = 0.61$ m.	127
3-12. Comparison of phase of $r$ , single statistical realization versus theory, $\Delta x = 1.22$ m.	127
3-13. Comparison of phase of $r$ , single statistical realization versus theory, $\Delta x = 1.83$ m.	128
3-14. Comparison of phase of $r$ , single statistical realization versus theory, $\Delta x = 2.44$ m.	128
3-15. Comparison of amplitude of $r$ , average of five statistical realizations versus theory.	130
3-16. Comparison of phase of $r$ , average of five statistical realizations versus theory, $\Delta x = 0$ .	130
3-17. Comparison of phase of $r$ , average of five statistical realizations versus theory, $\Delta x = 0.61$ m.	131

## LIST OF ILLUSTRATIONS (Continued)

<u>Figure</u>	<u>Page</u>
3-18. Comparison of phase of $r$ , average of five statistical realizations versus theory, $\Delta x = 1.22$ m.	131
3-19. Comparison of phase of $r$ , average of five statistical realizations versus theory, $\Delta x = 1.83$ m.	132
3-20. Comparison of phase of $r$ , average of five statistical realizations versus theory, $\Delta x = 2.44$ m.	132
3-21. Envelope of the received time-domain waveform--statistical signal realization.	134
3-22. Average received time-domain envelope--statistical signal realization.	134
3-23. Envelope of the received time-domain waveform--MPS signal realization.	137
3-24. Envelope of the received time-domain waveform--MPS signal realization.	137
3-25. Mean time delay, $\langle t \rangle$ , as a function of distance along the MPS grid.	138
3-26. Time delay jitter, $\sigma_t$ , as a function of distance along the MPS grid.	138
3-27. Peak signal amplitude as a function of distance along the MPS grid.	139
3-28. Mean time delay, $\langle t \rangle$ , as a function of distance along the MPS grid.	141
3-29. Time delay jitter, $\sigma_t$ , as a function of distance along the MPS grid.	141
3-30. Received envelope for MPS calculation from 44.4 to 45.0 km along the MPS grid.	142
3-31. Received envelope for statistical signal realization.	144
4-1. Thin phase-screen propagation geometry.	169
4-2. Power impulse response function for isotropic irregularities in the thin phase-screen approximation.	179

## LIST OF ILLUSTRATIONS (Continued)

<u>Figure</u>	<u>Page</u>
4-3. Power impulse response function for elongated irregularities in the thin phase-screen approximation.	180
4-4. Power impulse response function for isotropic and elongated irregularities in the thin phase-screen approximation.	180
4-5. Rytov approximation to scintillation index for isotropic irregularities with a Gaussian PSD.	192
4-6. Rytov approximation to scintillation index for elongated irregularities with a Gaussian PSD.	192
4-7. Percent difference in $S_4$ between the Rytov and the thin phase-screen approximation, isotropic irregularities.	194
4-8. Percent difference in $S_4$ between the Rytov and the thin phase-screen approximation, elongated irregularities.	194
4-9. Maximum percent difference in $S_4$ for isotropic irregularities.	195
4-10. Maximum percent difference in $S_4$ for elongated irregularities.	195
4-11. Mean time delay as a function of layer thickness and free-space propagation distance.	199
4-12. Normalized time delay jitter as a function of layer thickness and free-space propagation distance.	199
4-13. Relative time delay jitter accuracy of the thin phase-screen approximation, isotropic irregularities, $\alpha = 100$ .	201
4-14. Relative time delay jitter accuracy of the thin phase-screen approximation, isotropic irregularities, $\alpha = 1$ .	203
4-15. Relative time delay jitter accuracy of the thin phase-screen approximation, elongated irregularities, $\alpha = 1$ .	203

## LIST OF ILLUSTRATIONS (Continued)

<u>Figure</u>	<u>Page</u>
4-16. Maximum percent difference in $\sigma_{\tau}$ , isotropic irregularities.	205
4-17. Maximum percent difference in $\sigma_{\tau}$ , elongated irregularities.	205
4-18. Comparison of power impulse response function, thin phase-screen versus thick layer.	206
4-19. Comparison of power impulse response function, thin phase-screen versus thick layer.	207
4-20. Comparison of power impulse response function, thin phase-screen versus thick layer.	207
A-1. Generalized power spectrum for elongated irregularities, $\alpha = 10$ .	222
A-2. Generalized power spectrum for isotropic irregularities, $\alpha = 10$ .	223
A-3. Generalized power spectrum for elongated irregularities, $\alpha = 10$ .	224
A-4. Generalized power spectrum for isotropic irregularities, $\alpha = 10$ .	225
A-5. Generalized power spectrum for elongated irregularities, $\alpha = 5$ .	226
A-6. Generalized power spectrum for isotropic irregularities, $\alpha = 5$ .	227
A-7. Generalized power spectrum for elongated irregularities, $\alpha = 5$ .	228
A-8. Generalized power spectrum for isotropic irregularities, $\alpha = 5$ .	229
A-9. Generalized power spectrum for elongated irregularities, $\alpha = 1$ .	230
A-10. Generalized power spectrum for isotropic irregularities, $\alpha = 1$ .	231

## LIST OF ILLUSTRATIONS (Concluded)

<u>Figure</u>	<u>Page</u>
A-11. Generalized power spectrum for elongated irregularities, $\alpha = 1$ .	232
A-12. Generalized power spectrum for isotropic irregularities, $\alpha = 1$ .	233
A-13. Generalized power spectrum for elongated irregularities, $\alpha = 0.1$ .	234
A-14. Generalized power spectrum for isotropic irregularities, $\alpha = 0.1$ .	235
A-15. Generalized power spectrum for elongated irregularities, $\alpha = 0.1$ .	236
A-16. Generalized power spectrum for isotropic irregularities, $\alpha = 0.1$ .	237
A-17. Generalized power spectrum for elongated irregularities, $\alpha = 0.01$ .	238
A-18. Generalized power spectrum for isotropic irregularities, $\alpha = 0.01$ .	239
A-19. Generalized power spectrum for elongated irregularities, $\alpha = 0.01$ .	240
A-20. Generalized power spectrum for isotropic irregularities, $\alpha = 0.01$ .	241

## LIST OF TABLES

<u>Table</u>	<u>Page</u>
2-1. Analytic versus numerical MPS comparison of $1/e$ points of $r(\Delta x=0, f)$ .	81
2-2. Comparison of analytic and numerical MPS results for mean time delay and time delay jitter.	86

Blum

## SECTION 1 INTRODUCTION

### 1.1 BACKGROUND

For more than two decades it has been well known that propagation through the natural ionosphere can cause degradation of satellite signals (Yeh and Swenson, 1959; Skinner, et al., 1971; Pope and Fritz, 1971; Taur, 1976; Whitney and Basu, 1977; Johnson and Lee, 1978; Mullen, et al., 1978; Paulson and Hopkins, 1978; Fremouw, et al., 1978). It has also been widely reported for a similar period of time that the ionosphere is subject to even greater disturbances following high altitude nuclear explosions (Matsushita, 1959; Keyes and Tinsley, 1962; Rothwell, et al., 1963; Maeda, et al., 1964; Arendt and Soicher, 1964; Zinn, et al., 1966; Boquist and Snyder, 1967; Hoerlin, 1976; Glasstone and Dolan, 1977; King and Fleming, 1980). In both natural and artificially disturbed ionospheres, electron density irregularities can cause random variations in the amplitude and phase of a propagating wave. Such signal variations are called scintillation or fading and have been observed on satellite links through the natural ionosphere at frequencies up to the GHz range (Taur, 1976; Fremouw, et al. 1978).

If all frequency components of the received scintillating signal vary essentially identically with time, the propagation channel is referred to as nonselective or as a flat fading channel. When the scintillations exhibit statistical decorrelation at different frequencies within the signal bandwidth, the channel is referred to as frequency selective.

Frequency selective scintillations are therefore encountered when the bandwidth utilized by a communication link exceeds the coherence bandwidth of the ionospheric channel. This situation is more likely to occur when the system bandwidth is large, as in spread spectrum systems.

Such systems typically employ either direct sequence spectrum spreading over a large instantaneous bandwidth, or carrier frequency hopping of a small instantaneous signal spectrum over a large bandwidth. The effects of frequency selective scintillation are quite different for direct sequence and frequency hopped systems (Bogusch, et al., 1981). Only the case of an instantaneous wide bandwidth signal is considered in this work although the appropriate results presented here may easily be applied to the latter case.

Frequency selective scintillation is much more likely to occur if the ionosphere is more highly disturbed, as for example by nuclear explosions or by chemical releases (Knepp and Bogusch, 1979). Increased electron concentrations and irregular structure of the ionization can lead to intense signal scintillations and potentially significant frequency selective effects at frequencies as high as the 7-8 GHz SHF band (Knepp, 1977). Consequently, the effects of frequency selective propagation disturbances are of importance to spread spectrum satellite systems that may have to operate in highly disturbed environments.

In this report, several techniques are presented to determine the effects of ionization irregularities on a propagating wide bandwidth signal subject to frequency selective scintillation.

## **1.2 MPS PROPAGATION SIMULATION**

The multiple phase-screen (MPS) propagation simulation (Knepp, 1977; Wittwer, 1978) is the most general technique to obtain a solution to the parabolic wave equation. In this solution technique, the ionized medium is divided into a finite number of layers. The field fluctuation through each layer is calculated by replacing the layer by a phase-changing screen located at its center, whose statistical properties are determined from the statistics of the electron density fluctuations within the layer. At each phase-screen, the statistical phase is added to the electric field phase and the wave is then propagated to the next phase-screen or to the observer. For wide bandwidth waveforms, the numerical solution is obtained at a number of discrete frequencies centered about a carrier frequency and then a time-domain solution is obtained by the use of Fourier transform techniques.



The MPS propagation technique is quite general, and may be easily applied to problems involving numerous, separated, layers of ionization characterized by spatially varying electron density power spectra. Section 2 of this report describes the MPS numerical propagation simulation and its application to wide bandwidth signal generation.

The MPS propagation simulation can handle all levels of ionospheric disturbances from the least severe, where only minor phase fluctuations occur, to the most severe cases of frequency selective Rayleigh fading. Since the MPS simulation provides a direct solution to the parabolic wave equation, the results are exact given a certain description of the propagation environment. Thus the applicability of the MPS propagation simulation depends upon the accuracy of the description of the scattering medium. In most of the MPS results presented in this report, the propagation environment is described by a one-dimensional  $K^{-3}$  power-law phase power spectrum. This spectrum corresponds to a  $K^{-4}$  three-dimensional power spectrum for electron density fluctuations and is representative of many in-situ measurements (Dyson, et al, 1974; Phelps and Sagalyn, 1976) as well as numerical simulation of striation spectra (Scannapieco, et al., 1976).

Section 2 of this report describes the MPS propagation simulation in detail as it is applied to calculate realizations of received time-domain signals.

The word "realization" is used in this report to refer to a specific sample of a statistical process. For example, realizations of the phase-changing screen are generated in a random manner based upon a sequence of pseudo-random numbers generated numerically. However, once these "random" numbers are generated, the phase-screen is completely defined and known. Similarly, the wave field propagated through this phase-screen is subject to exact calculation. However, a different sequence of pseudo-random numbers will yield a different phase-screen realization and hence a different realization of the received electric field.

An important function of the MPS propagation simulation is to serve as an intermediate step in the analysis of the effects on receivers of a disturbed, ionized propagation environment. Thus realizations of the received signal amplitude and phase are important results of the simulation and in turn serve as direct input to detailed receiver simulations (Bogusch, et al., 1981; Knepp and Bogusch, 1979).

In Section 2 the MPS propagation simulation is applied to predict the effect of a large, striated barium cloud on a wide bandwidth signal passing through the disturbed ionization. These predictions are based on an analysis of several earlier barium releases (Prettie and Marshall, 1978) from which a model of barium cloud irregularity structure was obtained. The barium cloud is then represented as a single phase-screen in the MPS simulation. A large Gaussian phase lens is used to model the mean or deterministic ionization effects from the barium cloud and small level stochastic phase perturbations are added to represent the ionization fluctuations. This model is quite general and has been applied to describe several other observed barium clouds (Knepp and Bogusch, 1979). Results for the received wide bandwidth signal after propagation through the barium cloud are presented and analyzed. Scattering from various components of the barium cloud is considered independently and then in combination to give a useful and intuitive understanding of the elements of the scattering process that are important for wide bandwidth signals.

The Defense Nuclear Agency barium release experiment discussed above took place in December 1980 and the results for the wide bandwidth propagation experiment were provided by Dr. James Marshall (Marshall, 1982). The agreement between the 1979 predictions and the 1980 experiment is quite remarkable and is discussed in Section 2.

Major emphasis in Section 2 is also given to a comparison of the MPS results to theoretical results. As stated earlier, the MPS propagation simulation is the only effective method to provide signal realizations applicable to a wide range of propagation conditions. For comparison purposes, these signal realizations may be analyzed to obtain average quantities for which analytic solutions or approximations can be found.

MPS results for the two-position, two-frequency mutual coherence function  $\Gamma(\Delta x, \Delta \omega)$  are compared to a theoretical, strong scatter approximation developed in Section 4. Although the theoretical calculation is more restrictive than the MPS propagation technique, good agreement between numerical and theoretical results is shown. As an additional comparison, the time domain MPS results for the mean time delay and time delay jitter of a wide bandwidth PN spread spectrum signal are compared to theoretical moment method calculations (Yeh and Liu, 1977).

### 1.3 STATISTICAL SIGNAL GENERATION

In Section 3 a second analytical/numerical technique is described to generate realizations of the received signal after propagation of a wide bandwidth waveform through a layer of strongly turbulent media. These statistical signal realizations are generated to have Rayleigh amplitude statistics (Fante, 1975) and to have spatial and frequency correlation properties which obey the parabolic wave equation in the strong scatter limit. Although these statistical signal realizations apply only to the case of strong scattering, their generation requires only a fraction of the computer resources required for signal generation by wide bandwidth multiple phase-screen calculations. Furthermore, the limitation to the strong scatter regime is not of great significance since frequency selective scintillation only occurs during strong scattering conditions.

This statistical technique follows the basic formalism described in Wittwer (1980) and is based upon the solution for the two-frequency mutual coherence function,  $r$ , for spherical wave propagation with transmitter and receiver located on opposite sides of a thick finite layer of ionized electron density irregularities. An analytic solution is obtained for  $r$  in the strong scatter regime by use of the quadratic approximation for the phase structure-function. The thin phase-screen approximation to the thick layer is then utilized and great simplification to the analytic expression for  $r$  is obtained. The relationship between the impulse response function of the propagation channel and the two-frequency mutual coherence function and its Fourier transform is then used to directly obtain statistical realizations of wide bandwidth signals.

The accuracy of the thin phase-screen approximation is discussed and several comparisons of statistical signals with signals obtained directly from the MPS propagation simulation are shown in Section 3.

The analytic solution for  $r$  which is the foundation of this statistical technique to generate realizations is presented in Section 4.

#### 1.4 SOLUTION FOR TWO-FREQUENCY MUTUAL COHERENCE FUNCTION

An analytic solution is obtained in Section 4 for the two-position, two-frequency mutual coherence function for spherical wave propagation. This solution provides the basis of the statistical signal generation technique presented in Section 3 of this report. It is assumed that strong scattering conditions prevail and that the quadratic approximation to the phase structure-function is valid. Here the ionized scattering region occupies a thick, finite layer with transmitter and receiver located in free space on opposite sides of the layer. General analytic solutions are derived for two cases. In the first case the random slab is represented by a one-dimensional power spectrum of electron-density fluctuations corresponding to propagation through elongated irregularities as would occur for an equatorial satellite link to a ground station. In the second case the random slab is represented by isotropic ionization irregularities which corresponds to the physical geometry of propagation along the direction of the earth's magnetic field.

The case of isotropic irregularities represents a worst case condition while the case of infinitely elongated irregularities leads to less severe propagation conditions. Both cases taken together represent the extremes of the range of results to be expected for propagation through ionospheric fluctuations, or ionization irregularities caused by barium cloud instabilities or by nuclear detonations.

For both cases the complex general analytic results are simplified by use of the thin phase-screen approximation (zero slab thickness) to obtain useful analytic expressions for  $r$  as well as the resulting power impulse response function. It is shown that the impulse response to an incident power delta function reduces to an exponential form in the strong scattering limit and to a Gaussian form in the weak scattering limit. The

Gaussian form corresponds to pulse wander and dispersion while the exponential form corresponds to diffractive pulse spreading produced by multipath effects.

Since the thin phase-screen results developed in Section 4 are used in the statistical signal generation technique described in Section 3, the accuracy of the thin-screen approximation is a matter of some importance. This approximation is considered in some detail in Section 4 where comparisons of the thick layer cases to the thin phase-screen case are presented for the  $S_4$  scintillation index, the mean time delay,  $\langle \tau \rangle$ , and the time delay jitter,  $\sigma_\tau$ . It is found that the thin phase-screen approximation gives exact results for  $\langle \tau \rangle$  and accurate results for  $S_4$  and  $\sigma_\tau$ .

The simplification resulting in the thin phase-screen approximation for the two-frequency mutual coherence function for spherical waves also leads to simplified expressions for two very important parameters that describe the propagation medium. These parameters are the signal decorrelation distance (and time) and the coherence bandwidth. Both parameters are defined and discussed in Section 4 and it is shown that the signal decorrelation time and the coherence bandwidth both obey the principle of reciprocity.

## SECTION 2

### MPS NUMERICAL PROPAGATION SIMULATION

#### 2.1 PHASE-SCREEN TECHNIQUES

Random variations in the amplitude and phase of a propagating wave, called scintillations, are caused by propagation through a region in which the electron density is irregularly structured. In ionospheric plasmas, electron density structure is produced by plasma instabilities which cause the ionization to break up into long filaments, or striations, aligned with the earth's magnetic field lines (Linson and Workman, 1970). The instability mechanisms accounting for ionospheric irregularities have been the topic of debate for many years and are summarized in a recent review (Basu and Kelley, 1978). Roughly speaking, one may describe striations as long sheets or rods of relatively high electron density imbedded in a background of lower electron density.

Figure 2-1 illustrates the geometry of the problem. Propagation of satellite signals through a large striated region presents the problem of radio wave propagation through a thick medium composed of random fluctuations in the index-of-refraction. Consider for a moment a plane, unmodulated carrier wave traversing the striated region. The wave first suffers random phase perturbations due to variations in the phase velocity within the medium. These phase variations in the propagating wavefront introduce small random changes in the direction of propagation of the wave. Thus portions of the once plane wavefront now propagate in different directions relative to other portions. As the wave propagates farther, diffraction or angular scattering causes constructive and destructive interference which introduces fluctuations in amplitude as well as phase. These time varying amplitude and phase fluctuations represent an undesired complex modulation of the carrier.

The actual satellite signal encompasses a spectrum of frequencies because of the transmitted modulation. This transmitted signal can

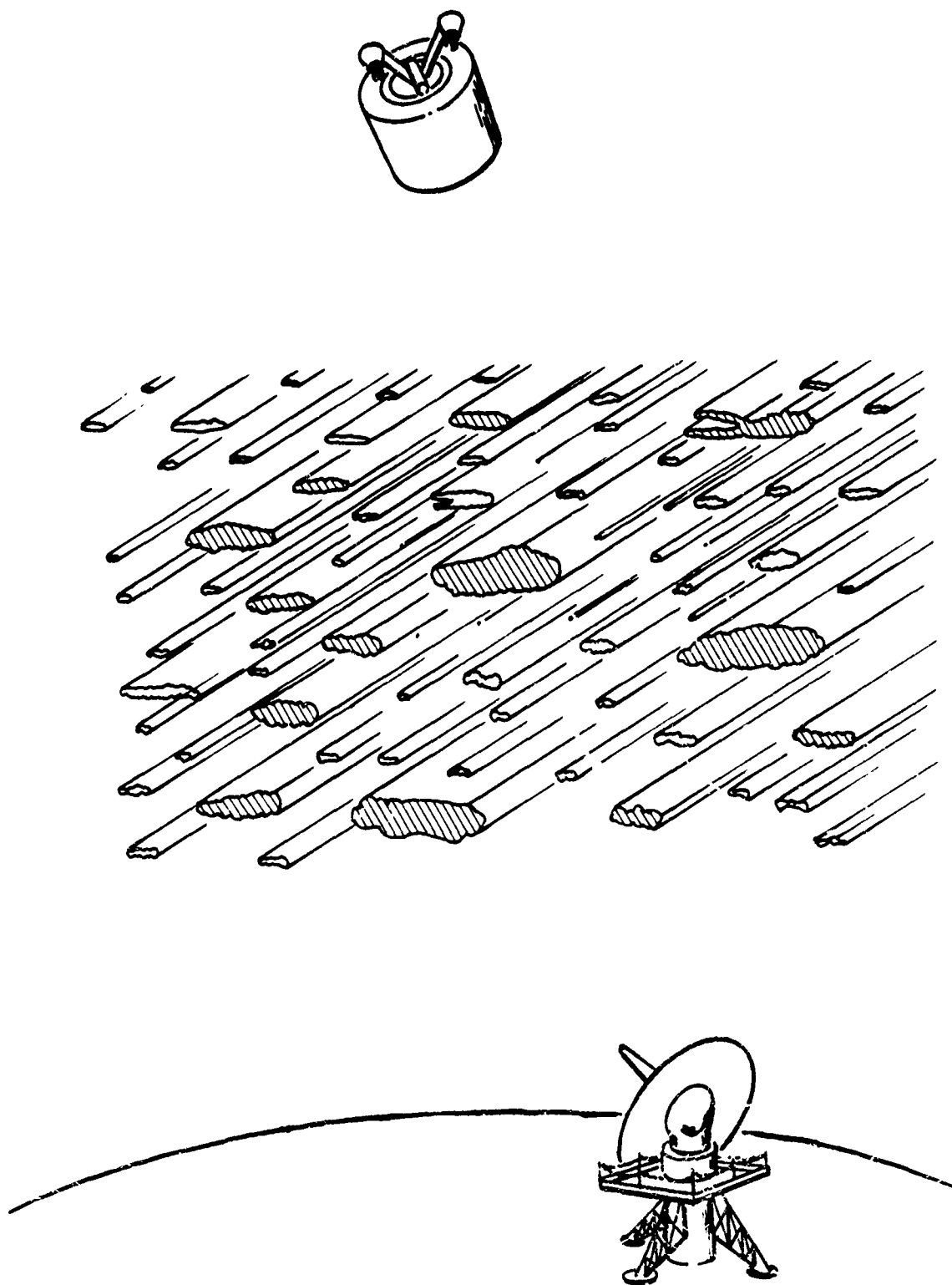


Figure 2-1. Propagation of signals through a disturbed transionospheric communications channel.

be Fourier decomposed, and the propagation of each spectral component can be analyzed. Because the phase velocity in an ionized medium depends on wave frequency, each spectral component experiences somewhat different phase perturbations and hence exhibits different amplitude and phase scintillations after propagating to the receiver. Thus the received signal spectrum is distorted by both the temporal (time selective) and dispersive (frequency selective) properties of the ionospheric channel.

Radio-wave propagation through an extended region of irregularities has been studied for many years by numerous researchers (Bramley, 1954; Ratcliffe, 1956; Mercier, 1962; Tatarskii, 1967 and 1971; Ishimaru, 1978 and references therein). Although partial solutions are available in both weak (Tatarskii, 1967) and strong scattering cases (Fante, 1975 and 1981), no general analytical solution has been obtained even for a single frequency, much less for a wide-band signal. However, the problem may be solved by the use of an analytical/numerical technique known as the multiple phase-screen (MPS) method (Knepp, 1977; Wittwer, 1978).

The use of phase-screen techniques to calculate the propagation of electromagnetic waves was formulated as early as 1956 by Ratcliffe. A number of researchers have used phase-screen techniques in the solution of problems involving propagation through random media (Mercier, 1961; Salpeter, 1967; Jokipii, 1970; Buckley, 1975; Rino, 1980). Recently, phase-screen techniques have been used in the simulation of adaptive optical systems (Brown, 1975) and in the propagation of high energy laser beams subject to thermal blooming (Fleck, et al., 1976). The use of phase-screen techniques to calculate the propagation of wide bandwidth signals is new.

The analytical foundation of the MPS technique was neatly set forth by Ratcliffe in 1956. The striated ionosphere is represented by a series of thin diffracting screens at various points along the propagation path. Each screen is perpendicular to the path and consists of a random phase equal to the integrated phase change due to electron content within the local region represented by the screen. An incident electromagnetic wave emerges from the screen with this random phase shift superimposed. Thus, at any position along the path, the wave can be represented by a complex field whose amplitude and phase are functions of position in a



plane perpendicular to the nominal direction of propagation. The rippled wave field can be thought of as a collection of uniform plane waves traveling in slightly different directions. This collection of plane waves, called the angular spectrum of the wave field, is given by the spatial Fourier transform of the field distribution over the diffracting screen. The angular spectrum can be propagated to the next diffracting screen by introducing the free-space phase-shift. Transforming back to spatial coordinates yields the incident electric field distribution, which is then perturbed by the random phase-shift in this screen. The modified angular spectrum is obtained and propagated to the next screen, and the process is repeated until the field distribution is obtained at the receiver plane.

In this section the MPS propagation simulation and its limitations are described with some results included from an earlier report (Knepp, 1977). Time-domain results after propagation through a strong dispersive Gaussian lens are presented and shown to be identical to analytic results. Also shown are predictions of the expected dispersive and scattering effects due to propagation of a pseudo-random phase-shift keyed modulated waveform through a finite sized barium cloud. Measured results from a later experiment have been provided by Dr. James Marshall and are shown to be very similar to the pre-experimental predictions.

## 2.2 FORMULATION

In the parabolic approximation, let the electric field be written

$$E(x,z,\omega) = U(x,z,\omega) \exp(-ikz) \quad (2-1)$$

so that the parabolic wave equation (Tatarskii, 1971) becomes

$$\frac{\partial^2 U}{\partial x^2} - 2ik \frac{\partial U}{\partial z} + 2k^2 \Delta n(x,z,\omega) U = 0 \quad (2-2)$$

where  $k$  is the wavenumber and  $\Delta n$  is the variation in the index-of-refraction. For ionization irregularities

$$2\Delta n = - \frac{\Delta N_e}{n_c} = - \frac{r_e \lambda^2}{\pi} \Delta N_e \quad (2-3)$$

where  $\Delta N_e$  is the variation in the electron density,  $n_c$  is the critical electron density and  $r_e$  is the classical electron radius ( $2.82 \times 10^{-15} \text{m}$ ). A derivation of Equation 2-2 is presented in Section 3 for the more general case where the propagation medium has a background ionization level. In Equation 2-2 it is assumed that the mean or background ionization level is zero. In writing Equation 2-2 it is also assumed that the z-direction is the direction of propagation. The striations or irregularities are assumed infinitely elongated in the y-direction as would effectively be the case for field aligned ionization and a satellite communication link between a synchronous satellite and an equatorial ground station. These assumptions limit the application of the MPS simulation to a two-dimensional geometry with no variation in the y-direction. The simulation could easily be extended to handle a three-dimensional geometry but at considerably greater cost in computer resources.

Now assume that the ionized region has been divided into a number of thin layers, with each layer perpendicular to the direction of propagation. Consider a layer of thickness  $\Delta z$  centered at zero z. For small  $\Delta z$ , the equation for propagation through this thin layer is obtained from Equation 2-2 with the first term neglected. The remaining differential equation is easily solved.

$$U(x, \frac{\Delta z}{2}, \omega) = U(x, -\frac{\Delta z}{2}, \omega) \exp \left\{ -ik \int_{-\Delta z/2}^{\Delta z/2} \Delta n(x, z', \omega) dz' \right\} \quad (2-4)$$

The exponential quantity is simply the geometric optics phase change imparted after propagation through the layer. Equation 2-4 states that transversal of a thin layer by a propagating wave is accomplished by simply adding the phase change associated with the layer to the phase of the electric field at the entrance to the layer.

Now collapse the irregularities in every thin layer to thin phase-screens whose effect is represented mathematically by Equation 2-4.

Now the ionized medium is represented by a series of thin phase-screens separated by free-space. Equation 2-2 is valid for free-space propagation in the region between the phase-screens if the last term of the equation is neglected. The resulting equation is easily solved using Fourier transform techniques. The solution for free-space propagation from  $z_1$  to  $z_2$  can be written

$$\begin{aligned}\hat{U}(K, z_2, \omega) &= \frac{1}{2\pi} \int_{-\infty}^{\infty} U(x, z_2, \omega) e^{-iKx} dx \\ &= \hat{U}(K, z_1, \omega) \exp[iK^2(z_2 - z_1)/2k]\end{aligned}\quad (2-5)$$

$$\begin{aligned}U(x, z_2, \omega) &= \int_{-\infty}^{\infty} \hat{U}(K, z_2, \omega) e^{iKx} dK \\ &= \int_{-\infty}^{\infty} \hat{U}(K, z_1, \omega) \exp[iK^2(z_2 - z_1)/2k + iKx] dK\end{aligned}\quad (2-6)$$

Equation 2-1 may be inserted into Equation 2-6 to write the equation governing free-space propagation in terms of the electric field

$$E(x, z_2, \omega) = e^{-ik(z_2 - z_1)} \int_{-\infty}^{\infty} \hat{E}(K, z_1, \omega) \exp[iK^2(z_2 - z_1)/2k + iKx] dK \quad (2-7)$$

Equations 2-4 and 2-7 may be used to propagate an electromagnetic wave from the transmitter to the receiver as follows. Assume that the incident wave is a plane wave as it approaches the first phase-screen. Immediately after passing through this phase-screen only the phase of the electric field is affected according to Equation 2-4. The suitably modified electric field is then Fourier transformed to obtain  $\hat{E}(K, z, \omega)$  at the exit of the first phase-screen. Free-space propagation to the next phase-screen (located at  $z_2$ ) is then accomplished according to Equation 2-7. Equation 2-7 is implemented numerically in two steps; first a multiplication in K-space by  $\exp(iK^2(z_2 - z_1)/2k)$  and then by an efficient fast Fourier transform. This brings the wave to the next phase-screen where the above process is repeated until the receiver plane is reached. Thus a numerically efficient solution to the parabolic wave equation is obtained.

In effect this solution is equivalent to replacing the scattering medium by a number of diffracting phase-screens separated by free-space. For example, if three phase-screens are used to represent the geometry of Figure 2-1, the resulting MPS geometry is shown in Figure 2-2.

This formulation in two dimensions assumes that no variations occur in the third or y dimension. This is often a good approximation for ionospheric propagation because the striated ionization is often elongated parallel to the earth's magnetic field (Paulson and Hopkins, 1978; Fremouw et al., 1978). The formulation can easily be extended to three dimensions, at the expense of a significant increase in numerical computation.

### 2.2.1 Phase Power Spectral Density

Specific realizations of the random phase  $\phi(x)$  that define a phase-screen are obtained by sampling a distribution of phase-shifts having statistical properties determined by the statistics of the electron density irregularities. These statistics are specified by the spatial power spectral density (PSD) of the irregularities or, equivalently, by their spatial autocorrelation function.

The relationship between the PSD of the phase and the PSD of the in-situ electron density irregularities is obtained as follows. From Equation 2-4 the phase that defines a phase-screen is given by

$$\phi(x) = -k \int_{-\Delta z/2}^{\Delta z/2} \Delta n(x, z') dz' \quad (2-8)$$

where the frequency dependence is temporarily omitted for convenience. Using relation 2-3 the phase autocorrelation function can be formed

$$\begin{aligned} B_{\phi}(\xi) &= \langle \phi(x) \phi^*(x+\xi) \rangle \\ &= r_e^2 \lambda^2 \int_{-\Delta z/2}^{\Delta z/2} \int_{-\Delta z/2}^{\Delta z/2} \langle \Delta N_e(x, z) \Delta N_e(x+\xi, z') \rangle dz dz' \quad (2-9) \end{aligned}$$

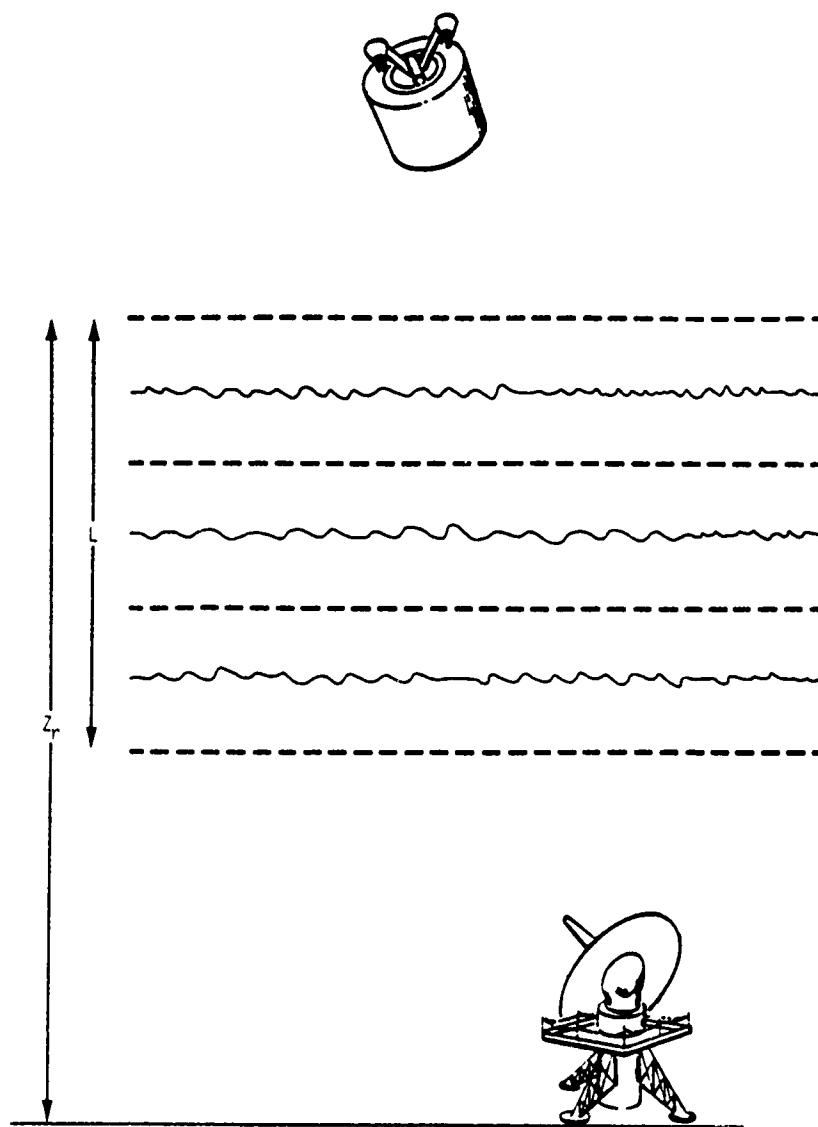


Figure 2-2. Multiple phase-screen representation of the geometry of Figure 2-1.

The quantity within the angle brackets is recognized as the correlation function of electron density fluctuations  $B_{N_e}(\xi, z-z')$ . The double integral here can be reduced to a single integration by a change of variables as explained in Papoulis, 1965, p. 325 with the result

$$B_{\phi}(\xi) = r_e^2 \lambda^2 \Delta z \int_{-\Delta z}^{\Delta z} (1-|z'|/\Delta z) B_{N_e}(\xi, z') dz' \quad (2-10)$$

If  $\Delta z$  is greater than the correlation length of the electron density fluctuations, the contribution of the second term in the integration will always be negligible so that the limits can be extended

$$B_{\phi}(\xi) = r_e^2 \lambda^2 \Delta z \int_{-\infty}^{\infty} B_{N_e}(\xi, z') dz' \quad (2-11)$$

Evaluation of this expression at  $\xi = 0$  gives for the variance of the phase fluctuations

$$\sigma_{\phi}^2 = r_e^2 \lambda^2 \Delta z \int_{-\infty}^{\infty} B_{N_e}(\xi=0, z') dz' \quad (2-12)$$

Multiplication of Equation 2-11 by  $\exp(-iK\xi)/2\pi$  and integration with respect to  $\xi$  gives

$$\begin{aligned} \frac{1}{2\pi} \int_{-\infty}^{\infty} B_{\phi}(\xi) e^{-iK\xi} d\xi &= (r_e^2 \lambda^2 \Delta z / 2\pi) \int_{-\infty}^{\infty} \int_{-\infty}^{\infty} B_{N_e}(\xi, z') e^{-iK\xi} dz' d\xi \\ &= S_{\phi}(K) \end{aligned} \quad (2-13)$$

The term on the left hand side of the equation is recognized as the phase PSD and thus the one-dimensional phase PSD is simply related to the integral of the two-dimensional autocorrelation function of in-situ electron density fluctuations. Now the relationships between one-dimensional PSD's and two-dimensional PSD's and autocorrelation functions are

$$B_1(x) = \int_{-\infty}^{\infty} S_1(K) e^{iKx} dK \quad (2-14)$$

$$S_1(K) = \frac{1}{2\pi} \int_{-\infty}^{\infty} B_1(x) e^{-iKx} dx \quad (2-15)$$

$$B_2(x,y) = \int_{-\infty}^{\infty} \int_{-\infty}^{\infty} S_2(K_x, K_y) e^{iK_x x + iK_y y} dK_x dK_y \quad (2-16)$$

$$S_2(K_x, K_y) = \frac{1}{4\pi^2} \int_{-\infty}^{\infty} \int_{-\infty}^{\infty} B_2(x,y) e^{-iK_x x - iK_y y} dx dy \quad (2-17)$$

With these transform relations in mind it is seen that Equation 2-13 has the form of Equation 2-17 and

$$S_{\phi}(K) = 2\pi r_e^2 \lambda^2 \Delta z S_{N_e}(K_x, K_z=0) \quad (2-18)$$

Equations 2-11 and 2-18 are general relationships between PSD's and auto-correlation functions of phase and electron density fluctuations.

### 2.2.2 Power Law Phase PSD

A number of different phase PSD's are available for use in the MPS propagation simulation. The most useful PSD is the power law form with phase variance, outer scale, and inner scale specified as input. The power law form is representative of many in-situ observations (Dyson, et al., 1974; Phelps and Sagalyn, 1976) as well as numerical simulations of striation spectra (Scannapieco, et al., 1976).

For this case the two-dimensional electron density PSD has the form (Shkarofsky, 1968)

$$S_{N_e}(K_x, K_z) = \frac{\sigma_{N_e}^2 (2\pi)^{-1} \ell_i^2 (\ell_i/L_0)^{(m-2)/2} K_{m/2} \left( \ell_i \sqrt{K_x^2 + K_z^2 + 1/L_0^2} \right)}{K_{(m-2)/2} (\ell_i/L_0) \left( \ell_i \sqrt{K_x^2 + K_z^2 + 1/L_0^2} \right)^{m/2}} \quad (2-19)$$

where  $K_n$  is the Bessel function of the third kind. The PSD has a

$$(K_x^2 + K_z^2)^{-m/2}$$

behavior for values of scale size between the inner scale  $\ell_i$  and the outer scale  $L_0$ . The corresponding two-dimensional autocorrelation function is given as

$$B_{N_e}(x, z) = \frac{\sigma_{N_e}^2 \left( L_0^{-1} \sqrt{x^2 + z^2} + \ell_i^2 \right)^{(m-2)/2} K_{(m-2)/2} \left( L_0^{-1} \sqrt{x^2 + z^2} + \ell_i^2 \right)}{(\ell_i/L_0)^{(m-2)/2} K_{(m-2)/2}(\ell_i/L_0)} \quad (2-20)$$

The corresponding one-dimensional phase PSD is obtained with the aid of Equations 2-12 and 2-18 as

$$S_\phi(K_x) = \frac{\sigma_\phi^2 (2\pi)^{-1/2} \ell_i (\ell_i/L_0)^{(m-1)/2} K_{m/2} \left( \ell_i \sqrt{K_x^2 + 1/L_0^2} \right)}{K_{(m-1)/2}(\ell_i/L_0) \left( \ell_i \sqrt{K_x^2 + 1/L_0^2} \right)^{m/2}} \quad (2-21)$$

where

$$\sigma_\phi^2 = \sigma_{N_e}^2 (2\pi \ell_i L_0)^{1/2} r_e^2 \lambda^2 \Delta z \frac{K_{(m-1)/2}(\ell_i/L_0)}{K_{(m-2)/2}(\ell_i/L_0)} \quad (2-22)$$

For the often used case of a  $K^{-3}$  one-dimensional phase PSD,  $m$  has a value of three and in the limit that  $L_0 \gg \ell_i$

$$\sigma_\phi^2 \approx 2(r_e \lambda)^2 L_0 \Delta z \sigma_{N_e}^2 \quad (2-23)$$

### 2.2.3 Gaussian Phase PSD

A second useful phase PSD is the Gaussian form

$$S_\phi(K_x) = \frac{1}{2} \pi^{-1/2} L_0 \sigma_\phi^2 \exp[-K_x^2 L_0^2/4] \quad (2-24)$$



which has the one-dimensional autocorrelation function

$$B_{\phi}(x) = \sigma_{\phi}^2 \exp[-x^2/L_0^2] \quad (2-25)$$

For the Gaussian PSD the relationship between the phase variance and the electron density variance is

$$\sigma_{\phi}^2 = \sqrt{\pi} (r_e \lambda)^2 L_0 \Delta z \sigma_{N_e}^2 \quad (2-26)$$

#### 2.2.4 Phase-Screen Generation

In this subsection, the numerical technique to generate a phase-screen realization for the numerical MPS propagation code is discussed. The goal here is to generate a stationary, random function  $\phi(n\Delta x)$  which represents the phase evaluated along the MPS grid. The spacing along the MPS grid is  $\Delta x$  and  $n$  is an integer representing the  $n$ 'th point on the grid. Typically  $2^{14}$  (16384) discrete points are used to represent the functions in the  $x$ -direction transverse to the direction of propagation. As will be shown,  $\phi(n\Delta x)$  is generated from initial knowledge of its PSD. In continuous notation, the phase may be written as the Fourier transform

$$\phi(x) = \int_{-\infty}^{\infty} \hat{\phi}(K) e^{iKx} dK \quad (2-27)$$

In the discrete\* case, as used in the MPS code

$$\phi(n\Delta x) = \sum_{m=0}^{N-1} \hat{\phi}(m\Delta K) e^{i2\pi mn/N} \Delta K \quad n=0, \dots, N-1 \quad (2-28)$$

Now if the Fourier transform of the phase was available, a phase-screen realization could be easily generated by using Equation 2-28. For the moment let us choose as the Fourier transform of the phase the quantity

---

\* In this section all discrete sums are taken over a range of the index from 0 to  $N-1$ .

$$\hat{\phi}(m\Delta K) = r_m [S(m\Delta K)L/2\pi]^{1/2} \quad (2-29)$$

where  $S(m\Delta K)$  represents discrete values of the known desired phase PSD. In the following it is proven that this choice is correct. Here  $\Delta K = 2\pi/L$ ,  $L$  is the length of the MPS grid,  $\Delta x = L/N$  and therefore  $\Delta x \Delta K = 2\pi/N$ .  $r_m$  is a complex number given as the sum of two independent Gaussian random variables with zero mean and variances of unity

$$r_m = \sqrt{1/2} (g_{1m} + ig_{2m}) \quad (2-30)$$

Successive values of  $g_{1m}$  and  $g_{2m}$  may be obtained numerically by sampling from a pseudo-random sequence of numbers with a Gaussian distribution. The factor of  $\sqrt{1/2}$  is included so that

$$\langle r_m r_n^* \rangle = \delta_{mn} \quad (2-31)$$

It is apparent that with the above choice for  $r_m$ ,  $\phi(n\Delta x)$  is the sum of a sequence of Gaussian variates and thus its real and imaginary parts both have a Gaussian or normal probability distribution. Since the phase of an individual phase-screen is a real quantity, one may choose either the real or imaginary part of  $\phi$  computed in this manner. Or since the real and imaginary parts are independent, each discrete Fourier transform may be used to generate two phase-screens with a savings in computer time.

Now since the  $r_m$  are independent, it is apparent that the Fourier coefficients defined in Equation 2-29 are also independent. Thus the phase power spectrum has the general form

$$\langle \hat{\phi}(m\Delta K) \hat{\phi}^*(n\Delta K) \rangle = \delta_{mn} S(m\Delta K) \quad (2-32)$$

which is a requirement if the phase is to be stationary (Tatarskii, 1971). That is, if Equation 2-32 is satisfied, then the phase autocorrelation function  $\langle \phi(m\Delta x) \phi^*(n\Delta x) \rangle$  depends only on the separation distance  $(m-n)\Delta x$  as it must for a stationary random variable.

In order to prove the validity of the choice of Equation 2-29 to give a realization of the phase-screen it is convenient to calculate the

discrete autocorrelation function. Under the ergodic hypothesis, ensemble averages or expectations of random fields may be replaced by spatial averages. Thus the phase autocorrelation function may be written

$$\begin{aligned} B_{\phi}(\xi) &= \langle \phi(x+\xi) \phi^*(x) \rangle \\ &= \frac{1}{L} \int_0^L \phi(x+\xi) \phi^*(x) dx \end{aligned} \quad (2-33)$$

In the discrete case of interest here

$$B_{\phi}(k\Delta x) = \frac{1}{L} \sum_n \phi(n\Delta x + k\Delta x) \phi^*(n\Delta x) \Delta x \quad (2-34)$$

Now the Fourier transform of  $\phi$  and  $\phi^*$  given by combining Equations 2-28 and 2-29 may be used in Equation 2-34 to obtain

$$\begin{aligned} B_{\phi}(k\Delta x) &= \frac{1}{L} \sum_n \sum_m \sum_{m'} (L/2\pi) [S(m\Delta K) S^*(m'\Delta K)]^{1/2} \\ &\quad \times r_m r_{m'} e^{i2\pi m(n+k)/N} e^{-i2\pi m'n/N} \Delta K^2 \Delta x \end{aligned} \quad (2-35)$$

Now

$$\sum_n e^{i2\pi mn/N} e^{-i2\pi m'n/N} = N \delta_{mm'} \quad (2-36)$$

So that Equation 2-35 becomes

$$B_{\phi}(k\Delta x) = \sum_m S(m\Delta K) e^{i2\pi mk/N} |r_m|^2 \Delta K \quad (2-37)$$

A comparison of the above equation to the continuous relationship between PSD and autocorrelation function as given by Equation 2-14 shows that the PSD of the numerically generated phase is  $S(m\Delta K) |r_m|^2$ . It is apparent that different values of the index  $m$  correspond to different spatial-frequency components of the PSD. Since  $|r_m|^2$  is the sum of the squares of two Gaussian variates, each of the Fourier components of the PSD of an

individual phase-screen is a chi-squared variate with two degrees of freedom and a mean value of  $S(m\Delta K)$ . Thus for any given phase-screen realization, the phase PSD will not, in general, be identical to the desired PSD. However, the average PSD of many such phase realizations may be obtained by taking the expected value of Equation 2-37. Since  $\langle |r_m|^2 \rangle = 1$

$$\text{AVG}[B_\phi(k\Delta x)] = \sum_m S(m\Delta K) e^{i2\pi mk/N\Delta K} \quad (2-38)$$

Therefore the average PSD obtained from many phase-screen realizations is the desired PSD,  $S(m\Delta K)$ , and Equation 2-29 is correct.

## 2.2.5 Criteria For MPS Application

The application of the MPS propagation code requires that the electric field and the phase be specified at a discrete number of grid points. The number and spacing of these points must in general satisfy the following criteria: 1) the phase distribution of a phase-screen must adequately represent the actual phase, 2) the wave should propagate without angular aliasing, and 3) edge effects or angular scattering off the end of the grid should be minimal.

### 2.2.5.1 Phase Representation

Adequate phase representation is assured if the phase-screen length  $L$  is at least 5 to 10 times as large as the phase decorrelation distance or equivalently the outer scale.

$$L > 5 L_0$$

The spacing between grid points,  $\Delta x$ , should be several times smaller than the inner scale. Thus

$$\Delta x < \lambda_i/3$$

The change in phase from one grid point to the next should be less than  $\pi$  to satisfy the Nyquist sampling theorem. Mathematically

$$\phi(x_2) - \phi(x_1) < \pi, \quad x_2 - x_1 = \Delta x$$

In terms of the distance between sample points  $\Delta x$ , this constraint can be written

$$\Delta x \left| \frac{d\phi}{dx} \right| < \pi$$

This inequality can be written in an rms sense as follows. Under the ergodic hypothesis discussed previously the autocorrelation function can be written

$$B_{\phi}(\xi) = \langle \phi(x+\xi) \phi^*(x) \rangle = \frac{1}{L} \int_0^L \phi(x+\xi) \phi^*(x) dx \quad (2-39)$$

Taking the second derivative with respect to  $\xi$  and integrating by parts

$$\frac{d^2 B_{\phi}}{d\xi^2} = - \left\langle \frac{d\phi(x+\xi)}{dx} \frac{d\phi^*(x)}{dx} \right\rangle \quad (2-40)$$

Equation 2-40 states the relationship between the autocorrelation function of the derivative of the phase and the second derivative of the phase autocorrelation function. In a mean square sense then

$$\left\langle \left( \frac{d\phi}{dx} \right)^2 \right\rangle = - \left. \frac{d^2 B_{\phi}(\xi)}{d\xi^2} \right|_{\xi=0}$$

Thus in an rms sense the above limit on the grid spacing  $\Delta x$  may be expressed as

$$\Delta x < \pi \left( - \left. \frac{d^2 B_{\phi}(\xi)}{d\xi^2} \right|_{\xi=0} \right)^{-1/2}$$

For a Gaussian phase PSD the second derivative term may be calculated from Equation 2-25 as  $-2\sigma_\phi^2/L^2$  so that the necessary condition is

$$\Delta x < \pi L_0 / \sqrt{2} \sigma_\phi$$

#### 2.2.5.2 Wave Propagation

In order to adequately represent propagation in free-space by the use of the Fourier transform relationship of Equation 2-7, it is necessary that the various functions involved be accurately sampled. To satisfy the Nyquist sampling criterion the difference in the function

$$\frac{K^2 \Delta z}{2k}$$

must be less than  $\pi$  when evaluated from one value of  $K$  to the next. Since the maximum value of  $K$  is  $\pi N/L$  where  $N$  is the number of grid points and  $L$  is the grid length, the necessary condition is

$$\frac{\pi^2 N^2 \Delta z}{2kL^2} - \frac{\pi^2 (N-1)^2 \Delta z}{2kL^2} < \pi$$

or

$$\frac{\pi^2 N \Delta z}{kL^2} < \pi$$

or

$$\Delta z < 2L \Delta x / \lambda$$

This condition may be relaxed somewhat in practice if the phase PSD is very small at large values of the wavenumber,  $K$ . In that case the high wavenumber values are cut off by the phase power spectrum and small inaccuracies in the phase are relatively unimportant.

#### 2.2.5.3 Edge Effects

Because of the discrete nature of the MPS grid representation, energy leaving one side of the grid appears on the other side. As the propagation distance  $z$  increases this effect becomes more important. This

effect must be controlled for a propagation solution to be valid. Since the scattering angle is given by

$$\theta = \frac{1}{k} \frac{d\phi}{dx} \quad (2-41)$$

where  $\phi$  is the phase at a phase-screen, the energy scattered at an angle  $\theta$  travels a distance  $z\theta$  perpendicular to the direction of propagation after propagating a distance  $z$ . To adequately insure against edge effects it is necessary that the MPS grid size  $L$  be greater than  $z\theta$  for each propagation step. Thus

$$L > \frac{z}{k} \left| \frac{d\phi}{dx} \right|$$

This expression may be represented in a mean square sense as in Section 2.2.5.1 as

$$L > \frac{z}{k} \left( - \frac{d^2 B_{\phi}(\xi)}{d\xi^2} \bigg|_{\xi=0} \right)^{1/2}$$

For a Gaussian phase PSD, the second derivative is  $-2\sigma_{\phi}^2/L_0^2$  so that the necessary condition is

$$L > \frac{\sigma_{\phi} \lambda z}{\sqrt{2} \pi L_0}$$

to minimize edge effects.

### 2.3 APPLICATION TO A GAUSSIAN LENS

In this section the numerical MPS propagation code is applied to the problem of scattering by a single, deterministic Gaussian phase lens. For this example of scattering from a non-random structure, theoretical results are obtained using the Fresnel-Kirchhoff integral equation and are shown to be identical to the numerical MPS results.

For this example a single Gaussian phase lens given by

$$\phi(x) = - \phi_0 \exp(-x^2/r_0^2) \quad (2-42)$$

is used at the first phase-screen location ( $z=0$ ) with  $\phi_0$  chosen as 10 radians and  $r_0$  set equal to the wavelength  $\lambda$ . Since  $\phi(x)$  is negative this Gaussian lens corresponds to a decrease in the ionization level below the ambient and acts as a convergent or focusing lens. A positive phase would correspond to an increase in ionization and would act as a divergent lens.

The intensity  $I = |E|^2$  was observed as a function of distance from the lens,  $z/\lambda$  as indicated in Figure 2-3. In this figure the observation screens are aligned, so that features of the diffraction pattern can be easily followed for changing propagation distance  $z/\lambda$ .

The focal length for a Gaussian lens is given by (Salpeter, 1967)

$$F = kr_0^2/2\phi_0 \quad (2-43)$$

where  $k$  is the wavenumber  $2\pi/\lambda$ . Taking  $r_0 = \lambda$  and  $\phi_0 = 10$  radians, the focal length  $F/\lambda$  is 0.31 which corresponds quite well with the value of  $z/\lambda = 0.5$ , shown in the figure where the intensity in the diffraction pattern at  $x = 0$  builds up to a maximum. At values of  $z/\lambda$  greater than the focal length, the diffraction pattern exhibits increasingly more complex patterns associated with interfering rays coming from the edges of the lens, rather than from the center.

An analytic relationship between the electric field at  $z = z_1$  and  $z = z_2$  is given by the Fresnel-Kirchhoff integral (Ratcliffe, 1956)

$$E(x, z_2) = [-i2\pi(z_2 - z_1)/k]^{-1/2} \int_{-\infty}^{\infty} e^{ik(z_2 - z_1)} \\ \times \exp\{-ik(x - \xi)^2/2(z_2 - z_1)\} E(\xi, z_1) d\xi \quad (2-44)$$

where  $E(x, z_1)$  is the electric field as a function of  $x$  in the  $z = z_1$  plane. For an initial electric field in the  $z = 0$  plane given by

$$E(x, 0) = \exp[-i\phi_0 \exp(-x^2/r_0^2)]$$



Equation 2-44 may be written as an infinite series by expanding  $\exp[-i\phi_0 \exp(-x^2/r_0^2)]$  in a Taylor series as

$$e^x = \sum_{n=0}^{\infty} \frac{x^n}{n!} \quad (2-45)$$

The resulting integral over  $\xi$  may then be analytically performed with the use of standard integral tables (Gradshteyn and Ryzhik, 1965). The resulting electric field in the  $z = z_2$  plane may be expressed as

$$E(x, z) = \frac{\exp[ikz + ikx^2/2z]}{\sqrt{ikz}} \times \sum_{n=0}^{\infty} \frac{(i\phi_0)^n}{n!} \left( \frac{2n}{k^2 r_0^2} - \frac{i}{kz} \right)^{-1/2} \exp \left( \frac{-x^2/2z^2}{\frac{2n}{k^2 r_0^2} - \frac{i}{kz}} \right) \quad (2-46)$$

This series is easily summed numerically and the results for several values of  $z/\lambda$  are shown in Figure 2-3 to be identical to the MPS code calculation for  $z/\lambda \leq 2$ .

For  $z/\lambda = 10$  the multiple phase-screen calculations deviate from the theoretical results because energy which has left one side of the grid is coming back onto the other side (this is the well known wrap-around or aliasing effect in discrete Fourier transforms). This point illustrates that care must be taken in the application of the MPS techniques to avoid erroneous numerical results.

## 2.4 APPLICATION TO A RANDOM PHASE-SCREEN

This section contains a second application of the multiple phase-screen propagation code to a problem for which analytic results are available - propagation through a thin phase-screen characterized by a Gaussian power spectral density. For this example, only one phase-screen is used to characterize the random medium. The screen is located at  $z = 0$  and is generated with a phase power spectral density (PSD) of

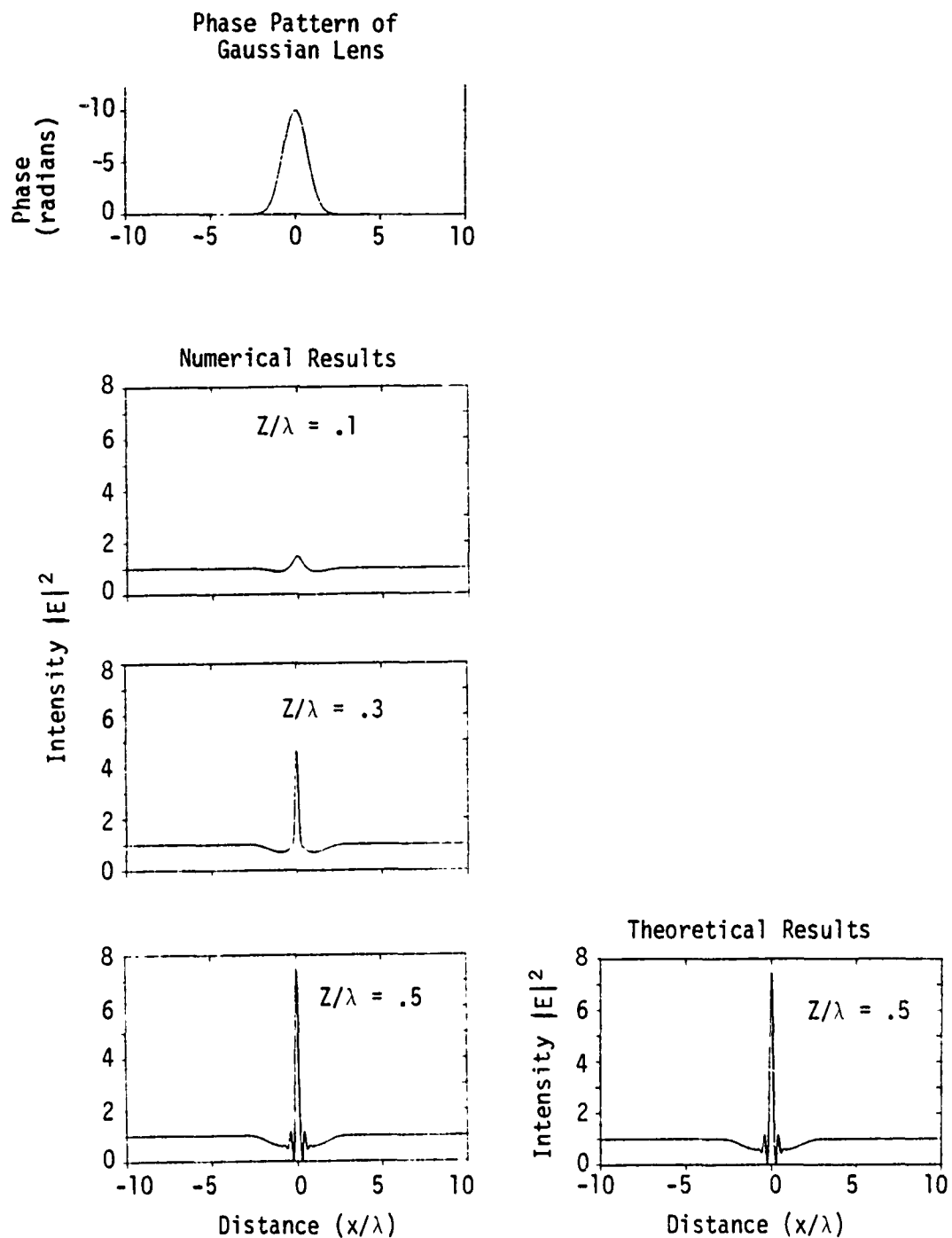


Figure 2-3(a). Diffraction pattern of a Gaussian lens--numerical results from simulation on left-hand side versus theoretical results on right-hand side.

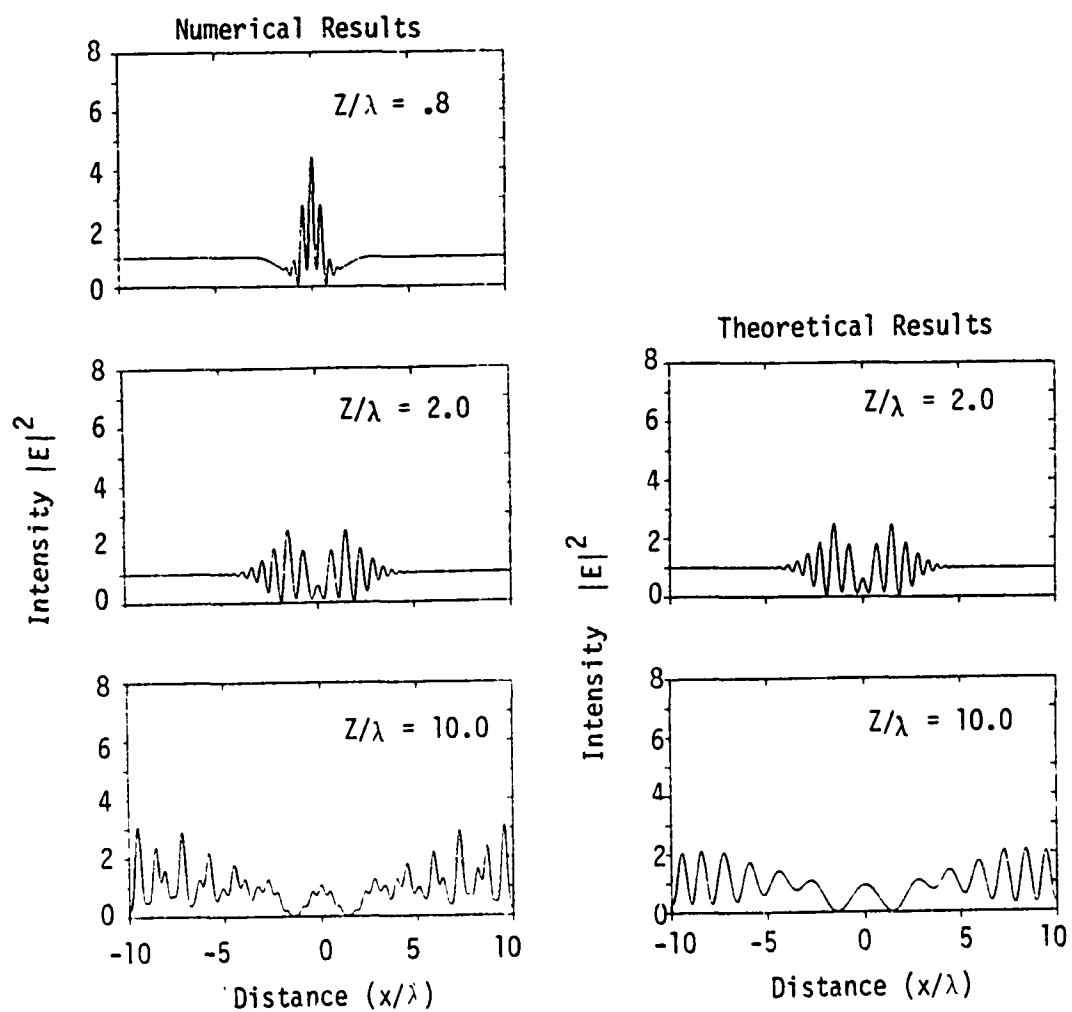


Figure 2-3(b). Diffraction pattern of a Gaussian lens--numerical results from simulation on left-hand side versus theoretical results on right-hand side.

$$S_{\phi}(K) = \frac{1}{2} \pi^{-1/2} L_0 \sigma_{\phi}^2 \exp [-K^2 L_0^2 / 4] \quad (2-47)$$

where the scale size  $L_0$  is chosen as  $\lambda$  and the phase standard deviation  $\sigma_{\phi}$  takes on the values 0.1, 1.0, and 10.0 radians. The MPS grid here is comprised of 2048 cells which represent a total length of  $30\lambda$ .

In the MPS simulation a plane wave then propagates through the single phase-screen and is observed at a number of different receiver plane locations corresponding to different values of the propagation distance from the phase-screen. At each receiver plane location defined by a value of  $z_r$ , the received electric field  $E(x, z_r)$  is observed.

To obtain statistical results for the received signal, the simulation is exercised ten times with ten different phase-screen realizations (each screen is generated using a different sequence of random numbers as discussed previously). Figure 2-4 shows a plot of one of the ten phase-screen realizations as a function of  $x/L_0$ , the normalized distance along the MPS grid perpendicular to the direction of propagation. Note the

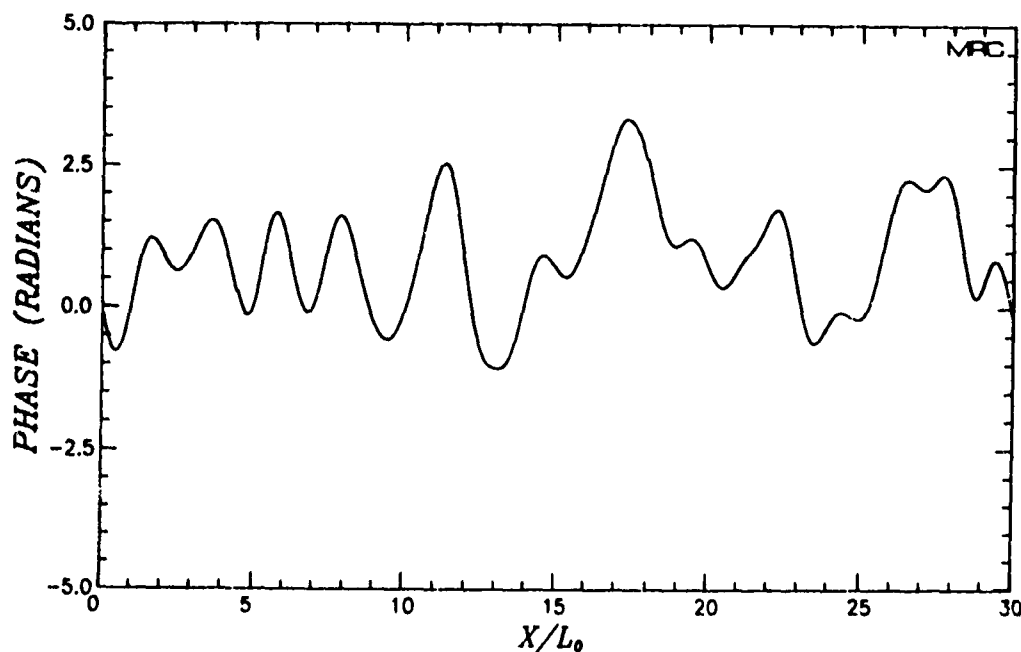


Figure 2-4. Realization of phase for a Gaussian PSD.

rather smooth plot with very little rapid phase variation. This plot is characteristic of a Gaussian PSD. The figure shows the phase over the entire MPS grid; note that the phase is generated to be continuous at the edges of the grid. This behavior is necessary to avoid errors associated with taking the Fourier transforms of discontinuous functions. Phase-screen realizations generated by the MPS code are always continuous as demonstrated here. Similarly, the received electric field also possesses this same type of continuity across the boundaries of the MPS grid.

The code has input options to provide for some statistical analysis of the generated phase-screens. Figures 2-5 and 2-6 show a comparison of the desired phase-screen PSD and autocorrelation functions versus the computed PSD and autocorrelation functions averaged over ten realizations. The phase standard deviation,  $\sigma_\phi$ , was 1 radian in the plots. As can be seen in the plots, the agreement between the desired PSD and autocorrelation functions and their numerically generated equivalents is quite good.

Figure 2-7 shows another example of a phase-screen realization which is generated using the same string of pseudo-random numbers as in the previous case. Here the phase PSD is a  $K^{-3}$  power law form with outer scale equal to the wavelength. Note that the large scale structure in both screens is quite similar since both are based on the same random number sequence. The appearance of the small scale structure in Figure 2-7 is caused by the relatively slow fall-off of the power law PSD with increasing wavenumber (decreasing scale size). Figure 2-8 shows a comparison of the MPS generated phase PSD averaged over ten realizations with the desired power law PSD. Again, in keeping with the results shown in the previous example, the agreement between numerical and desired results is quite good.

An additional check on the results of the MPS code for a Gaussian PSD is made possible by comparing analytic results for the scintillation index with theoretical results. The  $S_4$  scintillation index is defined as the normalized variance of the received power  $|E|^2$ , where  $E$  is the received complex voltage

$$S_4^2 = \frac{\langle (|E|^2 - \langle |E|^2 \rangle)^2 \rangle}{\langle |E|^2 \rangle^2} \quad (2-48)$$

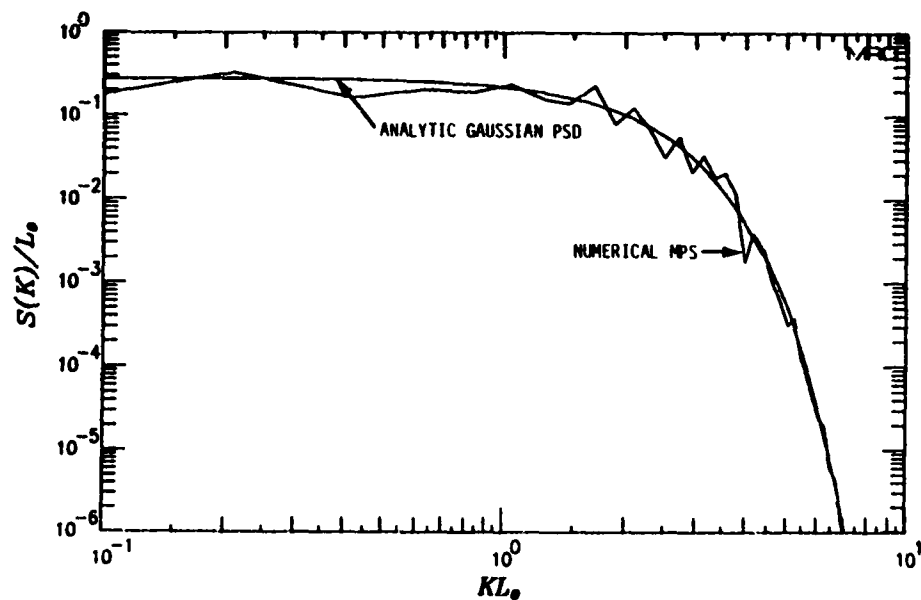


Figure 2-5. Comparison of numerically generated phase PSD with desired Gaussian PSD.

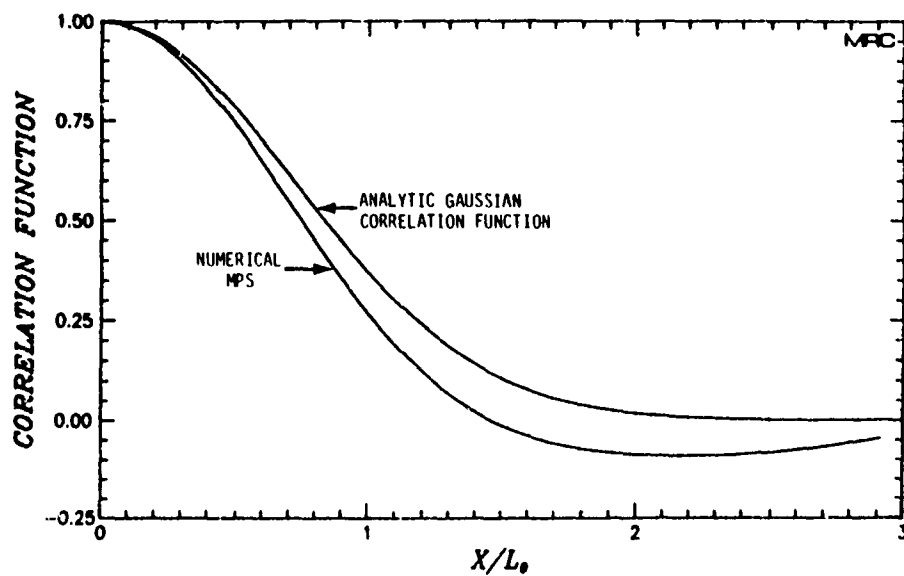


Figure 2-6. Comparison of correlation function of numerically generated phase with desired analytic correlation function.

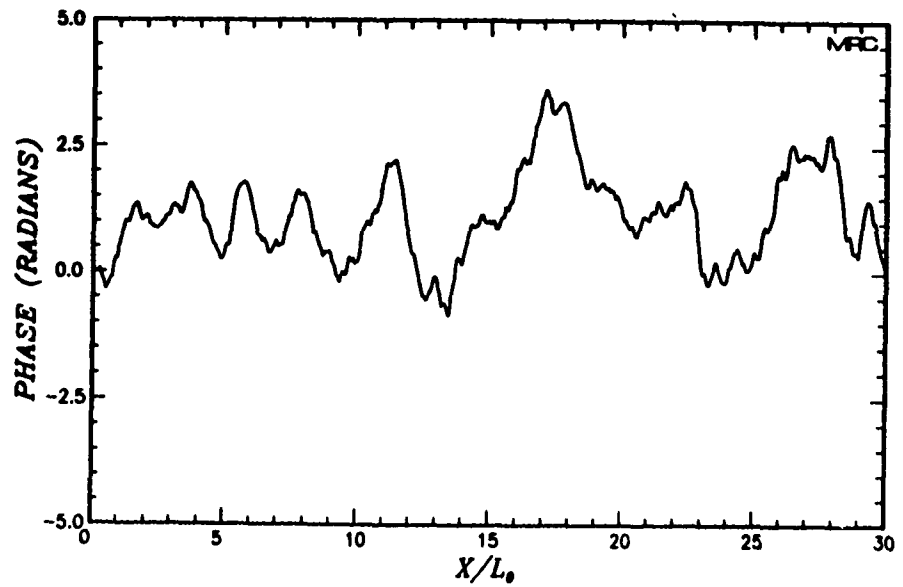


Figure 2-7. Realization of phase for a power law PSD.

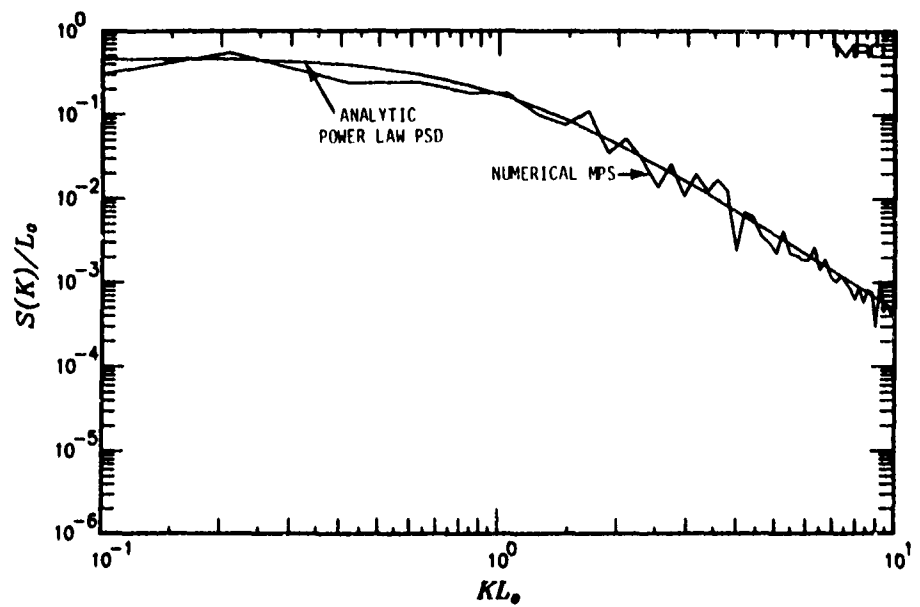


Figure 2-8. Comparison of numerically generated phase PSD with desired power law PSD.

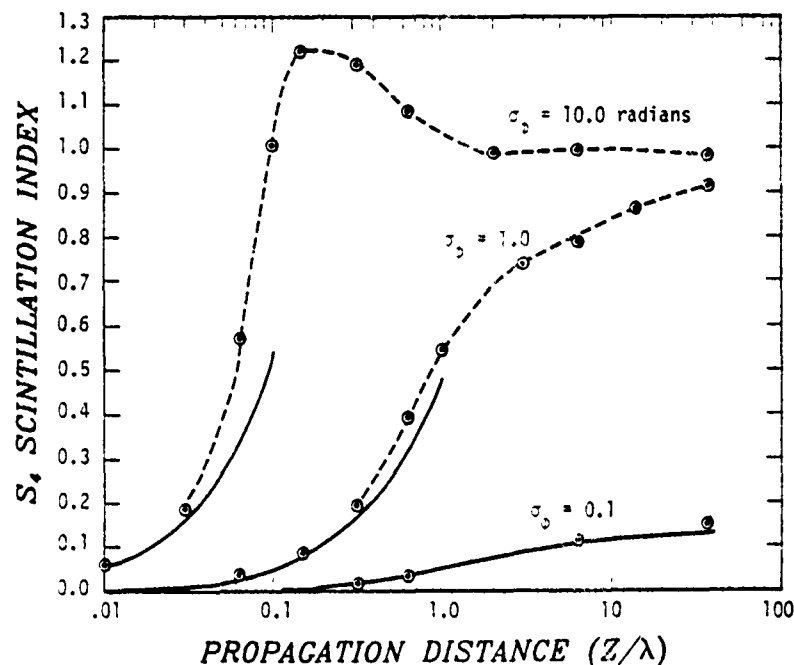


Figure 2-9.  $S_4$  scintillation index for Gaussian spectrum. The solid lines are analytic approximations valid for the weak-scatter case.

For weak scattering  $S_4^2$  is given in the thin phase-screen approximation (Salpeter, 1967) as

$$S_4^2 \approx 4 \int_{-\infty}^{\infty} S_{\phi}(K) \sin^2[K^2 z / 2k] dK \quad (2-49)$$

This integral is easily evaluated for the case of a Gaussian PSD and is plotted as a function of  $z/\lambda$  in Figure 2-9 for the three values of  $\sigma_{\phi}$  of 0.1, 1.0, and 10.0 radians. The numerical results are shown as circles in this figure and connected with dashed lines. Note the excellent agreement for small values of  $\sigma_{\phi}$  and small values of the propagation distance  $z/\lambda$  where the weak scattering theory holds. For the larger values of  $z/\lambda$ , and  $\sigma_{\phi} > 1.0$  radian the weak scattering result of Salpeter is no longer valid; in this case the scintillation index saturates at a value of unity as is predicted on theoretical grounds (Fante, 1975) and as is predicted by this and other numerical MPS calculations.



## 2.5 WIDE BANDWIDTH MPS CALCULATIONS

In the preceding formulation and examples, the MPS propagation simulation was applied to a single wave frequency. For dispersive or frequency selective ionospheric communication channels, it is necessary to first determine the Fourier components or spectrum of the transmitted signal. Then each of these Fourier components is propagated through an identical sequence of phase-screens. If  $\phi_c(x)$  is the phase distribution for the center or carrier frequency,  $\omega_c$ , then the corresponding phase shift at another frequency in the signal bandwidth is

$$\phi_\omega(x) = \frac{\omega_c}{\omega} \phi_c(x) \quad (2-50)$$

Once each signal Fourier component has been transmitted, then a Fourier transform is applied to obtain the resulting time-domain signal at the receiver.

Now if the transmitted waveform consists of a complex envelope modulated on a carrier it is shown in Section 3 that the received waveform can be expressed in terms of a complex modulation envelope as

$$v(x, z_r, t) = \text{Re} \left\{ e(x, z_r, t - t_d) e^{i(\omega_0 t + \theta_0)} \right\} \quad (2-51)$$

where the complex envelope is given by the Fourier transform

$$e(x, z_r, \tau) = (1/2\pi) \int_{-\infty}^{\infty} M(\nu) U(x, z_r, \nu + \omega_0) e^{i\nu\tau_d} d\nu \quad (2-52)$$

$M(\nu)$  is the spectrum of the transmitted signal envelope and  $U(x, z_r, \nu)$  is the solution to the parabolic wave equation for the case of irregularities infinitely elongated in the y-direction. For simplification in this section it is assumed that mean ionization effects are negligible in comparison to stochastic effects. In that case  $U(x, z_r, \nu)$  is a realization of the solution to the parabolic wave equation given by the MPS simulation for a particular value of frequency  $\nu$ .  $\theta_0$  is the total mean phase shift (at the carrier frequency) and  $t_d$  is the mean group time delay. These quantities are discussed in detail in Section 3 of this report.

In the following sections, the MPS propagation simulation is applied to obtain time-domain results for wide bandwidth signals after propagation through ionization irregularities. Two interesting cases are considered. In the first case time-domain results for scattering by a strong Gaussian lens are presented and compared to theoretical results in order to verify the MPS time-domain calculations. In the process some interesting properties of the scattering process are noted and discussed. In the second case the MPS code is used to predict the scattering properties of an ionized barium cloud through which a GPS-like pseudo-noise spread-spectrum navigation signal is transmitted on a carrier at 100 MHz.

### 2.5.1 Time-Domain Propagation Through a Strong Gaussian Lens

As an example of the MPS propagation simulation when frequency selective effects are important, the time-domain diffraction pattern of a Gaussian lens is numerically determined and compared to theory. In this example the single Gaussian phase lens is given by

$$\phi(x, f) = \frac{\phi_0 f_c}{f} \exp [-(x-x_0)^2/r_0^2] \quad (2-53)$$

where  $f_c$  is the carrier or center frequency and is 100 MHz here,  $\phi_0$  is 70 radians, the lens is located at the center of the 50 km MPS grid and has a half-width  $r_0$  of 400 m. Since the phase here is positive this Gaussian lens corresponds to an increase in ionization above the ambient and thus is a defocusing or divergent lens.

The transmitted waveform consists of a single, band-limited triangular pulse modulated on a carrier at 100 MHz. The spectrum of the transmitted pulse is given by

$$M(f) = \begin{cases} T_c \left( \frac{\sin \pi f T_c}{\pi f T_c} \right)^2, & |f| \leq \frac{1}{T_c} \\ 0, & \text{otherwise} \end{cases} \quad (2-54)$$

where  $T_c$  is roughly twice the total duration of this pulse.

If the pulse were not band-limited to  $\pm 1/T_c$ , the time domain waveform would be given as

$$m_{\infty}(\tau) = \int_{-\infty}^{\infty} T_c \left( \frac{\sin \omega T_c / 2}{\omega T_c / 2} \right)^2 e^{i\omega\tau} d\omega \quad (2-55)$$

$$= \begin{cases} 1 - \frac{|\tau|}{T_c} & , |\tau| \leq T_c \\ 0 & , \text{otherwise} \end{cases} \quad (2-56)$$

where  $\omega = 2\pi f$  and the subscript  $\infty$  refers to the infinite bandwidth case. In the case under consideration where the spectrum is limited to a total bandwidth of  $2/T_c$ , corresponding to the first nulls of the spectrum  $M(f)$ , the resulting transmitted time-domain waveform lacks the sharp triangle edges at  $\tau = 0$  and  $\pm T_c$  and is a smooth function with continuous first derivatives at these points. Also a loss of approximately 0.89 dB occurs at  $\tau = 0$  for the band-limited case as compared to the infinite bandwidth case.

The case of a single transmitted triangular waveform described above has an exact analog to the case of a ranging system that utilizes a pseudo-noise spread spectrum ranging signal. In this type of ranging system a high bandwidth phase-shift keyed signal is transmitted as a random sequence of pulses called a pseudo-noise (PN) code. A PN spread spectrum receiver is then used to correlate a local, receiver generated code with the actual received code. This correlation operation is performed in the receiver code correlator hardware. The code correlator output can be shown (Knepp and Bogusch, 1979; Bogusch, et al., 1981) to be identical to Equation 2-51 where Equations 2-52 and 2-54 define the appropriate quantities required in Equation 2-51.

Therefore the time-domain results to be presented in this section can be interpreted in either of two equally correct manners. On the one hand the results for the received signal may be interpreted as the received envelope after propagation of a single, band-limited modulated

triangular pulse through a disturbed channel. On the other hand, these same results may be interpreted as the output of the code correlator of a spread spectrum receiver. In the latter interpretation  $T_c$  is the duration of a chip of the pseudo-noise code and  $1/T_c$  is thus the chip rate. In this example the chip rate is taken as  $10.23 \times 10^6$  bps which is the rate used in the Global Positioning System (GPS). Thus the value of  $T_c$  is approximately 97.75 nsec and the two-sided bandwidth  $2/T_c$  which effectively limits the spectral region of interest is 20.46 MHz for this example.

For the case of no scintillation,  $U(x, z_r, \nu + \omega_0)$  is unity and the received signal is a smooth band-limited triangle. That is, for no scintillation

$$U(x, z_r, \nu + \omega_0) = 1 \quad (2-57)$$

and from Equation 2-52

$$e(x, z_r, \tau) = \frac{1}{2\pi} \int_{-\infty}^{\infty} M(\nu) e^{i\nu\tau} d\nu = (1 - |\tau|/T_c)_{BL} \quad (2-58)$$

where the subscript BL indicates that the triangular waveform is band-limited.

For a non-selective fading case, where the MPS solution to the parabolic wave equation,  $U(x, z_r, \nu + \omega_0)$  is independent of frequency  $\nu$  but the amplitude and phase of  $U$  are functions of  $x$ ,  $U$  can be written as

$$U(x, z_r, \nu + \omega_0) = U(x, z_r) \quad (2-59)$$

and the received complex envelope is then

$$e(x, z_r, \tau) = U(x, z_r)(1 - |\tau|/T_c)_{BL} \quad (2-60)$$

In this case the complex envelope retains the triangular form of the transmitted waveform in delay, but varies in amplitude and phase as a function of  $x$ , the distance along the MPS grid.

Note that the received signal here is a function of  $x$ , the distance along the MPS grid,  $z_r$ , the propagation distance, and  $\tau$ , the time delay. For a moving receiver, or for motion of the striations, the functional dependence on  $x$  is converted into time dependence by inclusion of an effective velocity which converts motion of the line-of-sight path into motion along the MPS grid. At a single position  $x$  or a single instant in time  $x/v_{\text{eff}}$ , it is possible to receive a signal that is non-zero over a range of delay values,  $\tau$ . This situation is the case when angular scattering acts to cause multipath effects where the signal propagates over a number of slightly different paths and thus arrives at the receiver at different delays corresponding to the different paths. The difference between time and time-delay in this context is discussed further in Section 3.2.3.1.

In the selective fading case  $U(x, z_r, v + u_0)$  is a random function of both  $x$  and  $v$  and the triangular waveform suffers distortion since each spectral component of the signal experiences different degrees of fading. The top portion of Figure 2-10 shows an example of the amplitude of the received triangular pulse for the case of non-selective fading. The bottom portions of the figure show examples of the received signal during selective fading conditions. The resulting distorted waveforms may be interpreted as being the superposition of a number of triangular signals which have propagated over different geometric paths to reach the receiver at a number of different time delays. Thus the distortion shown is always extended or elongated in the direction of increasing or positive time delay.

Most of the results to be presented for this deterministic example are obtained using the Fresnel-Kirchhoff Equation 2-46 valid for a single Gaussian lens discussed previously. These results were compared to MPS calculations and found to agree. With this in mind the two different but equivalent calculation methods will no longer be distinguished.

Now in the example under consideration, a single phase-screen defined by 16384 grid points over a distance of 50 km is used to represent the large Gaussian lens described by Equation 2-53. A plane wave

$$E(x, z=0) = 1 \quad (2-61)$$

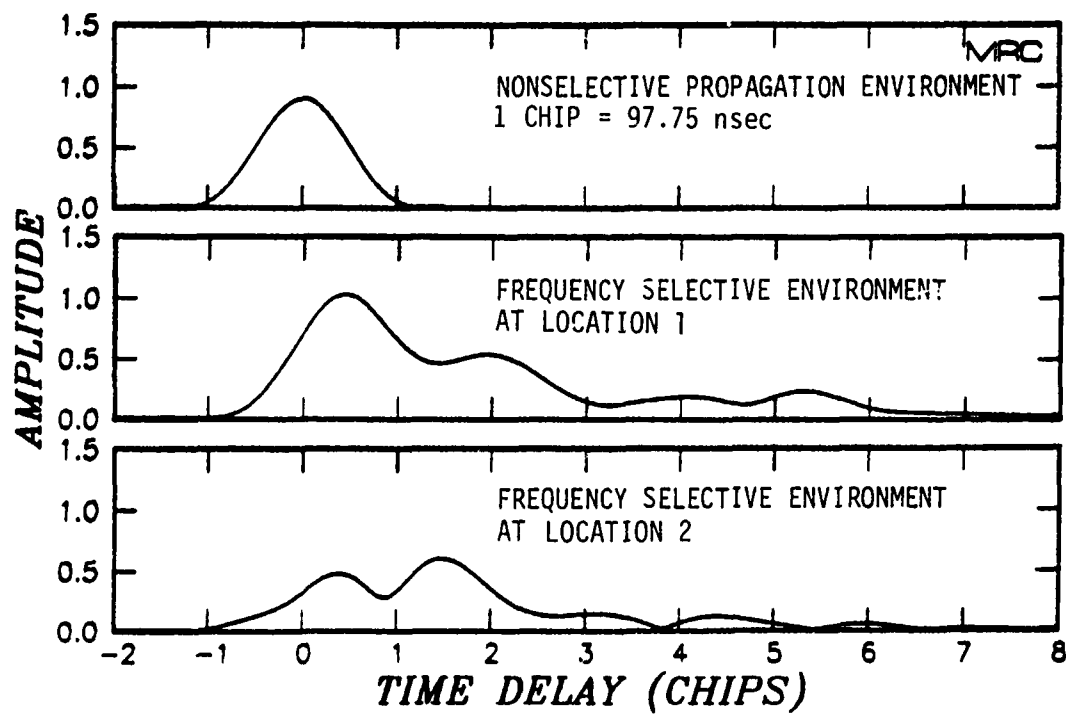


Figure 2-10. Example of envelope of wideband signal after propagation through nonselective and frequency selective propagation channels.

is incident on the lens. 64 distinct frequency components are used to represent the signal spectrum over the null-to-null bandwidth of 20.46 MHz centered at the carrier frequency of 100 MHz. Each of these frequency components of the signal is then propagated through the environment which consists of the single, strong Gaussian lens. The solution  $U(x, z_r, \nu + \omega_0)$  to the parabolic wave equation is obtained via MPS simulation at 64 values of the frequency  $\nu$  and several values of the propagation distance  $z_r$ . To obtain time-domain results for the received signal envelope Equation 2-52 is applied directly.

First consider the propagation of the single discrete frequency component at 100 MHz. Figures 2-11 to 2-15 show the received signal amplitude and phase for the 100 MHz frequency component of the spectrum at distances of 3, 5, 10, 50, and 100 km from the lens location. It can be seen that the effect of this defocusing lens is to cause energy to scatter away from the center of the lens toward the edges. Thus at distances of 3 and 5 km the energy can be seen to focus near the edges of the lens with a reduced signal level immediately below the lens center at a distance of zero on the figure. The geometric focal distance of a convergent lens of this size is 2.4 km (Equation 2-43) which corresponds reasonably well with the edge focusing observed at 5 km. At a propagation distance of 100 km it can be seen from Figure 2-15 that the signal level has faded 16 dB over a large 2 km region just below the center of the lens. At 100 km the usual ringing which occurs in any diffraction pattern is evident. Also note from Figure 2-15 that the signal level returns to 0 dB for distances greater than 10 km from the lens center. This corresponds to the incident plane wave which has propagated past the lens and remains undisturbed by the lens.

Figures 2-16 to 2-20 show the magnitude of the envelope of the received time-domain signal  $|e(x, z_r, \tau)|$  for propagation distances of 3, 10, 50, and 100 km from the Gaussian lens. In these three-dimensional figures the time-domain signal received at each succeeding value of  $x$  is plotted behind the preceding received time-domain signal. Thus the MPS  $x$ -axis is now directed into the figure.

In Figure 2-16 a 4 km interval centered immediately below the lens center is shown. Near the two ends of the  $x$  interval shown the

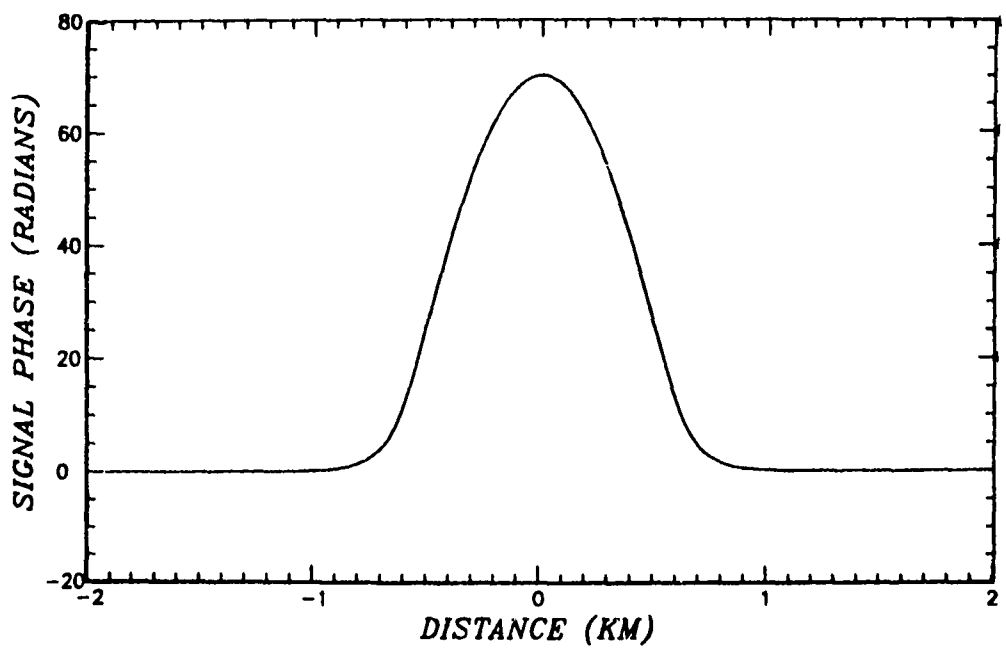
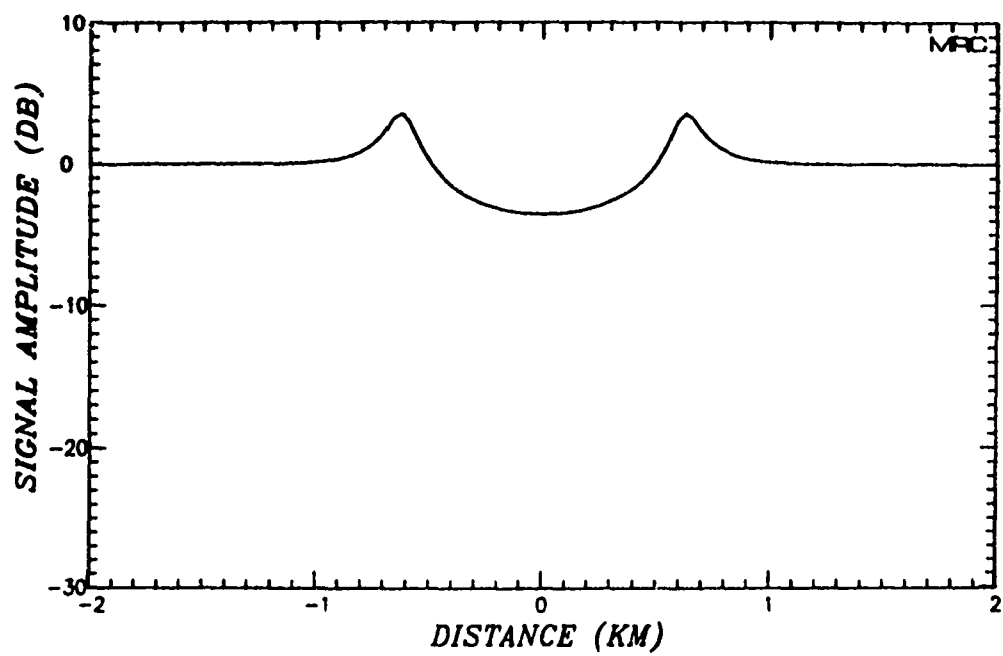


Figure 2-11. Signal amplitude and phase at 100 MHz, 3 km from a strong Gaussian lens.



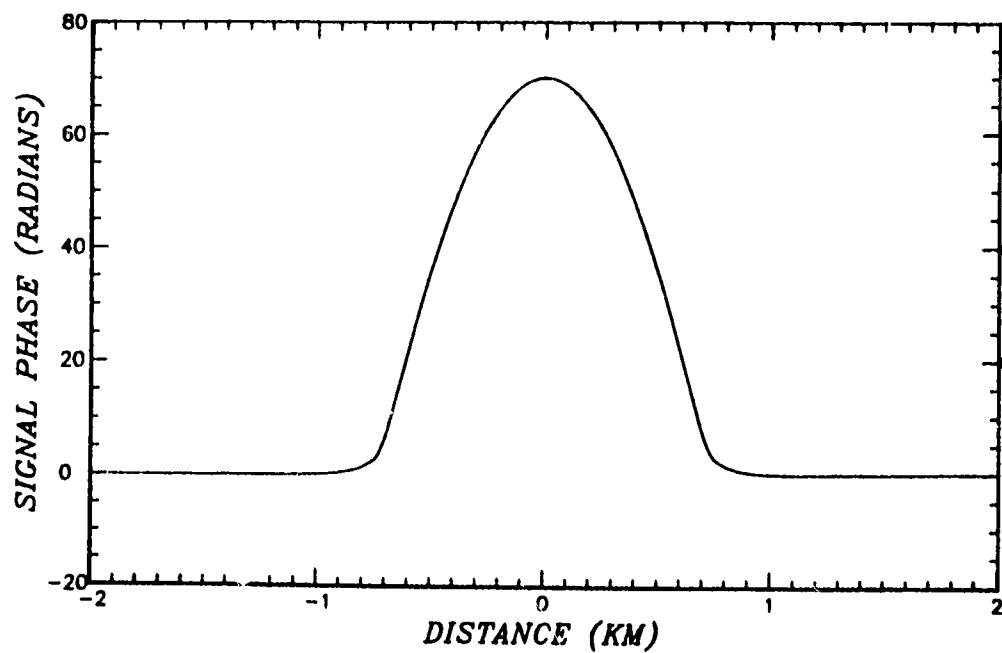
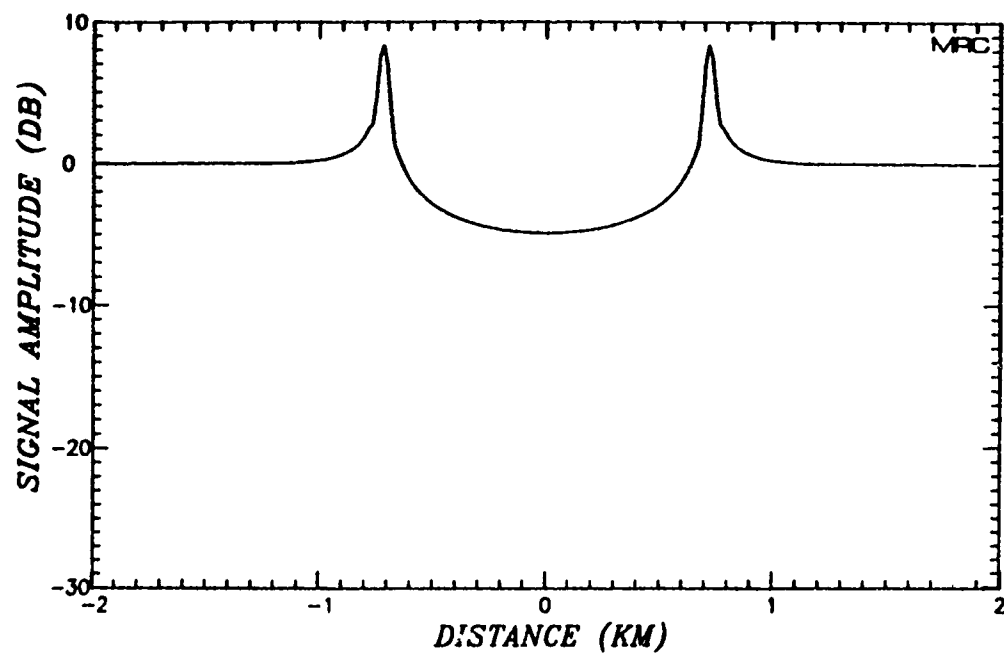


Figure 2-12. Signal amplitude and phase at 100 MHz, 5 km from a strong Gaussian lens.

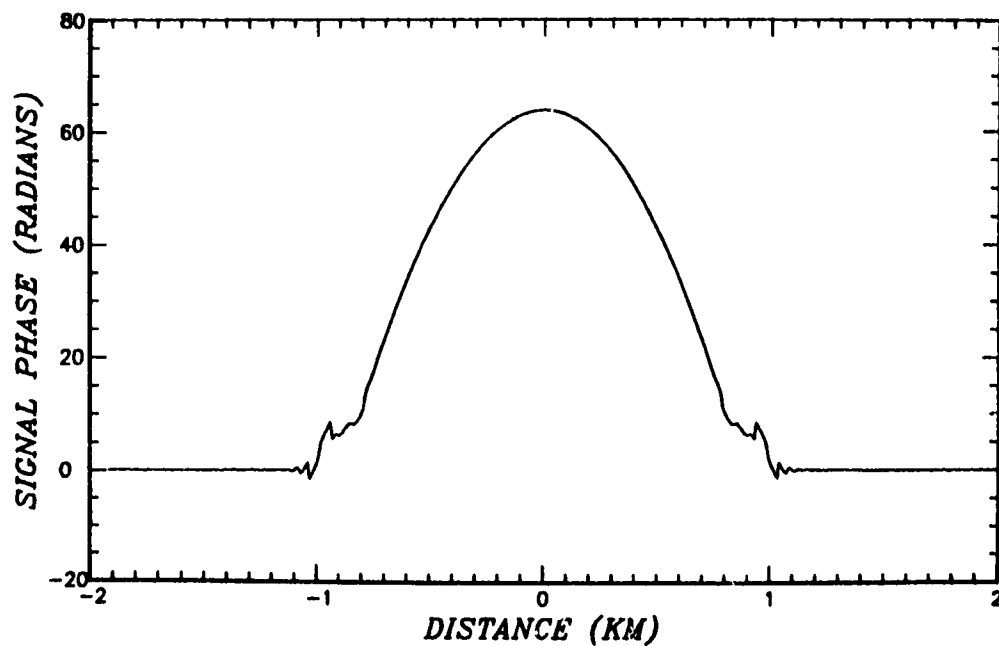
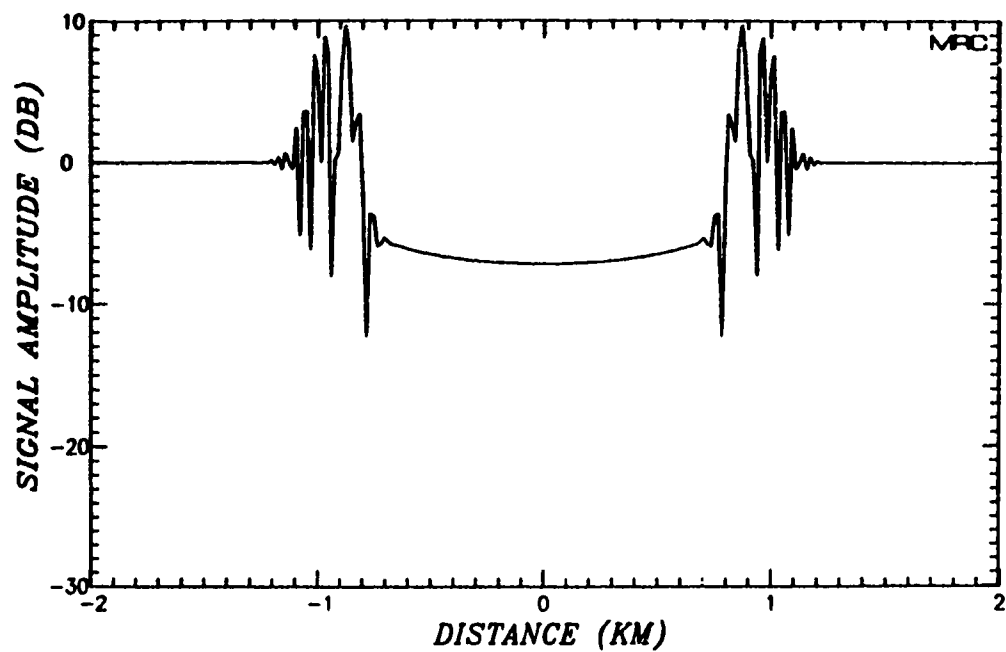


Figure 2-13. Signal amplitude and phase at 100 MHz, 10 km from a strong Gaussian lens.

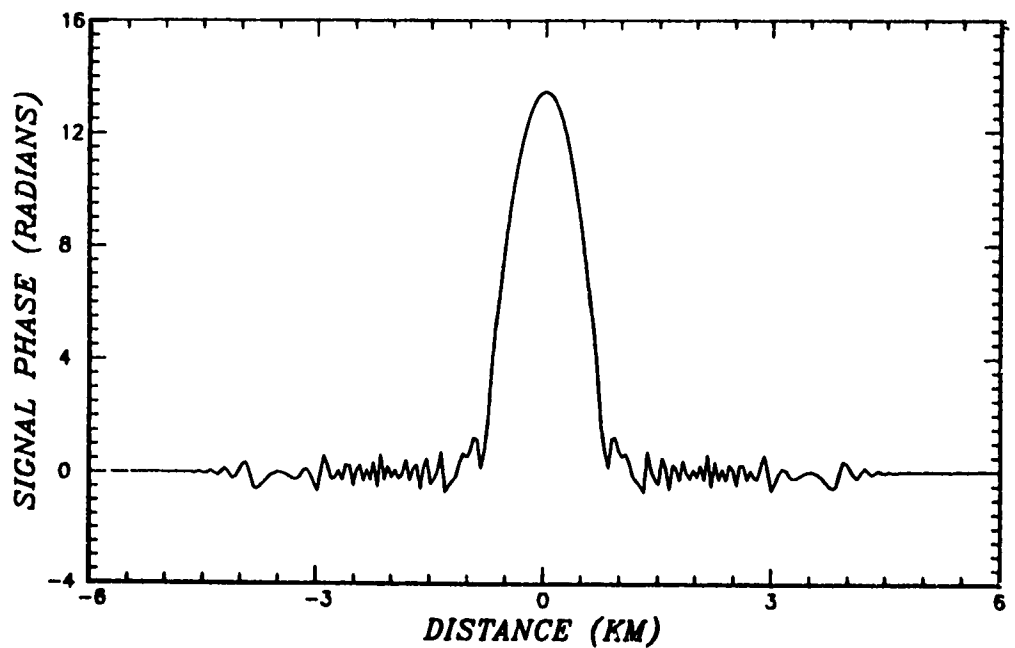
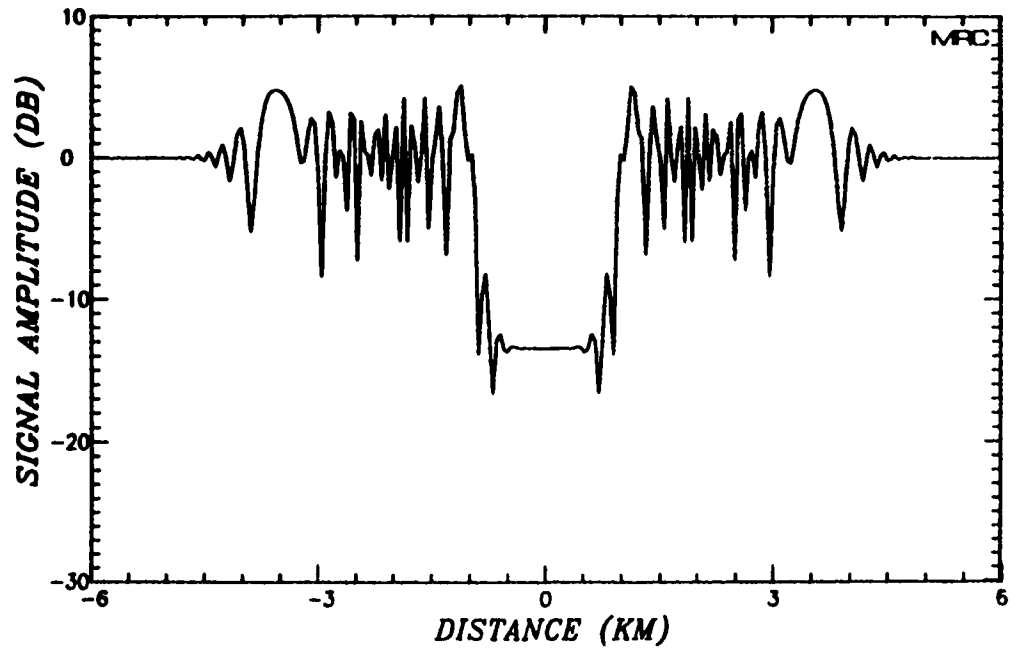


Figure 2-14. Signal amplitude and phase at 100 MHz, 50 km from a strong Gaussian lens.

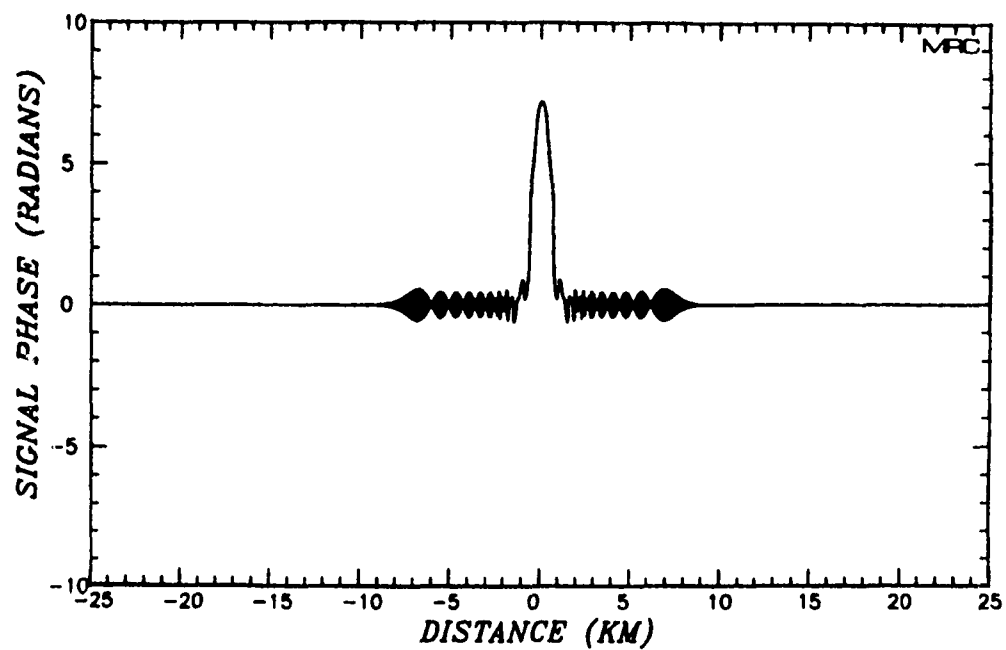
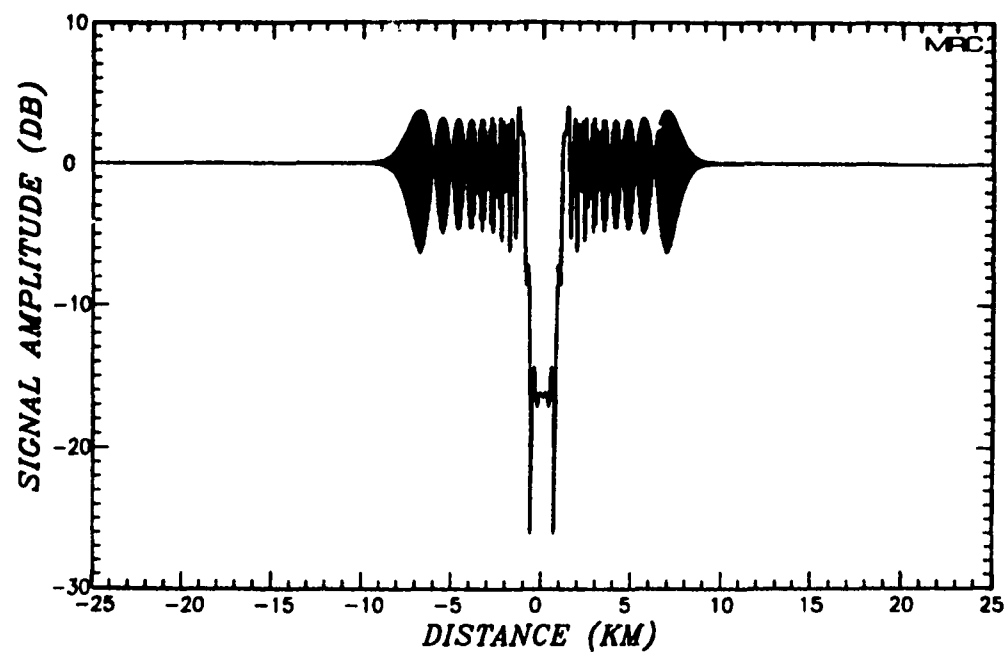


Figure 2-15. Signal amplitude and phase at 100 MHz, 100 km from a strong Gaussian lens.

received signal is identical to the transmitted signal and has the smooth shape of a band-limited triangular waveform. Near the central portion of the figure the received signal is delayed relative to the unperturbed signal. This effect is caused by the effectively greater ionization sampled by rays which travel through the center of the lens and hence experience increased time delay. Figure 2-16 also exhibits the effects of focusing which are shown as increases in signal level near the edges of the lens. This behavior was discussed previously in conjunction with Figure 2-11.

As the propagation distance increases the effects of diffraction become more evident. Figure 2-19 shows the received signal at a propagation distance of 100 km. The two main effects of the Gaussian lens are evident in this figure. First, in the central region of the figure corresponding to the region immediately below the lens center, there is a minimum in received power caused by the outward scattering of waves away from the lens center. Secondly, two secondary waves delayed up to 12 chips (1 chip = 97.75 nsec) with respect to the unperturbed wave are apparent. These two secondary waves which appear on the figure as large intersecting semicircles correspond to two outward propagating spherical waves which originate from points on the two edges of the original Gaussian lens, i.e., at  $x = \pm 400$  m.

For the MPS calculation of the scattering properties of this Gaussian lens, 16384 grid points are used to represent a spatial region 50 km in extent in the x-direction. In Figure 2-19 only 101 of these grid points are shown over a region of 20 km. Thus much of the fine detail available in the calculation is not shown in Figure 2-19.

Figure 2-20 shows a close-up of the MPS results for a propagation distance of 100 km. The 3 km region which extends to the center of the MPS grid immediately below the center of the Gaussian lens is shown. The fine details of the diffraction pattern at zero delay are shown as well as the reduced signal level directly below the center of the lens. Also note that the time delay of the wave that propagates directly through the center of the lens is correctly given by  $\phi_0/2\pi f$  which for a phase of 70 radians and a frequency of 100 MHz is  $1.11 \times 10^{-7}$  sec or 1.14 chips as shown in the figure.

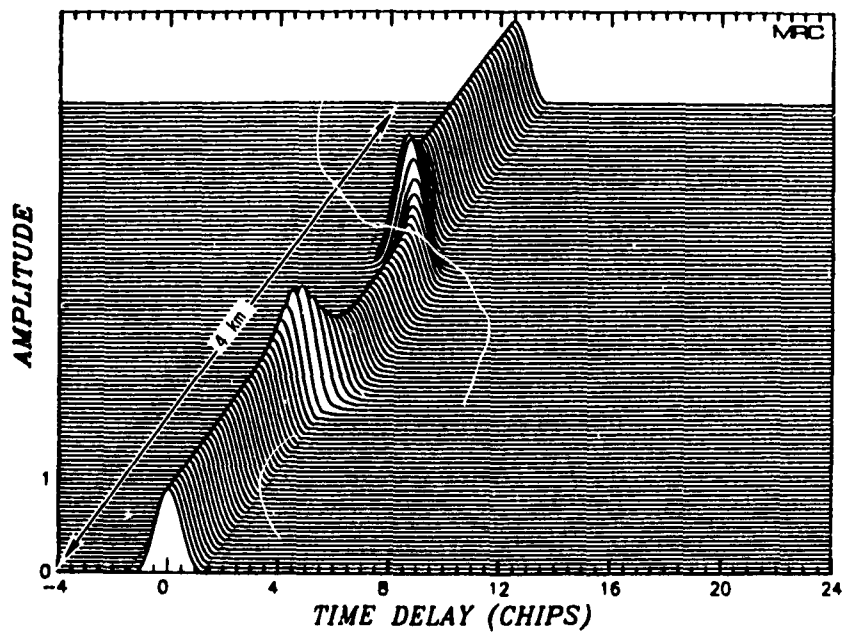


Figure 2-16. Envelope of time-domain waveform 3 km from a strong Gaussian lens.

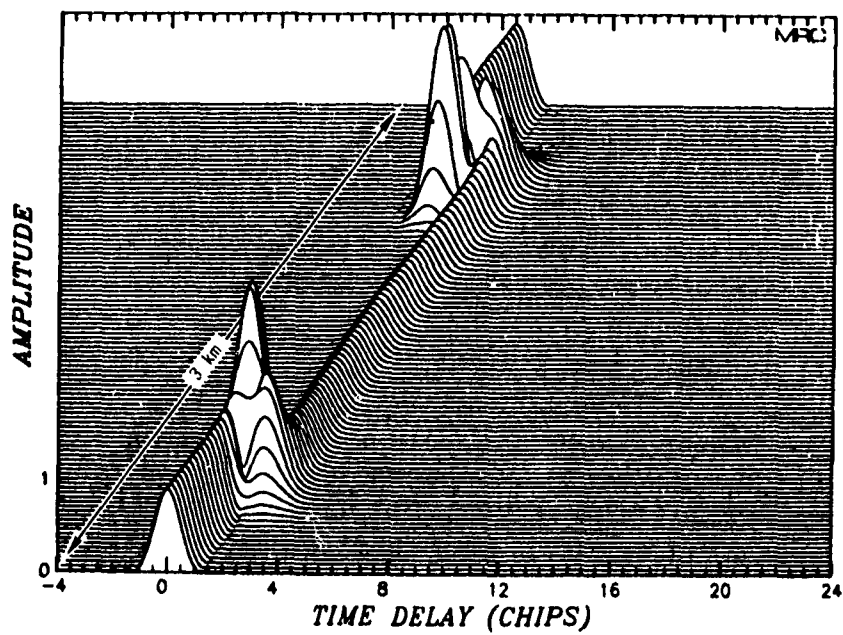


Figure 2-17. Envelope of time-domain waveform 10 km from a strong Gaussian lens.

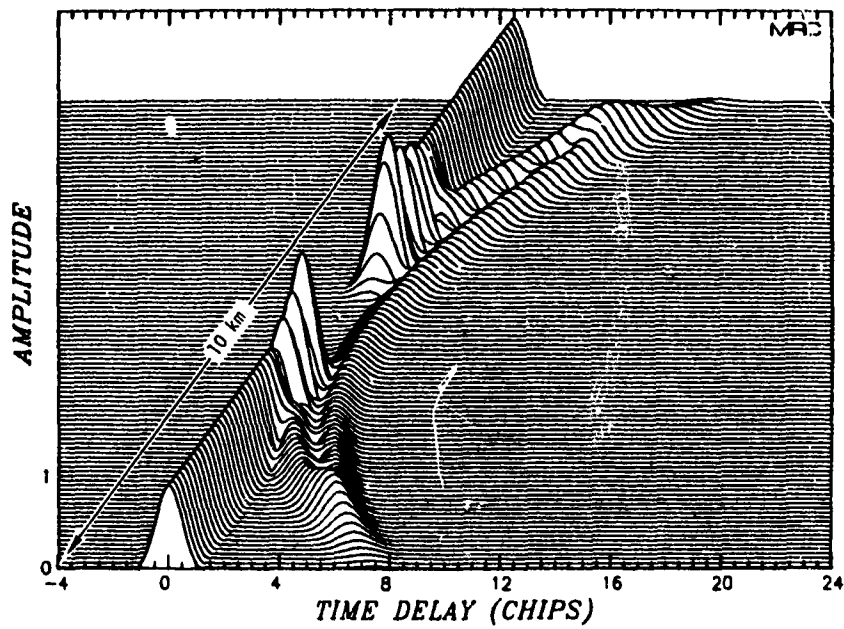


Figure 2-18. Envelope of time-domain waveform 50 km from a strong Gaussian lens.

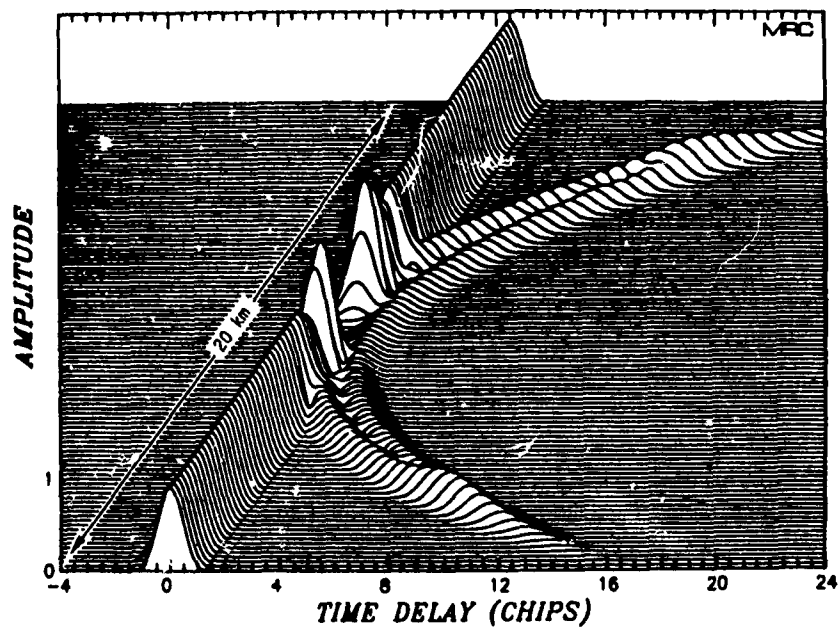


Figure 2-19. Envelope of time-domain waveform 100 km from a strong Gaussian lens.

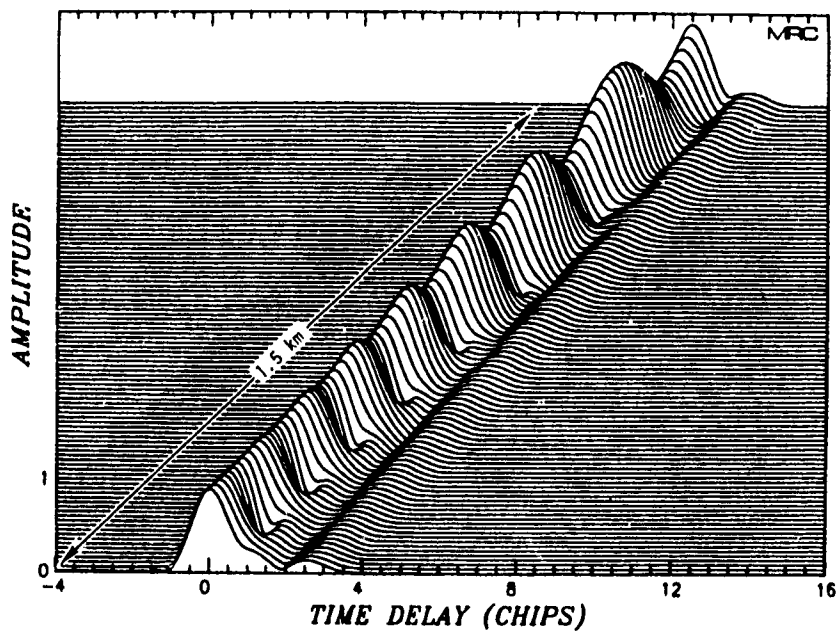
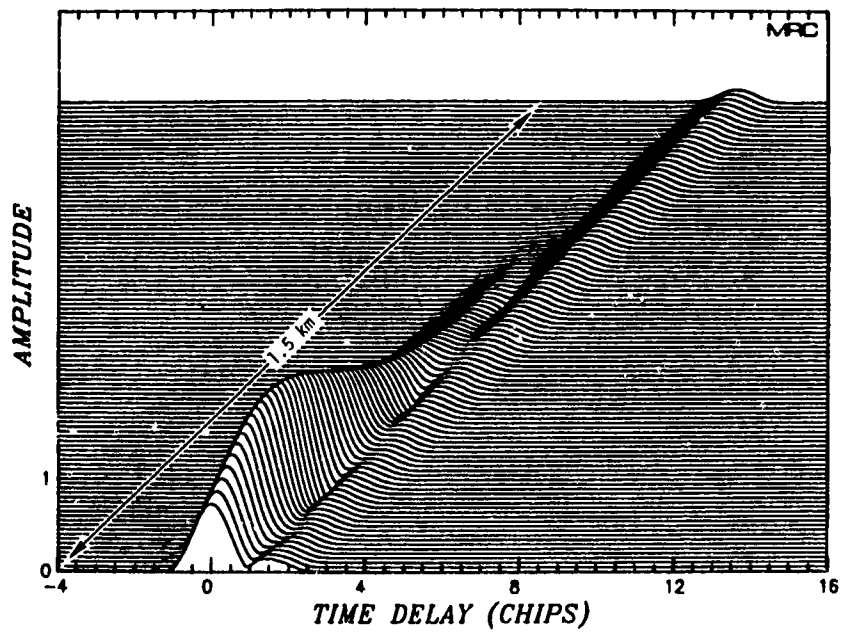


Figure 2-20. Envelope of time-domain waveform 100 km from a strong Gaussian lens.



This comprehensive example involves direct comparisons of the time-domain results from the MPS propagation simulation with theoretical results for the case of a strong dispersive Gaussian lens. Although the results are presented here as a straightforward example, many direct comparisons were performed during the work. Agreement between numerical MPS and theoretical results was obtained in all cases.

## 2.5.2 Time-Domain Propagation Through a Striated Barium Cloud

In this section the MPS propagation simulation is applied to predict the effect of a large, striated barium cloud on a wide bandwidth spread spectrum signal. Here the propagation environment caused by a striated, hour old, barium cloud is modeled as a single phase-screen. The phase-screen model is based on analysis of the data taken during the STRESS barium release series (Prettie and Marshall, 1978) 48 minutes after the release of barium cloud Esther. The propagation results are intended to provide predictions of the effects to be experienced during the PLACES\* barium release experiment scheduled for winter 1980. Back propagation data provided by Dr. Prettie were utilized to provide a phase-screen model\* of Esther at 48 minutes that is comprised of two parts: 1) a large deterministic Gaussian cloud which represents the unstriated portion of the overall barium cloud and, 2) the striations represented by a  $K^{-3}$  power-law phase PSD with phase standard deviation  $\sigma_\phi$  of 33 radians at the 100 MHz carrier frequency, with an outer scale of 390 m and an inner scale of 10 m. The deterministic Gaussian lens is given by

$$\phi(x,f) = \frac{280f_c}{f} \exp\{-(x-25)/5\}^2\} \quad \text{radians} \quad (2-62)$$

$f_c$  is the carrier frequency of 100 MHz and the distance  $x$  is given in kilometers. Figure 2-21 shows the phase-screen realization of the barium cloud used in the MPS simulation. The entire 50 km length of the MPS grid is shown in this figure. The component of the phase due to the

---

\* The details of this model are fully discussed in "Predictions of GPS X-set Performance During the PLACES Experiment," by Knepp and Bogusch, 1979. PLACES is the acronym for Position Location and Communication Effects Simulation.

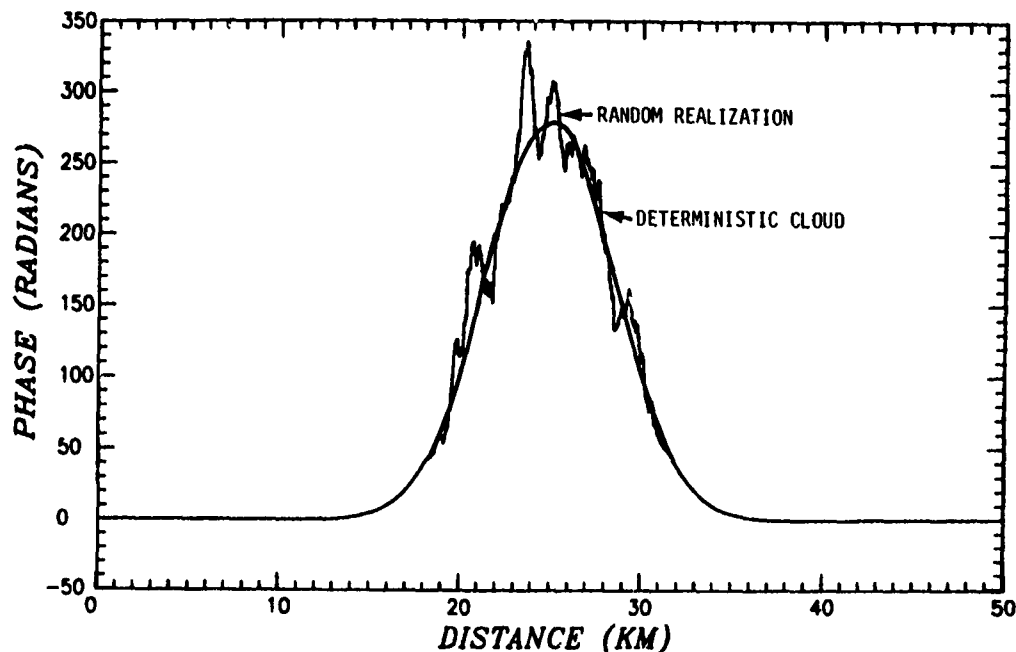


Figure 2-21. Phase-screen realization as model or scattering properties of barium cloud Esther.

deterministic Gaussian lens is plotted separately in the figure. Note that the phase-screen shown represents only a single realization of the barium cloud and thus leads to only one realization of the received signal. To obtain statistically significant results, a number of different phase-screen realizations would have to be generated using different random number sequences and the results of the propagation calculations would have to be averaged.

In the PLACES experiment the transmitted signal is a spread-spectrum pseudo-noise code at a chip rate of 10.23 Mbps. The chip duration  $T_c$  is again 97.75 nsec and the receiver is band-limited to the null-to-null bandwidth of the transmitted code, 20.46 MHz. Thus the three-dimensional plots of the received signal to be shown in this example are interpreted as the output of the receiver code correlator although no error is committed using the interpretation of transmitted and received triangular pulses discussed previously. As before 16384 MPS grid points are used to represent an actual grid 50 km in length. Again 64 distinct frequency components are used to represent the 20.46 MHz bandwidth.

For this example results are obtained with the deterministic Gaussian lens alone as well as with the entire barium cloud model. Figure 2-22 shows the time-domain signal scattered by the deterministic Gaussian lens alone at a propagation distance of 100 km. As the central point directly below the center of the barium cloud is approached from either side, increasing delay is experienced because of the increasing ionization (in the form of increased phase) along the propagation path. Directly below the cloud center the delay should be

$$\frac{\phi}{2\pi f_c} = \frac{280}{2\pi \cdot 100 \times 10^6} = 445.6 \text{ nsec} \quad (2-63)$$

or 4.56 chips as shown on the plot. Also note the increased pulse spreading in the time-domain which is apparent for that part of the received signal subject to the largest delay. This dispersive spreading is caused by the increased ionization near the center of the Gaussian lens. Finally this large barium cloud is also acting as a divergent lens to direct rays away from the lens center towards the edges of the lens. This slight edge focusing is apparent in the increased signal level near the barium cloud boundaries about 5 km from the center point.

Now consider the scattering effects of the complete PLACES barium cloud on the propagation of a 10.23 Mbps PN spread spectrum signal. Figure 2-23 shows the output of the receiver code correlator for the total PLACES barium cloud model (deterministic cloud plus striations). The entire 50 km MPS grid is shown in the figure by displaying the code correlator output at 101 equally spaced locations along the x-direction of the MPS grid. Note the increased time delay at the central portion of the cloud caused by mean electron density effects as modeled by the large Gaussian lens. Since all the striations are confined to the central region occupied by the barium cloud and each striation acts roughly as a single Gaussian lens, it is easy to explain the appearance of the undisturbed region of delay space directly beneath the center of the cloud in terms of the overlapping of a finite number of scattering patterns from strong Gaussian lenses. The effect of a single strong Gaussian lens is discussed in the preceding subsection.

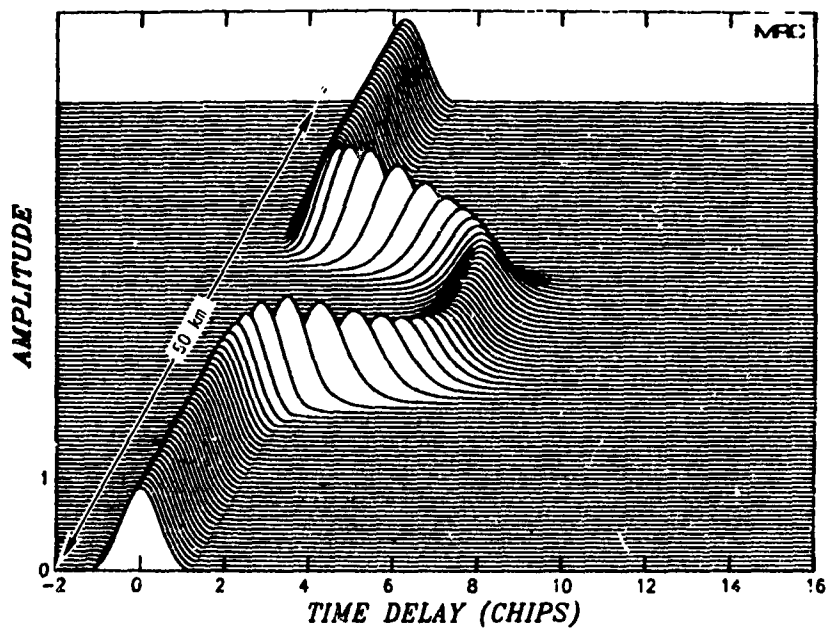


Figure 2-22. Envelope of time-domain signal after propagation through deterministic barium cloud.

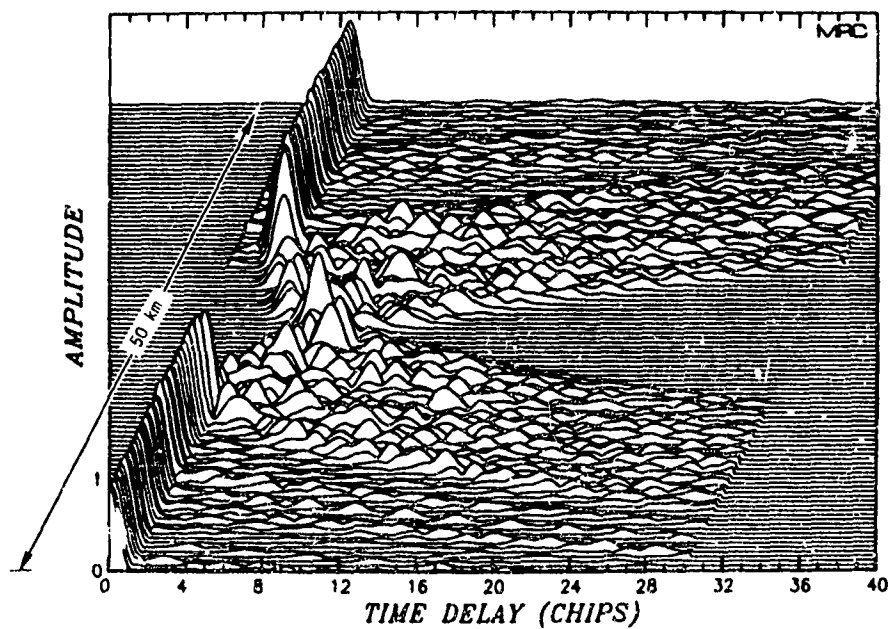


Figure 2-23. Envelope of received time-domain signal after propagation through an ionized, striated barium cloud.

Only 101 of the 16384 MPS grid points are displayed in Figure 2-23 so that there appears to be little continuity between successive individual code correlation functions. This strictly visual shortcoming is remedied in the next figure.

Figure 2-24 shows the amplitude of the code correlator output over the range from 26.50 km to 27.72 km corresponding to the scale shown on the plot of the barium cloud phase, Figure 2-21. The cloud center is located at 25 km on the MPS grid and so the 1.22 km region shown in Figure 2-24 is located just past the barium cloud center. Note how the overall signal time delay spread is increasing as the distance increases. This is due to the overlapping of the scattering patterns from the individual striations which make up the random part of the barium cloud.

Results from the actual PLACES experiment were provided by Dr. James Marshall (Marshall, 1982) and are shown in Figure 2-25. The actual experiment and these results are described in the above reference and will not be discussed here. However, it is noted that all the essential details of the experimental results were accurately predicted in advance by use of numerical MPS propagation simulation techniques. A comparison of Figures 2-23 and 2-25 shows that the major scattering features including the effects of the mean barium cloud and of the combined scattering pattern of the irregularities is accurately predicted. The total predicted time delay of around 30 chips is also in agreement in both figures. These results indicate that the MPS simulation can be used to accurately determine the effects of variations in the quantities that describe the barium cloud including mean ionization and electron density PSD.

## 2.6 HOMOGENEOUS FLUCTUATIONS - $\tau$ COMPARED TO THEORY

In this section numerical results from the MPS propagation code are compared to theoretical approximations for the two-frequency mutual coherence function and for the mean time delay and time delay jitter. Here the theoretical results for the two-position, two-frequency mutual coherence function are developed in Section 4 for the case of a homogeneous thick scattering layer. As explained in Section 4, the theoretical results

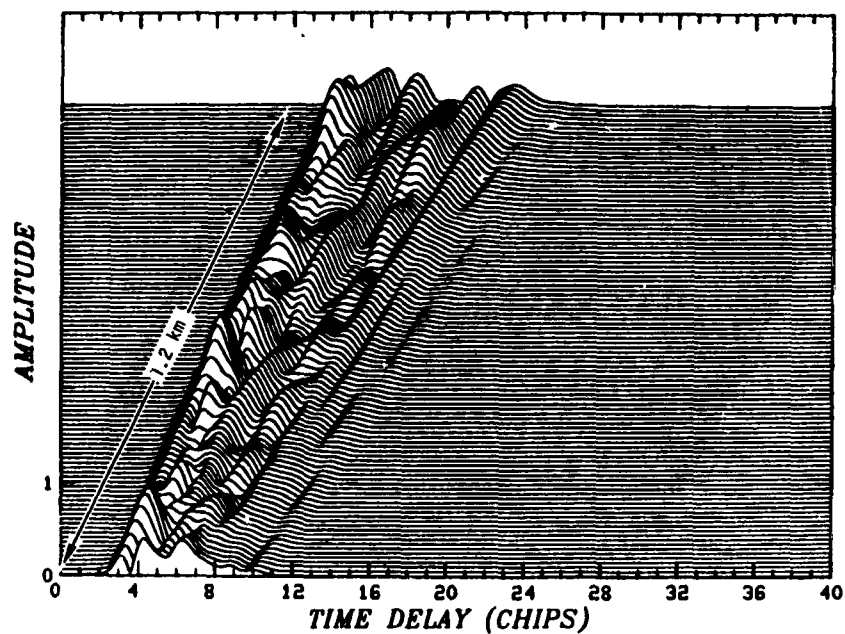


Figure 2-24. Close-up of central portion of Figure 2-23.

source: Marshall, 1982

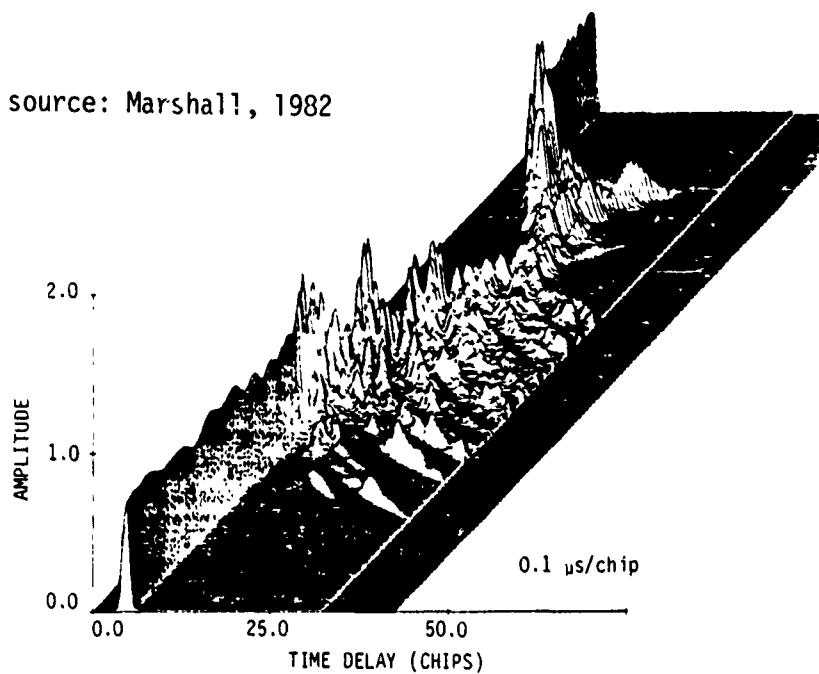


Figure 2-25. Received PN code correlator output, PLACES experiment, first beacon rocket.

are derived on the basis of a strong scattering assumption using a quadratic expansion for the phase structure-function (Sreenivasiah, et al, 1976; Sreenivasiah and Ishimaru, 1979).

First a detailed comparison of the analytic two-position, two-frequency mutual coherence function with several interesting MPS cases is presented. Then the results from a large number of MPS cases are compared to theoretical results on the basis of the  $e^{-1}$  point of  $r(\Delta x=0, \Delta f)$ .

Consider the case of plane wave propagation of a wide bandwidth signal through a strong scattering layer. The carrier frequency is 2.25 GHz, the phase standard deviation is 350 radians with a  $K^{-3}$  power-law PSD between the outer scale of 1 km and the inner scale of 10 m. The layer thickness is 1000 km and, after passage through the layer, the disturbed plane wave propagates an additional 1000 km in free-space. Ten equally spaced single phase-screens are used in the MPS simulation to represent the thick layer. Each grid consists of 16384 cells or points which represent a spatial extent of 10 km.

A total of 32 discrete frequencies are used to represent the signal spectrum over a two-sided bandwidth of 4.096 MHz. This bandwidth corresponds to the null-to-null bandwidth of a pseudo-noise (PN) spread spectrum code with a chip rate of  $2.048 \times 10^6 \text{ sec}^{-1}$  and with a chip duration of 488.3 nsec. Equivalently this null-to-null bandwidth may be used to represent a single modulated triangular pulse band-limited to 4.096 MHz with the form

$$m(\tau) \approx 1 - |\tau|/T_C, \quad |\tau| \leq T_C \quad (2-64)$$

where  $T_C$  is 488.3 nsec.

Figures 2-26 through 2-31 compare MPS results for the two-frequency mutual coherence function  $r(\Delta x, \Delta f)$  with the analytic results given by Equation 4-72. Figure 2-26 shows the magnitude of  $r$  as a function of  $\Delta f$  for parametric values of  $\Delta x$  which correspond to multiples of the distance between cells on the numerical MPS grid. The agreement between the MPS and the analytic results is seen to be quite good for this case with some bias toward a higher calculated correlation than predicted analytically.

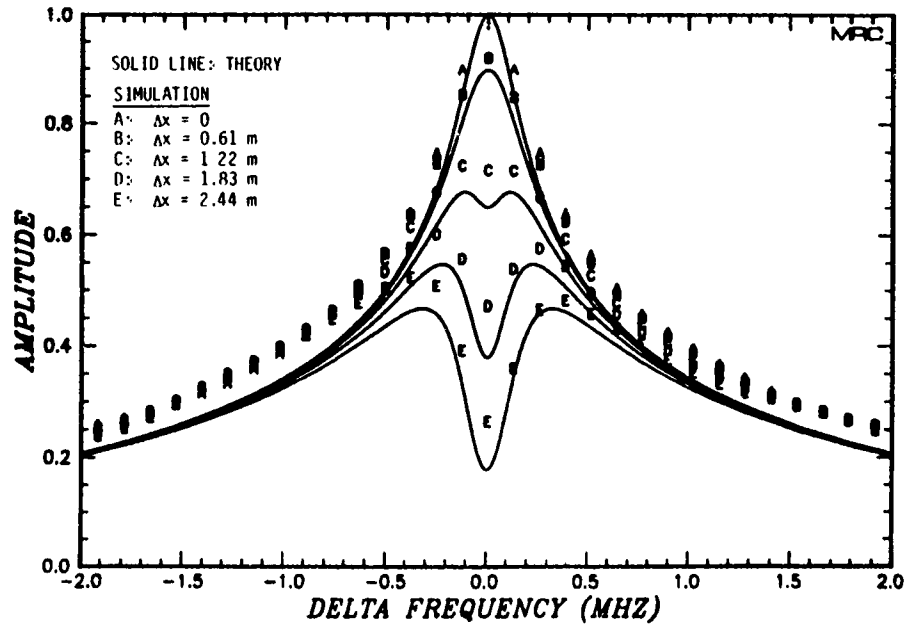


Figure 2-26. Comparison of magnitude of  $r$ , single MPS realization versus theory.

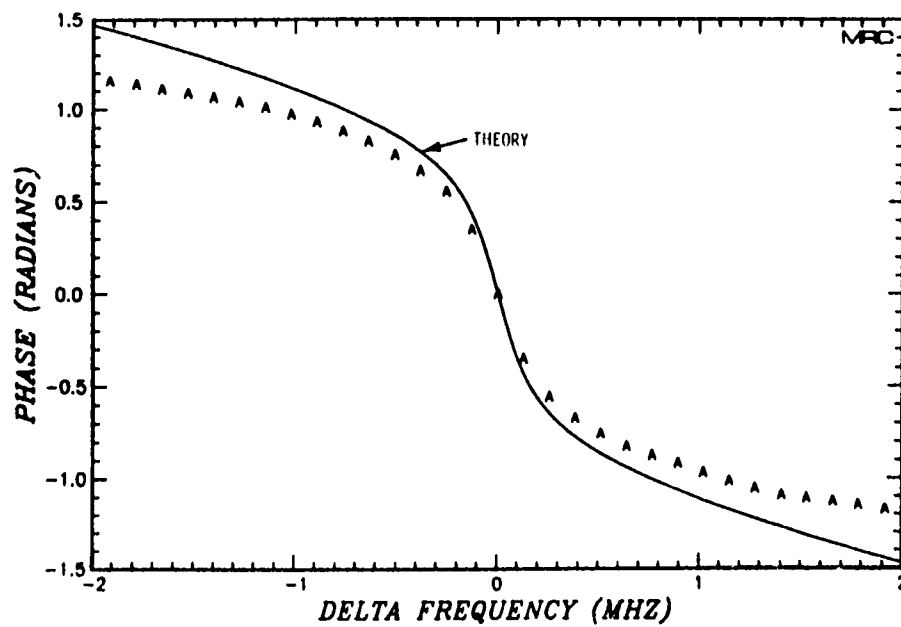


Figure 2-27. Comparison of phase of  $r$ , single MPS realization versus theory,  $\Delta x = 0$ .



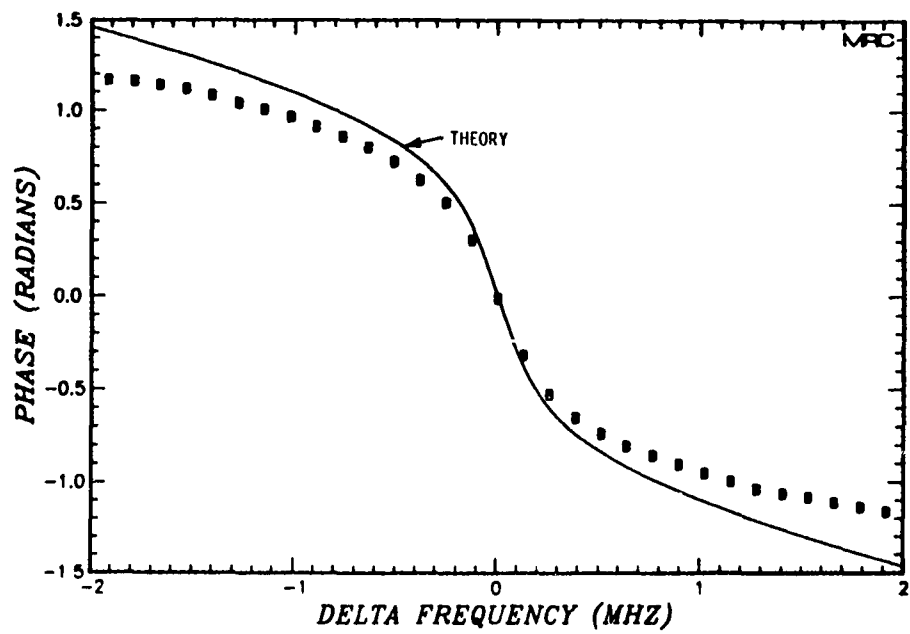


Figure 2-28. Comparison of phase of  $r$ , single MPS realization versus theory,  $\Delta x = 0.61$  m.

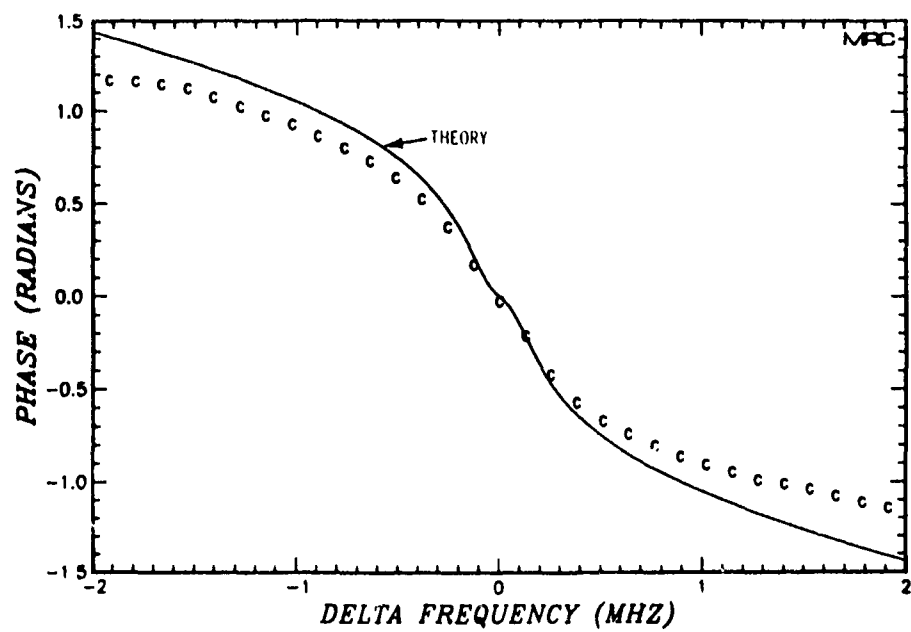


Figure 2-29. Comparison of phase of  $r$ , single MPS realization versus theory,  $\Delta x = 1.22$  m.

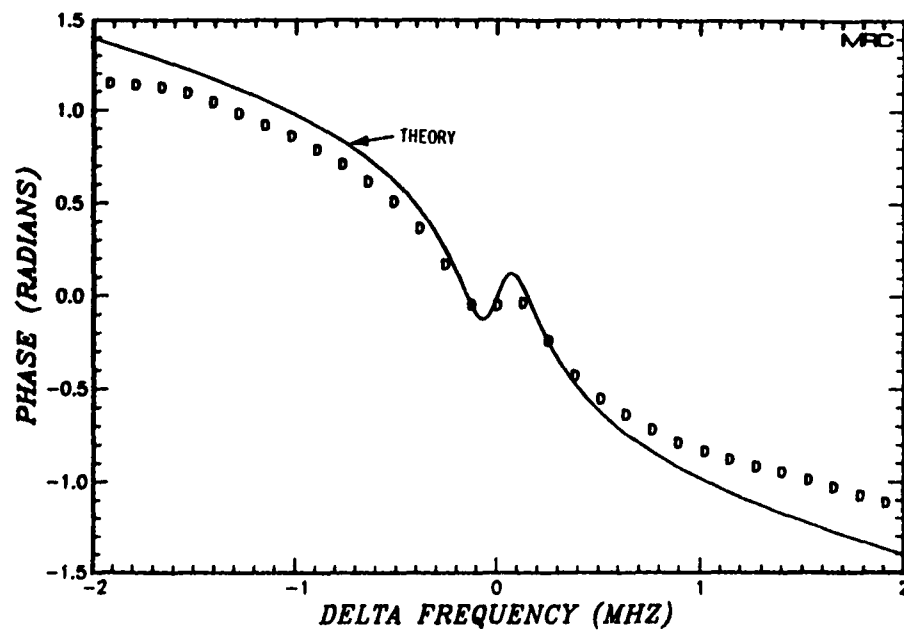


Figure 2-30. Comparison of phase of  $r$ , single MPS realization versus theory,  $\Delta x = 1.83$  m.

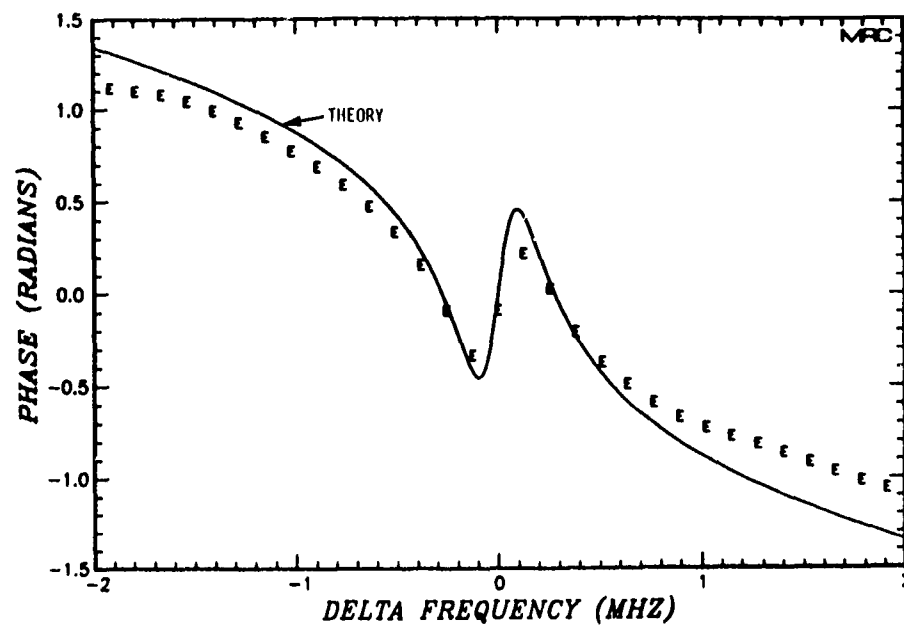


Figure 2-31. Comparison of phase of  $r$ , single statistical realization versus theory,  $\Delta x = 2.44$  m.

One of the assumptions involved in the strong scattering theory discussed in Section 4 is that the bandwidth of interest is small relative to the center frequency so that the refractive index may be taken to be independent of frequency within the frequency band of interest. As a result of this assumption the analytic two-frequency mutual coherence function is symmetric about the center frequency. As can be seen, the MPS result for  $r$  is not symmetric about zero  $\Delta f$  but is close enough to justify the analytic approximation. Since the index-of-refraction is a function of frequency, symmetry about zero  $\Delta f$  does not actually occur; but, as is shown in the figure, this symmetry can be a valid approximation.

Figures 2-27 through 2-31 compare the MPS results for the phase of  $r(\Delta x, \Delta f)$  with the analytic results. The numerical MPS results are shown at the same  $\Delta x$  values as shown in the amplitude results just compared. Again the comparison is quite good especially in the most important region near the carrier frequency where  $\Delta f$  is small. This region is important to time-domain calculations since in any modulation format most power is transmitted at or very close to the carrier frequency with a gradual decrease in transmitted power spectral density for frequencies farther displaced from the carrier frequency.

Figure 2-32 shows an example of the time-domain results for this homogeneous MPS case. The amplitude of the received triangular waveform,  $|e(x, z_r, \tau)|$  is plotted. 101 curves are shown in the figure as a three-dimensional plot with curves for successive  $x$ -values plotted behind those for prior  $x$ -values. Each individual curve represents the received time-domain signal observed at an individual MPS cell, separated from the next by 0.61035 m. This plot shows only the first 101 cells of the total of 16384 generated but is quite useful to display the time-domain results because of the homogeneous geometry.

Figure 2-33 shows the average pulse shape defined as the average over  $x$  of the amplitude of the received complex envelope

$$\langle |e(x, z_r, \tau)| \rangle_x$$

where the subscript on the angle brackets indicates that the averaging is performed over  $x$ . The curve shown is obtained by averaging only the first

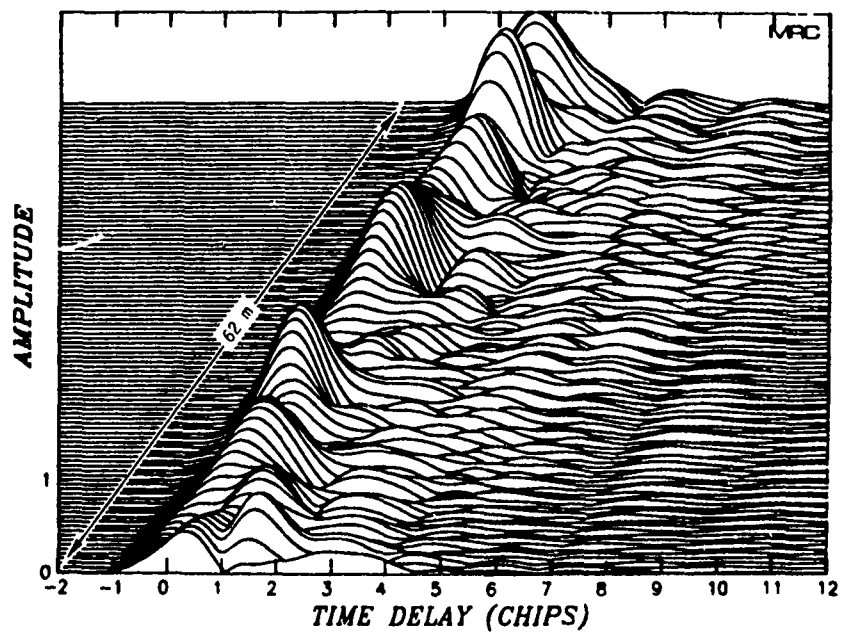


Figure 2-32. Envelope of received time-domain waveform--first 101 x-values from MPS simulation.

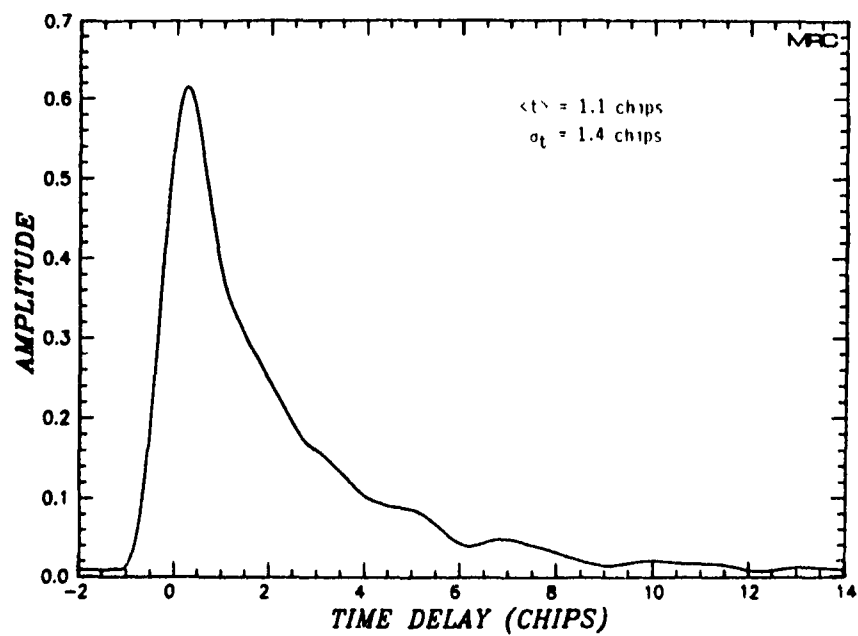


Figure 2-33. Average received time-domain envelope--MPS signal realization.

2048 points of the total 16384 point MPS realization. This case is discussed in more detail in Section 3 where a generated statistical signal realization is compared to the MPS results shown here.

Figures 2-34 to 2-37 show additional comparisons of MPS calculations of the magnitude of  $r$  with the analytic, strong scattering results of Section 4. The cases shown are calculated for a satellite communication system with an 80 MHz bandwidth spread spectrum signal at a carrier frequency of 7.5 GHz. All four cases have a  $K^{-3}$  one-dimensional phase power spectrum.

In Figures 2-34 to 2-36, the MPS grid length is 30 km with 16384 grid points, the striation layer thickness,  $L$ , is 14000 km with a free-space propagation distance  $z_r - L$  of 1000 km (see Figure 2-2). In all three figures the inner scale is 10 m. In Figure 2-34  $\sigma_\phi$  is 300 radians and the outer scale is 3 km. Figure 2-35 shows results for a similar case to Figure 2-34 but with a smaller phase standard deviation,  $\sigma_\phi$ , of 150 radians. In the comparison shown in Figure 2-36,  $\sigma_\phi$  is 100 radians and the outer scale is 1 km. The results shown in Figure 2-37 are for a layer thickness of 1000 km centered 1500 km from the receiver plane. Here the outer scale is 10 km, the inner scale is 10 m and the MPS grid length is 100 km with 16384 grid points.

The agreement between the MPS results and the analytic results is quite good for all these cases with the largest difference, on the order of 20 to 30 percent near the maximum frequency deviation  $\Delta f$  of 40 MHz shown for Figure 2-37. However, this case shows evidence of signal focusing with a measured  $S_u$  scintillation index of 1.15 characteristic of non-saturated scintillation; as such the strong scattering assumption involved in using a two term expansion for the phase structure-function is invalid.

In order to make possible a comparison of a large number of MPS calculations with analytic results, one feature of  $r(\Delta x=0, f)$  is selected for comparison purposes. Figure 2-38 shows the comparison of the selected measure  $f_r$ . The quantity  $f_r$  is defined such that, if the magnitude of  $r(\Delta f, \Delta x=0)$  is larger than  $1/e$  for  $f_{\min} \leq \Delta f \leq f_{\max}$ , then the value of

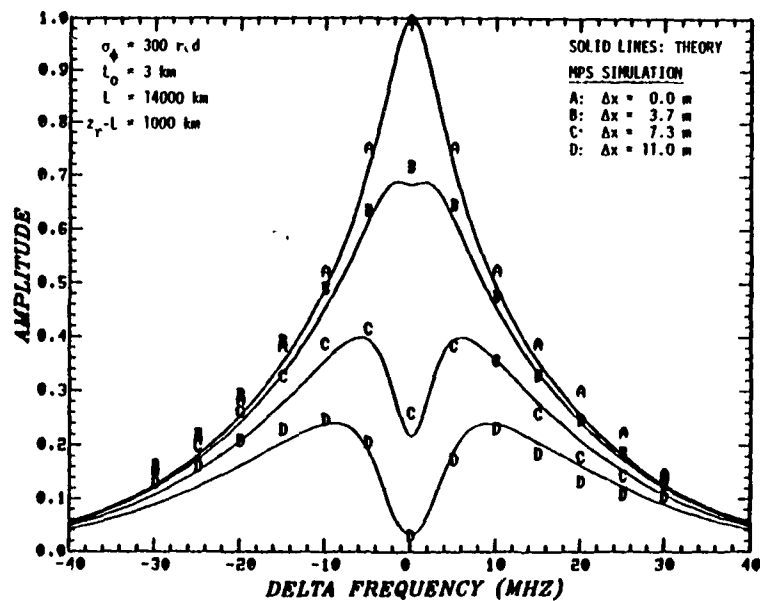


Figure 2-34. Comparison of amplitude of  $r$ , single MPS realization versus theory.

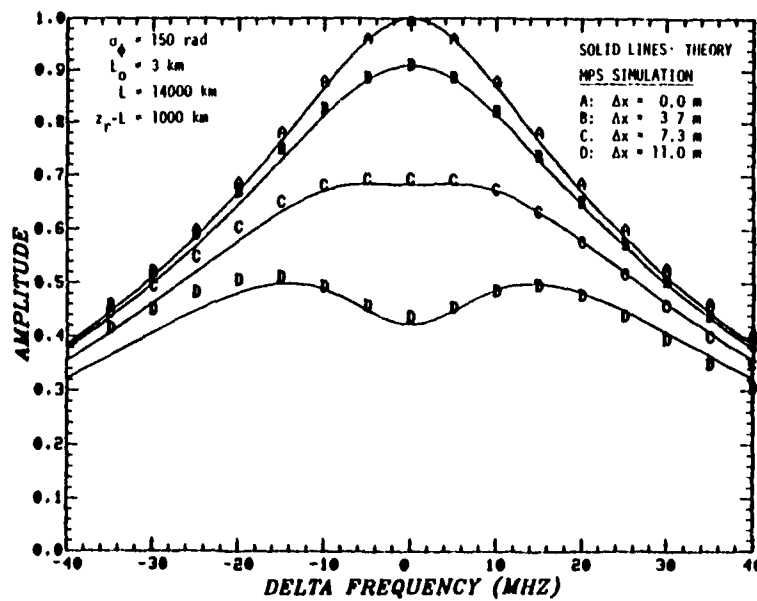


Figure 2-35. Comparison of amplitude of  $r$ , single MPS realization versus theory.

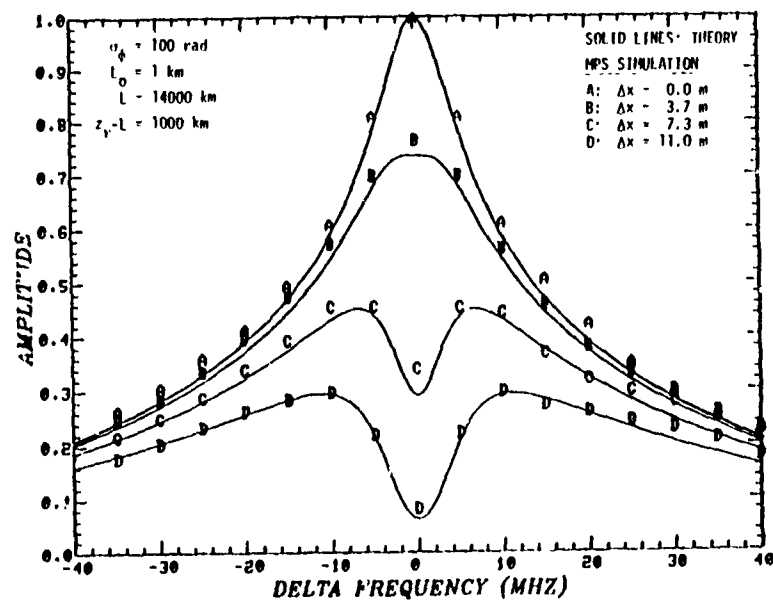


Figure 2-36. Comparison of amplitude of  $r$ , single MPS realization versus theory.

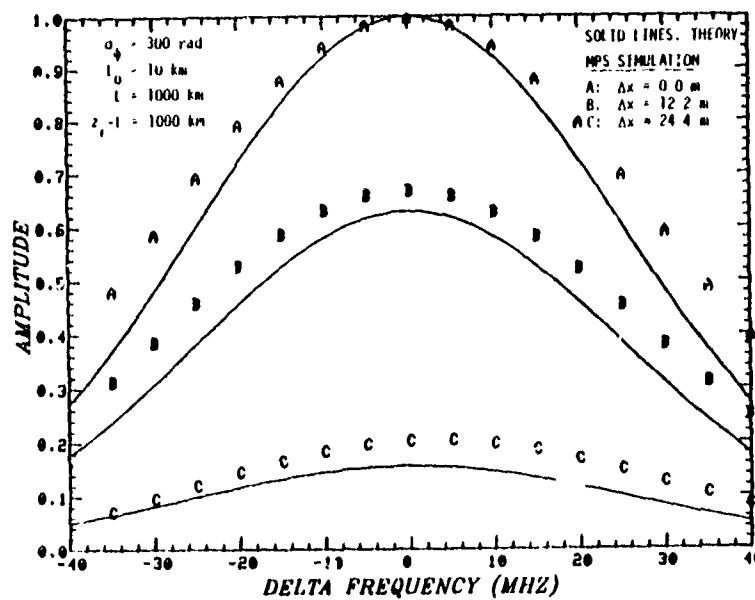


Figure 2-37. Comparison of amplitude of  $r$ , single MPS realization versus theory.

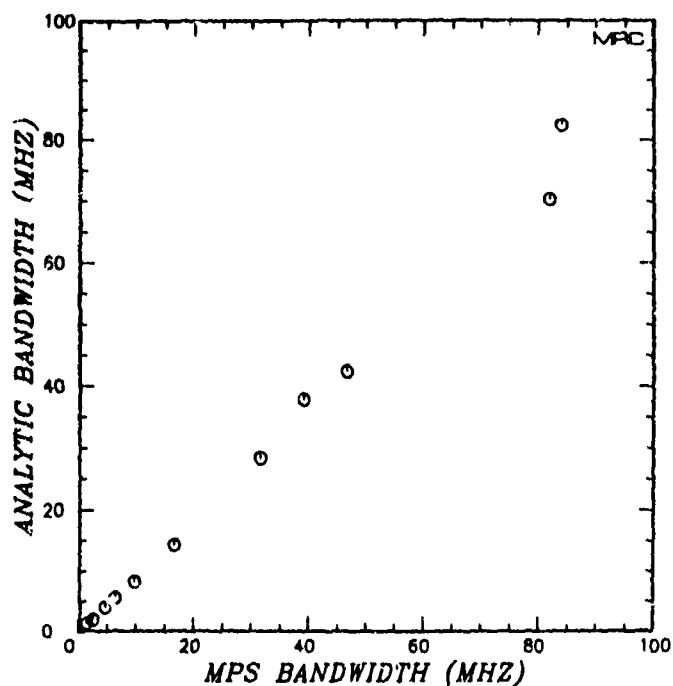


Figure 2-38. Comparison of two-sided bandwidth,  $f_r$ , many MPS calculations versus theory.

$f_r$  is  $f_{\max} - f_{\min}$ .  $f_r$  can thus be seen to be a measure of the two-sided bandwidth. Table 1 is a list of the two-sided bandwidth results presented in the figure and shows the pertinent MPS parameters that are used. In all cases a  $K^{-3}$  phase PSD is used, 16384 points comprise the MPS grid and the inner scale is fixed at 10 m.  $L_0$  is the outer scale,  $L$  is the scattering layer thickness and  $z_r - L$  is the free-space propagation distance between the receiver plane and the nearest edge of the scattering medium. Figure 2-2 depicts the MPS geometry. Because of the large number of varying quantities that are used here, statistical measures that describe the overall deviation are rather meaningless. Suffice it to say that the results are in quite good agreement. This agreement is somewhat unexpected because of the apparently severe limitations of the analytic calculation. However, for the most part, the MPS cases described here do indeed represent strong scattering situations and seem to agree quite well with the theory.



Table 2-1. Analytic versus numerical MPS comparison of 1/e points of  $r(\Delta x=0, f)$ .

$f_o$	$\sigma_\phi$	$L_o$	$L$	$z_r - L$	$f_r$	
					MPS	THEORY
0.1 GHz	33.0 rad	0.39 km	10 km	100 km	1.2 MHz	1.2 MHz
0.15	22.0	0.39	10	100	6.2	5.5
0.20	16.5	0.39	10	100	16.4	14.3
1.38	300	5	1000	1000	9.6	8.2
1.38	500	5	1000	1000	4.4	3.9
2.25	350	1	1000	1000	2.3	1.8
7.5	100	1	14000	1000	46.5	42.4
7.5	150	3	14000	1000	84.0	82.5
7.5	300	3	14000	1000	31.5	28.4
7.5	300	3*	14000	1000	39.0	37.8
7.5	300	10	1000	1000	82.0	70.2

\* For this case the inner scale is 100 m. For all other cases here the inner scale is 10 m.

## 2.7 COMPARISON OF $\langle \tau \rangle$ AND $\sigma_\tau$ TO THEORY

An important measure of the effects of scintillation on propagation of wide bandwidth signals is the mean time delay and the time delay standard deviation. These quantities are direct measures of the effects of time delay jitter in the mean sense and also serve as useful characterizations of the propagation environment.

Now let us define the mean time delay  $\langle \tau \rangle$  and the time delay jitter  $\sigma_\tau$  as

$$\langle \tau^m \rangle = \frac{\left\langle \int_{-\infty}^{\infty} |e(x, z_r, \tau)|^2 \tau^m d\tau \right\rangle_x}{\left\langle \int_{-\infty}^{\infty} |e(x, z_r, \tau)|^2 d\tau \right\rangle_x} \quad (2-65)$$

$$\langle \tau \rangle = \langle \tau' \rangle \quad (2-66)$$

$$\sigma_\tau^2 = \langle \tau^2 \rangle - \langle \tau \rangle^2 \quad (2-67)$$

where the subscript  $x$  on the angle bracket indicates that the average is obtained over the  $x$ -values along the MPS grid.  $e(x, z_r, \tau)$  is the received complex envelope as defined by

$$e(x, z_r, \tau) = \frac{1}{2\pi} \int_{-\infty}^{\infty} M(\nu) U(x, z_r, \nu + \omega_0) e^{i\nu\tau} d\nu \quad (2-68)$$

where  $M(\nu)$  is the transmitted signal spectrum and  $U(x, z_r, \nu + \omega_0)$  is a realization of the solution to the parabolic wave equation at a frequency  $\nu + \omega_0$ . It is apparent that  $U(x, z_r, \omega_0)$  is the received signal amplitude and phase at the carrier frequency. In the comparisons to be shown in this section, the transmitted signal is always a band-limited triangular wave with a spectrum given by Equation 2-54.

The ensemble average defined in Equations 2-65 to 2-67 is obtained in the case of a numerical MPS calculation by averaging the results over the MPS calculation grid, which here means averaging over all  $x$ -values. As can be seen,  $\langle \tau \rangle$  and  $\sigma_\tau$  are both functions of the receiver location  $z_r$ , but this dependence is omitted for notational convenience.

The numerical MPS results are to be compared to results derived following the moment method formulation of Yeh and Liu (1977), with the single exception that the ionization irregularities are assumed elongated infinitely in the  $y$ -direction so as to maintain the MPS geometry. The moment method results can be derived as

$$\langle \tau \rangle = \frac{\lambda \sigma_{\phi}^2 (2z_r - L) |A_2|}{4\pi \omega_0 A_0} \quad (2-69)$$

$$\begin{aligned} \sigma_{\tau}^2 = t^2(0) &+ \frac{\sigma_{\phi}^2}{\omega_0^2} \\ &+ \frac{\sigma_{\phi}^4 \lambda^2 A_2^2}{24\pi^2 \omega_0^2 A_0^2} (12z_r^2 - 16Lz_r + 6L^2) \\ &+ \frac{\sigma_{\phi}^2 \lambda^2 A_4}{2\pi^2 A_0 \omega_0^2} (3z_r^2 - 3Lz_r + L^2) \end{aligned} \quad (2-70)$$

where  $L$  is the thickness of the ionized region and the free-space propagation distance to the receiver is  $z_r - L$ .  $t^2(0)$  is the spread of the undisturbed time-domain waveform which here is

$$t^2(0) \equiv \frac{\int_{-\infty}^{\infty} \tau^2 |m(\tau)|^2 d\tau}{\int_{-\infty}^{\infty} |m(\tau)|^2 d\tau} \quad (2-71)$$

which for the case of a triangular pulse

$$m(\tau) = 1 - |\tau|/T_c, \quad |\tau| \leq T_c \quad (2-72)$$

becomes

$$t^2(0) = \frac{T_c^2}{10} \quad (2-73)$$

This result is a slight overestimate of the actual undisturbed waveform spread because it assumes (in effect) an infinite bandwidth. However, the approximation should be reasonably accurate since most of the power is contained within the first null-to-first null bandwidth used here.

The quantities  $A_0$  and  $A_2$  are defined by Equations 4-44 and 4-45 in Section 4.1.3.  $A_4$  is the coefficient of the next term in the expansion of the phase structure-function and is defined similarly to  $A_0$  and  $A_2$ . For the case of a  $K^{-3}$  Bessel function phase PSD with outer scale  $L_0$  and inner scale  $\ell_i$ ,

$$A_2/A_0 = \ell_i(L_0)/2L_0^2 \quad (2-74)$$

$$A_4/A_0 = 1/(8\ell_i^2L_0^2) \quad (2-75)$$

Note that the result for  $\langle \tau \rangle$  derived using the moment method of Yeh and Liu is identical to the thick layer result derived in Section 4.4.1 and presented in Equations 4-122 and 4-125. The second and third term of the result for  $\sigma_\tau^2$  is, in the thin layer approximation ( $L=0$ ), identical to the results of Equation 4-135 for a thin phase-screen. The  $A_4$  term is, of course, not included in the theoretical results of Section 4 where only a two term expansion of the phase structure-function is used.

Figures 2-39 and 2-40 provide a comparison of the MPS results with the theoretical results obtained following the moment method calculation of Yeh and Liu. The results shown here encompass all MPS calculations to date and involve five values of outer scale, three values of inner scale, a range of carrier frequencies from 100 MHz to 7.5 GHz and several different geometries. In all cases a  $K^{-3}$  phase power spectrum is assumed. Table 2 summarizes the important calculation parameters used and gives the values plotted.

Fairly good agreement is noted in all cases with a tendency for the analytic results to be somewhat larger than the MPS calculations. The 100 MHz carrier frequency calculation, listed first in Table 2, is omitted from the figure because it would have required a much larger scale for the gain of one additional point. The lack of agreement at the higher values of  $\langle \tau \rangle$  and  $\sigma_\tau$  may be caused by the impact of the narrow bandwidth approximation used in the theoretical calculation which becomes less appropriate with increasing scintillation severity or increasing bandwidth.

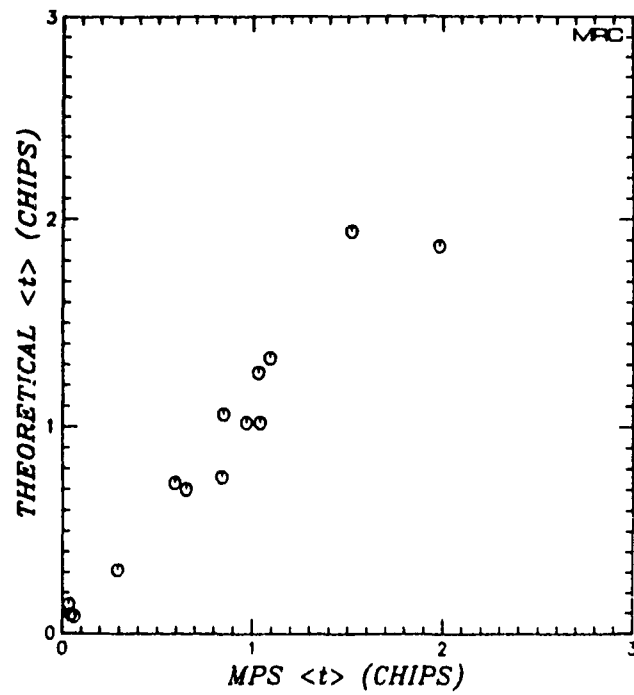


Figure 2-39. Comparison of mean time delay,  $\langle t \rangle$ , many MPS realizations versus theory.

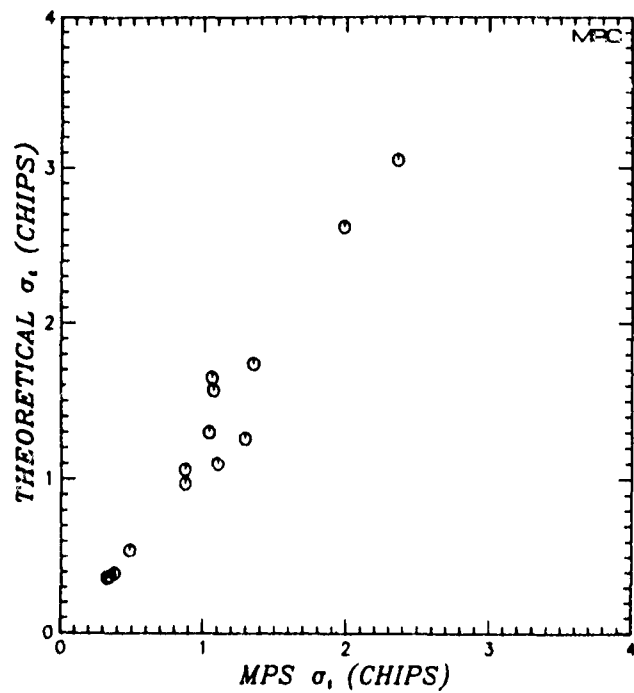


Figure 2-40. Comparison of time delay jitter,  $\sigma_t$ , many MPS realizations versus theory.

Table 2-2. Comparison of analytic and numerical MPS results for mean time delay and time delay jitter.

$f_o$	$T_c$	$\sigma_\phi$	$L_o$	$\ell_1$	$L$	$z_r - L$	$\langle \tau \rangle / T_c$		$\sigma_\tau / T_c$	
							MPS	THEORY	MPS	THEORY
0.1 GHz	97.5 nsec	33.0	0.39 km	10 m	10 km	100 km	8.0	9.5	9.6	14.2
0.15	97.6	22.0	0.39	10	10	100	2.0	1.9	2.4	3.1
0.20	97.6	16.5	0.39	10	10	100	0.6	0.7	1.1	1.1
1.38	97.6	100	3	10	14000	1000	0.85	1.1	1.1	1.1
1.38	97.6	100	5	10	1000	1000	0.06	0.08	0.34	0.37
1.38	97.6	300	5	10	1000	1000	0.65	0.7	0.87	1.1
1.38	97.6	500	5	10	1000	1000	1.5	1.8	2.0	2.6
2.25	488.3	350	1	10	1000	1000	1.1	1.3	1.4	1.8
7.5	25.0	30	1	10	14000	1000	0.04	0.09	0.32	0.36
7.5	25.0	100	1	10	14000	1000	1.0	1.0	1.1	1.3
7.5	25.0	100	3	10	14000	1000	0.03	0.14	0.37	0.39
7.5	25.0	150	3	10	14000	1000	0.29	0.31	0.48	0.54
7.5	25.0	300	3	10	14000	1000	1.1	1.3	1.1	1.6
7.5	25.0	300	3	30	14000	1000	0.97	1.0	1.3	1.3
7.5	25.0	300	3	100	14000	1000	0.84	0.76	0.87	0.97

## SECTION 3 STATISTICAL SIGNAL GENERATION

### 3.1 STATISTICAL SIGNAL REALIZATIONS

In this section a second technique is described to generate realizations of wide bandwidth signals after propagation through the ionosphere. This technique is referred to as statistical signal generation and relies on the properties of the solution to the parabolic wave equation under strong scattering conditions. This reliance renders statistical signal generation less general than the MPS propagation algorithm discussed in Section 2.

The basic formalism to generate statistical signal realizations was developed by Wittwer (1979 and 1980) for the case of isotropic irregularities. This section utilizes much of the initial formalism developed at that time.

This statistical signal generation technique is based on the solution for the two-position, two-frequency mutual coherence function  $\Gamma(\Delta x, \Delta \omega)$  for spherical waves described in Section 4. In that section the solution for  $r$  in the strong scattering limit is discussed in detail and its Fourier transform is presented. This Fourier transform,  $S(K, \tau)$ , is known as the generalized power spectrum (Wittwer, 1979) and its knowledge is a requirement for statistical signal generation. The formulation from Section 4 for  $S(K, \tau)$  in the thin phase-screen limit is used in this section as the basis of statistical signal generation. The thin phase-screen approximation is necessary to provide tractable expressions of  $S(K, \tau)$  for numerical evaluation. As shown in detail in the next section, the thin phase-screen approximation is highly accurate in all cases as an approximation to the geometry of a satellite communication link.

Hence, the major limitation on the accuracy of statistical signal generation is the strong scattering assumption which provides the

basis for the simplified solution for the two-frequency mutual coherence function. In the case of weak scattering, the MPS methods of Section 2 may easily be applied. For strong scattering cases, often of interest in the study of the effects of nuclear detonations on communications links, the statistical signal generation technique is more efficient.

Although statistical signal realizations are useful only for the case of strong scattering, their generation requires only a fraction of the computer resources required for signal generation by wide bandwidth MPS calculations.

Statistical signal generation is applicable to the case of elongated irregularities as handled by the MPS simulation or to the more general case of isotropic irregularities. Here the formulation is developed for both cases. Two detailed examples are presented for the case of elongated irregularities and are compared to exact MPS calculations that are described in Section 2.

### 3.2 FORMULATION

The scalar Helmholtz wave equation may be written as

$$(\nabla^2 + k_0^2 \epsilon_r(\vec{r})) E(\vec{r}, \omega) = 0 \quad (3-1)$$

where  $k_0$  is the free-space wavenumber,  $\epsilon_r$  is the relative permittivity and  $E(\vec{r}, \omega)$  is the electric field at the angular frequency  $\omega$ . The  $\exp(i\omega t)$  time dependence has been suppressed. If the permittivity,  $\epsilon_r(\vec{r})$ , is a random quantity with an average value plus a small, zero-mean random part, then

$$\epsilon_r(\vec{r}) = \langle \epsilon(\vec{r}) \rangle \left( 1 + \frac{\Delta \epsilon(\vec{r})}{\langle \epsilon(\vec{r}) \rangle} \right) \quad (3-2)$$

Now if the dielectric permittivity fluctuations are caused by electron density fluctuations, then

$$\langle \epsilon(\vec{r}) \rangle = 1 - \frac{\langle N_e(\vec{r}) \rangle}{n_c} = 1 - \frac{\omega_p^2(\vec{r})}{\omega^2} \quad (3-3)$$



$$\Delta\epsilon(\vec{r}) = - \frac{\Delta N_e(\vec{r})}{n_c} = - \frac{\Delta N_e(\vec{r})}{\langle N_e \rangle} \frac{\omega_p^2}{\omega^2} \quad (3-4)$$

where  $\langle N_e \rangle$  is the mean electron density,  $n_c$  is the critical electron density and  $\omega_p$  is the plasma frequency. These three quantities are related by

$$\omega_p^2 = 4\pi c^2 r_e \langle N_e \rangle \quad (3-5)$$

$$n_c = \frac{1}{\lambda^2 r_e} \quad (3-6)$$

where  $r_e$  is the classical electron radius ( $2.82 \times 10^{-15} \text{m}$ ) and  $c$  is the speed of light in free-space. Combining Equations 3-1 to 3-4, the scalar Helmholtz equation for a medium subject to electron density fluctuations combined with mean ionization is obtained

$$\nabla^2 E + k^2 \left( 1 - \frac{\frac{\Delta N_e}{\langle N_e \rangle} \frac{\omega_p^2}{\omega^2}}{1 - \omega_p^2/\omega^2} \right) E = 0 \quad (3-7)$$

Now  $k$  is the mean wavenumber for propagation in an ionized medium

$$k = \frac{\omega}{c} \langle \epsilon \rangle^{1/2} = \frac{\omega}{c} (1 - \omega_p^2/\omega^2)^{1/2} \quad (3-8)$$

where  $\omega$  is the radian frequency of the transmitted waveform. The mean wavenumber  $k$  is a function of propagation distance  $z$ , but this dependence is omitted for convenience of notation in the following.

Figure 3-1 shows the geometry of the problem where a spherical wave originates from a transmitter located at  $-z_t$  and propagates in free-space in the positive  $z$  direction, until it is incident on a layer of ionization irregularities of thickness  $L$ . After emerging from the layer of irregularities at  $z = L$ , the wave then propagates in free-space to a

receiver located in the plane  $z = z_r$ . This geometry is chosen to model transionospheric satellite communications links through ionization produced by natural causes, barium releases, or high altitude nuclear detonations.

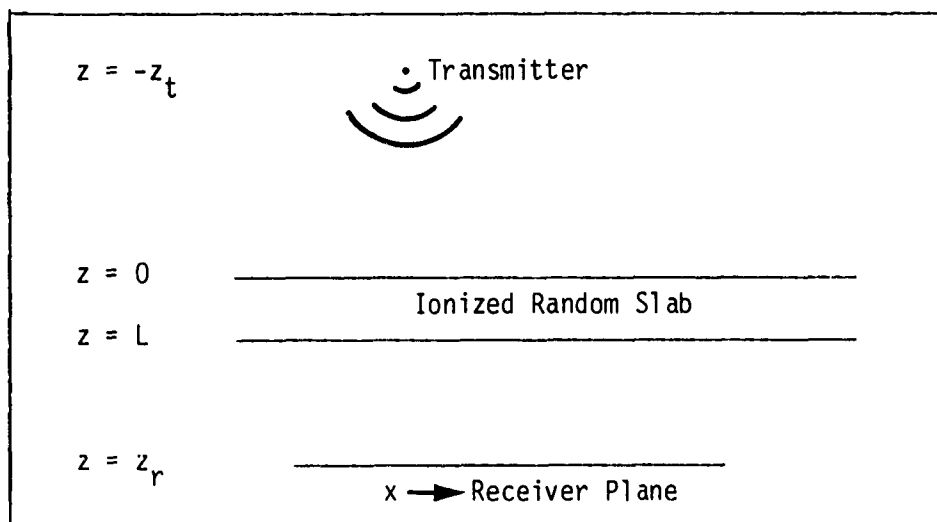


Figure 3-1. Geometry of transionospheric satellite communications link through a thick scattering layer.

Now make the substitution

$$E(\vec{r}, \omega) = U(\vec{r}, z, \omega) \exp \left\{ -i \int_{-z_t}^{z_r} k(z') dz' \right\} \quad (3-9)$$

into Equation 3-7 to obtain

$$\nabla_{\perp}^2 U + \frac{\partial^2 U}{\partial z^2} - 2ik \frac{\partial U}{\partial z} - k^2 \frac{\frac{\Delta N_e}{\langle N_e \rangle} \frac{\omega_p^2}{\omega^2}}{1 - \omega_p^2/\omega^2} U = 0 \quad (3-10)$$

where

$$\nabla_{\perp}^2 = \frac{\partial^2}{\partial x^2} + \frac{\partial^2}{\partial y^2}$$

is the transverse Laplacian.

The complex amplitude  $U$  can vary markedly over distances no smaller than the scale size of the electron density fluctuations  $\ell_s$ ; that is, the worst case variation of  $U$  in the direction of propagation can be characterized by  $U \sim \exp(-z^2/\ell_{\max}^2)$  where  $\ell_{\max} \geq \ell_s$ . Thus the second derivative  $\partial^2 U / \partial z^2$  is of the order of  $U/\ell_{\max}^2$ . On the other hand, the third term of Equation 3-10 is of the order of  $U/\lambda \ell_{\max}$ . Therefore, for  $\lambda \ll \ell_{\max}$ , or  $\lambda \ll \ell_s$  the second term of Equation 3-10 may be ignored with respect to the third term and the parabolic wave equation is obtained as:

$$\nabla_{\perp}^2 U - 2ik \frac{\partial U}{\partial z} - k^2 \frac{\frac{\Delta N_e}{\langle N_e \rangle} \frac{\omega_p^2}{\omega^2}}{1 - \omega_p^2/\omega^2} U = 0 \quad (3-11)$$

The solution to the parabolic wave equation at the receiver plane is  $U(\bar{\rho}, z_r, \omega)$ . As discussed in Section 2, if the ionization irregularities are infinitely elongated in the  $y$ -direction, there is no  $y$  variation. Then the multiple phase-screen propagation technique can be used to obtain Monte Carlo "realizations" of  $U(x, z_r, \omega)$ , the solution to the parabolic wave equation.

### 3.2.1 Wide Bandwidth Signals

Now, if instead of a monochromatic wave, the transmitted signal is composed of a spectrum of Fourier components,  $S(\omega)$ , then the time-domain signal at the receiver plane is

$$v(\bar{\rho}, z_r, t) = \frac{1}{2\pi} \int_{-\infty}^{\infty} S(\omega) U(\bar{\rho}, z_r, \omega) e^{i\theta(\omega)} e^{i\omega t} d\omega \quad (3-12)$$

where

$$\begin{aligned} \theta(\omega) &= - \int_{-z_t}^{z_r} k(z') dz' \\ &= - \frac{\omega}{c} \int_{-z_t}^{z_r} (1 - \omega_p^2(z')/\omega^2)^{1/2} dz' \end{aligned} \quad (3-13)$$

The propagation of wide bandwidth, modulated waveforms is of interest in this work. Thus let the real transmitted waveform be expressed as

$$\begin{aligned} s(t) &= \text{Re} \left\{ m(t) e^{i\omega_0 t} \right\} \\ &= \frac{1}{2} m(t) e^{i\omega_0 t} + \frac{1}{2} m^*(t) e^{-i\omega_0 t} \end{aligned} \quad (3-14)$$

where  $\omega_0$  is the carrier angular frequency and  $m(t)$  is the modulation waveform. For a pseudo-noise (PN) code,  $m(t)$  consists of a long sequence of pseudo-random polarity changes (binary PSK-modulated signal). The frequency-domain representation of the transmitted waveform is given by

$$\begin{aligned} S(\omega) &= \int_{-\infty}^{\infty} s(t) e^{-i\omega t} dt \\ &= \frac{1}{2} \int_{-\infty}^{\infty} m(t) e^{i(\omega_0 - \omega)t} dt + \frac{1}{2} \int_{-\infty}^{\infty} m^*(t) e^{-i(\omega_0 + \omega)t} dt \\ &= \frac{1}{2} M(\omega - \omega_0) + \frac{1}{2} M^*(\omega_0 + \omega) \end{aligned} \quad (3-15)$$

where  $M(\omega)$  is the Fourier transform of the modulation waveform:

$$M(\omega) = \int_{-\infty}^{\infty} m(t) e^{-i\omega t} dt \quad (3-16)$$

Combining Equations 3-12 and 3-15, the received waveform  $v$  can be expressed as

$$\begin{aligned} v(\bar{p}, z_r, t) &= \frac{1}{4\pi} \int_{-\infty}^{\infty} M(\omega - \omega_0) U(\bar{p}, z_r, \omega) e^{i\theta(\omega)} d\omega \\ &+ \frac{1}{4\pi} \int_{-\infty}^{\infty} M^*(-\omega - \omega_0) U(\bar{p}, z_r, \omega) e^{i\theta(\omega)} d\omega \end{aligned} \quad (3-17)$$

where

$$\theta(\omega) \equiv -\frac{\omega}{c} \int_{-z_t}^{z_r} (1 - \omega_p^2/\omega^2)^{1/2} dz' \quad (3-18)$$

Although the notation is changed, it is understood that the plasma frequency  $\omega_p$  depends on  $z'$ .

Now in the first term of Equation 3-17 expand  $\theta(\omega)$  in a Taylor series about  $\omega_0$ :

$$\theta_+(\omega) = \theta(\omega_0) + (\omega - \omega_0)\theta'(\omega_0) + \frac{(\omega - \omega_0)^2 \theta''(\omega_0)}{2!} + \dots \quad (3-19)$$

where the subscripted plus sign signifies the expansion about a positive carrier frequency and the primes denote differentiation with respect to  $\omega$ . From Equation 3-18

$$\theta(\omega_0) = -\frac{\omega_0}{c} \int_{-z_t}^{z_r} (1 - \omega_p^2/\omega_0^2)^{1/2} dz' \quad (3-20)$$

$$\theta'(\omega_0) = -\frac{1}{c} \int_{-z_t}^{z_r} (1 - \omega_p^2/\omega_0^2)^{-1/2} dz' \quad (3-21)$$

$$\theta''(\omega_0) = \frac{1}{c\omega_0^3} \int_{-z_t}^{z_r} (1 - \omega_p^2/\omega_0^2)^{-3/2} \omega_p^2 dz' \quad (3-22)$$

$$\theta'''(\omega_0) = -\frac{3}{c\omega_0^4} \int_{-z_t}^{z_r} (1 - \omega_p^2/\omega_0^2)^{-5/2} \omega_p^2 dz' \quad (3-23)$$

In the second term of Equation 3-17, expand  $\theta(\omega)$  in a Taylor series about  $-\omega_0$ :

$$\begin{aligned}\theta_-(\omega) &= \theta(-\omega_0) + (\omega + \omega_0)\theta'(-\omega_0) + \frac{(\omega + \omega_0)^2}{2!}\theta''(-\omega_0) + \dots \\ &= -\theta(\omega_0) - (-\omega - \omega_0)\theta'(\omega_0) - \frac{(-\omega - \omega_0)^2}{2!}\theta''(\omega_0) + \dots\end{aligned}\quad (3-24)$$

For notational simplicity, let  $\theta(\omega_0) = \theta_0$ ,  $\theta'(\omega_0) = \theta'_0$  and so forth. Retaining the first four terms in the Taylor series, the received waveform can be written as:

$$\begin{aligned}v(\bar{\rho}, z_r, t) &= \frac{1}{4\pi} \int_{-\infty}^{\infty} M(\omega - \omega_0) U(\bar{\rho}, z_r, \omega) \exp\{i\theta_0 + i\bar{\theta}(\omega - \omega_0) + i\omega t\} d\omega \\ &\quad + \frac{1}{4\pi} \int_{-\infty}^{\infty} M^*(-\omega - \omega_0) U(\bar{\rho}, z_r, \omega) \exp\{-i\theta_0 - i\bar{\theta}(-\omega - \omega_0) - i\omega t\} d\omega\end{aligned}\quad (3-25)$$

where

$$\bar{\theta}(v) \equiv v\theta'_0 + \frac{1}{2} v^2\theta''_0 + \frac{1}{6} v^3\theta'''_0 \quad (3-26)$$

In the first integral let  $v = \omega - \omega_0$  and in the second integral use the substitution  $v = -\omega - \omega_0$ . Then Equation 3-25 for the received waveform becomes

$$\begin{aligned}v(\bar{\rho}, z_r, t) &= \frac{e^{i(\omega_0 t + \theta_0)}}{4\pi} \int_{-\infty}^{\infty} M(v) U(\bar{\rho}, z_r, v + \omega_0) \exp\{i\bar{\theta}(v) + i v(t - t_d)\} dv \\ &\quad + \frac{e^{-i(\omega_0 t + \theta_0)}}{4\pi} \int_{-\infty}^{\infty} M^*(v) U(\bar{\rho}, z_r, -v - \omega_0) \exp\{-i\bar{\theta}(v) - i v(t - t_d)\} dv\end{aligned}\quad (3-27)$$

where  $\theta_0$  can be seen to be the total mean phase-shift (caused by dispersion alone) at the carrier frequency and  $t_d$  is the mean group time delay (i.e., the group delay at the carrier frequency):

$$\theta_0 = -\frac{\omega_0}{c} \int_{-z_t}^{z_r} (1 - \omega_p^2/\omega_0^2)^{1/2} dz' \quad (3-28)$$

$$t_d \equiv -\theta_0' = \frac{1}{c} \int_{-z_t}^{z_r} (1 - \omega_p^2/\omega_0^2)^{-1/2} dz' \quad (3-29)$$

### 3.2.2 Total Phase Shift, Time Delay, and Doppler Frequency

For cases where the entire region between transmitter and receiver is uniformly ionized, these two equations may be written as

$$\theta_0 = -\frac{\omega_0 R}{c} (1 - \omega_p^2/\omega_0^2)^{1/2} \quad (3-30)$$

$$t_d = R/V_g \quad (3-31)$$

where  $R$  is the total propagation distance and  $V_g$  is the group velocity

$$V_g = c (1 - \omega_p^2/\omega_0^2)^{1/2} \quad (3-32)$$

For cases of interest where  $\omega_0^2 \gg \omega_p^2$  (otherwise the wave cannot propagate without attenuation), and utilizing the relationship

$$\omega_p^2 = 4\pi c^2 n_e \langle N_e \rangle$$

the total phase shift and time delay can be written as

$$\theta_0 \approx -\frac{\omega_0}{c} R + \frac{2\pi c r_e \dot{N}_T}{\omega_0} \quad (\text{radians}) \quad (3-33)$$

$$t_d \approx \frac{R}{c} + \frac{2\pi c r_e N_T}{\omega_0^2} \quad (\text{seconds}) \quad (3-34)$$

where

$$R = z_t + z_r$$

$$N_T = \int_{-z_t}^{z_r} \langle N_e(z') \rangle dz'$$

$R$  is the total propagation distance and  $N_T$  is known as the total electron content.

The well known Doppler shift due to range and ionization variations is

$$\begin{aligned} f_{\text{dop}} &= \frac{1}{2\pi} \frac{d\theta_0}{dt} \\ &\approx -\frac{f_0}{c} \dot{R} + \frac{c r_e \dot{N}_T}{\omega_0} \end{aligned} \quad (3-35)$$

The first terms of Equations 3-33 and 3-34 are simply the free-space phase-shift and time delay which are proportional to the total propagation distance  $R$ . Variations in this distance with respect to time produce the well known Doppler shift and effects of time delay. The second term of Equations 3-33 to 3-35 represents contributions to propagation phase, time delay and Doppler shift caused by mean ionization. Note that increasing total electron content (positive  $\dot{N}_T$ ) causes positive Doppler shift and increasing time delay. This is opposite to the effect of range variation, where increasing time delay is associated with negative Doppler shift.



It is evident from the parabolic wave equation, 3-10, and from the definition of  $k$ , Equation 3-8, that

$$U(\bar{\rho}, z_r, \omega) = U^*(\bar{\rho}, z_r, -\omega)$$

With this fact in mind, it is seen that the two terms of Equation 3-27 are complex conjugates of one another so that the received signal is real, as it should be. This waveform can be written in terms of a complex modulation envelope,

$$\begin{aligned} v(\bar{\rho}, z_r, t) &= \frac{1}{2} e(\bar{\rho}, z_r, t-t_d) e^{i(\omega_0 t + \theta_0)} + \frac{1}{2} e^*(\bar{\rho}, z_r, t-t_d) e^{-i(\omega_0 t + \theta_0)} \\ &= \text{Re} \left\{ e(\bar{\rho}, z_r, t-t_d) e^{i(\omega_0 t + \theta_0)} \right\} \end{aligned} \quad (3-36)$$

where the received complex envelope is

$$e(\bar{\rho}, z_r, \tau) = \frac{1}{2\pi} \int_{-\infty}^{\infty} M(\nu) U(\bar{\rho}, z_r, \nu + \omega_0) e^{i\phi(\nu) + i\nu\tau} d\nu \quad (3-37)$$

Note that Equation 3-36 has the same general form as Equation 3-14 - a wave modulated on a carrier at angular frequency  $\omega_0$  with an additional phase-shift and time delay as given by Equations 3-28 and 3-29.

In Equation 3-27 the received complex envelope  $e(\bar{\rho}, z_r, \tau)$  is given as the integral over frequency of the Fourier transform of the transmitted complex envelope multiplied by the solution to the parabolic wave equation  $U$ . Since the value of the resultant received signal  $v$  is a function of the carrier frequency  $\omega_0$ , the  $\omega_0$  dependence must appear explicitly in Equation 3-37. Although the  $\omega_0$  dependence is not explicitly shown in writing  $e(\bar{\rho}, z_r, \tau)$ , the received complex envelope does indeed depend upon the carrier frequency as shown explicitly in Equation 3-37.

### 3.2.3 Impulse Response Function

Now let us assume that the complex received electric field  $e(\bar{\rho}, z_r, \tau)$  represents the response of a linear system to some input signal  $m(\tau)$ . Then in general one can write

$$e(\bar{\rho}, z_r, \tau) = \int_{-\infty}^{\infty} m(t') h(\bar{\rho}, z_r, \tau - t') dt' \quad (3-38)$$

which simply states that the output signal is the convolution of the input signal with the impulse response,  $m(\tau) * h(\tau)$ . Now with the following substitution obtained directly from Equation 3-16

$$M(v) = \int_{-\infty}^{\infty} m(t') e^{-i v t'} dt'$$

Equation 3-37 can be written as

$$e(\bar{\rho}, z_r, \tau) = \frac{1}{2\pi} \int_{-\infty}^{\infty} m(t') \int_{-\infty}^{\infty} U(\bar{\rho}, z_r, v + \omega_0) e^{i\bar{\theta}(v)} e^{i v (\tau - t')} dv dt' \quad (3-39)$$

Now comparison of Equations 3-38 and 3-39 yields the important result for the impulse response function

$$h(\bar{\rho}, z_r, \tau) = \frac{1}{2\pi} \int_{-\infty}^{\infty} U(\bar{\rho}, z_r, v + \omega_0) e^{i\bar{\theta}(v)} e^{i v \tau} dv \quad (3-40)$$

Equation 3-40 gives a direct result for the impulse response of an ionized medium in terms of the frequency domain solution to the parabolic wave equation. It is apparent from Equation 3-40 that the impulse response  $h$  does depend upon the carrier frequency  $\omega_0$  although this dependence is not explicitly shown in writing  $h$ .

Notice that Equation 3-40 represents a Fourier transform relationship for the impulse response function. The transform of the impulse response function is composed of the product of two terms. One term,

$U(\bar{p}, z_r, \nu + \omega_0)$ , is the solution to the parabolic wave equation and represents random effects due to fluctuating plasma. The second term

$$e^{i\bar{\theta}(\nu)}$$

is the transfer function of a smooth ionized medium and can cause pulse dispersion. Since the two transfer functions appear in a product relationship, it is convenient to separate the generation of signal structures into a two step process. The first step consists of generating realizations of the impulse response function with only fluctuating plasma effects. The second step adds the effect of the gross ionization.

With the above thought in mind, let us consider a method to generate a realization of the impulse response function for the case where  $\bar{\theta}(\nu) = 0$ . In addition, consider for the moment the generation of the impulse response function for the case where there is no y-variation. This situation corresponds to the case of elongated irregularities considered in Section 4 and to the two-dimensional MPS propagation simulation discussed in Section 2. Now the impulse response function satisfies the equation

$$h(x, z_r, \tau) = \frac{1}{2\pi} \int_{-\infty}^{\infty} U(x, z_r, \nu + \omega_0) e^{i\nu\tau} d\nu \quad (3-41)$$

The following initial development is limited to this two-dimensional case; however we shall return to the general three-dimensional case later.

### 3.2.3.1 Distinction Between Time (t) and Time Delay ( $\tau$ )

Recall that the x or  $\bar{p}$  dimension corresponds to a displacement on the receiver plane as shown in Figure 3-1. In an actual physical situation, the x-variation is converted into variation with time by effective motion of the propagation path through the irregularities. Thus,

$$t = \frac{x}{v_{\text{eff}}} \quad (\text{sec}) \quad (3-42)$$

where the effective velocity is a function of many system and environmental parameters including wind velocities, platform velocity, plasma velocity and propagation path geometry. This effective motion may be caused by motion of the irregularities, by motion of the line-of-sight through the irregularities or by a combination of both. Note that the time ( $t$ ) variation of the fluctuations is assumed to be very slow relative to the time ( $\tau$ ) variation of the modulated waveform. In other words, the bandwidth of the fluctuations is small compared to the bandwidth of the modulation. This consideration is important since the solution to the parabolic wave equation is obtained simultaneously at a number of frequencies over the signal bandwidth. For the solution to be accurate, the medium cannot vary over the time duration of the modulation waveform.

### 3.2.4 Statistics of a Realization

At this point it is useful to consider the technique discussed in Section 2.2.4 to generate phase-screen realizations as it might be applied to generate realizations of the complex electric field.

First a pseudo-random realization of the Fourier transform of the electric field is chosen as

$$\hat{E}(m\Delta K) = r_m (S(m\Delta K)L/2\pi)^{1/2} \quad (3-43)$$

where  $\hat{E}$  is a realization of the Fourier transform of the electric field,  $S$  is the desired power spectral density (PSD),  $L$  is the length of the grid and  $r_m$  is a complex Gaussian random variable such that

$$\langle r_m r_n^* \rangle = \delta_{nm} \quad (3-44)$$

The electric field itself is then obtained by taking the discrete Fourier transform of Equation 3-43

$$E(x\Delta x) = \sum_{m=0}^{N-1} \hat{E}(m\Delta K) e^{i2\pi xm/N\Delta K}, \quad x = 0, \dots, N-1 \quad (3-45)$$

The most important properties of the electric field are immediately evident from the preceding brief discussion. First, since the electric field is a linear combination of a number of Gaussian variates, both its real and imaginary parts possess Gaussian probability distributions. Thus the realization of received signal amplitude is the square root of the sum of the squares of the inphase and quadrature phase parts, and

$$\{(\text{Real } E)^2 + (\text{Imaginary } E)^2\}^{1/2}$$

possesses a Rayleigh probability distribution.

In the following, a formulation is developed to generate realizations of the received electric field which are restricted to possess Rayleigh amplitude distributions. Fortunately this limitation is not at all restrictive for the case of a nuclear disturbance since large spatial regions can experience Rayleigh fading statistics.

Finally it is evident from Equations 3-43 and 3-44 that the electric field power spectrum has the form

$$\langle \hat{E}(m\Delta K) \hat{E}^*(n\Delta K) \rangle \sim \delta_{mn} S(m\Delta K) \quad (3-46)$$

which is a requirement if the electric field is to be stationary (Tatarskii, 1971). Thus the resulting autocorrelation function generated by the method described in Section 2.2.4 is dependent only on the distance between measurement points.

### 3.3 IMPULSE RESPONSE FUNCTION GENERATION

In this section techniques are developed to generate realizations of the impulse response function  $h(x, z_r, \tau)$  defined in Section 3.2.3. Once this function is available, Equation 3-38 or its equivalent may be applied to obtain a realization of the complex received electric field. It is shown here that it is possible to generate the Fourier transform of the impulse response function  $U(x, z_r, \nu)$  in essentially the

same manner as realizations of the phase are generated. Note that the independent variable pairs  $v-\tau$  and  $x-K$  are used to unambiguously denote Fourier transform pairs.

### 3.3.1 Realizations of the Parabolic Wave Equation Solution

In this section a realization of the impulse response function is obtained by first generating a realization of its Fourier transform  $U(x,v)$ . Thus given the Fourier transform pair,

$$U(x,v) = \int_{-\infty}^{\infty} h(x,\tau) e^{-i v \tau} d\tau \quad (3-47)$$

$$h(x,\tau) = \frac{1}{2\pi} \int_{-\infty}^{\infty} U(x,v) e^{i v \tau} dv \quad (3-48)$$

first generate a realization of  $U(x,v)$  as illustrated in the following. Then take the transform to obtain a realization of the impulse response function  $h(x,\tau)$ . Note that Equation 3-48 is Equation 3-41 with the  $z_r$  and  $\omega_0$  dependence removed for convenience. Both of these dependencies play an important role in the results but are unnecessary complications to the formulation.

Now  $U(x,v)$  can be written as the Fourier transform

$$U(x,v) = \int_{-\infty}^{\infty} \int_{-\infty}^{\infty} h(K,\tau) e^{i K x} e^{-i v \tau} dK d\tau \quad (3-49)$$

where  $h(K,\tau)$  is recognized as the Fourier transform of the impulse response function with respect to  $x$ .  $h(K,\tau)$  is not the impulse response function which is denoted as  $h(x,\tau)$ . In the discrete case Equation 3-49 may be written

$$U(x\Delta x, p\Delta v) = \sum_{m=0}^{N-1} \sum_{s=0}^{M-1} h(m\Delta K, s\Delta\tau) e^{i m \Delta K x} e^{-i p s \Delta v \Delta \tau} \Delta K \Delta \tau$$

$$x=0, \dots, N-1; \quad p=0, \dots, M-1 \quad (3-50)$$

where  $N$  discrete points are used to represent a total distance of  $L$  so that the point spacing  $\Delta x = L/N$ . By the Nyquist sampling theorem, the minimum spatial frequency is  $\Delta Q = 1/L$ . The minimum spatial radian frequency is then  $2\pi/L$ . Similarly  $T$  is the total time duration of the  $M$  samples used to represent the delay space functional dependence. Thus the delay increment is  $\Delta \tau = T/M$ . By the Nyquist sampling theorem the minimum frequency is  $\Delta f = 1/T$ , or the minimum radian frequency is  $2\pi/T$ . The total, two-sided spatial bandwidth is  $B_s = 1/\Delta x$ , and the total, two-sided delay bandwidth is  $B_d = 1/\Delta \tau$ . For later convenience also define the total radian bandwidth as  $B_v = 2\pi B_d$ . With the substitutions just discussed Equation 3-50 becomes

$$U(\ell \Delta x, p \Delta \tau) = \sum_{m=0}^{N-1} \sum_{s=0}^{M-1} h(m \Delta K, s \Delta \tau) e^{i 2 \pi \ell m / N} e^{-2 \pi p s / M} \Delta K \Delta \tau$$

(3-51)

Now choose as a realization of the Fourier transform the quantity

$$h(m \Delta K, s \Delta \tau) = \left[ \frac{L B_v}{(2\pi)^2} S(m \Delta K, s \Delta \tau) \right]^{1/2} r_{ms}$$

(3-52)

where  $S(K, \tau)$  is the generalized power spectrum given by either Equation 4-97 or 4-99 in Section 4.  $r_{ms}$  is a complex random variable such that

$$r_{ms} = \frac{1}{2} (g_{1m} + i g_{2m})(g_{1s} + i g_{2s})$$

(3-53)

where the  $g$ 's are independent, Gaussian random variables with zero mean and unity variance. With this definition for the random quantity  $r_{ms}$  it is easy to show that

$$\langle r_{ms} r_{nr}^* \rangle = \delta_{mn} \delta_{sr}$$

(3-54)

and

$$\langle r_{ms} \rangle = 0$$

(3-55)

Now it must be shown that the choice for the Fourier transform, Equation 3-52, is correct. Let us calculate the autocorrelation function of  $U(x, \nu)$  and show that it is indeed the two-frequency mutual coherence function. The continuous autocorrelation function of  $U(x, \nu)$  is given as

$$B_U(x, \nu) = \langle U(x' + x, \nu' + \nu) U^*(x', \nu') \rangle$$

$$= \frac{1}{LB_\nu} \int_0^L \int_{-B_\nu/2}^{B_\nu/2} U(x' + x, \nu' + \nu) U^*(x', \nu') dx' d\nu' \quad (3-56)$$

where ergodicity is assumed and ensemble averages are replaced by averages over distance and frequency. Now the preceding equation may be written discretely as

$$B_U(x, \nu) = B_U(\ell \Delta x, p \Delta \nu)$$

$$= \frac{1}{LB_\nu} \sum_{k=0}^{N-1} \sum_{q=0}^{M-1} U(k \Delta x + \ell \Delta x, q \Delta \nu + p \Delta \nu) U^*(k \Delta x, q \Delta \nu) \Delta x \Delta \nu$$

$$\ell = 0, \dots, N-1; \quad p = 0, \dots, M-1 \quad (3-57)$$

From Equation 3-51 the Fourier transform of  $U$  may be substituted into Equation 3-57 to obtain

$$B_U(\ell \Delta x, p \Delta \nu) = \frac{1}{LB_\nu} \sum_{k=0}^{N-1} \sum_{q=0}^{M-1} \sum_{m=0}^{N-1} \sum_{s=0}^{M-1} \sum_{n=0}^{N-1} \sum_{r=0}^{M-1}$$

$$\times h(m \Delta K, s \Delta \tau) \exp\{i 2 \pi (k + \ell) m / N - i 2 \pi (q + p) s / M\}$$

$$\times h^*(n \Delta K, r \Delta \tau) \exp\{-i 2 \pi k n / N + i 2 \pi q r / M\} \Delta x \Delta \nu (\Delta K \Delta \tau)^2$$

$$\ell = 0, \dots, N-1; \quad p = 0, \dots, M-1 \quad (3-58)$$



Now substitute the realization of the Fourier transform given by Equation 3-52 into Equation 3-58 to obtain

$$\begin{aligned}
 B_U(\Delta x, p\Delta v) &= \frac{1}{(2\pi)^2} \sum_{k=0}^{N-1} \sum_{q=0}^{M-1} \sum_{m=0}^{N-1} \sum_{s=0}^{M-1} \sum_{n=0}^{N-1} \sum_{r=0}^{M-1} \\
 &\times \{S(m\Delta K, s\Delta\tau) S^*(n\Delta K, r\Delta\tau)\}^{1/2} r_{ms} r_{nr}^* \\
 &\times \exp\{i2\pi(k+\ell)m/N - i2\pi(q+p)s/M\} \\
 &\times \exp\{-i2\pi kn/N + i2\pi qr/M\} \Delta x \Delta v (\Delta K \Delta\tau)^2
 \end{aligned} \tag{3-59}$$

Now since

$$\sum_{k=0}^{N-1} e^{i2\pi km/N} e^{-i2\pi kn/N} = N\delta_{mn} \tag{3-60}$$

and

$$\sum_{q=0}^{M-1} e^{-i2\pi qs/M} e^{+i2\pi qr/M} = M\delta_{sr} \tag{3-61}$$

Equation 3-59 may easily be reduced to

$$\begin{aligned}
 B_U(\Delta x, p\Delta v) &= \frac{NM\Delta x \Delta v}{(2\pi)^2} \sum_{m=0}^{N-1} \sum_{s=0}^{M-1} S(m\Delta K, s\Delta\tau) \\
 &\times |r_{ms}|^2 \exp\{i2\pi\ell m/N - i2\pi ps/M\} (\Delta K \Delta\tau)^2 \\
 &= \sum_{m=0}^{N-1} \sum_{s=0}^{M-1} S(m\Delta K, s\Delta\tau) |r_{ms}|^2 \exp\{i2\pi\ell m/N - i2\pi ps/M\} \Delta K \Delta\tau
 \end{aligned} \tag{3-62}$$

It is apparent that a Fourier transform relationship exists between the correlation function  $B_U$  and the function  $S(m\Delta K, s\Delta\tau) |r_{ms}|^2$ . Thus the power spectrum of the single generated realization  $U(\Delta x, p\Delta v)$  is

$$S(m\Delta K, s\Delta\tau) |r_{ms}|^2$$

where  $S(K, \tau)$  is the desired generalized power spectrum discussed in Section 4 of this report.

It is apparent that each of the Fourier components of the power spectrum is independent of Fourier components at other values of  $K$  and  $\tau$  because of the choice of the random number  $r_{ms}$ . Because of this delta correlation property of the power spectrum, the autocorrelation function  $B_H$  is only a function of  $\Delta x$  and  $\Delta v$  as it should be in accordance with the description of the two-position, two-frequency mutual coherence function,  $r$ , given in Section 4. Since the random numbers  $r_{ms}$  are Gaussian variates,  $|r_{ms}|^2$  is a chi-squared variate with two degrees of freedom. Since  $\langle |r_{ms}|^2 \rangle = 1$  the mean value of the power spectrum is the desired value. In other words, each realization of  $U(\Delta x, \Delta v)$  is dependent upon a sequence of random numbers,  $r_{ms}$ , and thus has a spectrum which is not identically equal to the desired spectrum. However, the average PSD of a large number of such realizations is given as

$$\text{Avg} \{ S(m\Delta K, s\Delta\tau) |r_{ms}|^2 \} = S(m\Delta K, s\Delta\tau) \quad (3-63)$$

which is exactly the result desired.

The average autocorrelation function determined by averaging over a number of numerically generated realizations is obtained by taking the average of Equation 3-62

$$\text{Avg} \{ B_H(\Delta x, \Delta v) \} = \sum_{m=0}^{N-1} \sum_{s=0}^{M-1} S(m\Delta K, s\Delta\tau) \exp\{i2\pi m\Delta x/N - i2\pi s\Delta v/M\} \Delta K \Delta\tau \quad (3-64)$$

This equation may be rewritten in its continuous form as

$$\text{Avg} \{ B_H(x, v) \} = \int_{-\infty}^{\infty} \int_{-\infty}^{\infty} S(K, \tau) e^{iKx} e^{-i\tau v} dK d\tau = r(x, v) \quad (3-65)$$

which is identical to Equations 4-84 or 4-87 and proves that the formula given in Equation 3-52 for the Fourier transform of a single realization is indeed correct as claimed.

At this point it has been proven that Equations 3-51 and 3-52 may be used to generate a realization of the solution  $U(x,v)$  to the parabolic wave equation. This realization has  $r(x,v)$  as its autocorrelation function and  $S(K,\tau)$ , the generalized power spectrum, as the Fourier transform of  $r$ . In order to facilitate numerical generation of realizations, the formulation for  $S(K,\tau)$  has been specialized with little loss of generality to the case of scattering by a thin phase-screen.

The equations for  $S(K,\tau)$  are given in Section 4 for two cases. Equation 4-97 is valid for the case of irregularities that are infinitely elongated perpendicular to the direction of propagation. Equation 4-99 is valid for isotropic irregularities. Appendix A is devoted to numerical evaluation of the two equations and shows a number of plots of  $S(K,\tau)$  for an interesting selection of parameters.

The specialization to the thin phase-screen case mentioned above is discussed in detail in Section 4 where results are presented for both thick and thin layers to show the effect of layer thickness on the  $S_4$  scintillation index, the mean time delay and the time delay jitter. In general, for satellite communication links through ionospheric disturbances, the thin phase-screen approximation is quite accurate and enjoys a distinct advantage in usefulness over the thick layer solution.

### 3.3.2 Realizations of the Impulse Response Function

At this point a method has been described to generate discrete realizations of  $U(x,v)$ , the solution to the parabolic wave equation, directly from the computed two-frequency mutual coherence function. In order to generate realizations of the impulse response function  $h(x,\tau)$  it is necessary to apply the Fourier transform relationships given by Equations 3-47 and 3-48. In the discrete case, Equation 3-48 becomes

$$h(\ell\Delta x, s\Delta\tau) = \frac{1}{2\pi} \sum_{p=0}^{M-1} U(\ell\Delta x, p\Delta v) e^{i2\pi ps/M\Delta v} \quad (3-66)$$

$\ell=0, \dots, N-1; s=0, \dots, M-1$

Substitution of Equation 3-52 into Equation 3-66 yields

$$h(\ell\Delta x, s\Delta\tau) = \frac{1}{2\pi} \sum_{m=0}^{N-1} \sum_{r=0}^{M-1} \sum_{p=0}^{M-1} h(m\Delta K, r\Delta\tau) e^{i2\pi\ell m/N} e^{i2\pi p(s-r)/M} \Delta K \Delta\tau \Delta\nu \quad (3-67)$$

$$\ell=0, \dots, N-1; s=0, \dots, M-1$$

but since

$$\sum_{p=0}^{M-1} e^{i2\pi p(s-r)/M} = M\delta_{sr} \quad (3-68)$$

Equation 3-67 reduces to

$$h(\ell\Delta x, s\Delta\tau) = \frac{M}{2\pi} \sum_{m=0}^{N-1} h(m\Delta K, s\Delta\tau) e^{i2\pi\ell m/N} \Delta K \Delta\tau \Delta\nu \quad (3-69)$$

$$\ell=0, \dots, N-1; s=0, \dots, M-1$$

Now use Equation 3-52 to specify a random realization of the Fourier transform and simplify by using the relationships for  $\Delta K$ ,  $\Delta\tau$ , and  $\Delta\nu$  to obtain

$$h(\ell\Delta x, s\Delta\tau) = (B\sqrt{L})^{1/2} \sum_{m=0}^{N-1} [S(m\Delta K, s\Delta\tau)]^{1/2} r_{ms} e^{i2\pi\ell m/N} \quad (3-70)$$

$$\ell=0, \dots, N-1; s=0, \dots, M-1$$

This equation is the final statement of the method to generate realizations of the impulse response function after transionospheric propagation. Note the interesting property observed here that the values of the impulse response function are uncorrelated (or delta-correlated) in delay. This property occurs because the random variable  $r_{ms}$  obeys the correlation relationship specified by Equation 3-54.

Again it is quite important to note that the impulse response function generated in this manner is a complex Gaussian variate whose amplitude  $\{h(x, \tau)h^*(x, \tau)\}^{1/2}$  follows a Rayleigh probability distribution function. The importance of this fact is illustrated in the following

section where two examples of statistically generated signals are given and compared to multiple phase-screen calculations.

### 3.4 RAYLEIGH COMPONENT OF THE COMPOSITE SIGNAL

This section describes the steps which must be taken to generate statistical realizations of the impulse response function. Several examples are discussed and results compared to MPS results presented in Section 2 of this report.

One very important problem remains to be resolved before statistical signal realizations can be generated. The problem is caused by the fact, discussed in the previous section, that the choice of Gaussian random variables results in Rayleigh amplitude statistics for the generated signal. The reason for the problem is obvious - the analytically calculated generalized power spectrum  $S(K, \tau)$  includes all scattering effects, but the limitation imposed by requiring that the generated signal have Rayleigh statistics effectively requires the user to generate only the Rayleigh portion of the signal.

The solution to this problem is pragmatic. Arbitrarily divide the received signal into two disjoint parts. One part, called the dispersive component, represents the effects of large phase structure on the signal. The other signal component, called the Rayleigh signal component, is that part of the received signal which obeys Rayleigh statistics and represents severe diffractive or angular scattering effects. These two signal components have some similarities to the focus and scattering signal components upon which Fremouw's (Fremouw, et al., 1978) two-component signal statistical model is based.

Now for the case of a phase power spectrum which represents a range of scale sizes, the scattering processes are well understood. Large scale sizes, such that the focal length of the irregularities is greater than the propagation distance, cause large phase effects but cause little amplitude scintillation. This is another way of saying that larger scale sizes cause dispersion and not diffraction. Small scale sizes, whose focal lengths are less than the propagation distance, contribute to the  $S_4$  scintillation index because these small sizes are responsible for diffraction or angular scattering effects.

Now it is also well known (Fante, 1975) that for saturated scintillation, the signal amplitude statistics are Rayleigh and the  $S_4$  scintillation index is thus unity. It is also known that weak scattering predictions of the scintillation index in either the Born approximation or the Rytov approximation give accurate results for  $S_4 \leq 0.5$  (Crane, 1977).

Now assume for the moment that saturated, strong scattering occurs for  $S_4 > 0.5$ . That is, with the heuristic assumption that for  $S_4 > 0.5$ , the amplitude statistics are basically Rayleigh and the scintillation index is effectively unity, the  $S_4$  scintillation index can be accurately used to separate the Rayleigh signal component from the dispersive component. That is, since the scintillation index can be expressed as the integral over wavenumber of the phase PSD times a Fresnel filter factor, the integral may be used to define a scale size which separates dispersive effects from diffractive effects.

In this section the discussion is limited to a  $K^{-3}$  one-dimensional phase PSD. The integral expression for  $S_4$  is used to define an outer scale size for the Rayleigh signal component,  $L_R$ , which is in turn used to define a new phase PSD with phase standard deviation  $\sigma_{\phi R}$ . The Rayleigh phase standard deviation,  $\sigma_{\phi R}$ , and the Rayleigh outer scale size,  $L_R$ , are then used to define the generalized power spectrum for purposes of statistical signal generation. The effect of this ad hoc procedure is to generate only that portion of the signal that obeys Rayleigh statistics. The rest of this subsection describes the details involved in obtaining the effective PSD for the Rayleigh component of the received signal.

In the thin phase-screen approximation (Salpeter, 1967) the  $S_4$  scintillation index is given as an integral over wavenumber by

$$S_4^2 = 4 \int_{-\infty}^{\infty} S_{\phi}(K_x) \sin^2 (K_x^2 z^*/2k) dK_x \quad (3-71)$$

(elongated irregularities)

$$S_4^2 = 4 \int_{-\infty}^{\infty} \int_{-\infty}^{\infty} S_{\phi}(K_x, K_y) \sin^2 [(K_x^2 + K_y^2) z^*/2k] dK_x dK_y \quad (3-72)$$

(isotropic irregularities)

where

$$\frac{1}{z^*} = \frac{1}{z_t} + \frac{1}{z_r} \quad (3-73)$$

The geometry is shown in Figure 3-1 where the layer thickness  $L$  is taken as zero in the thin phase-screen limit. The transmitter emits a spherical wave which propagates a distance  $z_t$  in free-space until it penetrates the scattering layer. The wave then propagates a distance  $z_r$  to the receiver. The phase power spectra are given as

$$S_{\phi}(K_x) = \frac{\sigma_{\phi}^2 \Gamma[(n-2)/2] L_0}{\sqrt{\pi} \Gamma[(n-3)/2] (1 + K_x^2 L_0^2)^{(n-2)/2}} \quad (3-74)$$

(elongated irregularities)

$$S_{\phi}(K_x, K_y) = \frac{\sigma_{\phi}^2 \Gamma[(n-1)/2] L_0}{\pi \Gamma[(n-3)/2] [1 + (K_x^2 + K_y^2) L_0^2]^{(n-1)/2}} \quad (3-75)$$

(isotropic irregularities)

where  $\Gamma$  is the gamma function. It is seen that these two PSD follow the relationship (Rufenach, 1975)

$$S_{\phi}(K_x) = \int_{-\infty}^{\infty} S_{\phi}(K_x, K_y) dK_y \quad (3-76)$$

so that in both cases the one-dimensional phase PSD has the desired power law form  $K^{-n+2}$ .

### 3.4.1 Rayleigh Signal Component for Elongated Irregularities

Now in the case of elongated irregularities, the substitution

$$V = K_x^2 z^* / 2k \quad (3-77)$$

may be applied, and the integral expression Equation 3-71 may be written as

$$S_4^2 = \frac{8 \sqrt{2} \sigma_\phi^2 \Gamma[(n-2)/2]}{\sqrt{\pi} \Gamma[(n-3)/2] \xi^{1/2}} \int_0^\infty \frac{\sin^2(V^2) dV}{(1+2V^2/\xi)^{(n-2)/2}} \quad (3-78)$$

where

$$\xi = z^*/kL_0^2 = \lambda z^*/2\pi L_0^2 \quad (3-79)$$

Now define the value  $V'$  such that the scintillation index is 0.5

$$(0.5)^2 = \frac{8 \sqrt{2} \sigma_\phi^2 \Gamma[(n-2)/2]}{\sqrt{\pi} \Gamma[(n-3)/2] \xi^{1/2}} \int_0^{V'} \frac{\sin^2(V^2) dV}{(1+2V^2/\xi)^{(n-2)/2}} \quad (3-80)$$

$V'$  is the cutoff value chosen so that wavenumbers smaller than  $\sqrt{2} kV'/z^*$  contribute a value of 0.5 to the scintillation index in the weak scatter approximation. Since this weak scattering expression is valid for  $S_4 \leq 0.5$  (Crane, 1977),  $V'$  is a well defined quantity. Now define the outer scale cutoff value,  $L_R$ , such that scale sizes larger than or equal to  $L_R$  contribute a value of 0.5 to the  $S_4$  integration, or

$$L_R = (z^*/2kV')^{1/2} = (\lambda z^*/4\pi V')^{1/2} \quad (3-81)$$

Equation 3-81 can be rewritten as

$$L_R/L_0 = (\lambda z^*/4\pi L_0^2 V')^{1/2} = (\xi/2V')^{1/2} \quad (3-82)$$

Hence  $L_R$  is the scale size which separates large scale sizes from the small scale sizes that cause the major scintillation effects. Now it is apparent that the value of  $L_R/L_0$  is dependent upon the spectral index of the one-dimensional phase fluctuations,  $2-n$ , the outer scale,  $L_0$ , the parameter  $\xi$  and the phase standard deviation,  $\sigma_\phi$ . In the case of interest here the one-dimensional phase PSD has a spectral index of -3, so  $n$  is taken as 5.

Figure 3-2 shows  $L_R/L_0$  as a function of  $\sigma_\phi$  with  $\xi$  treated parametrically. Values of  $\xi$  ranging from  $10^{-6}$  to 1 are shown. For a constant value of  $\xi$ , there is a minimum value of the phase standard deviation



below which no solution is found for  $L_R/L_0$ . Values of  $\sigma_\phi$  below the minimum value correspond to the situation where all irregularities are close to the phase-screen and cause only dispersive effects. Recall that the focal length for an irregularity of strength  $\phi_0$  is

$$F = \pi L_0^2 / \lambda \phi_0 \quad (3-83)$$

so that

$$F/z^* = \pi L_0^2 / \lambda z^* \phi_0 \quad (3-84)$$

So as  $\sigma_\phi$  or equivalently  $\phi_0$  increases for a given  $\lambda z^*/L_0^2$  or  $\xi$  value, the focal length becomes smaller than the effective propagation distance. Thus as  $\sigma_\phi$  increases, more and more irregularities contribute to angular scattering and thus add contributions to the value of  $S_4$ .

As  $\sigma_\phi$  continues to increase for a fixed  $\xi = \lambda z^*/2\pi L_0^2$ , the focal distance for more and more of the ionization irregularities becomes smaller than the effective propagation distance  $z^*$ . Eventually, for  $\sigma_\phi$  large enough, all the ionization scale sizes contribute to the  $S_4$  calculation so that the received signal is said to have no dispersive signal component. In that case all the original phase irregularities contribute to the Rayleigh signal component and  $L_R = L_0$ .

Now that a scale size  $L_R$  has been chosen to characterize those sizes which contribute to the Rayleigh part of the scattered signal, let us choose an entire phase PSD corresponding to the Rayleigh signal component with outer scale size  $L_R$ . For this Rayleigh PSD to match the original PSD at small scale sizes, as it should, the two PSD's must have identical limits for  $K_x$  large. In the limit for  $K_x$  large

$$S_\phi(K_x) \approx \frac{\sigma_\phi^2 L_0}{(K_x L_0)^{n-2}} = \sigma_\phi^2 K_x^{2-n} L_0^{3-n} \quad (3-85)$$

which must be identical to the Rayleigh signal component PSD. Now for the case of a  $K^{-3}$  one-dimensional phase PSD,  $n = 5$  in Equation 3-74 and

$$\sigma_{\phi}^2 L_0^{-2} = \sigma_{\phi R}^2 L_R^{-2} \quad (3-86)$$

Thus the choice

$$\sigma_{\phi R} = \sigma_{\phi} L_R / L_0 \quad (3-87)$$

yields a new Rayleigh signal PSD with scale size dependence identical to the original phase PSD scale size dependence at small scale sizes (large  $K$  values).

With the aid of Equation 3-87 it is possible to place the value of the phase standard deviation of the Rayleigh signal component,  $\sigma_{\phi R}$ , on the curves shown in Figure 3-2. Figure 3-2 can also be cast into the form of Figure 3-3 which shows the resulting Rayleigh phase standard deviation,  $\sigma_{\phi R}$ , as a function of the original phase standard deviation,  $\sigma_{\phi}$ . For a fixed value of the parameter  $\xi$  there is a minimum value of  $\sigma_{\phi}$  below which angular scattering is negligible and  $S_4$  does not reach the value of 0.5. For this case no Rayleigh signal component is observed. As  $\sigma_{\phi}$  increases with constant  $\xi$  the value of

$$F/z^* = \pi L_0^2 / \lambda z^* \sigma_{\phi}$$

decreases so that all scale sizes eventually contribute to the Rayleigh signal component and there is no dispersive component. For that case the Rayleigh spectrum is identical to the original spectrum with

$$\sigma_{\phi R} = \sigma_{\phi} \text{ and } L_R = L_0.$$

This case corresponds to the upper portion of the plot where  $\sigma_{\phi R}$  would be larger than  $\sigma_{\phi}$  if any curves appeared there.

Returning to Figure 3-2 it is seen that for a constant value of  $\xi$ , there is a minimum value of  $\sigma_{\phi}$  below which  $S_4$  does not reach 0.5. These minimum values appear as vertical lines on the figure. In this case of weak scattering there is no Rayleigh signal component. For intermediate values of  $\sigma_{\phi}$  larger than the minimum, there is both a dispersive signal component and a Rayleigh signal component; here  $L_R$  and  $\sigma_{\phi R}$  may be read

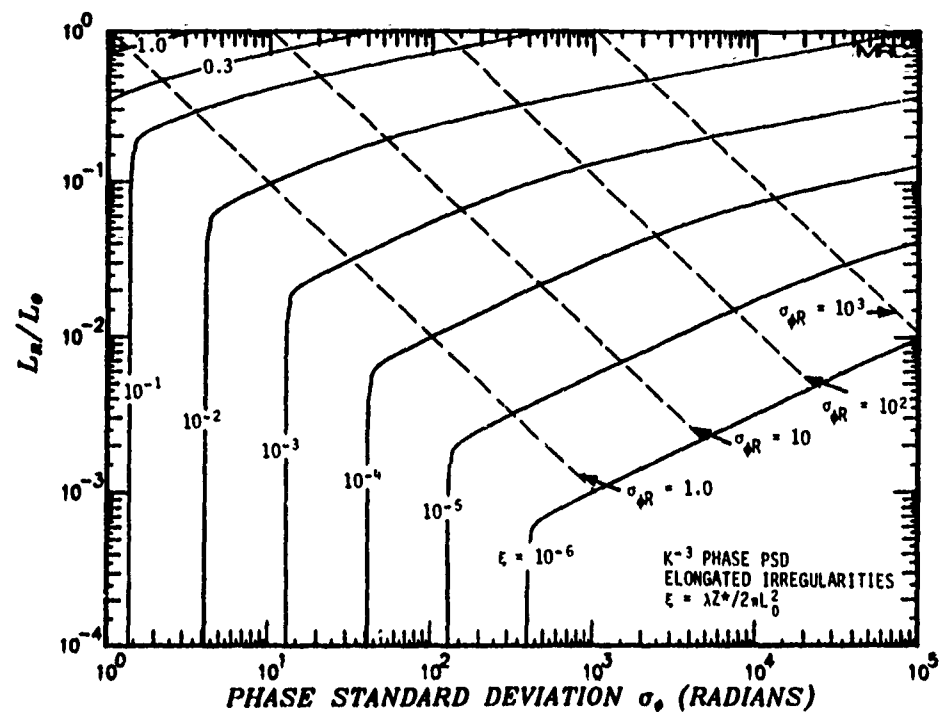


Figure 3-2. Rayleigh signal component outer scale versus  $\sigma_\phi$  and  $\sigma_{\phi R}$ , elongated irregularities.

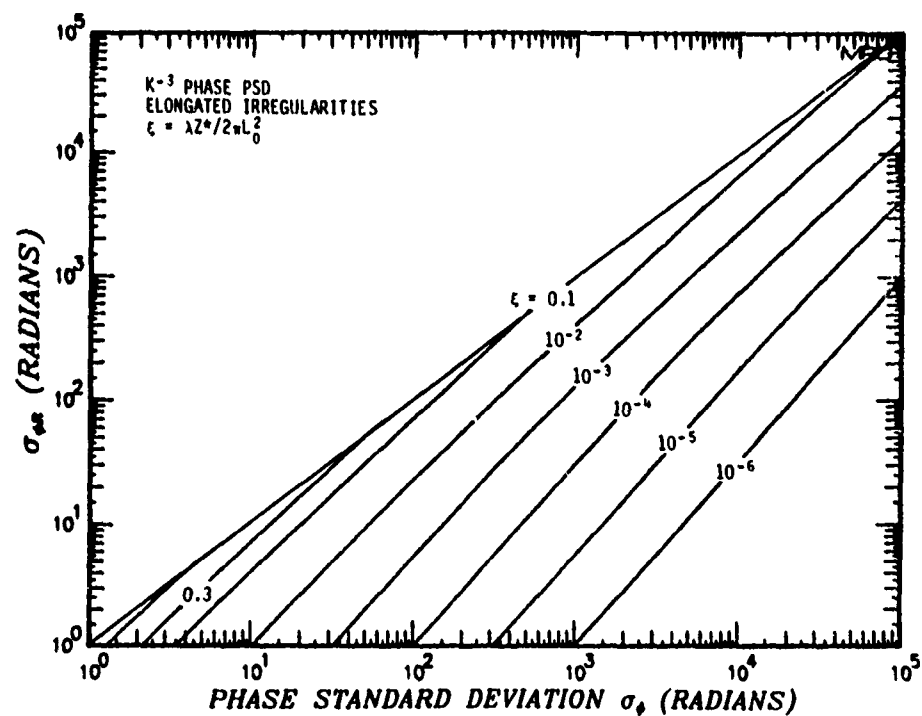


Figure 3-3. Rayleigh signal component  $\sigma_{\phi R}$  versus  $\sigma_\phi$ , elongated irregularities.

from the figure. For still larger  $\sigma_\phi$  values on any constant  $\xi$  curve, angular scattering effects dominate and the Rayleigh signal may be generated directly from the original values of  $L_0$  and  $\sigma_\phi$  with no dispersive signal component.

As discussed in Section 4.3, an important signal parameter which characterizes whether dispersive or diffractive effects dominate is defined as

$$\alpha = \omega_0 / \sigma_\phi \omega_{coh} \quad (3-88)$$

For  $\alpha$  greater than unity angular scattering or diffraction effects dominate the signal structure. For  $\alpha$  less than unity dispersive effects predominate. Therefore, it is necessary that the value of  $\alpha$  for the Rayleigh signal component be greater than unity or else the heuristic basis for the choice of the Rayleigh PSD loses merit. For a  $K^{-3}$  one-dimensional phase PSD the value of  $\alpha$  is given in Equation 4-106 as

$$\alpha \approx \frac{\ln(L_0/\ell_i) \lambda z^* \sigma_\phi}{2\pi L_0^2} \quad (3-89)$$

Now for the Rayleigh signal component

$$\alpha_R \approx \frac{\ln(L_R/\ell_R) \lambda z^* \sigma_{\phi R}}{2\pi L_R^2} \quad (3-90)$$

Now Equation 3-87 may be used in Equation 3-90 to obtain

$$\alpha_R \approx \ln(L_R/\ell_R) \frac{\lambda z^*}{2\pi L_0^2} \frac{\sigma_\phi}{\sigma_{\phi r}} \sigma_\phi \quad (3-91)$$

Since results already exist for  $\sigma_{\phi R}$  as a function of  $\sigma_\phi$  with  $\xi$  as a parameter it is easy to compute  $\alpha_R$  as a function of  $\sigma_\phi$  with  $\xi$  taken parametrically.

Figure 3-4 shows the value of  $\alpha_R$ , for the Rayleigh signal component, as a function of  $\sigma_{\phi}$  for the composite signal for values of the parameter  $\xi$  ranging from  $10^{-6}$  to 100. The ratio of outer scale to inner scale  $L_R/\lambda_R$  is taken as 100 in the figure; this value is a reasonable minimum. Values of the phase standard deviation for the Rayleigh signal component,  $\sigma_{\phi_R}$ , are also shown parametrically ranging from 1 to 1000 radians. As can be seen in the figure, the minimum value of  $\alpha_R$  is 2.5 for  $\sigma_{\phi_R}$  greater than 1.0 radian. Since values of  $\sigma_{\phi_R}$  less than 1.0 radian are prohibited (see the discussion of Figure 3-3), the value of 2.5 is a true minimum for  $\alpha_R$ .

The fact that  $\alpha_R$  for the Rayleigh signal component is always greater than unity is important for two reasons. The first reason, already discussed, is that the Rayleigh signal component is thus characterized by angular scattering or diffractive effects. The second reason is that the time delay jitter for the Rayleigh signal component is then independent of  $\alpha$  and is simply related to the coherence bandwidth,  $\omega_{coh}$ , defined in Section 4.1.5.2.

From Equation 4-135 the time delay jitter for the composite signal is given by

$$\sigma_{\tau} = \left( \frac{1}{2} + \frac{1}{\alpha^2} \right)^{1/2} \frac{1}{\omega_{coh}} \quad (3-92)$$

Now it will be shown that the time delay jitter is always inversely proportional to the coherence bandwidth if the signal has a Rayleigh component. Furthermore, if the signal has a Rayleigh component, the value of the coherence bandwidth is the same as it is for the composite signal.

Now if  $\alpha$  is large, diffraction is the dominant effect and the time delay jitter becomes

$$\sigma_{\tau} \approx \frac{1}{\sqrt{2} \omega_{coh}} \quad (3-93)$$

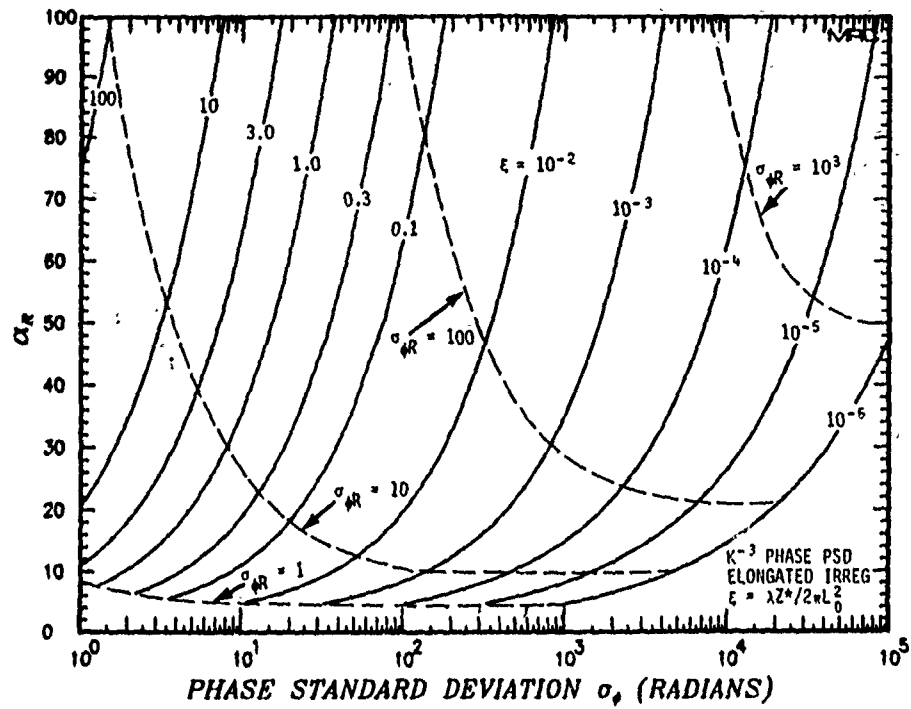


Figure 3-4. Rayleigh signal component  $\alpha_R$  versus  $\sigma_\phi$ , elongated, irregularities,  $L_R/\lambda_R = 100$ .

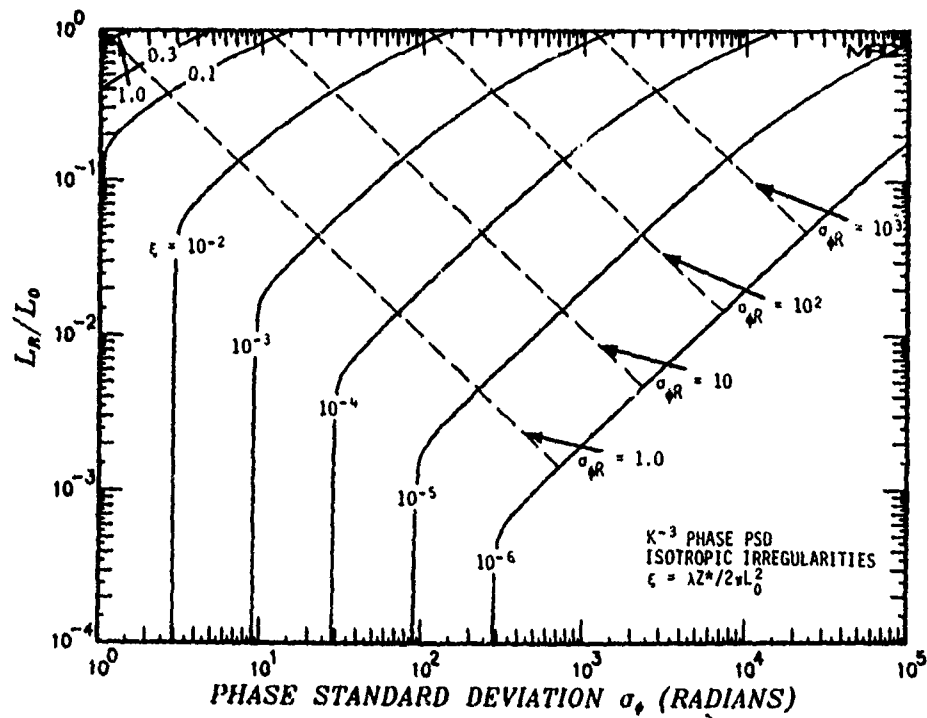


Figure 3-5. Rayleigh signal component outer scale versus  $\sigma_\phi$  and  $\sigma_{\phi R}$ , isotropic irregularities.

If  $\alpha$  is small, dispersive effects dominate and the Rayleigh signal component must be generated to isolate the diffractive processes. If the Rayleigh signal component exists, then  $\alpha_R$  is greater than unity and

$$\sigma_{\tau R} \approx \frac{1}{\sqrt{2} \omega_{\text{coh}R}} \quad (3-94)$$

where the additional R subscripts are used to denote the Rayleigh signal component.

Now for a  $K^{-3}$  one-dimensional phase PSD, the value of  $\omega_{\text{coh}}$  is given by Equation 4-74

$$\omega_{\text{coh}} = \frac{2\pi\omega_0 L_0^2}{\ln(L_0/\ell_i) \lambda z^* \sigma_\phi^2} \quad (3-95)$$

where  $A_0$  and  $A_2$  are taken from Equations 4-44 and 4-45. Equation 3-95 is valid for the composite signal. Now since, from Equation 3-87

$$L_R^2/\sigma_{\phi R}^2 = L_0^2/\sigma_\phi^2 \quad (3-96)$$

the value of the coherence bandwidth for the Rayleigh signal component is approximately identical to the value of the coherence bandwidth for the composite signal,

$$\omega_{\text{coh}R} \approx \omega_{\text{coh}}$$

since the only difference is the logarithmic term which will have little effect.

At this point it is useful to consider the important signal parameter  $\ell_0$  defined in Equation 4-73 as the signal decorrelation distance. For a  $K^{-3}$  one-dimensional phase PSD the values of  $A_0$  and  $A_2$  are given by Equations 4-44 and 4-45 and the value of the signal decorrelation distance is given by

$$\ell_0^2 = \frac{2L_0^2(z_r+z_t)^2}{\ln(L_0/\ell_i)\sigma_\phi^2 z_t^2} \quad (3-97)$$

The value of the signal decorrelation distance for the Rayleigh signal component may be written as

$$\ell_{0R}^2 = \frac{2L_R^2(z_r+z_t)^2}{\ln(L_R/\ell_i)\sigma_{\phi R}^2 z_t^2} \quad (3-98)$$

Equation 3-96 may be substituted into Equation 3-98 with the result that

$$\ell_{0R} \approx \ell_0 \quad (3-99)$$

Exact equality is not obtained because of the differences in the logarithm term. This important result states that, if a Rayleigh signal component exists, its signal decorrelation distance is approximately equal to the signal decorrelation distance of the original composite signal.

### 3.4.2 Rayleigh Signal Component for Isotropic Irregularities

In the case of isotropic irregularities the transformations

$$K_\perp^2 = K_x^2 + K_y^2 \quad (3-100)$$

and

$$V = K_\perp^2 Z^*/2k \quad (3-101)$$

may be introduced into Equation 3-72 and the identical definition of  $V'$  established as was used in the case of elongated irregularities so that

$$(0.5)^2 = \frac{8\sigma_\phi^2 \Gamma[(n-1)/2]}{\Gamma[(n-3)/2]\xi} \int_0^{V'} \frac{\sin^2(V)dV}{(1+2V/\xi)^{(n-1)/2}} \quad (3-102)$$



defines  $V'$ . The calculation of the Rayleigh signal component parameters  $\sigma_{\phi R}$ ,  $L_R$  and  $\alpha_R$  may be accomplished with the same procedures used in the elongated irregularity case.

Figures 3-5, 3-6, and 3-7 show the results for  $L_R/L_0$ ,  $\sigma_{\phi R}$  and  $\alpha_R$  as functions of the value of the phase standard deviation  $\sigma_\phi$  of the composite signal and various values of the parameter  $\lambda Z^*/2\pi L_0^2$ . As can be seen the general behavior of these results is similar to the results for the case of elongated irregularities.

### 3.5 EXAMPLES OF STATISTICALLY GENERATED SIGNALS

#### 3.5.1 Example 1: Diffraction Important

In this section examples of two statistically generated signals are presented and the results compared to the MPS results presented in Section 2. These two examples present interesting tests of the signal generation algorithms since one case is dominated by diffractive effects and the other is dominated by dispersive effects.

First consider the MPS calculation described in detail in Section 2.6. In this example the carrier frequency is 2.25 GHz, the phase standard deviation is 350 radians, the outer scale is 1 km and the inner scale is 10 m. The incident wave is plane (infinite  $z_t$ ) and the scattering layer is 1000 km thick with an additional free-space propagation distance of 1000 km from the exit of the layer to the receiver plane. This MPS calculation is applicable only to a two-dimensional geometry and thus corresponds to the theoretical development for the infinitely elongated irregularity case.

Now since the computed values of the generalized power spectrum  $S(K, \tau)$  have been specialized to the thin phase-screen case for convenience, it is necessary to find the thin phase-screen geometry equivalent to the MPS geometry just described. For the case at hand the single thin phase-screen is centered in the scattering layer and is located a distance of 1500 km from the receiver plane. The value of  $\lambda z_r/2\pi L_0^2$  is then 0.031831. Now using the results shown in Figures 3-2 and 3-3 it is seen that for the Rayleigh signal component

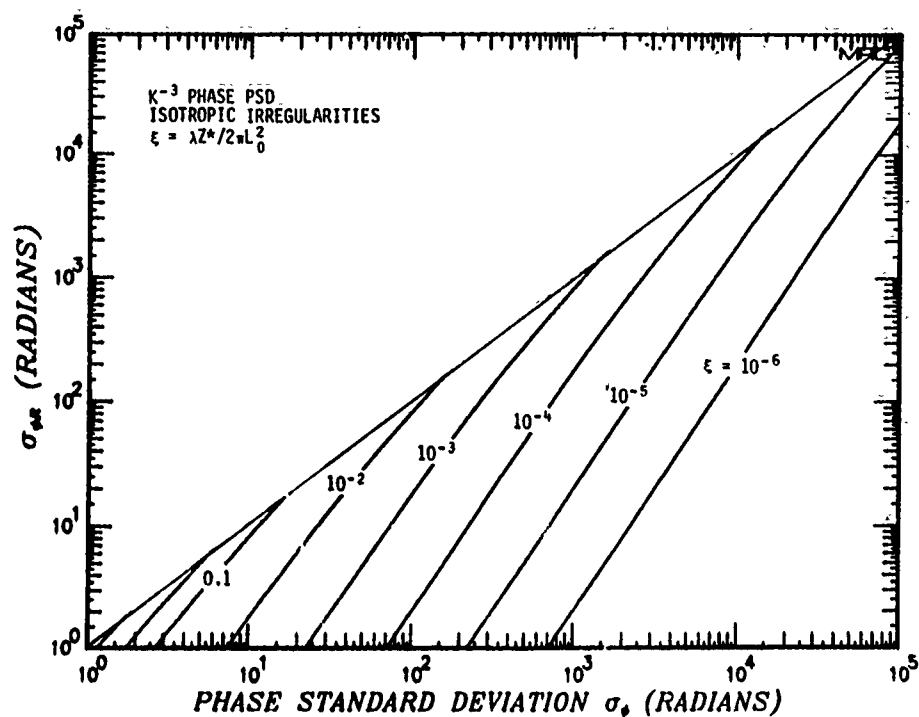


Figure 3-6. Rayleigh signal component  $\sigma_{\phi R}$  versus  $\sigma_{\phi}$ , isotropic irregularities.

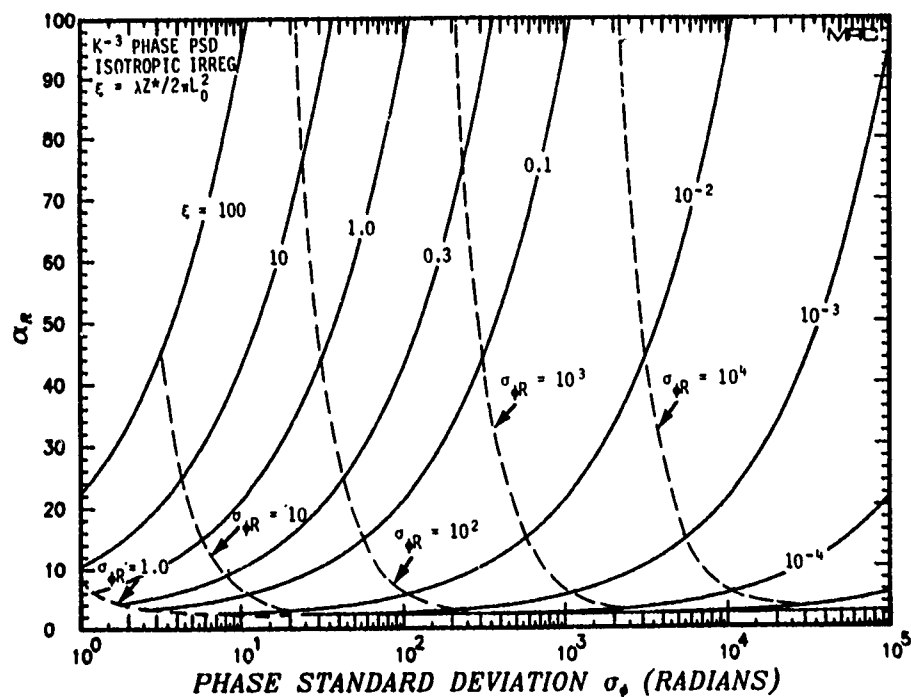


Figure 3-7. Rayleigh signal component  $\alpha_R$  versus  $\sigma_{\phi}$ , isotropic irregularities,  $L_R/l_R = 100$ .

$$\sigma_{\phi R} = 194 \text{ rad}$$

$$L_R = 564 \text{ m}$$

Now in order to obtain results for comparison to the MPS results presented in Section 2.6, it is convenient to numerically generate the solution to the parabolic wave equation  $U(x, z_r, v + \omega_0)$  by taking the Fourier transform of the impulse response function

$$U(x, z_r, v + \omega_0) = \int_{-\infty}^{\infty} h(x, z_r, \tau) e^{-i v \tau} d\tau \quad (3-103)$$

Equivalently  $U$  may be directly obtained from Equation 3-51. Equation 3-103 is identical to Equation 3-47 where the  $z_r$  and  $\omega_0$  dependence are included for completeness. Note that the impulse response function  $h$  is also dependent upon the carrier frequency. Realizations of the impulse response are obtained in discrete form using Equation 3-70. The generalized power spectrum  $S(K, \tau)$  is given for the case of elongated irregularities by

$$S(K, \tau) = \frac{\alpha_R \omega_{\text{coh}R} \ell_{0R}}{2^{3/2} \pi} \exp \left\{ -\frac{1}{4} K^2 \ell_{0R}^2 - \frac{1}{2} \alpha^2 \left[ \frac{1}{4} K^2 \ell_{0R}^2 - \omega_{\text{coh}R} \tau \right]^2 \right\} \quad (3-104)$$

where the parameters  $\alpha_R$ ,  $\ell_{0R}$ , and  $\omega_{\text{coh}R}$  are given by Equations 4-106, 4-73, and 4-74, respectively and of course refer to the Rayleigh component of the received signal which is the only component one can generate with this technique.  $A_0$  and  $A_2$  which are required in Equations 4-73 and 4-74 may be obtained from Equations 4-44 and 4-45. The carrier frequency dependence of the impulse response function is evident in the expressions for the parameters  $\alpha$ ,  $\omega_{\text{coh}}$ , and  $\ell_0$ .

The Fourier transform given by Equation 3-103 may be implemented discretely by using Equations 3-51 and 3-52 from the earlier development. In order to directly compare to the MPS case, 32 discrete frequencies are used over a bandwidth of 4.096 MHz. The same number (32) of delay cells are used with delay spacing

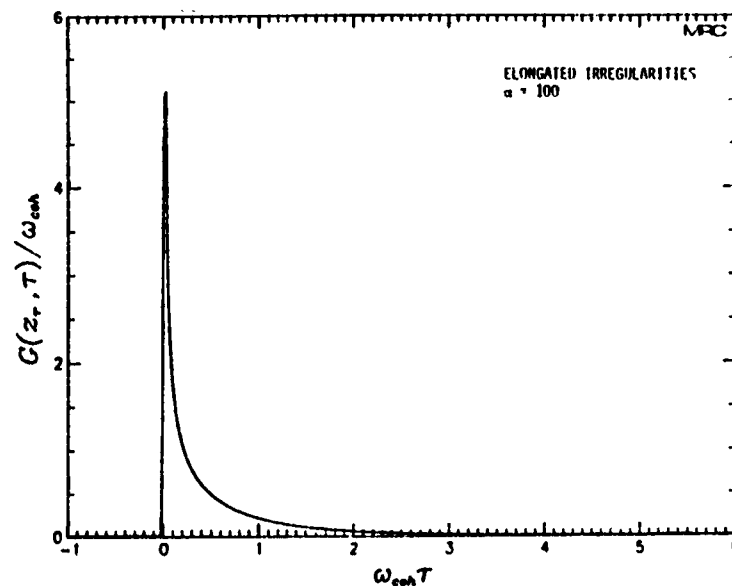


Figure 3-8. Normalized power impulse response function,  $\alpha = 100$ .

$$\Delta\tau = 244.1 \times 10^{-9} \text{ sec}$$

and thus a total time-delay interval

$$\tau = 32 \Delta\tau = 7.812 \times 10^{-6} \text{ sec}$$

Values of the important Rayleigh signal parameters  $\omega_{\text{cohR}}$  and  $\alpha_R$  are given in the plane wave, thin phase-screen case as

$$\omega_{\text{cohR}} = -\pi\omega_0 A_0 / \lambda A_2 Z_r \sigma_{\phi R}^2 = 0.795 \times 10^6 \text{ rad/sec}$$

$$\alpha_R = \omega_0 / \sigma_{\phi R} \omega_{\text{cohR}} = 91.7$$

To perform the integration over  $\tau$  which is required in Equation 3-51 or Equation 3-103, the variable  $\tau$  ranged discretely from  $-2.44 \times 10^{-7}$  to  $7.32 \times 10^{-6}$  sec so that values of  $\omega_{\text{cohR}}\tau$  ranged from -0.19 to 5.82. As can be seen from Figure 3-8 which shows the normalized power impulse response

function defined in Section 4.3, the range of non-zero values of the power impulse response is about

$$0 \leq \omega_{\text{coh}} \tau \leq 3$$

for  $\alpha = 100$ . In the case at hand  $\alpha$  is close to 100 and so the range of values taken in the numerical calculation includes all important  $\tau$  values.

Another way to check the accuracy of the numerical calculation is to form the integral

$$\sum_{m=0}^{N-1} \sum_{s=0}^{M-1} S(m\Delta K, s\Delta\tau) \Delta K \Delta\tau$$

This integral is the discrete equivalent of

$$\int_{-\infty}^{\infty} \int_{-\infty}^{\infty} S(K, \tau) dK d\tau$$

and should be equal to unity since the continuous integral is equal to  $\Gamma(\Delta x=0, \Delta f=0)$  according to Equation 4-84 or 4-87. This important quantity is always formed and checked in every statistical signal generation.

For this example there are 1024 cells in the x-direction, with a total length of 208.33 m and a spacing of 0.20345 m which is precisely three times the grid spacing used in the MPS calculation.

In order to obtain results for statistical averaging purposes, the statistical signal generation algorithm is performed five times with five different random number sequences. As described above, for each individual signal generation calculation, 32 frequencies are generated with 1024 x-points for each frequency. This signal is referred to as a single statistical realization and is similar to a MPS frequency selective signal realization.

Figures 3-9 to 3-14 show a comparison of the mutual coherence function  $\Gamma(\Delta x, \Delta f)$  for a single statistical realization versus the strong scattering theory described in Section 4. Figure 3-9 shows the amplitude

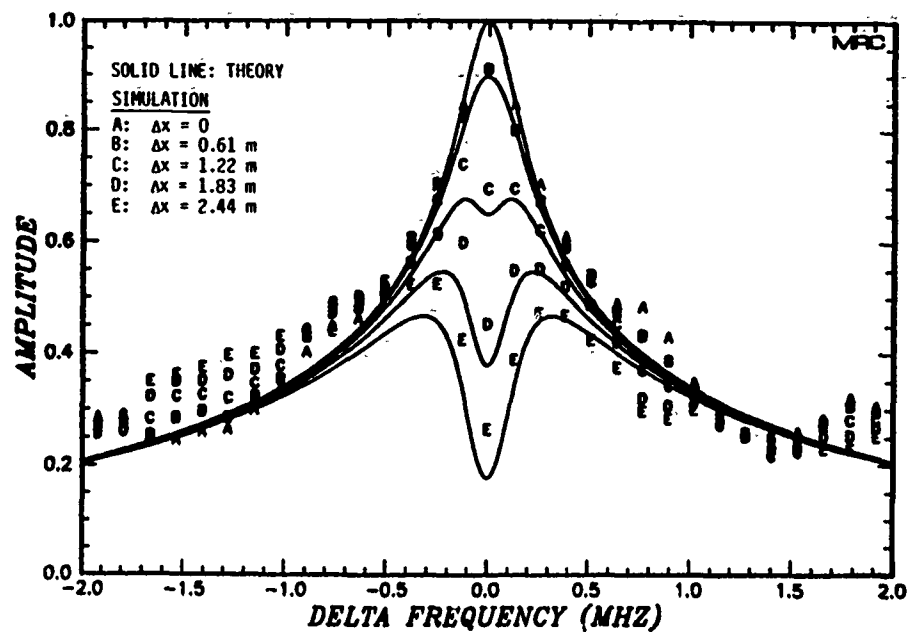


Figure 3-9. Comparison of magnitude of  $r$ , single statistical realization versus theory.

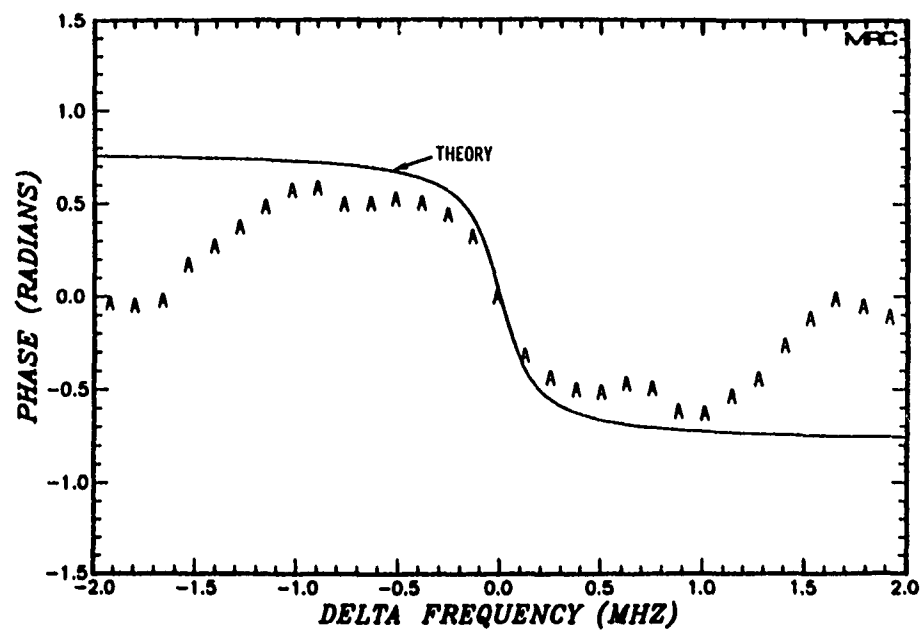


Figure 3-10. Comparison of phase of  $r$ , single statistical realization versus theory,  $\Delta x = 0$ .

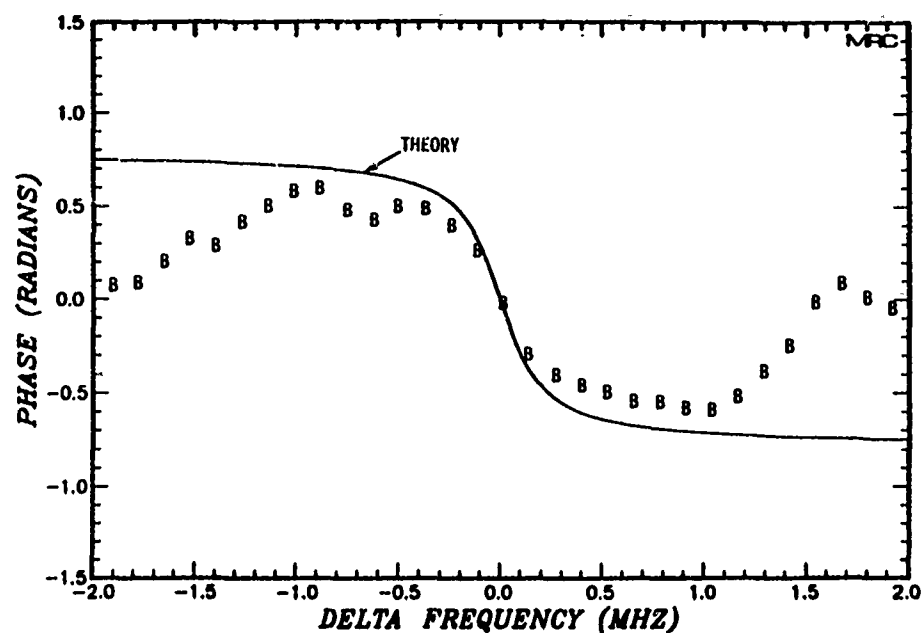


Figure 3-11. Comparison of phase of  $r$ , single statistical realization versus theory,  $\Delta x = 0.61$  m.

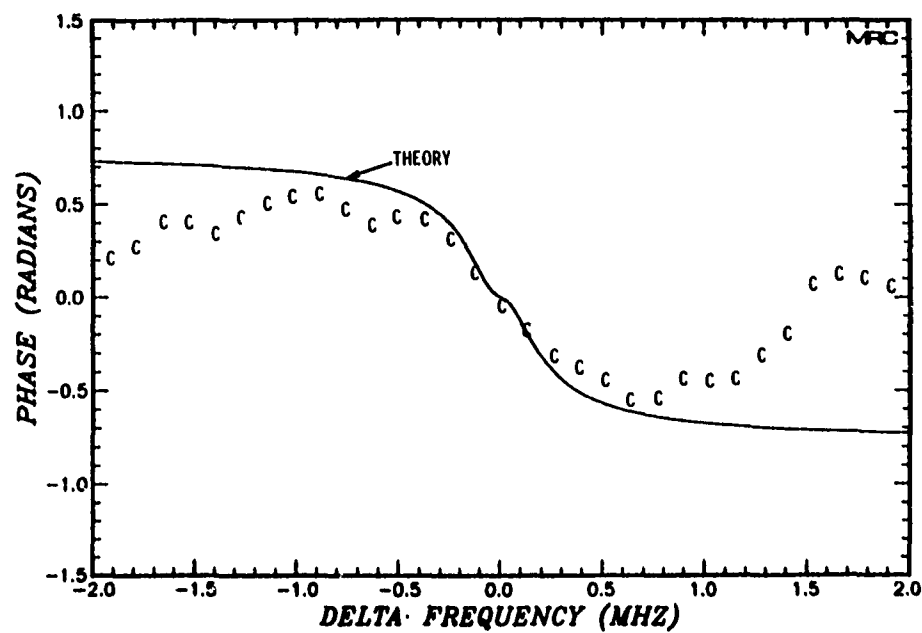


Figure 3-12. Comparison of phase of  $r$ , single statistical realization versus theory,  $\Delta x = 1.22$  m.

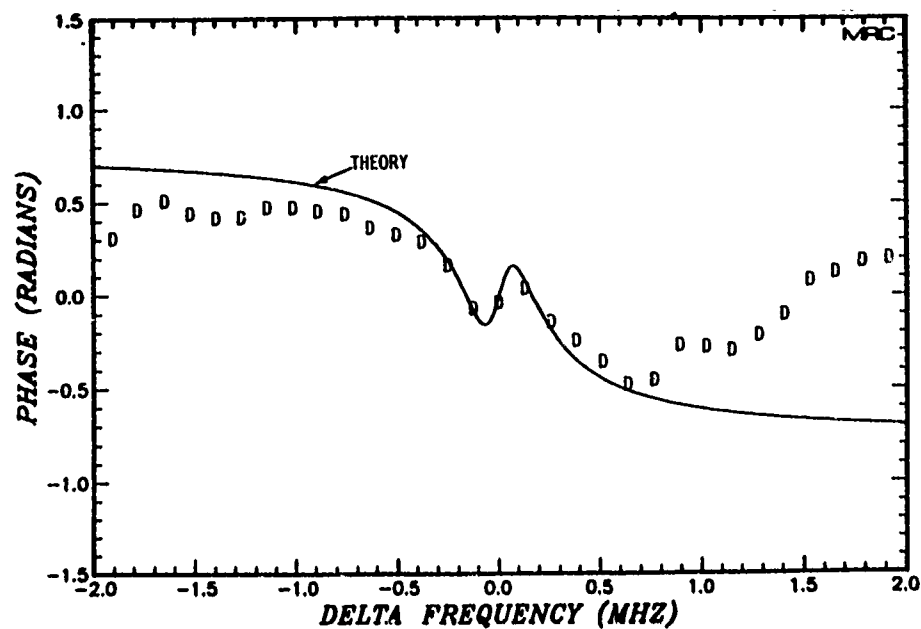


Figure 3-13. Comparison of phase of  $r$ , single statistical realization versus theory,  $\Delta x = 1.83$  m.

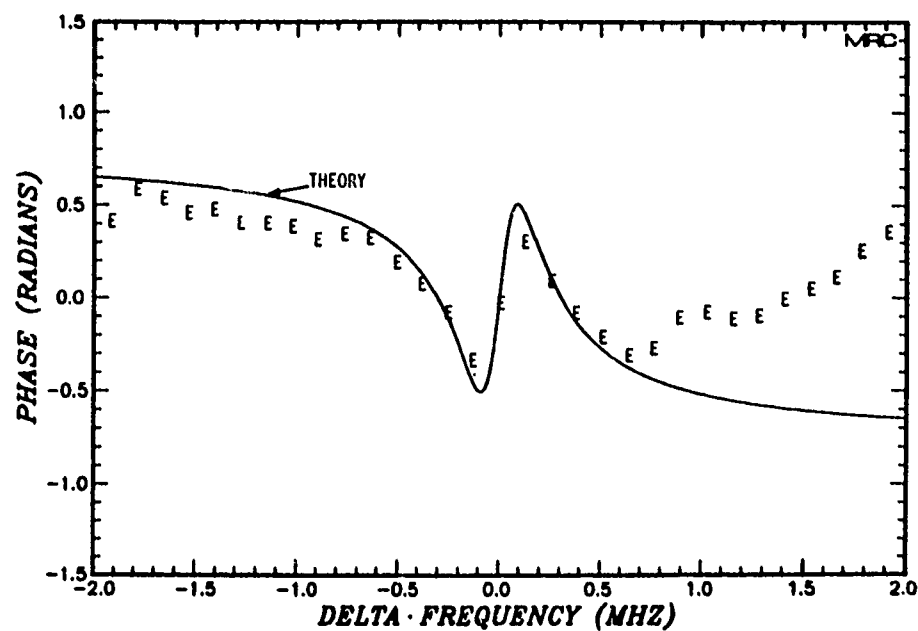


Figure 3-14. Comparison of phase of  $r$ , single statistical realization versus theory,  $\Delta x = 2.44$  m.



of  $r$  corresponding to values of  $\Delta x$  of 0.0, 0.61 m, 1.22 m, 1.83 m and 2.44 m versus theory. These values of  $\Delta x$  are chosen to correspond to the MPS values presented in Figures 2-26 to 2-31. The theoretical results presented here are similar to those presented in Figures 2-26 to 2-31 except that here the thin phase-screen theoretical limit is taken. It is seen that the difference in the phase of  $r$  between the thick layer theory and the thin phase-screen theory is simply a term that is linearly proportional to the frequency deviation from the carrier frequency. In Section 4 the received time-domain signal is shown to be related to the Fourier transform of  $r$  so that this phase term that is proportional to frequency yields only an additional time delay. As can be seen in Figure 3-9 the agreement between statistical results and theory is good but is somewhat worse than the agreement between the MPS results and theory.

Figures 3-10 to 3-14 compare the phase of  $r$  computed from the single statistical realization versus the thin phase-screen theory. Agreement is very good in the most important region close to zero  $\Delta f$  where the power in the spectrum of the modulation waveform is concentrated, but elsewhere the phase of  $r$  diverges somewhat from the analytic results.

Figures 3-15 to 3-20 compare the value of  $r$  obtained by averaging the results of five independent statistical realizations to the analytic, thin phase-screen results. It is apparent in Figure 3-15 that the average amplitude of  $r$  compares quite well to the theory and, in fact, does better than the MPS calculation at matching the theoretical thin phase-screen results. The agreement with theory is quite good for the entire range of  $\Delta f$  for all five of the  $\Delta x$  values shown.

Figures 3-16 to 3-20 show a comparison of the phase of  $r$  for the average of five statistical realizations versus the analytic thin phase-screen value. As expected from the averaging process, the variations in the phase are reduced in comparison to the variations observed for the case of a single realization. In all five figures the average statistical phase and the analytic phase agree quite well near zero  $\Delta f$  but disagree somewhat for  $|\Delta f|$  greater than about 1 MHz. This minor disagreement in the phase of  $r$  does not appear to be important to the resulting time-domain signals to be presented next. The most important aspect of these comparisons is the good agreement between numerical results and theory near zero

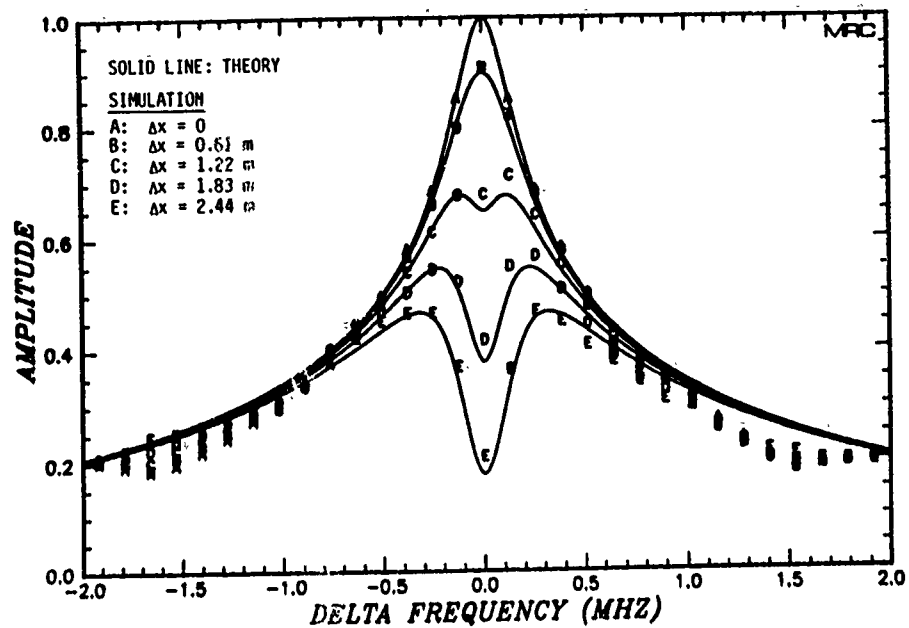


Figure 3-15. Comparison of amplitude of  $r$ , average of five statistical realizations versus theory.

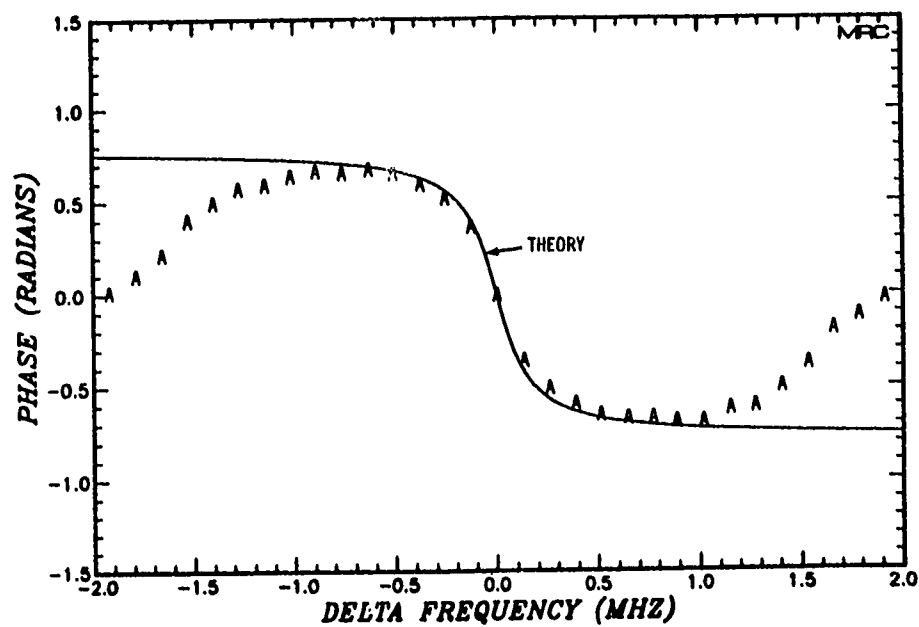


Figure 3-16. Comparison of phase of  $r$ , average of five statistical realizations versus theory,  $\Delta x = 0$ .

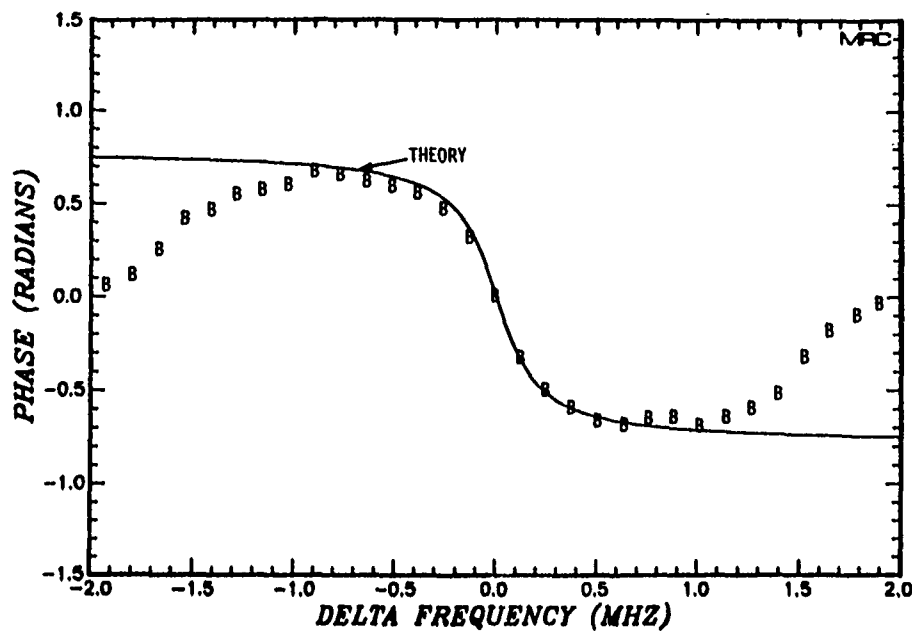


Figure 3-17. Comparison of phase of  $r$ , average of five statistical realizations versus theory,  $\Delta x = 0.61$  m.

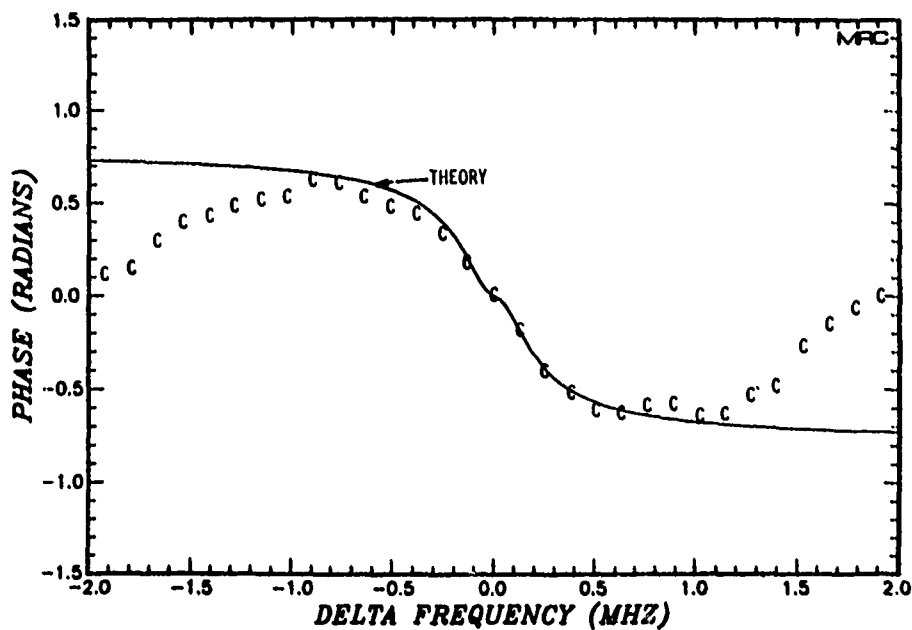


Figure 3-18. Comparison of phase of  $r$ , average of five statistical realizations versus theory,  $\Delta x = 1.22$  m.

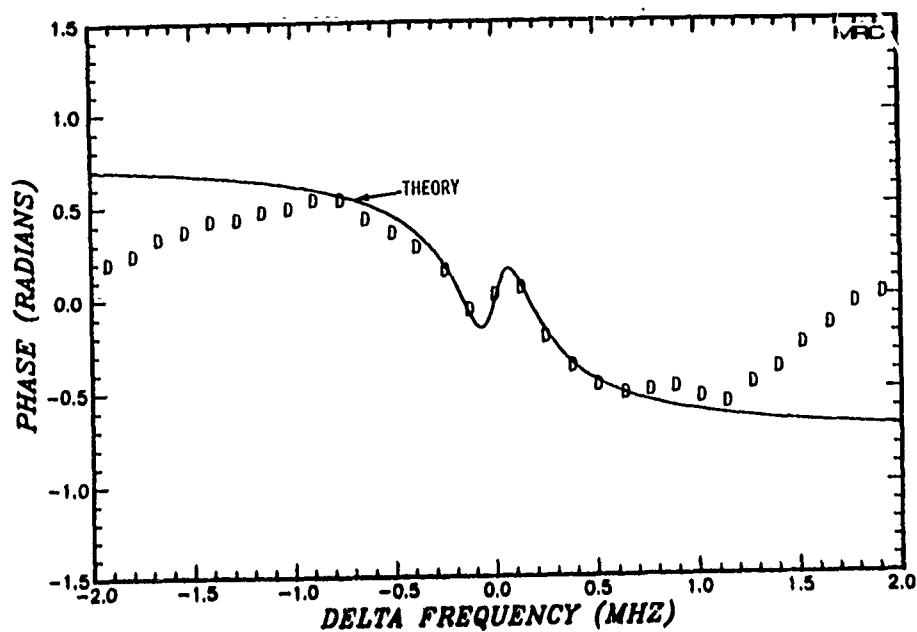


Figure 3-19. Comparison of phase of  $r$ , average of five statistical realizations versus theory,  $\Delta x = 1.83$  m.

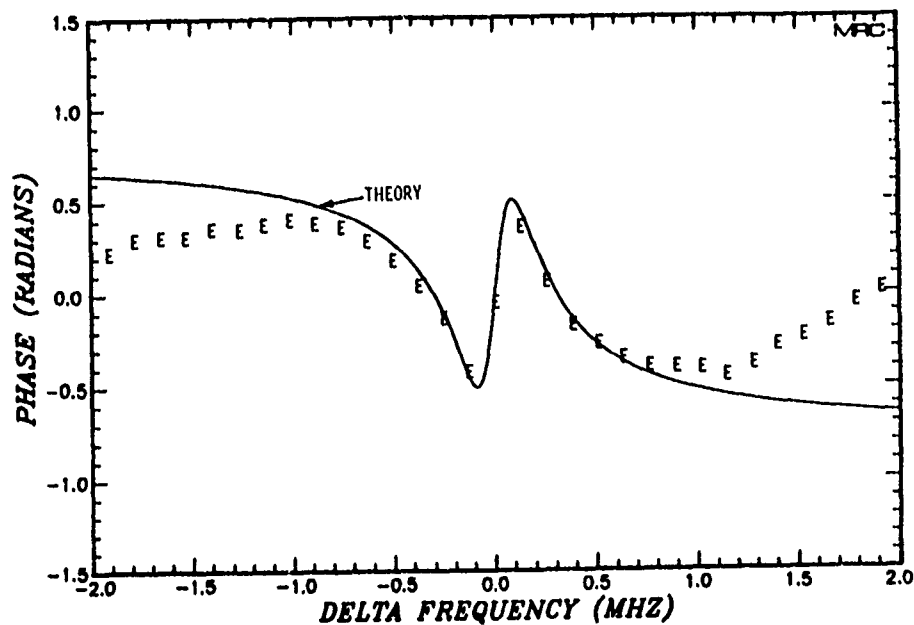


Figure 3-20. Comparison of phase of  $r$ , average of five statistical realizations versus theory,  $\Delta x = 2.44$  m.

$\Delta f$ . This region is the most critical since zero  $\Delta f$  corresponds to the carrier frequency where most of the energy in the modulation waveform is concentrated.

Figure 3-21 shows an example of the envelope of the received triangular waveform as determined by the statistical signal generation technique. The received complex envelope is given by

$$e(x, z_r, \tau) = \frac{1}{2\pi} \int_{-\infty}^{\infty} M(v) U(x, z_r, v + \omega_0) e^{iv\tau} dv \quad (3-105)$$

where  $M(v)$  is the Fourier transform of the transmitted pulse

$$M(f) = \begin{cases} T_c \left( \frac{\sin \pi f T_c}{\pi f T_c} \right)^2 & |f| \leq \frac{1}{T_c} \\ 0 & |f| > \frac{1}{T_c} \end{cases} \quad (3-106)$$

where  $v = 2\pi f$  and  $T_c$  is 488.3 nsec, twice the duration of the transmitted triangular pulse.  $U(x, z_r, v + \omega_0)$  is determined from the discrete form of Equation 3-103 where the impulse response function  $h(x, z_r, \tau)$  is the statistically generated impulse response function obtained using Equation 3-70. In Figure 3-21 samples of the amplitude  $|e(x, z_r, \tau)|$  are shown for 101 values of  $x$  separated in distance by 0.61 m, the MPS grid interval. Thus Figure 3-21 is directly comparable to Figure 2-32 in Section 2. The time domain results shown in these two figures are both independent realizations of a stochastic process and hence cannot be identical. However, the similarity in overall structure indicates that the statistically generated realization is an adequate approximation to the exact MPS calculation.

Figure 3-22 shows the average pulse shape of the received time domain signal which is obtained by averaging all the 5120 realizations of  $|e(x, z_r, \tau)|$  generated in five runs with 1024  $x$ -samples per run. This average pulse shape is found to be quite similar to the result for the MPS calculation shown in Figure 2-33. The overall appearance of the two pulse shapes is very similar with a noticeable concentration of power at small

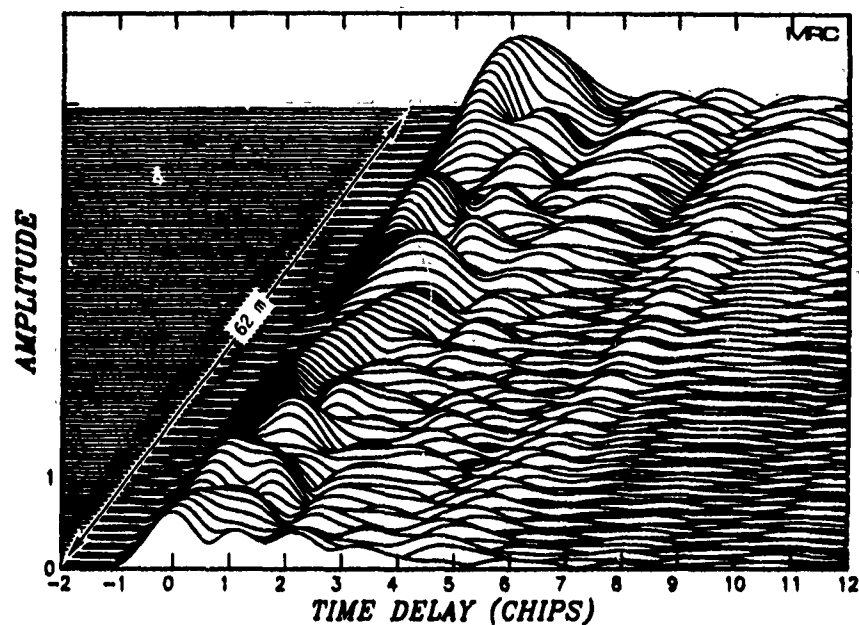


Figure 3-21. Envelope of the received time-domain waveform-- statistical signal realization.

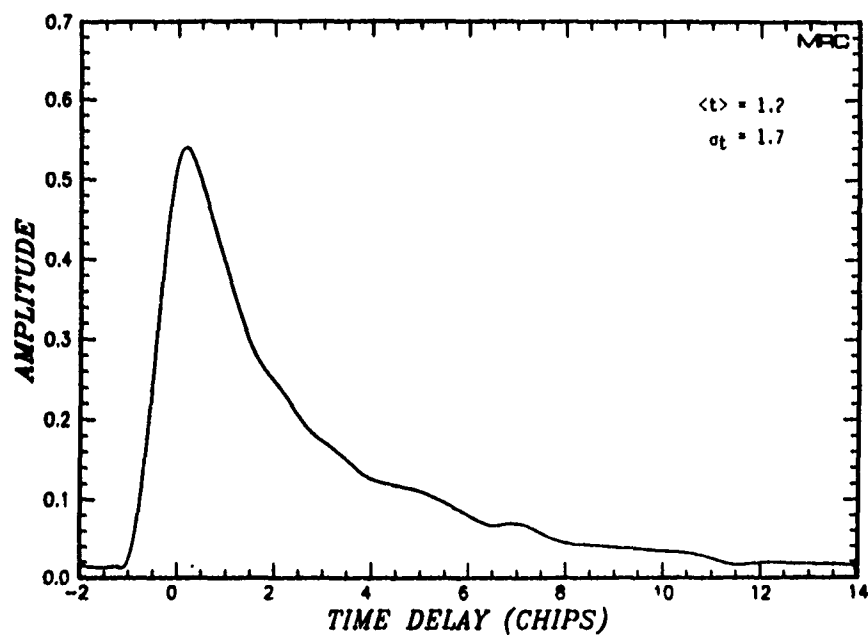


Figure 3-22. Average received time-domain envelope--statistical signal realization.

delays for the MPS case as compared to a slightly more spread out situation for the statistical signal generator case. For the MPS case shown in Figure 2-33, the mean time delay,  $\langle \tau \rangle$ , is 1.1 chips and the time delay jitter,  $\sigma_\tau$ , is 1.4 chips. For the statistical signal shown in Figure 3-22 the mean time delay is 1.2 chips and the time delay jitter is 1.7 chips. In both cases a chip is the unit of time  $T_c$  here equal to 488.3 nsec. The theoretical result in the thin phase-screen case is 1.3 chips for the mean time delay and 1.8 chips for the time delay jitter.

Thus rather good agreement is obtained for the MPS results and the statistical signal results when compared to theory. One should keep in mind that the MPS calculation is a direct solution to the parabolic wave equation and involves no approximations. The theoretical calculation requires a number of approximations to obtain solutions for average quantities and hence suffers in accuracy relative to the very general MPS calculation. The theoretical calculation includes both dispersion and diffraction effects but the statistical signal generation technique is only applicable to the diffraction effects. The rather good agreement shown in this example indicates that the heuristic method devised to calculate the Rayleigh or diffraction part of the composite signal is adequate to the task.

### 3.5.2 Example 2: Focusing Important

As another example of statistical signal generation consider a case where large scale structure leads to focusing and to other effects of large phase irregularities. As in the previous example the MPS results are compared to the statistically generated results.

The scattering geometry is identical to that of the previous example. A plane wave propagates through a 1000 km thick scattering layer and then propagates in free-space an additional 1000 km to the receiver plane. The carrier frequency here is 7.5 GHz, the phase standard deviation is 300 radians, the outer scale is 10 km and the inner scale is 10 m. In the MPS calculation, ten phase-screens are uniformly spaced over 1000 km to represent the thick scattering medium. A grid of length 100 km is divided into 16384 points to represent the signal amplitude and phase.

For this example, 32 discrete frequencies are used over a two-sided bandwidth of 80 MHz. This bandwidth is chosen as the null-to-null bandwidth of a PN spread spectrum code with chip rate of  $40 \times 10^6$  chips/sec or to represent a single, band-limited, triangular, modulated waveform with  $T_c$  equal to  $25 \times 10^{-9}$  sec.

Figures 3-23 to 3-30 show the resulting time-domain waveform and some related measurements from the MPS realization. Figure 3-23 shows 101 samples of the magnitude of the envelope of the received time-domain waveform. Each of these 101 samples is taken from equally spaced points along the entire MPS calculation grid. Thus each curve is separated in distance by 990 m and very little resolution along the x-axis is shown. More resolution is shown in Figure 3-24 which shows the received time-domain envelope for the first 101 MPS grid points. The spacing between each grid point is 6.1035 m corresponding to 16384 cells equally spaced over a 100 km distance so that the 101 curves shown in the figure correspond to a total distance of 616 m along the MPS grid.

The effect of the large scale phase irregularities is apparent in Figure 3-23 and 3-24 in the appearance of many noticeable instances of signal focusing where the peak amplitude is greater than unity. This focusing results in a measured value of the  $S_4$  scintillation index of 1.15. Values of  $S_4$  greater than unity are indicative of focusing effects. The focal length for the largest (10 km) irregularities is given by

$$\frac{\pi L_0^2}{\lambda \sigma_\phi}$$

which is 26,180 km. Thus the receiver plane is well inside the focal distance of the largest irregularities and this example is dominated by large phase effects. These large phase effects are apparent in Figure 3-23 where the received signal is seen to vary in mean time delay with no dispersive signal spreading. Dispersive effects are not strong enough here to cause pulse spreading.

Figures 3-25 and 3-26 further illustrate the point. These figures show the mean time delay  $\langle \tau \rangle$  and the time delay jitter  $\sigma_\tau$  as a function of distance along the MPS grid. As can be seen the mean time



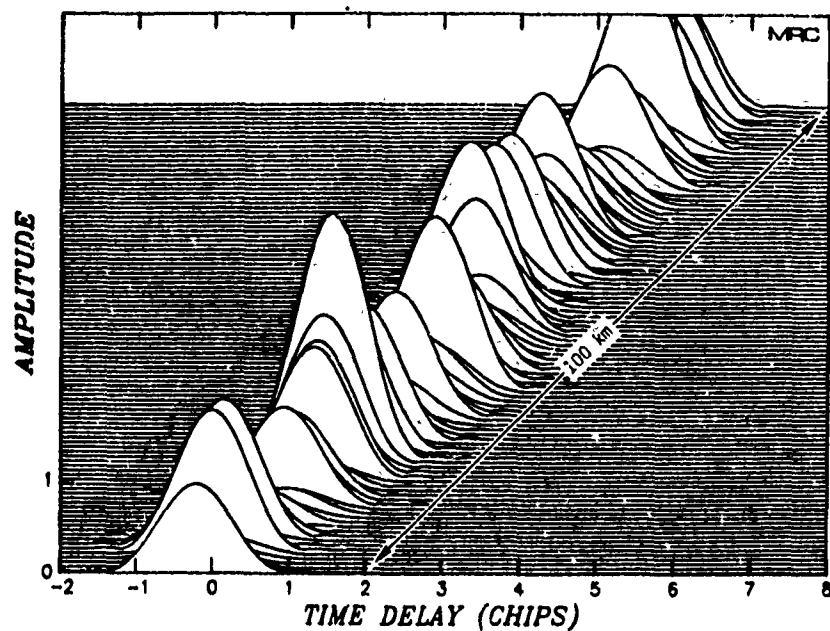


Figure 3-23. Envelope of the received time-domain waveform--MPS signal realization.

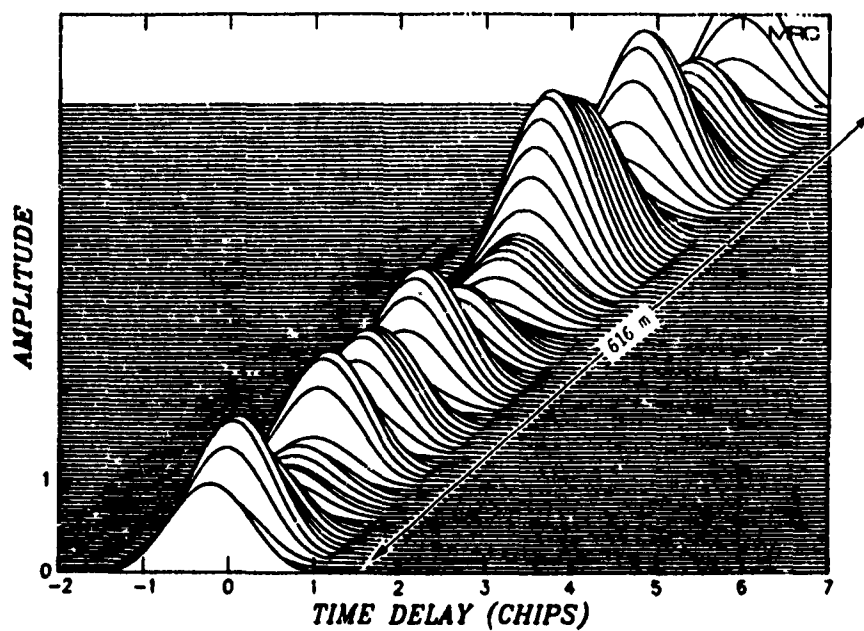


Figure 3-24. Envelope of the received time-domain waveform--MPS signal realization.

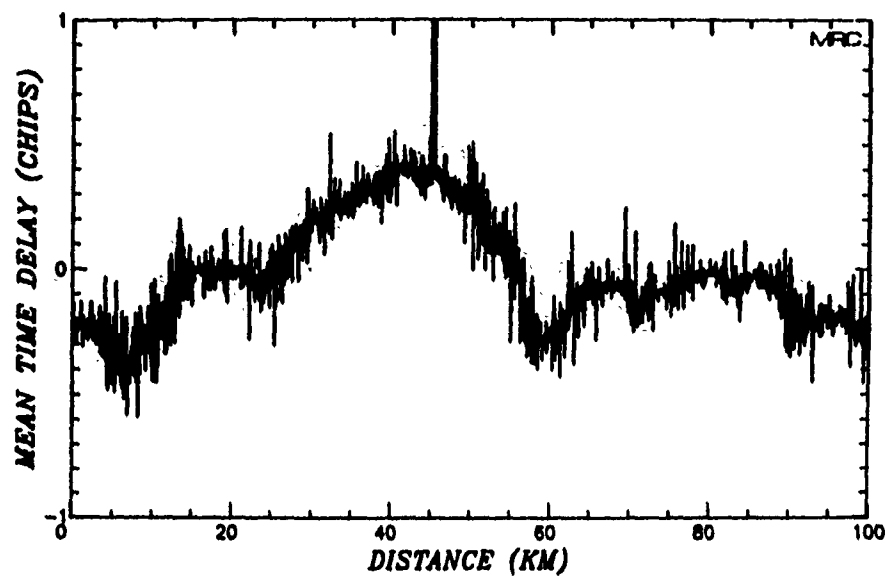


Figure 3-25. Mean time delay,  $\langle t \rangle$ , as a function of distance along the MPS grid.

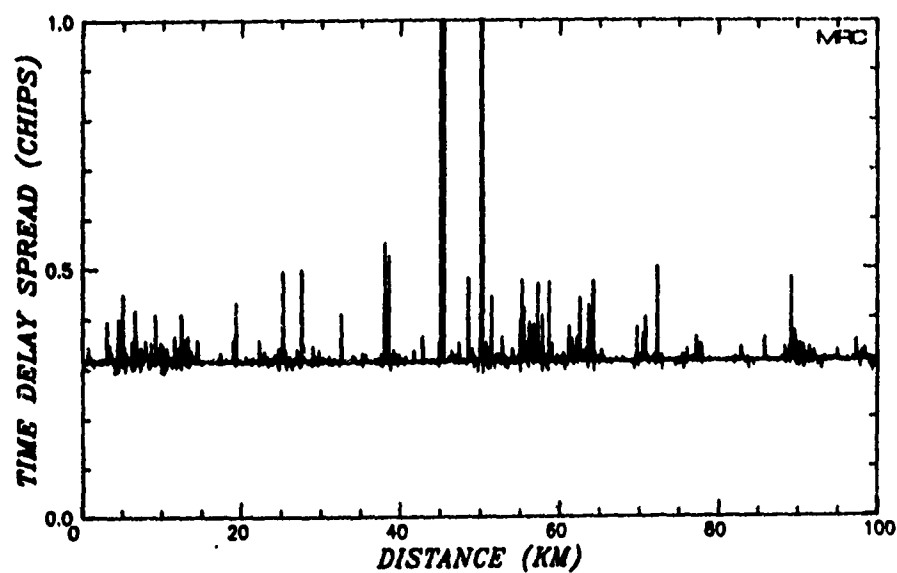


Figure 3-26. Time delay jitter,  $\alpha_t$ , as a function of distance along the MPS grid.

delay varies slowly with distance and corresponds to the location of the signal peaks shown in Figure 3-23. Notice the negative mean time delay (early arrival) at the beginning of the realization and the increasingly late time of arrival (positive delay) around 40 km in the realization. Both of these features are evident in Figure 3-23.

Figure 3-26 shows the value of  $\sigma_T$  obtained for each individual MPS cell in the MPS grid as a function of distance along the MPS grid. For the most part the value of  $\sigma_T$  is constant and equal to the spread of a triangular signal,  $0.316 T_C$  (see Equation 2-73). Thus the major dispersive effect in this MPS calculation is increased time delay that is accompanied by very little pulse broadening.

However in the range from 40 to 50 km along the MPS grid there is some very interesting phenomena occurring with evidence of isolated, high measurements of  $\langle \tau \rangle$  and  $\sigma_T$ . Figure 3-27 shows the peak amplitude of the received time-domain envelope as a function of distance along the

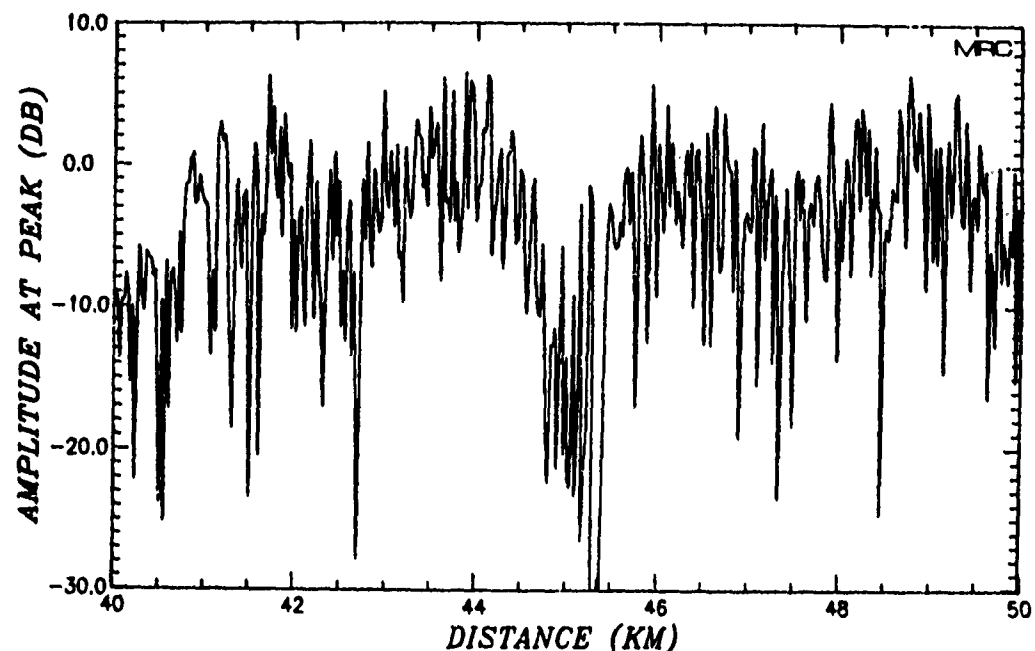


Figure 3-27. Peak signal amplitude as a function of distance along the MPS grid.

MPS calculation grid. Notice that there is an extended region of about 10 dB fading at around 40 km and a region of very deep fading or defocusing near 45 km. These deep fading regions are responsible for the large observed values of  $\langle \tau \rangle$  and  $\sigma_\tau$ .

Figures 3-28 and 3-29 show closeups of the plots of  $\langle \tau \rangle$  and  $\sigma_\tau$  for the region from 40 km to 50 km on the MPS grid. It can be seen that the large values of  $\langle \tau \rangle$  and  $\sigma_\tau$  near 45 km coincide with the region of the deepest signal fades shown in Figure 3-27. It is also apparent that the isolated large  $\langle \tau \rangle$  and  $\sigma_\tau$  measurements coincide with small regions where the signal level is very low. These isolated, large  $\langle \tau \rangle$  and  $\sigma_\tau$  measurements are not artifacts or errors in the simulation but rather they are caused by large phase decorrelation across the signal spectrum which has a much higher probability of occurrence during deep fading conditions. The reason for the higher than normal phase decorrelation during deep fades is that, in general, fades are caused by cancellation of signals coming from different directions. For very deep fades to occur, such cancellation must occur over much of the signal bandwidth. Under these circumstances very little change in frequency (or direction of arrival) is required to obtain quite a large change in signal phase.

Figure 3-30 shows the received time-domain signal for the range from 44.5 km to 46.1 km on the MPS grid. Notice the increased mean time delay of about 0.4 chips at the front of the figure caused by propagation through a large striation. At the back of the figure, corresponding to the very deep fade location, phase decorrelation across the signal spectrum causes a very extended received time-domain waveform so that some aliasing is apparent. This type of deep fading behavior is associated with the occurrence of focusing and defocusing and is not modeled by the statistical signal generation of Rayleigh fading signals. However this behavior is handled correctly in the MPS propagation simulation.

Figure 2-37 in Section 2 shows a comparison of the magnitude of the two-frequency mutual coherence function calculated from the MPS realization versus the theoretical strong scatter solution given in Section 4. As seen in the figure, there is some disparity between the two calculations. The source of the differences lies in the fact that the theoretical calculation is a strong scatter approximation not exactly valid for the focusing/defocusing conditions characteristic of this MPS calculation.

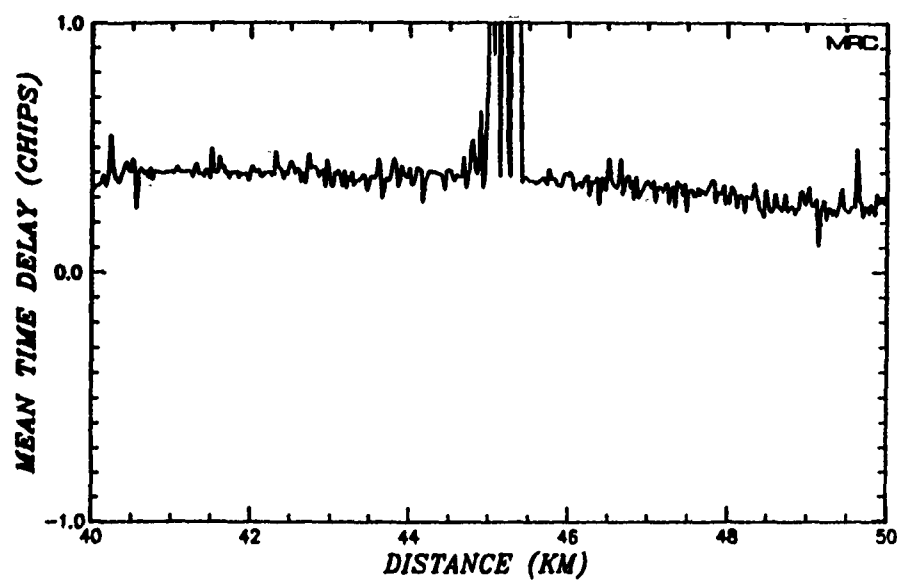


Figure 3-28. Mean time delay,  $\langle t \rangle$ , as a function of distance along the MPS grid.

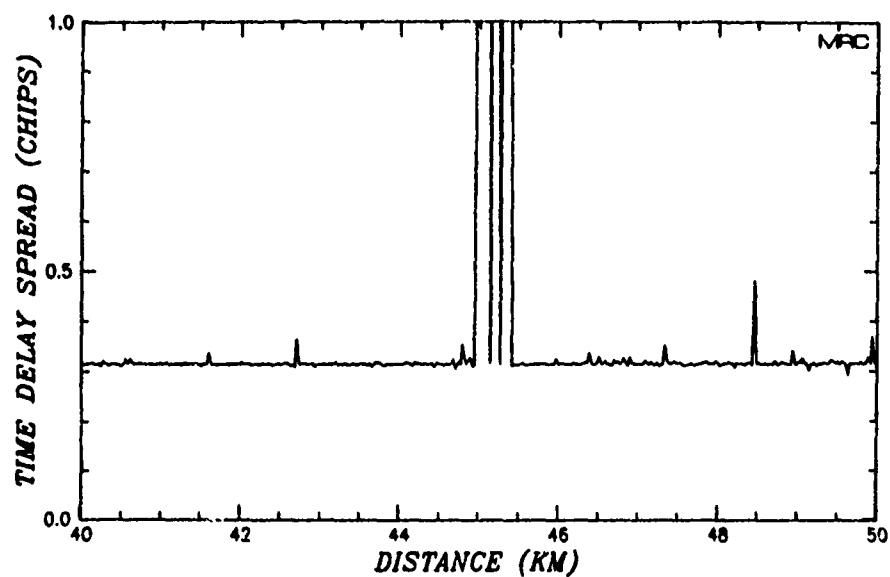


Figure 3-29. Time delay jitter,  $\alpha_t$ , as a function of distance along the MPS grid.

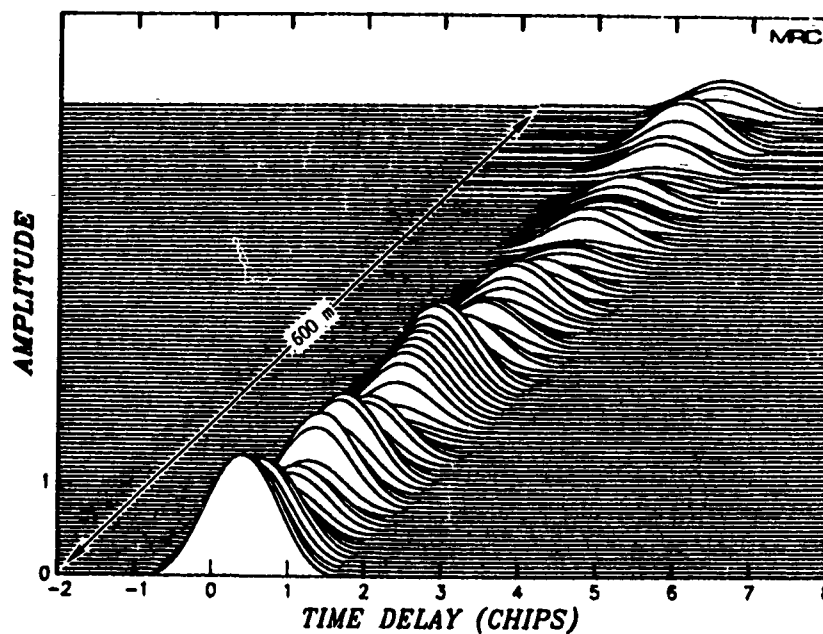


Figure 3-30. Received envelope for MPS calculation from 44.4 to 45.0 km along the MPS grid.

In order to generate the Rayleigh portion of this time-domain signal it is first necessary to determine the values of the phase standard deviation  $\sigma_{\phi R}$  and the outer scale  $L_R$  of the Rayleigh signal component. These values may be obtained from Figures 3-2 and 3-3 for the value of  $\xi$  of  $9.5 \times 10^{-5}$  as

$$\sigma_{\phi R} = 5.0 \text{ rad}$$

$$L_R = 168 \text{ m}$$

Values of the important signal parameters  $\alpha_R$  and  $\omega_{cohR}$  are found as

$$\omega_{cohR} = -\pi \omega_0 A_0 / \lambda A_2 z_r \sigma_{\phi R}^2 = 5.97 \times 10^8 \text{ rad/sec}$$

$$\alpha_R = \omega_0 \sigma_{\phi R} / \omega_{cohR} = 15.8$$

where the inner scale for the Rayleigh signal component is taken as 1.68 m. Since the inner scale always appears in the logarithm for a  $K^{-3}$  one-dimensional phase power spectrum, small changes in its value have little effect.

As is the case in the previous example, it is desired to obtain a statistical realization of the received complex envelope for comparison to the MPS results. Thus realizations of the function  $U(x, z_r, v + \omega_0)$  are required.

Again  $U(x, z_r, v + \omega_0)$  is generated at 32 discrete frequencies over the null-to-null 80 MHz bandwidth which corresponds to a chip duration,  $T_c$ , of  $2.5 \times 10^{-8}$  sec and a PN code rate of 40 Mbps. Thus 32 delay cells are used with

$$\Delta\tau = 1.25 \times 10^{-8} \text{ sec}$$

and a total delay interval of

$$T = 32 \Delta\tau = 4.0 \times 10^{-7} \text{ sec}$$

To generate the impulse response function  $h(x, z_r, \tau)$  the discrete values of the delay  $\tau$  range from

$$-2.5 \times 10^{-8} \text{ sec} \leq \tau \leq 3.625 \times 10^{-7} \text{ sec}$$

which corresponds to

$$-14.93 \leq \omega_{\text{coh}} \tau \leq 216.5$$

Figure 4-3 for  $\alpha$  equal to 10 shows that all the power in the impulse response function is contained within the limits

$$-0.5 \leq \omega_{\text{coh}} \tau \leq 4$$

so that the range cited above is more than sufficient to obtain all the power. In fact the samples of  $S(K, \tau)$  are negligible outside the limits

$$-0.5 \leq \omega_{\text{coh}} \tau \leq 4$$

Thus, in this example, the impulse response function  $h(x, z_r, \tau)$  has properties similar to a delta function since it is non-zero at only a few values of delay. The transform of the impulse response function  $U(x, z_r, \nu + \omega_0)$  is then relatively constant with frequency  $\nu$  and thus exhibits high correlation properties with respect to  $\nu$ .

As in the previous example, 1024 cells are used to represent the variation in  $x$  with a value of  $\Delta x$  of 2.03 m which is precisely 3 times the value used in the MPS calculation.

Figure 3-31 shows the amplitude of the received complex envelope  $|e(x, z_r, \tau)|$  as a function of  $x$  and  $\tau$ . 101 curves are shown each representing the received signal as a function of  $\tau$  and separated in distance  $x$  by 6.10 m. This figure should be compared to Figure 3-24 which shows

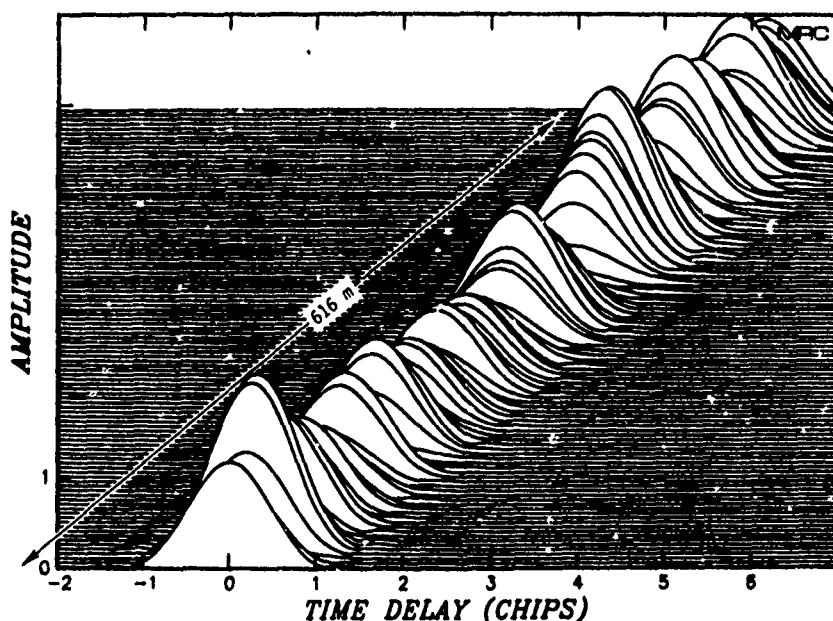


Figure 3-31. Received envelope for statistical signal realization.



similar results for the MPS calculation. It is apparent that this realization of the Rayleigh component of the received signal has none of the focusing/defocusing properties or the large slow variations in mean time delay evident in the MPS calculation. This behavior is, of course, a consequence of the definition of the Rayleigh signal component which is that portion of the signal with Rayleigh fading statistics.

Comparison of Figures 3-24 and 3-31 show that the statistical calculation for the individual time-domain signals are similar to the MPS calculation. However the large scale focusing and defocusing effects are not represented. In addition, the large slow changes in the mean arrival time caused by large scale phase variations are also not included in the statistical realization.

Numerical calculation of the two-frequency mutual coherence function for this statistical signal realization shows constant correlation with frequency for both amplitude and phase of  $r$  for all values of  $\Delta x$ . This correlation property has already been discussed and is another indication of the absence of severe frequency selective scattering and diffractive effects in this example.

It should be noted that the comparisons shown in this example emphasize the differences in the signal realizations formed by the MPS simulation and the statistical signal generation technique. This approach was taken because it yields an interesting discussion of the different aspects of electromagnetic wave propagation. For the study of the effects of strong scintillation on receiver performance, it is always sufficient to consider only Rayleigh fading, which is the worst case for a one-way propagation path through strongly turbulent ionized media.

## SECTION 4

### TWO-FREQUENCY MUTUAL COHERENCE FUNCTION

In this section an analytic solution is obtained for the two-position, two-frequency mutual coherence function for spherical wave propagation. It is assumed that strong scattering conditions prevail and that the quadratic approximation to the phase structure-function is therefore valid.

This approximation was used by Sreenivasiah, et al., (1976) for the case of plane wave propagation. Furthermore, Sreenivasiah and Ishimaru (1979) have recently generalized their previous results to obtain the two-frequency mutual coherence function for beam wave propagation in homogeneous turbulence using the quadratic structure-function approximation. More recently the two-position, two-frequency mutual coherence function was obtained for spherical wave propagation using the extended Huygens-Fresnel principle (Fante, 1981). Although the quadratic structure-function approximation can sometimes lead to difficulties (Wandzura, 1980) it is appropriate for calculation of the two-frequency mutual coherence function but not for calculation of higher moments of the field (Fante, 1980). Fante discusses the accuracy of the quadratic structure-function approximation (Fante, 1981) for the case of atmospheric turbulence with a Kolmogorov power spectrum of irregularities. He has found that the accuracy is a function of the irregularity power spectrum and of the strength of the turbulence (Private Communication, 1982), with accuracy increasing for stronger scattering.

The strong scatter solution presented in this section forms the basis of the statistical signal generation technique described in Section 3 of this report. Here the turbulent ionized medium occupies a thick finite layer with transmitter and receiver located in free-space on opposite sides of the layer.

General analytic solutions are derived for two cases. In the first case the random slab is represented by a one-dimensional power spectrum of electron-density fluctuations which corresponds to propagation through elongated irregularities as would occur for an equatorial satellite link to a ground station. In the second case the random slab is represented by isotropic ionization irregularities which would occur in the ionosphere for propagation roughly along the direction of the earth's magnetic field. Both cases taken together represent the extremes of the range of results to be expected for propagation through ionospheric fluctuations, or ionization irregularities caused by barium cloud instabilities or by nuclear detonations.

The complex general analytic results obtained for the two cases of interest are simplified by the use of the thin phase-screen approximation (zero slab thickness) to obtain tractable expressions for the two-frequency mutual coherence function as well as its Fourier transform, referred to as the generalized power spectrum.

The accuracy of the thin phase-screen approximation is a matter of some importance to this work. This approximation is considered in some detail in this section where comparisons of the case of a thick layer to the thin phase-screen case are presented for the  $S_4$  scintillation index, the mean time delay, and the time delay standard deviation.

#### 4.1 FORMULATION

Consider a monochromatic spherical wave  $E(\bar{\rho}, z, \omega, t)$  which originates from a transmitter located at  $(0, 0, -z_t)$  and propagates in free-space in the positive  $z$  direction where it is incident on an ionization irregularity layer which extends from  $0 \leq z \leq L$ . After emerging from the layer at  $z = L$ , the wave then propagates in free-space to a receiver located at  $(0, 0, z_r)$ . This geometry is shown in Figure 3-1 in the preceding section. As the wave propagates, its phase substantially behaves as  $(-ikz + i\omega t)$  so write

$$E(\bar{\rho}, z, \omega, t) = U(\bar{\rho}, z, \omega) \exp\{i(\omega t - \int k(z') dz')\} \quad (4-1)$$

where  $\langle k(z) \rangle$  is the mean wave number given by

$$\langle k(z) \rangle = \frac{\omega}{c} (1 - N_e/n_c)^{1/2} = k (1 - k_p^2/k^2)^{1/2} \quad (4-2)$$

where  $c$  is the speed of light in a vacuum,  $N_e$  is the mean ionization density,  $n_c$  is the critical electron density and is related to the classical electron radius  $r_e$  by  $n_c = \pi/(\lambda^2 r_e)$ , ( $r_e = 2.82 \times 10^{-15}$  m).

It has been shown that  $U(\bar{\rho}, z, \omega)$  satisfies the parabolic wave equation under the Markov approximation, (Tatarskii, 1971; Yeh and Liu, 1977)

$$\nabla_{\perp}^2 U - 2i\langle k(z) \rangle \frac{\partial U}{\partial z} - \langle k^2(z) \rangle \frac{\frac{\Delta N_e}{\langle N_e \rangle} \frac{\omega_p^2}{\omega^2}}{(1 - \omega_p^2/\omega^2)} U = 0 \quad (4-3)$$

where  $\Delta N_e$  is a small variation in the ionization level and  $\omega_p = k_p c$  is the circular plasma frequency of the background ionization. The exponential time dependence has been suppressed and it has been assumed that  $\omega_p \ll \omega$ , otherwise signal attenuation would be the dominant effect.

#### 4.1.1 Power Impulse Response Function

Now consider the case where the transmitted waveform is no longer a monochromatic wave, but can be expressed as a waveform modulated on a carrier

$$m(t)e^{i\omega_0 t}$$

where  $m(t)$  is the transmitted modulation waveform or transmitted complex envelope and  $\omega_0$  is the carrier angular frequency. Now if  $M(\omega)$  is the spectrum of the transmitted complex envelope,

$$M(\omega) = \int_{-\infty}^{\infty} m(t)e^{-i\omega t} dt \quad (4-4)$$

then the received complex envelope can be expressed as

$$e(\bar{\rho}, z_r, t) = \frac{1}{2\pi} \int_{-\infty}^{\infty} M(\omega) U(\bar{\rho}, z_r, \omega + \omega_0) e^{i\omega t} d\omega \quad (4-5)$$

where  $U(\bar{\rho}, z_r, \omega)$  is the solution to the parabolic wave equation at the receiver plane  $z_r$ . This result is proven in Section 3 of this report.

The average received power is given by

$$I(z_r, t) = \langle ee^* \rangle = \frac{1}{4\pi^2} \int_{-\infty}^{\infty} \int_{-\infty}^{\infty} M(\omega) M^*(\omega') \langle U(\bar{\rho}, z_r, \omega + \omega_0) U^*(\bar{\rho}, z_r, \omega' + \omega_0) \rangle \\ \times e^{i(\omega - \omega')t} d\omega d\omega' \quad (4-6)$$

The two-frequency mutual coherence function,  $r$ , is the quantity in the angle brackets. Under the assumption (to be justified later) that  $r$  is a function only of the transverse spatial and frequency differences, Equation 4-6 may be transformed using the sum and difference transformation

$$\omega_d = \omega - \omega' \\ \omega_s = \frac{1}{2} (\omega + \omega') \quad (4-7)$$

$$I(z_r, t) = \frac{1}{4\pi^2} \int_{-\infty}^{\infty} \int_{-\infty}^{\infty} M(\omega_s + \omega_d/2) M^*(\omega_s - \omega_d/2) r(\Delta\bar{\rho}=0, z_r, \omega_d) \\ \times e^{i\omega_d t} d\omega_s d\omega_d \quad (4-8)$$

Since the input signal is  $m(t)$ , the input power is given by

$$I(t) = m(t)m^*(t) = \frac{1}{4\pi^2} \int_{-\infty}^{\infty} \int_{-\infty}^{\infty} M(\omega) M^*(\omega') e^{i(\omega - \omega')t} d\omega d\omega' \quad (4-9)$$

Using the same sum and difference transformation, the input power may be written

$$I(t) = \frac{1}{4\pi^2} \int_{-\infty}^{\infty} \int_{-\infty}^{\infty} M(\omega_s + \omega_d/2) M^*(\omega_s - \omega_d/2) e^{i\omega_d t} d\omega_d d\omega_s \quad (4-10)$$

Now if the input power  $I(t)$  is a delta function

$$I(t) = \delta(t) = \frac{1}{2\pi} \int_{-\infty}^{\infty} e^{i\omega_d t} d\omega_d \quad (4-11)$$

it is apparent that

$$\frac{1}{2\pi} \int_{-\infty}^{\infty} M(\omega_s + \omega_d/2) M^*(\omega_s - \omega_d/2) d\omega_s = 1 \quad (4-12)$$

So for the special case of an input power delta function, the output power at the receiver is

$$G(z_r, t) = \frac{1}{2\pi} \int_{-\infty}^{\infty} r(\Delta p=0, z_r, \omega_d) e^{i\omega_d t} d\omega_d \quad (4-13)$$

where the new symbol  $G$  has been introduced for this important function.

Now to find the output power response to a general input  $I(t)$ , first multiply Equation 4-10 by  $\exp(-i\omega_d' t)$  and integrate with respect to  $t$

$$\begin{aligned} \int_{-\infty}^{\infty} I(t) e^{-i\omega_d' t} dt &= \frac{1}{4\pi^2} \iiint_{-\infty}^{\infty} M(\omega_s + \omega_d/2) M^*(\omega_s - \omega_d/2) e^{i(\omega_d - \omega_d') t} d\omega_d d\omega_s dt \\ &= \frac{1}{2\pi} \int_{-\infty}^{\infty} M(\omega_s + \omega_d'/2) M^*(\omega_s - \omega_d'/2) d\omega_s \end{aligned} \quad (4-14)$$

The above result comes about because the  $t$  integration yields a delta function,  $2\pi\delta(\omega_d - \omega_d')$ . Now use Equation 4-14, just derived, in Equation 4-8 to obtain

$$\begin{aligned}
 I(z_r, t) &= \frac{1}{2\pi} \int_{-\infty}^{\infty} \int_{-\infty}^{\infty} I(t') e^{-i\omega_d t'} \Gamma(\Delta\bar{\rho}=0, z_r, \omega_d) e^{i\omega_d t} d\omega_d dt' \\
 &= \int_{-\infty}^{\infty} I(t') \frac{1}{2\pi} \int_{-\infty}^{\infty} \Gamma(\Delta\bar{\rho}=0, z_r, \omega_d) e^{i\omega_d(t-t')} d\omega_d dt' \\
 &= \int_{-\infty}^{\infty} I(t') G(z_r, t-t') dt' \quad (4-15)
 \end{aligned}$$

The second expression above is recognized as a convolution. Thus the output power due to a general input power is given by the convolution of the input power with the power impulse response function  $G(z_r, t)$ .

The derivation above follows the basic outline given in Ishimaru (1978) and is included in this report to serve as an aid to the notation and to emphasize the importance of the power impulse response function  $G(z_r, t)$ . It will be seen that the moments of  $G(z_r, t)$  serve as useful definitions of the mean time delay and time delay jitter which may be used to characterize the severity of the propagation medium.

#### 4.1.2 Two-Frequency Mutual Coherence Function

Thus the two-frequency mutual coherence function  $\Gamma$  is important for the calculation of pulse propagation in a random medium and it serves as a basis from which to calculate the important power impulse response function and its moments. Under the Markov approximation,  $\Gamma$  satisfies the following equation (Tatarskii, 1971; Yeh and Liu, 1977).

$$\begin{aligned}
 \frac{\partial \Gamma}{\partial z} + \frac{i}{2k_1 k_2} (k_2 \nabla_{\perp 1}^2 - k_1 \nabla_{\perp 2}^2) \Gamma \\
 - \frac{1}{8} [2k_1 \beta_1 k_2 \beta_2 A(\bar{\rho}_1 - \bar{\rho}_2) - (k_1^2 \beta_1^2 + k_2^2 \beta_2^2) A(0)] \Gamma = 0 \quad (4-16)
 \end{aligned}$$

where

$$\Gamma = \langle U(x_1, y_1, z, \omega_1) U^*(x_2, y_2, z, \omega_2) \rangle$$

and  $k_1$  and  $k_2$  are the wavenumbers at two frequencies  $\omega_1$  and  $\omega_2$ , respectively, and  $\nabla_{\perp 1}^2$  is the two-dimensional Laplacian

$$\nabla_{\perp 1}^2 = \frac{\partial^2}{\partial x_1^2} + \frac{\partial^2}{\partial y_1^2}$$

with a similar definition for  $\nabla_{\perp 2}^2$ .

Following Yeh and Liu (1977) let

$$\beta_1 = \frac{\omega_p^2 / \omega_1^2}{1 - \omega_p^2 / \omega_1^2} \quad (4-17)$$

with a similar definition for  $\beta_2$ .

The function  $A(\bar{\rho})$  is the integral of the autocorrelation function of electron density fluctuations,  $B_{\xi}$ , in the direction of propagation

$$A(\bar{\rho}_1 - \bar{\rho}_2) = \int_{-\infty}^{\infty} B_{\xi}(\bar{\rho}_1 - \bar{\rho}_2, z') dz' \quad (4-18)$$

where

$$\bar{\rho}_1 - \bar{\rho}_2 = (x_1 - x_2, y_1 - y_2)$$

$$\xi = \frac{\Delta N_e}{\langle N_e \rangle}$$

so that

$$A(\bar{\rho}_1 - \bar{\rho}_2) = 2\pi \int_{-\infty}^{\infty} \int_{-\infty}^{\infty} e^{i\bar{K}_{\perp} \cdot (\bar{\rho}_1 - \bar{\rho}_2)} \Phi_{\xi}(\bar{K}_{\perp}, K_z=0) d^2 K_{\perp} \quad (4-19)$$



where  $\phi_\xi$  is the power spectrum of electron density fluctuations. Equations 4-18 and 4-19 depend upon the validity of the Markov approximation where it is assumed that the electron density fluctuations are delta-correlated in the direction of propagation (Fante, 1975). That is

$$\beta_\xi(\bar{\rho}_1 - \bar{\rho}_2, z_1 - z_2) = A(\bar{\rho}_1 - \bar{\rho}_2) \delta(z_1 - z_2) \quad (4-20)$$

Now the sum and difference substitutions

$$X = (x_1 + x_2)/2$$

$$\zeta = x_1 - x_2$$

$$Y = (y_1 + y_2)/2$$

$$\eta = y_1 - y_2$$

$$k_s = (k_1 + k_2)/2$$

$$k_d = k_1 - k_2$$

and the assumption that the frequencies of interest are much greater than the plasma frequency so that

$$\beta_1 \approx \omega_p^2 / \omega_1^2$$

$$\beta_2 \approx \omega_p^2 / \omega_2^2$$

enable Equation 4-16 to be rewritten as

$$\begin{aligned} \frac{\partial \Gamma}{\partial z} - \frac{i}{2(k_s^2 - k_d^2/4)} [k_d \nabla_d^2 + \frac{1}{4} k_d \nabla_s^2 - 2k_s \nabla_s \cdot \nabla_d] \Gamma \\ - \frac{1}{8} \left[ \frac{2k_p^4}{k_1 k_2} A(\zeta, \eta) - \left( \frac{1}{k_1^2} + \frac{1}{k_2^2} \right) k_p^4 A(0) \right] \Gamma = 0 \end{aligned} \quad (4-21)$$

where

$$\nabla_d^2 = \frac{\partial^2}{\partial \zeta^2} + \frac{\partial^2}{\partial \eta^2}$$

$$\nabla_s^2 = \frac{\partial^2}{\partial X^2} + \frac{\partial^2}{\partial Y^2}$$

$$\nabla_s \cdot \nabla_d = \frac{\partial^2}{\partial \zeta \partial X} + \frac{\partial^2}{\partial \eta \partial Y}$$

$\Gamma$  is now written in terms of the above sum and difference arguments as  $\Gamma(\zeta, \eta, z, \omega_d)$  where  $\omega_d = ck_d$ .

The unknown two-frequency mutual coherence function may be written as  $\Gamma = \Gamma_1 \Gamma_0$  where  $\Gamma_0$  is the exact free-space solution in the parabolic approximation

$$\Gamma_0 = \left( \frac{1}{z+z_t} \right)^2 \exp \left\{ \frac{-ik_1(x_1^2 + y_1^2) + ik_2(x_2^2 + y_2^2)}{2(z+z_t)} \right\} \quad (4-22)$$

which under the sum and difference transformation used previously becomes

$$\Gamma_0 = \left( \frac{1}{z+z_t} \right)^2 \exp \left\{ \frac{-ik_s(\zeta X + \eta Y) - ik_d[(X^2 + Y^2)/2 + (\zeta^2 + \eta^2)/8]}{(z+z_t)} \right\} \quad (4-23)$$

Substituting  $\Gamma = \Gamma_1 \Gamma_0$  into Equation 4-21 and neglecting near zone terms of the order of  $k_s \zeta^2 / (z+z_t)$  and smaller, one obtains

$$\begin{aligned}
& \frac{\partial \Gamma_1}{\partial z} - \frac{i}{2} \frac{k_d}{(k_s^2 - k_d^2/4)} \nabla_d^2 \Gamma_1 + \frac{1}{(z+z_t)} \left[ \zeta \frac{\partial}{\partial \zeta} + \eta \frac{\partial}{\partial \eta} \right] \Gamma_1 \\
& - \frac{1}{8} \left[ \frac{2k_p^4 A(\zeta, \eta)}{k_1 k_2} - \left( \frac{1}{k_1^2} + \frac{1}{k_2^2} \right) k_p^4 A(0) \right] \Gamma_1 \\
& + \text{terms with } \frac{\partial \Gamma_1}{\partial X} + \frac{\partial \Gamma_1}{\partial Y} = 0
\end{aligned} \tag{4-24}$$

Equation 4-24 is valid in the region  $0 \leq z \leq L$  with boundary condition

$$\Gamma_1(\zeta, \eta, z=0, \omega_d) = 1 \tag{4-25}$$

Since the boundary condition is independent of  $X$  and  $Y$ , and the equation has no terms other than the derivatives with respect to  $X$  and  $Y$ , it is apparent that

$$\frac{\partial \Gamma_1}{\partial X} = \frac{\partial \Gamma_1}{\partial Y} = 0$$

Now the substitutions

$$z' = z + z_t \tag{4-26}$$

$$\theta = \zeta/z' = \zeta/(z+z_t) \tag{4-27}$$

$$\phi = \eta/z' = \eta/(z+z_t) \tag{4-28}$$

yield the following

$$\begin{aligned} \frac{\partial \Gamma_1}{\partial z'} - \frac{i}{2} \frac{k_d}{(k_s^2 - k_d^2/4)} \frac{1}{z'^2} \left[ \frac{\partial^2}{\partial \theta^2} + \frac{\partial^2}{\partial \phi^2} \right] \Gamma_1 \\ - \frac{1}{8} \left[ \frac{2k_p^4 A(z'(\theta+\phi))}{k_1 k_2} - \left( \frac{1}{k_2^2} + \frac{1}{k_1^2} \right) k_p^4 A(0) \right] \Gamma_1 = 0 \end{aligned} \quad (4-29)$$

The additional substitution  $\Gamma_1 = \Gamma_2 \Gamma_3$  where

$$\Gamma_3 = \exp \left\{ - \frac{1}{8} A(0) (z' - z_t) k_p^4 \left( \frac{1}{k_1} - \frac{1}{k_2} \right)^2 \right\} \quad (4-30)$$

yields the simplified equation for  $\Gamma_2$

$$\frac{\partial \Gamma_2}{\partial z'} - \frac{i}{2} \frac{k_d}{k_s^2} \frac{1}{z'^2} \left[ \frac{\partial^2}{\partial \theta^2} + \frac{\partial^2}{\partial \phi^2} \right] \Gamma_2 - \frac{1}{4} \frac{k_p^4}{k_s^2} [A(z'(\theta+\phi)) - A(0)] \Gamma_2 = 0 \quad (4-31)$$

where  $k_d$  has been neglected with respect to  $k_s$ . The effect of this assumption is to restrict the validity of the solution to a small range of wavelengths centered about  $k_s$ .

Again following Sreenivasiah (1976) and Yeh and Liu (1977), expand the function  $A(z'(\theta+\phi))$  in a Taylor series and neglect all but the first two terms so that

$$A(z'(\theta+\phi)) \approx A_0 + z'^2(\theta+\phi)^2 A_2 \quad (4-32)$$

Equation 4-32 is the analytic expression of the quadratic phase structure-function approximation.

### 4.1.3 $A_0$ and $A_2$ CALCULATION

#### 4.1.3.1 Isotropic Irregularities

The  $A_0$  and  $A_2$  coefficients may be calculated for isotropic irregularities by performing the angular integration in Equation 4-19 to obtain

$$A(\bar{\rho}_1 - \bar{\rho}_2) = 4\pi^2 \int_0^\infty J_0(K_\perp \rho) \phi_\xi(K_\perp, K_z=0) K_\perp dK_\perp \quad (4-33)$$

where

$$K_\perp^2 = K_x^2 + K_y^2$$

$$\rho = |\bar{\rho}_1 - \bar{\rho}_2|$$

The  $J_0$  Bessel function may be expanded in a power series and coefficients of equal powers of  $\rho$  equated to obtain

$$A_0 = 4\pi^2 \int_0^\infty \phi_\xi(K_\perp, K_z=0) K_\perp dK_\perp \quad (4-34)$$

$$A_2 = -\pi^2 \int_0^\infty \phi_\xi(K_\perp, K_z=0) K_\perp^3 dK_\perp \quad (4-35)$$

#### a) Gaussian PSD

For a Gaussian power spectrum of the form

$$\phi_\xi(\bar{K}) = \frac{\sigma_N^2}{\langle N_e \rangle^2} \frac{L_0^3}{8\pi^{3/2}} \exp\{-K^2 L_0^2/4\} \quad (4-36)$$

with corresponding autocorrelation function

$$B(r) = \frac{\sigma_{N_e}^2}{\langle N_e \rangle^2} \exp \{-r^2/L_0^2\} \quad (4-37)$$

it can be shown that

$$A_0 = L_0 \pi^{1/2} \frac{\sigma_{N_e}^2}{\langle N_e \rangle^2} \quad (4-38)$$

$$A_2 = - \frac{\pi^{1/2}}{L_0} \frac{\sigma_{N_e}^2}{\langle N_e \rangle^2} \quad (4-39)$$

b) Power law PSD

Consider a power law spectrum of the form

$$\Phi_{\xi}(K) = \frac{\sigma_{N_e}^2 (2\pi)^{-3/2} \ell_i (\ell_i/L_0)^{(p-1)/3} K_{p/2} \left( \ell_i \sqrt{K^2 + 1/L_0^2} \right)}{\langle N_e \rangle^{2K} (p-3)/2 (\ell_i/L_0) \left( \ell_i \sqrt{K^2 + 1/L_0^2} \right)^{p/2}} \quad (4-40)$$

which has a  $K^{-p}$  behavior for  $1/K$  ranging from  $L_0$ , the outer scale to  $\ell_i$ , the inner scale. The corresponding autocorrelation function is

$$B(r) = \frac{\sigma_{N_e}^2 \left( L_0^{-1} \sqrt{r^2 + \ell_i^2} \right)^{(p-3)/2} K_{(p-3)/2} \left( L_0^{-1} \sqrt{r^2 + \ell_i^2} \right)}{\langle N_e \rangle^2 (\ell_i/L_0)^{(p-3)/2} K_{(p-3)/2} (\ell_i/L_0)} \quad (4-41)$$

For the general  $K^{-p}$  power law spectrum it can be shown that

$$A_0 = \left( (2\pi \ell_i L_0)^{1/2} \frac{K_{p-2}}{2} (\ell_i/L_0) / \frac{K_{p-3}}{2} (\ell_i/L_0) \right) \frac{\sigma_{N_e}^2}{\langle N_e \rangle^2} \quad (4-42)$$

$$A_2 = - \left( (\pi/(2\ell_i L_0))^{1/2} \frac{K_{p-4}}{2} (\ell_i/L_0) / \frac{K_{p-3}}{2} (\ell_i/L_0) \right) \frac{\sigma_{N_e}^2}{\langle N_e \rangle^2} \quad (4-43)$$

For  $\ell_i \ll L_0$  and the commonly used  $K^{-4}$  spectrum

$$A_0 = 2L_0 \frac{\sigma_{N_e}^2}{\langle N_e \rangle^2} \quad (4-44)$$

$$A_2 = - \frac{\ln(L_0/\ell_i)}{L_0} \frac{\sigma_{N_e}^2}{\langle N_e \rangle^2} \quad (4-45)$$

#### 4.1.3.2 Elongated Irregularities

For the case of irregularities infinitely elongated in the y-direction, there is no y variation and the two-dimensional equivalent to Equation 4-19 is

$$A(x_1-x_2) = 2\pi \int_{-\infty}^{\infty} e^{iK_x(x_1-x_2)} \phi_{\xi}(K_x, K_z=0) dK_x \quad (4-46)$$

Here the exponential may be expanded as the Taylor cosine series since  $\phi$  is real. The results for the coefficients  $A_0$  and  $A_2$  are identical to Equations 4-42 and 4-43 with the exception that the three-dimensional PSD for electron density fluctuations is replaced by the two-dimensional PSD. The two-dimensional PSD is

$$S_{N_e}(K_x, K_z) = \frac{\sigma_N^2 (2\pi)^{-1} k_0^2 (l_i/L_0)^{(p-3)/2} K_{(p-1)/2} \left( l_i \sqrt{K_x^2 + K_z^2 + 1/L_0^2} \right)}{\langle N_e \rangle^2 K_{(p-3)/2} (l_i/L_0) \left( l_i \sqrt{K_x^2 + K_z^2 + 1/L_0^2} \right)^{(p-1)/2}} \quad (4-47)$$

The two-dimensional autocorrelation function corresponding to this two-dimensional PSD is given by Equation 4-41. It is now easy to show that the values of  $A_0$  and  $A_2$  for infinitely elongated irregularities are identical to the values for isotropic irregularities.

In the work that follows, the ratio of the constants  $A_0$  and  $A_2$  appears often. At this point it is noted that for a three-dimensional  $K^{-p}$  power law electron density spectrum

$$\frac{A_0}{A_2} = -L_0^2(2p-8) \quad , \quad p > 4 \quad (4-48)$$

Remember that the corresponding one-dimensional phase PSD which is often used in this report has a  $K^{-(p-1)}$  power law form.

#### 4.1.4 $\sigma_\phi^2$ CALCULATION

It is useful to establish the relationship between the coefficient  $A_0$  and the variance of phase fluctuations,  $\sigma_\phi^2$ . For a layer of ionization  $\Delta z$  thick the incremental phase-shift is given by

$$\Delta\phi(x, y) = \frac{k_0}{2} \int_{-\Delta z/2}^{\Delta z/2} \frac{\Delta N_e(x, y, z) dz}{n_c} \quad (4-49)$$

where we have assumed that the critical electron density,  $n_c$ , is much greater than the mean electron density and have expanded the formula for the index-of-refraction (neglecting collisions) in a power series and retained only the first two terms. Now from the correlation function of the phase fluctuations



$$\langle \Delta\phi(x_1, y_1) \Delta\phi(x_2, y_2) \rangle = \frac{k_0^2 \langle N_e \rangle^2}{4n_c^2} \int_{-\frac{\Delta z}{2}}^{\frac{\Delta z}{2}} \int_{-\frac{\Delta z}{2}}^{\frac{\Delta z}{2}} \frac{\langle \Delta N_e(x_1, y_1, z) \Delta N_e(x_2, y_2, z') \rangle}{\langle N_e \rangle^2} dz dz' \quad (4-50)$$

The double integration can be reduced to a single integration by a change of variables (Papoulis, 1965, p. 325), so that

$$\langle \Delta\phi(x_1, y_1) \Delta\phi(x_2, y_2) \rangle = \frac{\Delta z k_0^2 \langle N_e \rangle^2}{4n_c^2} \int_{-\Delta z}^{\Delta z} B_{\xi}(\bar{\rho}_1 - \bar{\rho}_2, \eta) (1 - |\eta|/\Delta z) d\eta \quad (4-51)$$

If  $\Delta z$  is greater than the correlation length of electron density fluctuations, then the contribution of the second term is negligible and the integration limits may be changed to plus and minus infinity. Evaluation of the resulting expression at  $\bar{\rho}_1 - \bar{\rho}_2 = 0$  yields

$$\sigma_{\phi}^2 = \frac{k_0^2 \langle N_e \rangle^2}{4n_c^2} LA_0 = \frac{1}{4} k_p^4 LA_0 / k_0^2 \quad (4-52)$$

where Equation 4-18 is used for  $A_0$  and  $L$  is the total thickness of the layer of ionization irregularities. For a  $K^{-4}$  three-dimensional ionization power spectrum,  $A_0$  is given by Equation 4-44 and

$$\sigma_{\phi}^2 = 2(\lambda r_e)^2 L L_0 \sigma_{N_e}^2 \quad (4-53)$$

where  $\sigma_{N_e}^2$  is the variance of the electron density fluctuations.

#### 4.1.5 THE SOLUTION

Now that general expressions have been derived for the coefficients  $A_0$  and  $A_2$ , the solution for the two-frequency mutual coherence function may be continued. Introduce the additional substitutions

$$a = \frac{1}{2} k_d / k_s^2 \quad (4-54)$$

$$b = \frac{1}{4} k_p^4 / k_s^2 \quad (4-55)$$

$$v = (abA_2)^{1/2} z' = a_1 z' \quad (4-56)$$

$$\mu = \left( \frac{1}{a^3 b A_2} \right)^{1/4} \theta = a_2 \theta \quad (4-57)$$

$$\epsilon = \left( \frac{1}{a^3 b A_2} \right)^{1/4} \phi = a_2 \phi \quad (4-58)$$

With these substitutions Equations 4-31 and 4-32 may be combined to yield

$$\frac{\partial \Gamma_2}{\partial v} - i \frac{1}{v^2} \left[ \frac{\partial^2}{\partial \mu^2} + \frac{\partial^2}{\partial \epsilon^2} \right] \Gamma_2 - (\mu^2 + \epsilon^2) v^2 \Gamma_2 = 0 \quad (4-59)$$

The boundary condition becomes

$$\Gamma_2(\mu, \epsilon, v = (abA_2)^{1/2} z_t, \omega_d) = 1$$

An analytic solution of the form

$$\Gamma_2 = f(v) \exp\{-g(v)(\mu^2 + \epsilon^2)\} \quad (4-60)$$

may be substituted into Equation 4-59 to obtain the following two equations, the first consisting of terms independent of  $(\mu^2 + \epsilon^2)$

$$\frac{\partial f}{\partial v} + \frac{i4fg}{v^2} = 0 \quad (4-61)$$

and the second consisting of terms with the factor  $(\mu^2 + \epsilon^2)$

$$\frac{\partial g}{\partial v} + \frac{i4g^2}{v^2} + v^2 = 0 \quad (4-62)$$

This pair of equations may be solved exactly with the result

$$f(v) = \frac{\alpha v}{\alpha v_t \cosh \alpha(v-v_t) + \sinh \alpha(v-v_t)} \quad (4-63)$$

$$g(v) = \frac{1}{4} i v \left[ 1 - \alpha v \left( \frac{\alpha v_t \sinh \alpha(v-v_t) + \cosh \alpha(v-v_t)}{\alpha v_t \cosh \alpha(v-v_t) + \sinh \alpha(v-v_t)} \right) \right] \quad (4-64)$$

where

$$\alpha = 2e^{i3\pi/4}$$

$$v_t = (abA_2)^{1/2} \quad z_t = a_1 z_t$$

Equations 4-30 and 4-60 may be multiplied to obtain the desired solution for  $r_1$  in the ionized layer where

$$0 \leq z \leq L$$

or

$$z_t \leq z' \leq L + z_t$$

In transcribing Equation 4-30,  $k_d$  has again been neglected with respect to  $k_s$  to obtain

$$r_1(\theta, \phi, z', \omega_d) = \exp [-A_0(z' - z_t) k_p^4 k_d^2 / 8 k_s^4] \\ \times f(a_1 z') \exp [-a_2^2 (\theta^2 + \phi^2) g(a_1 z')] \quad (4-65)$$

In accordance with the definitions given by Equations 4-33 and 4-34,  $A_0$  is used to replace  $A(0)$  in the expression for  $r_1$ .

To complete the solution it is necessary to solve for  $\Gamma_1$  in the region

$$L \leq z \leq z_r$$

or

$$L + z_t \leq z' \leq z_r + z_t$$

Equation 4-65 serves as the boundary condition at  $z' = L + z_t$ . Since the region  $z' \geq L + z_t$  corresponds to free-space with no ionization, Equation 4-29 is appropriate where the last term, which is dependent on the function  $A$ , may be neglected since  $A$  is zero in the absence of ionization irregularities. Also, in keeping with previous assumptions, the  $k_d^2$  term is ignored with respect to the  $k_s^2$  term in Equation 4-29.

The Fourier transform pair

$$\Gamma_1(\theta, \phi, z', \omega_d) = \int_{-\infty}^{\infty} \int_{-\infty}^{\infty} e^{i(K_\theta \theta + K_\phi \phi)} \hat{\Gamma}_1(K_\theta, K_\phi, z', \omega_d) dK_\theta dK_\phi \quad (4-66)$$

$$\hat{\Gamma}_1(K_\theta, K_\phi, z', \omega_d) = (1/2\pi)^2 \int_{-\infty}^{\infty} \int_{-\infty}^{\infty} e^{-i(K_\theta \theta + K_\phi \phi)} \Gamma_1(\theta, \phi, z', \omega_d) d\theta d\phi \quad (4-67)$$

may be substituted into the suitably modified Equation 4-29 to obtain the algebraic equation

$$\frac{\partial \hat{\Gamma}_1}{\partial z'} + \frac{i k_d}{2 k_s^2} \frac{1}{z'^2} (K_\theta^2 + K_\phi^2) \hat{\Gamma}_1 = 0 \quad (4-68)$$

Equation 4-68 may be solved and the boundary condition 4-65 applied at  $z' = L + z_t$  with the result

$$\begin{aligned} \hat{\Gamma}_1(K_\theta, K_\phi, z_t + z_r, \omega_d) &= \hat{\Gamma}_1(K_\theta, K_\phi, L + z_t, \omega_d) \\ &\times \exp [-i\gamma(K_\theta^2 + K_\phi^2)] \end{aligned} \quad (4-69)$$

where

$$\gamma = \frac{1}{2} \frac{k_d}{k_s^2} \frac{(z_r - L)}{(L + z_t)(z_t + z_r)} \quad (4-70)$$

The final result may then be obtained by taking the Fourier transform of Equation 4-65 to obtain  $\hat{r}_1(K_\theta, K_\phi, z' + z_t, \omega_d)$  and then taking the inverse Fourier transform of Equation 4-69. The appropriate Fourier transform pairs are given by Equations 4-66 and 4-67. The required integrals are easily found in Gradshteyn and Ryzhik (1965) and the result may be written as

$$\begin{aligned} r_I(z, n, z_r, \omega_d) &= r_I(z, n, z' = z_t + z_r, \omega_d) \\ &= \exp \left\{ -\sigma_\phi^2 \omega_d^2 / 2 \omega_0^2 \right\} f[a_1(L + z_t)] \\ &\times \exp \left\{ -\frac{(z^2 + n^2) a_2^2 g[a_1(L + z_t)] / (z_r + z_t)^2}{1 + i 4 \gamma a_2^2 g[a_1(L + z_t)]} \right\} \\ &\times \{1 + i 4 \gamma a_2^2 g[a_1(L + z_t)]\}^{-1} \end{aligned} \quad (4-71)$$

where the  $\theta$  and  $\phi$  coordinates have been transformed into the  $z$  and  $n$  coordinates according to the transformation of Equations 4-27 and 4-28. The subscript I on  $r$  has been introduced to denote that the solution is applicable to the case of isotropic ionization irregularities. The case of elongated irregularities follows. The first exponential term in Equation 4-71 comes from the first exponential term in Equation 4-65 where the relationship between  $\sigma_\phi^2$  and  $A_0$  given by Equation 4-52 has been utilized to simplify the resulting exponential.

#### 4.1.5.1 Elongated Irregularities

For transionospheric propagation the case of elongated irregularities may be more appropriate than that of isotropic ionization irregularities. To model elongated irregularities, assume that the striations are long tubes, infinite in the  $y$ -direction shown in Figure 3-1.

For this case the solution proceeds in the same manner as described for the case of isotropic irregularities.

The development differs since there is no  $y$  dependence in the case of elongated irregularities. Thus the factor of 4 in Equation 4-61 becomes a factor of 2 for elongated irregularities. The resulting solution for the function  $f$  is then the square root of the result obtained for the isotropic irregularity case. Equation 4-62 for  $g$  remains unchanged. In the succeeding development, the only difference occurs because one-dimensional Fourier transforms are involved rather than two-dimensional transforms as are used for the isotropic irregularity case. The final result for  $r_1$  for the case of elongated irregularities is

$$\begin{aligned} r_E(z, z_r, \omega_d) = & \exp \left\{ -\sigma_\phi^2 \omega_d^2 / 2 \omega_0^2 \right\} \{ f[a_1(L+z_t)] \}^{1/2} \\ & \times \exp \left\{ - \frac{z^2 a_2^2 g[a_1(L+z_t)] / (z_r+z_t)^2}{1 + i4\gamma a_2^2 g[a_1(L+z_t)]} \right\} \\ & \times \{ 1 + i4\gamma a_2^2 g[a_1(L+z_t)] \}^{-1/2} \end{aligned} \quad (4-72)$$

where  $f$  and  $g$  are defined by Equations 4-63 and 4-64. The subscript  $E$  on  $r$  refers to the elongated irregularities.

#### 4.1.5.2 Thin Phase-Screen Approximation

Further simplification is obtained if the thick scattering layer is replaced by an equivalent thin phase-screen with infinitesimal thickness and the same overall phase variance,  $\sigma_\phi^2$ . As will be seen the accuracy of the thin phase-screen approximation is a function of the propagation geometry, the wavelength and the electron density PSD.

The thin phase-screen approximation has been used by many authors and is treated in detail by Mercier (1962) and Salpeter (1967). Wernik, et al., (1973) and Bramley (1977) have examined the accuracy of the thin phase-screen approximation for the calculation of the

scintillation index. Rino (1980) and Rino et al. (1981) have utilized this approximation to obtain numerical propagation results and to successfully model observed data from the DNA Wideband satellite experiment.

Here the accuracy of the thin phase-screen approximation is examined in detail as it affects the calculation of the scintillation index and the mean time delay and time delay jitter. It will be seen that the maximum error in the use of the thin phase-screen approximation is small; therefore this useful approximation is invoked here to simplify the mathematics and to aid in understanding the results.

Now taking the limit as the layer thickness approaches zero and utilizing the substitutions,

$$\ell_0^2 = \frac{-A_0(z_t + z_r)^2}{A_2 z_t^2 \sigma_\phi^2} \quad (4-73)$$

$$\omega_{coh} = \frac{\pi \omega_0 \ell_0^2 z_t}{\lambda z_r (z_t + z_r)} = \frac{-\pi \omega_0 A_0 (z_t + z_r)}{\lambda A_2 z_t z_r \sigma_\phi^2} \quad (4-74)$$

simplified expressions are found for the two-position, two-frequency mutual coherence function in the thin phase-screen approximation

$$\begin{aligned} r_I(\zeta, \eta, z_r, \omega_d) = & \exp \{-\sigma_\phi^2 \omega_d^2 / 2 \omega_0^2\} \\ & \times \exp \left( \frac{-(\zeta^2 + \eta^2) / \ell_0^2}{1 + i \omega_d / \omega_{coh}} \right) (1 + i \omega_d / \omega_{coh})^{-1} \end{aligned} \quad (4-75)$$

$$r_E(\zeta, z_r, \omega_d) = \exp \{-\sigma_\phi^2 \omega_d^2 / 2 \omega_0^2\} \\ \times \exp \left( \frac{-\zeta^2 / \ell_0^2}{1 + i \omega_d / \omega_{coh}} \right) (1 + i \omega_d / \omega_{coh})^{-1/2} \quad (4-76)$$

Thus the thin phase-screen approximation allows the complicated expressions 4-71 and 4-72 to be written in terms of the simplified parameters  $\ell_0$  and  $\omega_{coh}$ . In the following it will be seen that  $\ell_0$ , the signal decorrelation distance, and  $\omega_{coh}$ , the coherence bandwidth, are two very important parameters which describe the characteristics of the signal fluctuations.

Figure 4-1 shows the thin phase-screen model of the general propagation geometry shown in Figure 3-1. The distance from the transmitter to the phase-screen is  $z_t$  and the additional distance to the receiver is  $z_r$ . The total free-space propagation distance is  $z_t + z_r$ . It is apparent from Equation 4-74 that the coherence bandwidth is a reciprocal quantity. That is, an interchange of transmitter and receiver does not affect its value. However the decorrelation distance  $\ell_0$  is not reciprocal.  $\ell_0$  is a measure of the average distance between fades at the receiver and depends on the path geometry.

A more useful measure is the signal decorrelation time,  $\tau_0$ , which is a measure of the inverse fading rate or inverse fading bandwidth.  $\tau_0$  is a time-domain measure of fading whereas  $\ell_0$  is a spatial measurement. The signal decorrelation time is given by the equation

$$\tau_0 = \frac{\ell_0}{V_{eff}} \quad (4-77)$$

where  $V_{eff}$  is the relative velocity of the line-of-sight at the receiver location. Although this velocity is a function of transmitter and receiver motion as well as irregularity motion, it is sufficient to consider the case where the transmitter and receiver are stationary and the phase-screen is in motion. Assume that the scattering layer consists of



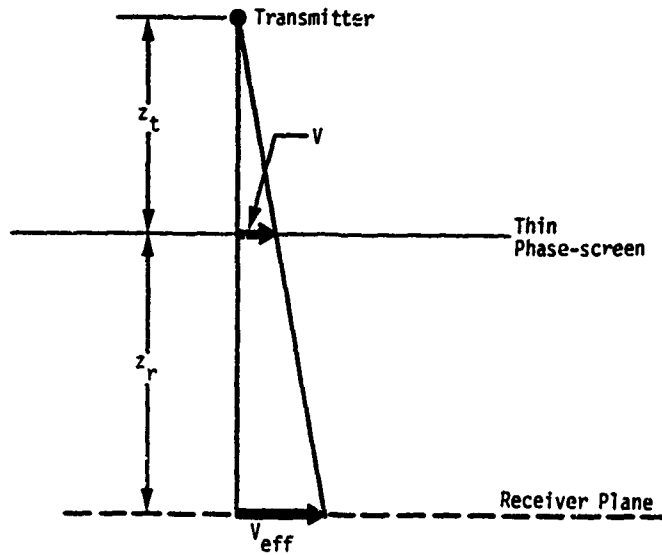


Figure 4-1. Thin phase-screen propagation geometry.

striations moving in unison at a velocity  $V$  perpendicular to the line-of-sight. Then the projection of these striations at the receiver location due to a signal originating at  $z_t$  has velocity

$$v_{eff} = \frac{V(z_r + z_t)}{z_t} \quad (4-78)$$

Combining Equations 4-73, 4-77 and 4-78, the received signal decorrelation time is obtained as

$$\tau_0^2 = \frac{-A_0}{A_2 V^2 \sigma_\phi^2} \quad (4-79)$$

It is apparent that  $\tau_0$  is only a function of the layer velocity and is reciprocal as it should be.

For the often used  $K^{-2}$  in situ power spectrum of one-dimensional electron density fluctuations,  $A_0/A_2$  may be obtained from Equations 4-44 and 4-45 and the signal decorrelation time is given by

$$\tau_0 = \frac{\sqrt{2} L_0}{\ln(L_0/\ell_1) \sigma_\phi V} \quad (4-80)$$

## 4.2 GENERALIZED POWER SPECTRUM

At this point it is convenient to introduce the generalized power spectrum which is defined as the Fourier transform of the two-frequency mutual coherence function. The generalized power spectrum serves two useful purposes. First, it is the basic function which is used in statistical signal generation as discussed in Section 3. Second, it acts as an intermediate function from which to easily determine the power impulse response function. This latter aspect is considered in detail in the following subsection.

For the cases of isotropic and elongated irregularities, the generalized power spectra are defined as

$$S_I(K_\zeta, K_\eta, z_r, \tau) = (2\pi)^{-3} \int_{-\infty}^{\infty} \int_{-\infty}^{\infty} \int_{-\infty}^{\infty} \Gamma_I(\zeta, \eta, z_r, \omega_d) \times \exp [-i(\zeta K_\zeta + \eta K_\eta) + i\omega_d \tau] d\zeta d\eta d\omega_d \quad (4-81)$$

$$S_E(K_\zeta, z_r, \tau) = (2\pi)^{-2} \int_{-\infty}^{\infty} \int_{-\infty}^{\infty} \Gamma_E(\zeta, z_r, \omega_d) \exp [-i\zeta K_\zeta + i\omega_d \tau] d\zeta d\omega_d \quad (4-82)$$

The inverse transforms are given by

$$\Gamma_I(\zeta, \eta, z_r, \omega_d) = \int_{-\infty}^{\infty} \int_{-\infty}^{\infty} \int_{-\infty}^{\infty} S_I(K_\zeta, K_\eta, z_r, \tau) \exp [+i(\zeta K_\zeta + \eta K_\eta) - i\omega_d \tau] dK_\zeta dK_\eta d\tau \quad (4-83)$$

$$\Gamma_E(\zeta, z_r, \omega_d) = \int_{-\infty}^{\infty} \int_{-\infty}^{\infty} S_E(K_\zeta, z_r, \tau) \exp [i\zeta K_\zeta - i\omega_d \tau] dK_\zeta d\tau \quad (4-84)$$

In the case of elongated irregularities, the one-dimensional generalized power spectrum is given by Equation 4-82. For the case of isotropic irregularities, the one-dimensional generalized power spectrum is given as the integral over the two-dimensional spectrum (Rufenach, 1975).

$$S_I(K_\zeta, z_r, \tau) = \int_{-\infty}^{\infty} S_I(K_\zeta, K_\eta, z_r, \tau) dK_\eta \quad (4-85)$$

Equation 4-81 is easily integrated with respect to  $K_\eta$  to obtain

$$S_I(K_\zeta, z_r, \tau) = (2\pi)^{-2} \int_{-\infty}^{\infty} \int_{-\infty}^{\infty} \Gamma_I(\zeta, \eta=0, z_r, \tau) \exp [-i\zeta K_\zeta + i\omega_d \tau] d\zeta d\omega_d \quad (4-86)$$

where  $\Gamma_I$  is evaluated at zero  $\eta$  because the integration yields a delta function. The inverse transform of Equation 4-86 is

$$\Gamma_I(\zeta, \eta=0, z_r, \tau) = \int_{-\infty}^{\infty} \int_{-\infty}^{\infty} S_I(K_\zeta, z_r, \tau) \exp [i\zeta K_\zeta - i\omega_d \tau] dK_\zeta d\tau \quad (4-87)$$

The integrals of Equations 4-81 and 4-82 can be computed by recognizing that the interior integrals in these two equations with respect to  $\zeta$  and  $\eta$  are related to quantities computed above. That is, from Equation 4-81

$$\begin{aligned} (2\pi)^{-2} \int_{-\infty}^{\infty} \int_{-\infty}^{\infty} \Gamma_I(\zeta, \eta, z_r, \omega_d) \exp [-i(\zeta K_\zeta + \eta K_\eta)] d\zeta d\eta \\ = \hat{\Gamma}_I(K_\zeta, K_\eta, z_r, \omega_d) \\ = (z_t + z_r)^2 \hat{\Gamma}_I(K_\theta, K_\phi, z = z_r, \omega_d) \end{aligned} \quad (4-88)$$

where  $\hat{r}_1$  is given by Equation 4-69. The  $(z_t+z_r)^2$  term results from the transformation

$$\theta = \zeta/(z_t+z_r) \quad (4-89)$$

$$\phi = \eta/(z_t+z_r) \quad (4-90)$$

relating angles and distance perpendicular to the direction of propagation.

In the case of infinitely elongated irregularities it can similarly be shown that the interior integral of Equation 4-82 may be written as

$$\begin{aligned} (1/2\pi) \int_{-\infty}^{\infty} \Gamma_E(\zeta, z_r, \omega_d) \exp[-i\zeta K_\zeta] d\zeta \\ = \hat{\Gamma}_E(K_\zeta, z_r, \omega_d) \\ = (z_t+z_r) \hat{r}_1(K_\theta, z=z_r, \omega_d) \end{aligned} \quad (4-91)$$

where  $\hat{r}_1$  in Equation 4-91 is the one-dimensional equivalent of the two-dimensional result given by Equation 4-69.

Equations 4-88 and 4-91 may be substituted into Equations 4-81 and 4-82 to obtain simplified expressions for the generalized power spectra

$$S_I(K_\zeta, K_\eta, z_r, \tau) = (1/2\pi) \int_{-\infty}^{\infty} \hat{r}_I(K_\zeta, K_\eta, z_r, \omega_d) \exp(i\omega_d \tau) d\omega_d \quad (4-92)$$

$$S_E(K_\zeta, z_r, \tau) = (1/2\pi) \int_{-\infty}^{\infty} \hat{r}_E(K_\zeta, z_r, \omega_d) \exp(i\omega_d \tau) d\omega_d \quad (4-93)$$

The Fourier transforms of Equations 4-92 and 4-93 cannot be performed analytically except for the case of a thin phase-screen. In this special case it is possible to show directly from Equation 4-69 and its equivalent for elongated irregularities that

$$\hat{r}_I(K_\zeta, K_\eta, z_r, \omega_d) = \frac{\ell_0^2}{4\pi} \exp\{-\sigma_\phi^2 \omega_d^2 / 2\omega_0^2\} \exp\left\{-\frac{1}{4} (K_\zeta^2 + K_\eta^2) \ell_0^2 (1 + i\omega_d/\omega_{coh})\right\}$$

(thin phase-screen) (4-94)

$$\hat{r}_E(K_\zeta, z_r, \omega_d) = \frac{\ell_0}{2\sqrt{\pi}} \exp\{-\sigma_\phi^2 \omega_d^2 / 2\omega_0^2\} \exp\left\{-\frac{1}{4} K_\zeta^2 \ell_0^2 (1 + i\omega_d/\omega_{coh})\right\}$$

(thin phase-screen) (4-95)

In the thin phase-screen approximation the preceding four equations can be combined to yield for the generalized power spectra

$$S_I(K_\zeta, K_\eta, z_r, \tau) = \frac{\omega_{coh} \ell_0^{2\alpha}}{2^{5/2} \pi^{3/2}} \exp\left\{-(K_\zeta^2 + K_\eta^2) \ell_0^2 / 4 - \frac{1}{2} \alpha^2 [\omega_{coh} \tau - (K_\zeta^2 + K_\eta^2) \ell_0^2 / 4]^2\right\}$$

(thin phase-screen) (4-96)

$$S_E(K_\zeta, z_r, \tau) = \frac{\omega_{coh} \ell_0^\alpha}{2^{3/2} \pi} \exp\left\{-K_\zeta^2 \ell_0^2 / 4 - \frac{1}{2} \alpha^2 [\omega_{coh} \tau - K_\zeta^2 \ell_0^2 / 4]^2\right\}$$

(thin phase-screen) (4-97)

where  $\ell_0$  and  $\omega_{coh}$  are given by Equations 4-73 and 4-74. The parameter  $\alpha$  is given by the equation

$$\alpha = \omega_0 / \sigma_\phi \omega_{coh} \quad (4-98)$$

and will be shown to be an important measure of the ratio of the propagation distance to the focal distance of the largest irregularities.

The one-dimensional generalized power spectrum for isotropic irregularities is given by Equation 4-85; for the thin phase-screen approximation of Equation 4-96 the integral is obtained from the tables as

$$S_I(K_\zeta, z_r, \tau) = \frac{\omega_{coh} \ell_0 \beta^{1/2}}{4\pi^{3/2}} \exp\{-K_\zeta^2 \ell_0^2/4 - \frac{1}{2} \alpha^2 [K_\zeta^2 \ell_0^2/4 - \omega_{coh} \tau]^2\} \\ \times \exp(\beta^2/4 \alpha^2) K_{1/4}(\beta^2/4 \alpha^2) \quad (4-99)$$

where

$$\beta = \alpha^2 [K_\zeta^2 \ell_0^2/4 - \omega_{coh} \tau] + 1 \quad (4-100)$$

Equations 4-97 and 4-99 are the one-dimensional forms of the generalized power spectra which are used in the statistical generation of realizations of the signal received after propagation through a strongly turbulent medium. Appendix A shows plots of these functions for a range of values of the parameter  $\alpha$ . It is important to note that the one-dimensional generalized power spectrum is required for the case of isotropic irregularities since statistical realizations of the received signal are desired that are a function of one spatial dimension only. Generation of these realizations is discussed in detail in Section 3 of this report.

### 4.3 POWER IMPULSE RESPONSE FUNCTION SOLUTION

In this subsection the impulse response function due to a transmitted power delta function is determined in the thin phase-screen approximation. Equation 4-13 gives the power impulse response function as

$$G(z_r, \tau) = (1/2\pi) \int_{-\infty}^{\infty} \Gamma(\Delta \bar{p}=0, z_r, \omega_d) e^{i\omega_d \tau} d\omega_d \quad (4-13)$$

Now it is easy to prove from Equation 4-86 that for zero  $\Delta \bar{p}$

$$G_I(z_r, \tau) = \int_{-\infty}^{\infty} S_I(K_\zeta, z_r, \tau) dK_\zeta \quad (4-101)$$

Equation 4-101 is true because the  $K_z$  integration on the right-hand side of Equation 4-86 yields the delta function  $2\pi\delta(z)$  which is then integrated with respect to  $z$  to yield the right hand side of Equation 4-13. An expression identical to Equation 4-101 is found for the case of elongated irregularities. Thus Equation 4-101 may be applied to the generalized power spectra given by Equations 4-97 and 4-99 to analytically determine the power impulse response functions:

$$G_I(z_r, \tau) = \frac{\omega_{coh}}{2} \exp \{-(\alpha\omega_{coh}\tau)^2/2\} \exp \{(1-\alpha^2\omega_{coh}\tau)^2/2\alpha^2\} \\ \times \phi_c \{(1-\alpha^2\omega_{coh}\tau)/\sqrt{2}\alpha\} \quad (4-102)$$

$$G_E(z_r, \tau) = \frac{\omega_{coh}}{2\pi} \exp \{-(\alpha\omega_{coh}\tau)^2/2\} (1-\alpha^2\omega_{coh}\tau)^{1/2} \\ \times \exp \{(1-\alpha^2\omega_{coh}\tau)^2/4\alpha^2\} K_{1/4} \{(1-\alpha^2\omega_{coh}\tau)^2/4\alpha^2\} \quad (4-103)$$

where  $\phi_c(x)$  is the complementary error function

$$\phi_c(x) = \frac{2}{\sqrt{\pi}} \int_x^\infty \exp(-y^2) dy$$

and  $K_{1/4}(x)$  is the modified Bessel function (Abramowitz and Stegun, 1965).

#### 4.3.1 Limiting Values

It is apparent that the power impulse response function  $G$  depends upon the parameter  $\alpha$  defined by Equation 4-98. Using Equation 4-74 for  $\omega_{coh}$  it can readily be shown that

$$\alpha = \frac{-A_2 \lambda z_t z_r}{\pi A_0 (z_t + z_r)} \quad (4-104)$$

Thus  $\alpha$  is a reciprocal quantity and does not depend on the relative placement of the transmitter and receiver.

For a Gaussian irregularity spectrum the values of  $A_0$  and  $A_2$  are obtained from Equations 4-38 and 4-39 and

$$\alpha = \frac{\lambda \sigma_{\phi} z_t z_r}{\pi L_0^2 (z_t + z_r)} \quad (\text{Gaussian PSD}) \quad (4-105)$$

For a  $K^{-4}$  in situ three-dimensional electron density spectrum or a  $K^{-3}$  one-dimensional phase PSD, Equations 4-44 and 4-45 give  $A_0$  and  $A_2$  with the result

$$\alpha = \frac{2n(L_0/\lambda) \lambda \sigma_{\phi} z_t z_r}{2\pi L_0^2 (z_t + z_r)} \quad (K^{-4} N_e \text{ PSD}) \quad (4-106)$$

It is apparent that  $\alpha$  is a measure of the severity of the scattering since it is directly proportional to the phase standard deviation. Recalling from Section 2.3 that the focal distance of a Gaussian lens is given as

$$F = \pi L_0^2 / \lambda \phi_0$$

where  $L_0$  is the scale size and  $\phi_0$  is the peak phase, it is seen that  $\alpha$  is proportional to  $Z/F$  where  $Z$  is the effective propagation distance. Here the peak phase for a single lens,  $\phi_0$ , and the phase standard deviation,  $\sigma_{\phi}$ , are taken as roughly equivalent. Thus large values of  $\alpha$  correspond to situations where  $Z \gg F$  and phase fluctuations have been fully converted to amplitude fluctuations through the process of diffraction. Small values of  $\alpha$  correspond to situations where phase fluctuations have not yet been converted to amplitude fluctuations, as would occur close to a random phase-screen. Thus the value of  $\alpha$  is a measure of the relative importance of scattering and dispersion with large values indicating strong scattering effects and small values indicating strong dispersive effects.



In order to calculate the power impulse response function in the large  $\alpha$  limit it is convenient to write Equation 4-101 as

$$G_I(z_r, \tau) = \int_{-\infty}^{\infty} \int_{-\infty}^{\infty} S_I(K_\zeta, K_\eta, z_r, \tau) dK_\zeta dK_\eta \quad (4-107)$$

where  $S_I$  is given in the thin phase-screen approximation by Equation 4-96. For large values of  $\alpha$  it can be shown (Stakgold, 1967, p.21)

$$\lim_{\alpha \rightarrow \infty} \frac{\alpha}{\sqrt{\pi}} \exp \{-\alpha^2 x^2\} = \delta(x)$$

Thus for large  $\alpha$  the generalized power spectrum of Equation 4-96 is given by

$$\begin{aligned} \lim_{\alpha \rightarrow \infty} S_I(K_\zeta, K_\eta, z_r, \tau) &= \frac{\omega_{coh} \ell_0^2}{2^{5/2} \pi} \exp \left\{ - (K_\zeta^2 + K_\eta^2) \ell_0^2 / 4 \right\} \\ &\times \delta \left\{ \frac{1}{\sqrt{2}} (\omega_{coh} \tau - (K_\zeta^2 + K_\eta^2) \ell_0^2 / 4) \right\} \end{aligned} \quad (4-108)$$

In this case the integration specified by Equation 4-107 can easily be performed with the result

$$\lim_{\alpha \rightarrow \infty} G_I(z_r, \tau) = \begin{cases} \omega_{coh} \exp(-\omega_{coh} \tau), & \tau > 0 \\ 0, & \tau < 0 \end{cases} \quad (4-109)$$

For the case of infinitely elongated irregularities it is recognized that the generalized power spectrum can be written as

$$\begin{aligned} \lim_{\alpha \rightarrow \infty} S_E(K_\zeta, z_r, \tau) &= \frac{\omega_{coh} \ell_0}{2^{3/2} \pi^{1/2}} \exp \left\{ - K_\zeta^2 \ell_0^2 / 4 \right\} \\ &\times \delta \left\{ \frac{1}{\sqrt{2}} (\omega_{coh} \tau - K_\zeta^2 \ell_0^2 / 4) \right\} \end{aligned} \quad (4-110)$$

With this simplification in mind the power impulse response function is easily found from Equation 4-101

$$\lim_{\alpha \rightarrow \infty} G_E(z_r, \tau) = \begin{cases} (\omega_{coh}/\pi\tau)^{1/2} \exp(-\omega_{coh}\tau) & , \quad \tau \geq 0 \\ 0 & , \quad \tau < 0 \end{cases} \quad (4-111)$$

Equations 4-109 and 4-111 give the power impulse response function for the case of large  $\alpha$  where scattering and diffraction effects dominate dispersive or phase effects.

In the limit of small  $\alpha$ , corresponding to the case that dispersion dominates over diffraction, the generalized power spectra of Equations 4-97 and 4-99 take on the identical form

$$\begin{aligned} \lim_{\alpha \rightarrow 0} S_I(K_\zeta, z_r, \tau) &= \lim_{\alpha \rightarrow 0} S_E(K_\zeta, z_r, \tau) \\ &= \frac{\alpha \omega_{coh} \ell_0}{2^{3/2} \pi} \exp \left\{ -K_\zeta^2 \ell_0^2 / 4 - \alpha^2 \omega_{coh}^2 \tau^2 / 2 \right\} \end{aligned} \quad (4-112)$$

Equation 4-112 follows directly from Equation 4-97 for  $S_E$ . For the case of isotropic irregularities, Equation 4-112 follows from Equation 4-99 where use is made of the fact that

$$\lim_{\alpha \rightarrow 0} \left\{ \exp(\beta^2/4\alpha^2) K_{1/4}(\beta^2/4\alpha^2) \right\} = \sqrt{2\pi} \frac{\alpha}{\beta}$$

Equations 4-101 and 4-112 may then be combined to obtain the power impulse response function in the limit that dispersion is dominant. That is,

$$\begin{aligned} \lim_{\alpha \rightarrow 0} G_I(z_r, \tau) &= \frac{\alpha \omega_{coh}}{\sqrt{2\pi}} \exp \left\{ -(\alpha \omega_{coh} \tau)^2 / 2 \right\} \\ &= \lim_{\alpha \rightarrow 0} G_E(z_r, \tau) \end{aligned} \quad (4-113)$$

It is noted that Equation 4-13 gives a Fourier transformation relationship between  $r$  and  $G$ . The inverse transform may be evaluated at zero  $\omega_d$  with the result

$$r(\Delta\bar{p}=0, z_r, \omega_d=0) = \int_{-\infty}^{\infty} G(z_r, \tau) d\tau \quad (4-114)$$

Since  $r(0, z_r, 0)$  is unity, the above equation provides a check on the derivation. It is easily shown that all the expressions for the impulse response given here obey the normalization condition of Equation 4-114.

Figures 4-2 and 4-3 show the power impulse response function for values of  $\alpha$  of 1, 3, 10, and 100 for the case of isotropic irregularities and for  $\alpha$  values of 1, 3, and 10 for the case of elongated irregularities. These curves are plotted directly from Equations 4-102 and 4-103; consequently the figures strictly apply to cases where the thin phase-screen approximation is valid. However, as will be seen in the following, this restriction is a minor one.

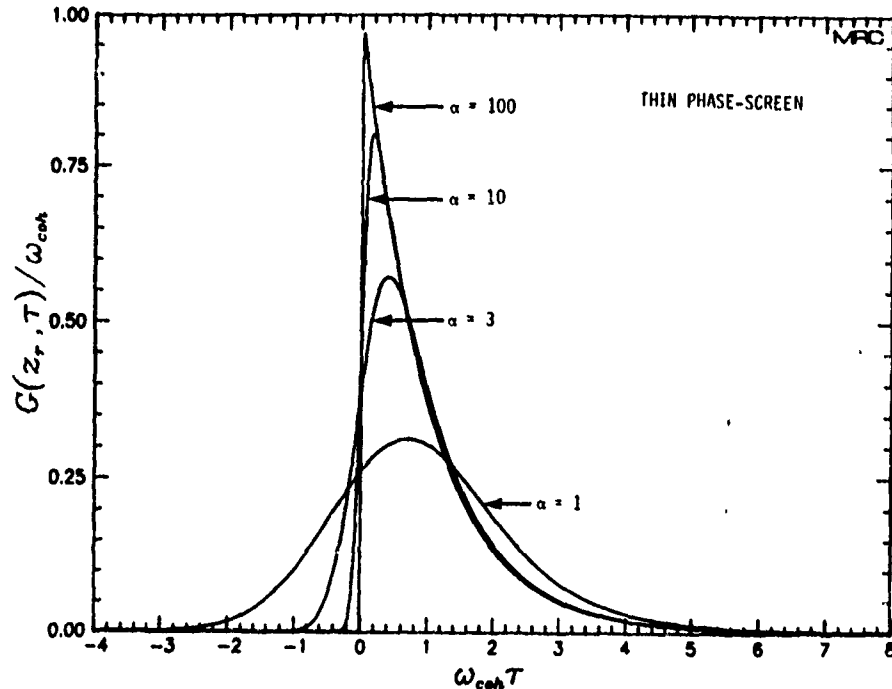


Figure 4-2. Power impulse response function for isotropic irregularities in the thin phase-screen approximation.

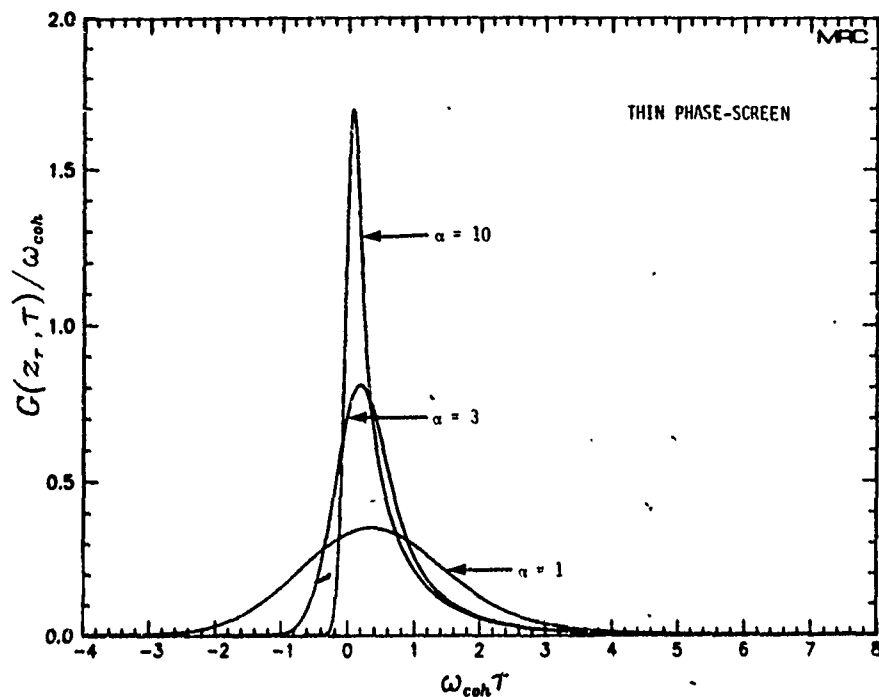


Figure 4-3. Power impulse response function for elongated irregularities in the thin phase-screen approximation.

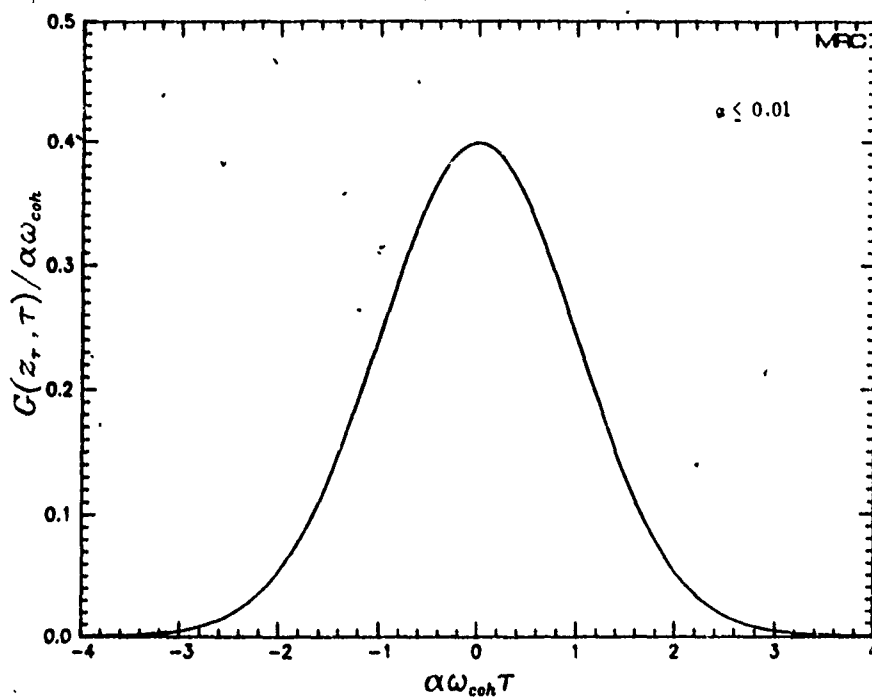


Figure 4-4. Power impulse response function for isotropic and elongated irregularities in the thin phase-screen approximation.

In order to simplify the presentation of these results, the power impulse response function is normalized by dividing by the coherence bandwidth and choosing  $\omega_{\text{coh}}\tau$  as the abscissa. In both figures it is apparent that the power impulse response function changes from a roughly Gaussian shape at unity  $\alpha$  to an exponential shape for larger  $\alpha$ . In the case of isotropic irregularities, the power impulse response function is very close to its asymptotic exponential form for a value of  $\alpha$  of 100.

Figure 4-4 shows the power impulse response function for the case of  $\alpha \leq 0.01$ . Note that a different convention is used for plotting purposes than is used in the previous two figures. For this range of  $\alpha$  dispersive effects are dominant and the isotropic and elongated irregularity cases are identical. For  $\alpha \leq 0.01$  it is evident that the small  $\alpha$ , asymptotic form of the power impulse response function, given by Equation 4-113, is reached for  $\alpha \approx 0.01$ . Equation 4-98, which defines  $\alpha$ , may be rewritten as

$$\alpha\omega_{\text{coh}} = \omega_0/\sigma_\phi$$

For most cases of interest involving lossless propagation through ionization, the carrier frequency is large with respect to the phase standard deviation and the right-hand side of the above expression is large. In that case the limit of small  $\alpha$  corresponds to the limit of large coherence bandwidth,  $\omega_{\text{coh}}$ . Thus

$$\lim_{\alpha \rightarrow 0} G_I(z_r, \tau) \approx \lim_{\omega_{\text{coh}} \rightarrow \infty} G_I(z_r, \tau) \quad (4-115)$$

The expression on the right-hand side of Equation 4-115 is recognized from Equation 4-113 as a Dirac delta function (Stakgold, 1967, p. 21), which may be written as

$$\lim_{\omega_{\text{coh}} \rightarrow \infty} G_I(z_r, \tau) = \delta(\tau) \quad (4-116)$$

Thus in the small  $\alpha$  limit, dispersion or phase effects dominate, and the power impulse response function is a delta function.

#### 4.4 MEAN TIME DELAY AND TIME DELAY JITTER

Two important measures of the effect of scintillation on wide bandwidth signals are the mean time delay and the time delay jitter. The mean time delay and time delay jitter of the received signal may be obtained (Yeh and Liu, 1977) or these measurements may be applied directly to the power impulse response function to obtain results which are indeed measurements of the propagation channel. With the latter approach in mind define

$$\langle \tau \rangle = \int_{-\infty}^{\infty} \tau G(z_r, \tau) d\tau \quad (4-117)$$

$$\sigma_{\tau}^2 = \int_{-\infty}^{\infty} \tau^2 G(z_r, \tau) d\tau - \langle \tau \rangle^2 \quad (4-118)$$

The mean time delay and the time delay jitter are functions of the receiver location but this functional dependence is omitted here for economy of notation. The mean time delay and the time delay jitter are simply related to the two-frequency mutual coherence function since from Equation 4-13

$$G(z_r, \tau) = \frac{1}{2\pi} \int_{-\infty}^{\infty} \Gamma(\xi=0, \eta=0, z_r, \omega_d) e^{i\omega_d \tau} d\omega_d \quad (4-13)$$

Both integrals 4-117 and 4-118 may be performed directly since the  $\tau$  integrations yield Dirac delta functions or a derivative of a Dirac delta function. The results are

$$\langle \tau \rangle = i \left. \frac{\partial \Gamma}{\partial \omega_d} \right|_{\omega_d=0} \quad (4-119)$$

$$\sigma_{\tau}^2 = - \left. \frac{\partial^2 \Gamma}{\partial \omega_d^2} \right|_{\omega_d=0} + \left. \frac{\partial \Gamma}{\partial \omega_d} \right|^2 \Big|_{\omega_d=0} \quad (4-120)$$

Equations 4-119 and 4-120 are general results and apply to both elongated and isotropic irregularities and are not limited to the case of a thin phase-screen.

#### 4.4.1 Mean Time Delay $\langle \tau \rangle$

Equation 4-119 may be easily applied to the two-frequency mutual coherence functions given by Equations 4-71 and 4-72 and results obtained that are valid for the thick layer geometry shown in Figure 3-1. After much algebra the results are found to be

$$\langle \tau_I \rangle = \frac{\sigma_\phi^2 |A_2|}{3k_0^2 c A_0} \left\{ \frac{6z_t^2 z_r + L(9z_t z_r - 3z_t^2) + L^2(3z_r - 5z_t) - 2L^3}{(z_t + z_r)(z_t + L)} \right\} \quad (4-121)$$

$$\langle \tau_E \rangle = \frac{1}{2} \langle \tau_I \rangle \quad (4-122)$$

An intuitive explanation for the factor of one-half in the relationship between the mean time delay for isotropic and elongated irregularities is that the elongated irregularities cause scattering in only one plane whereas isotropic irregularities cause scattering in both planes perpendicular to the propagation path.

It is noted that the expression given in Equation 4-121 is reciprocal. Interchange of transmitter and receiver is accomplished by the substitutions

$$z_r' = z_r - L \quad (4-123)$$

$$z_t' = z_t + L \quad (4-124)$$

where the prime quantities are the values after the interchange. These equations apply to the thick scattering layer geometry shown in Figure 3-1.

For a transmitted plane wave  $z_t$  increases to infinity and the mean time delay simplifies to

$$\lim_{z_t \rightarrow \infty} \langle \tau_I \rangle = \frac{\sigma_\phi^2 |A_2|}{k_0^2 c A_0} (2z_r - L) \quad (4-125)$$

This result can be shown to be identical to Equation 54 of Yeh and Liu, 1977 neglecting contributions from the transmitted signal in the referenced work. Now for a transmitted plane wave and the thin phase-screen approximation,  $L$  in Equation 4-125 is neglected and

$$\lim_{z_t \rightarrow \infty} \langle \tau_I \rangle = \frac{2\sigma_\phi^2 |A_2|}{k_0^2 c A_0} z_{\text{reff}} \quad (4-126)$$

where the receiver location in the thin phase-screen approximation is written as  $z_{\text{reff}}$  to indicate that the receiver location may depend on the thickness of the scattering layer to be represented by an equivalent thin screen. One logical location for a thin phase-screen chosen to represent a thick layer is the center of the original layer. In this case

$$z_{\text{reff}} = z_r - \frac{1}{2} L \quad (4-127)$$

For this choice, and the case of an incident plane wave, the phase-screen approximation, Equation 4-126, gives a result identical to the exact calculation, Equation 4-125.

In the more general spherical wave case the thin phase-screen limit is obtained by setting the layer thickness  $L$  equal to zero in Equation 4-121 and taking  $z_t$  and  $z_r$  as  $z_{\text{teff}}$  and  $z_{\text{reff}}$  to indicate that these values depend on the original layer thickness. The result may be written as

$$\langle \tau_I \rangle = \frac{2\sigma_\phi^2 |A_2|}{k_0^2 c A_0} \frac{z_{\text{teff}} z_{\text{reff}}}{(z_{\text{teff}} + z_{\text{reff}})} \quad (4-128)$$



which is reciprocal as it should be. Now to locate a thin phase-screen at the center of a layer of thickness  $L$  let

$$z_{\text{teff}} = z_t + L/2 \quad (4-129)$$

$$z_{\text{reff}} = z_r - L/2 \quad (4-130)$$

It is quickly shown that the resulting expression for the mean time delay

$$\langle \tau_I \rangle = \frac{\sigma_\phi^2 |A_2|^2}{2k_0^2 c A_0} \left( \frac{4z_r z_t + 2L(z_r - z_t) - L^2}{z_r + z_t} \right) \quad (4-131)$$

is not identical to the original thick layer result, Equation 4-121, in the general spherical wave case.

In summary, the thin phase-screen result for the mean time-delay is exact for plane wave propagation, but not for the more general case of spherical wave propagation. The full expression given by Equation 4-121 is valid for a thick layer and spherical wave propagation.

Another choice of a thin phase-screen location is discussed by Fante (1981) where it is shown that the location may be chosen as a function of the PSD to give the exact result for  $\sigma_\tau$ . However this choice of location does not give the correct result for the two-position mutual coherence function.

#### 4.4.2 $\langle \tau \rangle$ and $\sigma_\tau$ - Thin Phase-Screen Approximation

In the thin phase-screen approximation the simplified expressions for  $r_I$  and  $r_E$  given by Equations 4-75 and 4-76 may be used in Equations 4-119 and 4-120 to compute the mean time delay and time delay jitter. The results are the following expressions

$$\langle \tau_I \rangle = 1/\omega_{\text{coh}} \quad (4-132)$$

$$\langle \tau_E \rangle = 1/2\omega_{\text{coh}} \quad (4-133)$$

$$\sigma_{\tau I}^2 = \left(1 + \frac{1}{\alpha^2}\right) \frac{1}{\omega_{coh}^2} \quad (4-134)$$

$$\sigma_{\tau E}^2 = \left(\frac{1}{2} + \frac{1}{\alpha^2}\right) \frac{1}{\omega_{coh}^2} \quad (4-135)$$

where the parameters  $\omega_{coh}$  and  $\alpha$  are defined in Equations 4-74 and 4-98 respectively. In the following these simple expressions for the thin phase-screen approximation are compared to exact results for a thick scattering layer. It will be shown that the thin phase-screen calculations of the mean time delay and the time delay jitter are valid under a wide range of conditions and are therefore very useful.

#### 4.5 VALIDITY OF THE THIN PHASE-SCREEN APPROXIMATION .

In the following sections of this report the validity of the thin phase-screen approximation is investigated for calculations of the scintillation index in the weak-scatter approximation (Salpeter, 1967) and for the mean time delay and time delay jitter in the strong scatter limit. The scintillation index calculation is included here because this result is important for the statistical signal generation technique described in Section 3 of this report. The results included here are somewhat similar to those developed by Wernick, et al. (1973) with the difference that the results shown here model a thick layer with a centrally located phase-screen as opposed to a phase-screen located at the layer bottom. It can easily be demonstrated that the centrally located phase-screen gives better agreement with exact weak-scattering calculations.

The geometry under consideration is shown in Figure 3-1 with the single exception that the transmitted wave is assumed plane so that the transmitter is located at infinity. This transmitter placement is solely for analytical convenience in this subsection.

#### 4.5.1 $S^2$ -Rytov Approximation

From Tatarskii (1967, Equation 7.21) the perturbation of the logarithm of the electric field in the Rytov approximation is given as

$$\psi(\vec{r}) = \frac{k^2}{2\pi} \int \frac{u_0(\vec{r}')}{u_0(\vec{r})} \Delta n(\vec{r}') \frac{e^{-ik|\vec{r}-\vec{r}'|}}{|\vec{r}-\vec{r}'|} dV' \quad (4-136)$$

The unperturbed incident field  $u_0(\vec{r})$  is here taken as a plane wave traveling in the positive  $z$  direction

$$u_0(\vec{r}) = \exp\{-ikz\} \quad (4-137)$$

$\Delta n(\vec{r})$  is the variation in the index-of-refraction and the integration is over the entire extent of the fluctuations.

As usual the factor  $|\vec{r}-\vec{r}'|$  in the exponential is expanded in the Fresnel approximation as

$$|\vec{r}-\vec{r}'| \approx (z-z') + \frac{(x-x')^2 + (y-z')^2}{2(z-z')} \quad (4-138)$$

and as  $z-z'$  in the denominator. Expression 4-138 is valid as long as the wavelength,  $\lambda$ , is less than the inner scale size,  $\ell$ , so that the scattering of even the smallest eddies is in the forward direction (Fante, 1975).

Substituting the incident field into the integral expression given by Equation 4-136, one obtains

$$\psi(0,0,z) = \frac{k^2}{2\pi} \int \Delta n(\vec{r}') \frac{\exp\{-ik(x'^2+y'^2)/2(z-z')\}}{(z-z')} dV' \quad (4-139)$$

The mean-square log-amplitude fluctuation is given as

$$\sigma_X^2 = \langle (\text{Re } \psi)^2 \rangle \quad (4-140)$$

and depends upon the correlation function of the index-of-refraction fluctuations which can be written as

$$\langle \Delta n(\vec{r}') \Delta n(\vec{r}'') \rangle = \int_{-\infty}^{\infty} S_n(\vec{K}) e^{i\vec{K} \cdot (\vec{r}' - \vec{r}'')} d\vec{K} \quad (4-141)$$

Now assume that the irregularities are uncorrelated in the direction of propagation (this simplifying assumption is equivalent to the Markov approximation; Fante, 1975) so that

$$\begin{aligned} \langle \Delta n(\vec{r}') \Delta n(\vec{r}'') \rangle &= \delta(z' - z'') A(\vec{\rho}' - \vec{\rho}'', z') \\ &= 2\pi \delta(z' - z'') \int_{-\infty}^{\infty} S_n(\vec{K}_{\perp}, K_z=0; z') e^{i\vec{K}_{\perp} \cdot (\vec{\rho}' - \vec{\rho}'')} d\vec{K}_{\perp} \quad (4-142) \end{aligned}$$

Here  $\vec{\rho}$  and  $\vec{K}_{\perp}$  are the vector and associated wavenumber in the plane normal to the direction of propagation. It is evident that the spectra  $S_n(\vec{K})$  and  $S_n(\vec{K}_{\perp}, K_z=0; z')$  must be both real and even for Equations 4-141 and 4-142 to be valid.

Thus from Equation 4-139, the log-amplitude fluctuation  $\chi$  or the real part of  $\psi$  may be written as

$$\chi(0,0,z_r) = \frac{k^2}{2\pi} \int_{-\infty}^{\infty} \frac{\Delta n(\vec{r}') \cos[k(x'^2 + y'^2)/2(z_r - z')]}{(z_r - z')} dV' \quad (4-143)$$

Utilizing Equation 4-142 for the correlation function of the index-of-refraction fluctuations, one obtains the mean-square log-amplitude fluctuation

$$\begin{aligned} \sigma_{\chi}^2 &= \frac{k^4}{2\pi} \int_{-\infty}^{\infty} dV' \int_{-\infty}^{\infty} dV'' \frac{\delta(z' - z'')}{(z_r - z')(z_r - z'')} \int_{-\infty}^{\infty} d\vec{K}_{\perp} S_n(\vec{K}_{\perp}, K_z=0; z') e^{i\vec{K}_{\perp} \cdot (\vec{\rho}' - \vec{\rho}'')} \\ &\quad \times \cos[k(x'^2 - y'^2)/2(z_r - z')] \cos[k(x''^2 + y''^2)/2(z_r - z'')] \quad (4-144) \end{aligned}$$

The exponential factor may be expanded as  $\cos[K_x(x'-x'')+K_y(y'-y'')]$  and all integrations may be easily done with the aid of a table of integrals to obtain

$$\sigma_x^2 = 2\pi k^2 \int_0^L dz' \int_{-\infty}^{\infty} d\bar{K}_{\perp} S_n(\bar{K}_{\perp}, 0; z') \sin^2[(z_r - z')(K_x^2 + K_y^2)/2k] \quad (4-145)$$

Now a general mathematical description for three-dimensional index-of-refraction fluctuations subject to a Gaussian power spectrum is given by

$$S_n(\bar{K}; z') = \epsilon \frac{L_0^3 \sigma_n^2}{8\pi^{3/2}} \exp\{-K_x^2 + \epsilon^2 K_y^2 + K_z^2\} L_0^2/4\} \quad (4-146)$$

where  $\epsilon$  represents an elongation factor. The limit as  $\epsilon$  approaches infinity corresponds to the case of elongated irregularities. A value of unity for  $\epsilon$  corresponds to isotropic fluctuations perpendicular to the direction of propagation. Note that the normalization here is such that

$$\int_{-\infty}^{\infty} S_n(\bar{K}; z') d\bar{K} = \sigma_n^2 \quad (4-147)$$

For the case of isotropic irregularities the integral can be performed by transforming to polar coordinates. For elongated irregularities the integration is more complex and the limit as  $\epsilon$  tends to infinity must be taken after performing the  $K_y$  integration. Then perform the  $z'$  integration and finally the  $K_x$  integration to obtain

$$S_{4I}^2 = 2\sigma_{\phi}^2 \left\{ 1 + \frac{1}{4\xi_L} [\tan^{-1} 4(\xi_z - \xi_L) - \tan^{-1}(4\xi_z)] \right\} \quad (4-148)$$

$$S_{4E}^2 = 2\sigma_{\phi}^2 \left\{ 1 + \frac{1}{2\xi_L} (1+16(\xi_z - \xi_L)^2)^{1/4} \sin\left(\frac{1}{2} \tan^{-1} 4(\xi_z - \xi_L)\right) - (1+16\xi_z^2)^{1/4} \sin\left(\frac{1}{2} \tan^{-1} 4\xi_z\right) \right\} \quad (4-149)$$

where the weak scattering approximation

$$S_4^2 = 4\sigma_x^2 \quad (4-150)$$

has been utilized to obtain the scintillation index and the substitution

$$\sigma_\phi^2 = \sqrt{\pi} k^2 L L_0 \sigma_n^2 \quad (4-151)$$

which is valid for a Gaussian PSD has been utilized. The subscripts I and E refer to the case of isotropic and elongated irregularities, respectively. For ease of notation the additional substitutions

$$\xi_z = \lambda z_r / 2\pi L_0^2 \quad (4-152)$$

$$\xi_L = \lambda L / 2\pi L_0^2 \quad (4-153)$$

have been incorporated into Equations 4-148 and 4-149. Equations 4-148 and 4-149 are the expressions for the scintillation index for a thick layer in the Rytov approximation.

#### 4.5.2 $S_4^2$ -Thin Phase-Screen Approximation

The thin phase-screen results for the scintillation index may be obtained directly from Salpeter (1967) as

$$S_{4I}^2 = 4 \int_{-\infty}^{\infty} S_\phi(K_x, K_y) \sin^2 [(K_x^2 + K_y^2) z_e / 2k] dK_x dK_y \quad (4-154)$$

$$S_{4E}^2 = 4 \int_{-\infty}^{\infty} S_\phi(K_x) \sin^2 [K_x^2 z_e / 2k] dK_x \quad (4-155)$$

where  $z_e$  is the distance from the phase-screen to the observer and the phase power spectral density is given by

$$S_\phi(K_x, K_y) = \frac{L_0^2 \sigma_\phi^2}{4\pi} \exp\{- (K_x^2 + K_y^2) L_0^2 / 4\} \quad (4-156)$$

$$S_{\phi}(K_x) = \frac{L_0 \sigma_{\phi}^2}{2\sqrt{\pi}} \exp\{-K_x^2 L_0^2/4\} \quad (4-157)$$

Equation 4-157 is the one-dimensional equivalent to the power spectral density given by Equation 4-156. The final results for the scintillation index in the weak-scatter, thin phase-screen approximation are then

$$S_{4I}^2 = 2\sigma_{\phi}^2 [1 - (1+16\xi_e^2)^{-1}] \quad (4-158)$$

$$S_{4E}^2 = 2\sigma_{\phi}^2 [1 - (1+16\xi_e^2)^{-1/4} \cos(\frac{1}{2} \tan^{-1} 4\xi_e)] \quad (4-159)$$

where

$$\xi_e = \lambda z_e / 2\pi L_0^2 \quad (4-160)$$

In the following subsection, the results for the scintillation index in the thick layer Rytov approximation are compared to the above results in the thin phase-screen approximation. For the purposes of the comparison it is assumed that the phase-screen is located at the center of the thick layer, that is

$$z_e = z_r - \frac{1}{2} L \quad (4-161)$$

#### 4.5.3 Comparison of Results

Figures 4-5 and 4-6 show the thick layer results for the normalized scintillation index  $S_4/\sqrt{2}\sigma_{\phi}$  as a function of the normalized free-space propagation distance  $\lambda(z_r-L)/2\pi L_0^2$  for values of the normalized layer thickness  $\xi_L$  ranging from 0.0001 to 10. Figure 4-5 is a direct plot of the results of Equation 4-148 and is valid for isotropic irregularities. Figure 4-6 is a plot of the results of Equation 4-149 and is valid for infinitely elongated irregularities.

As shown in these two figures the value of  $S_4/\sqrt{2}\sigma_{\phi}$  peaks at unity for  $\lambda(z_r-L)/2\pi L_0^2$  large. For values of normalized layer thickness,  $\xi_L$ , smaller than the normalized free-space propagation distance  $\xi_L - \xi_L$  by a

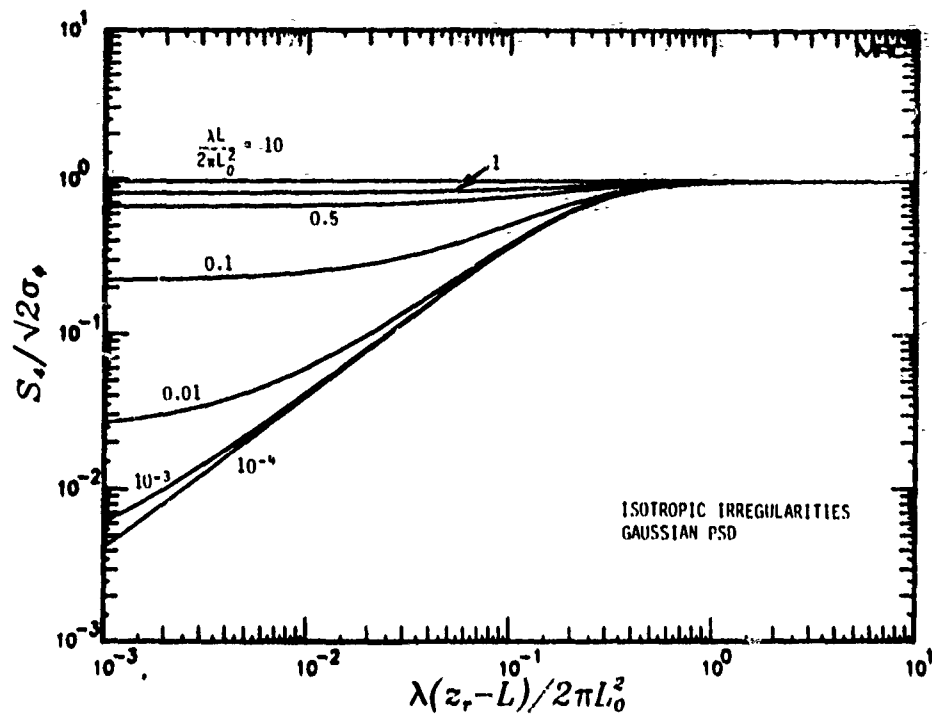


Figure 4-5. Rytov approximation to scintillation index for isotropic irregularities with a Gaussian PSD.

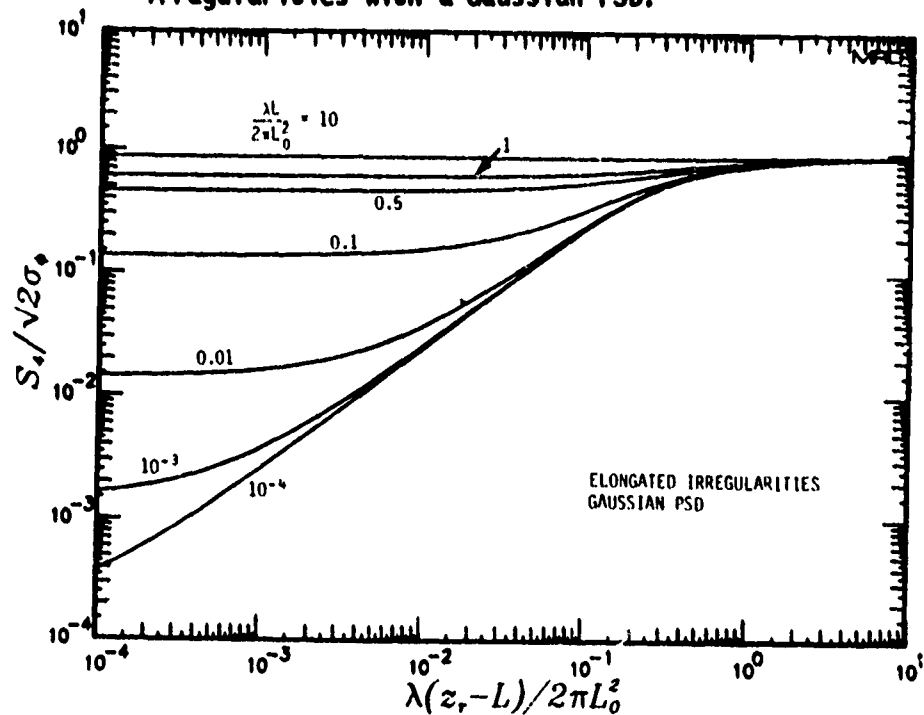


Figure 4-6. Rytov approximation to scintillation index for elongated irregularities with a Gaussian PSD.



factor of ten or more, the actual layer thickness is unimportant and the result is independent of layer thickness for very small layer thickness. One must be careful not to use the results shown in these two figures as evidence that the thin phase-screen approximation is useful only for situations where the normalized free-space propagation distance is ten or more times the normalized layer thickness.

Figures 4-7 and 4-8 show the differences between the scintillation index calculation in the Rytov approximation and in the thin phase-screen approximation where the phase-screen is located at the center of the original thick layer. The abscissa is the normalized free-space propagation distance,  $\xi_z - \xi_L$ , and the ordinate is the error quantity

$$\left| \frac{S_4^2(\text{Rytov}) - S_4^2(\text{phase-screen})}{S_4^2(\text{Rytov})} \right|^{1/2}$$

plotted in percent. Values of the normalized layer thickness,  $\xi_L$ , shown here range from 0.0001 to 10. In all cases the error is small even when the normalized free-space propagation distance and the normalized layer thickness are identical. For a fixed normalized layer thickness the difference between the two approximations increases with decreasing normalized free-space propagation distance until a fixed maximum difference is reached. This fixed maximum difference corresponds to the thick layer geometry where the receiver is located at the edge of the original thick layer, that is at  $z_r = L$ . Note that the value of the maximum difference depends on the normalized thickness as is shown further in the next two figures.

Figures 4-9 and 4-10 show the values of the percent difference between the Rytov thick layer calculation of  $S_4$  and the thin phase-screen calculation of  $S_4$  for a thick layer geometry in which the receiver is located at the edge of the scattering layer, that is  $\xi_z = \xi_L$  in Equations 4-148 and 4-149. In the thin phase-screen approximation the phase-screen is located at the center of the layer so that  $\xi_e = \xi_L/2$  in Equations 4-158 and 4-159. In both the case of isotropic irregularities (Figure 4-9), and the case of infinitely elongated irregularities (Figure 4-10), the maximum difference is fifty

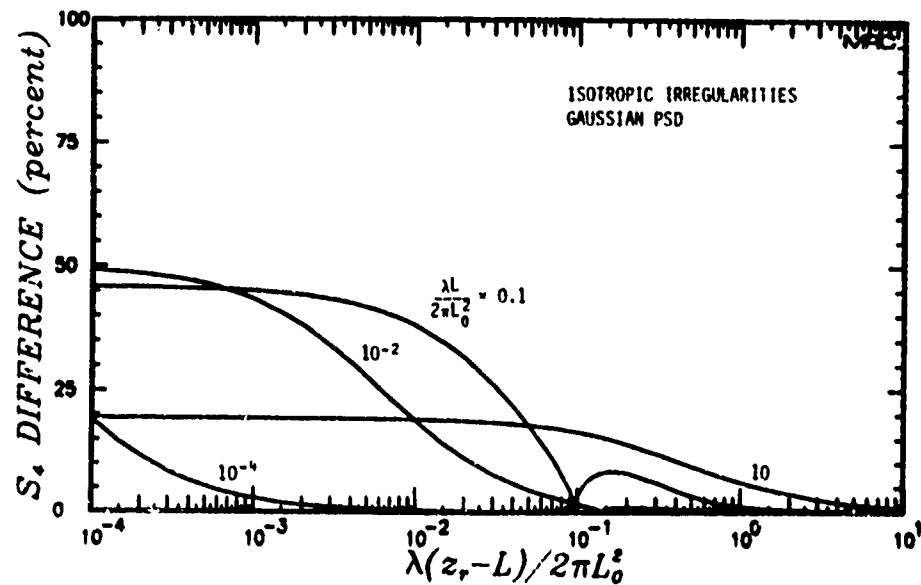


Figure 4-7. Percent difference in  $S_4$  between the Rytov and the thin phase-screen approximation, isotropic irregularities.

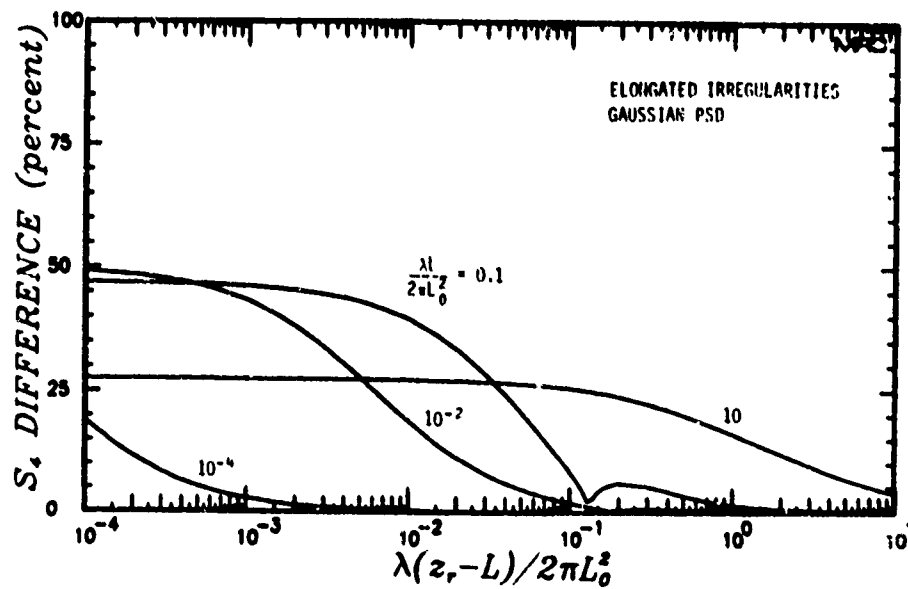


Figure 4-8. Percent difference in  $S_4$  between the Rytov and the thin phase-screen approximation, elongated irregularities.

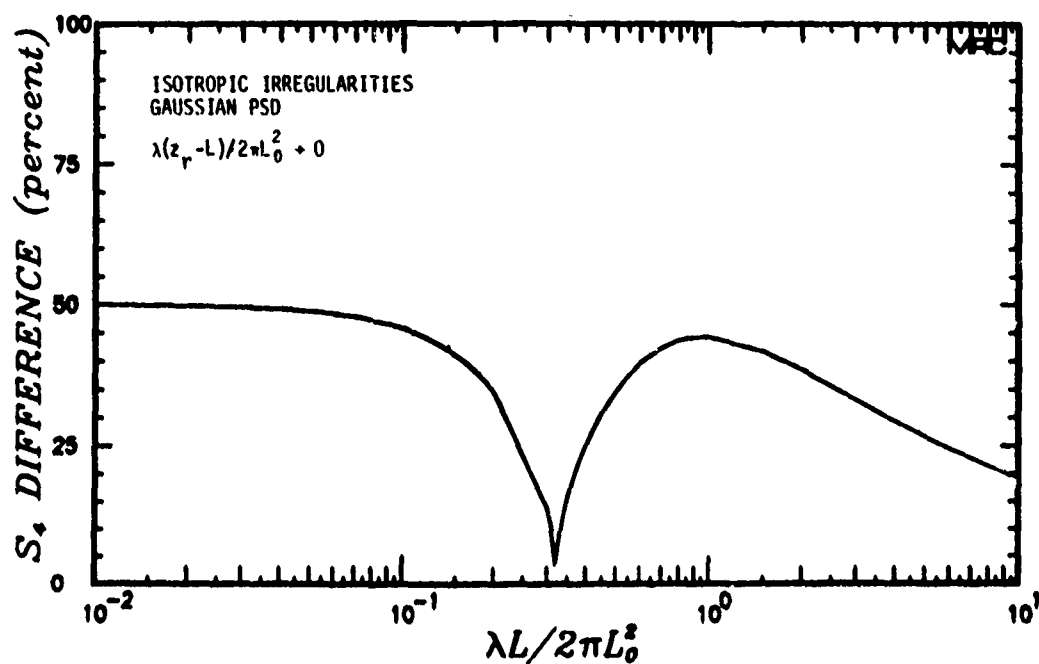


Figure 4-9. Maximum percent difference in  $S_4$  for isotropic irregularities.

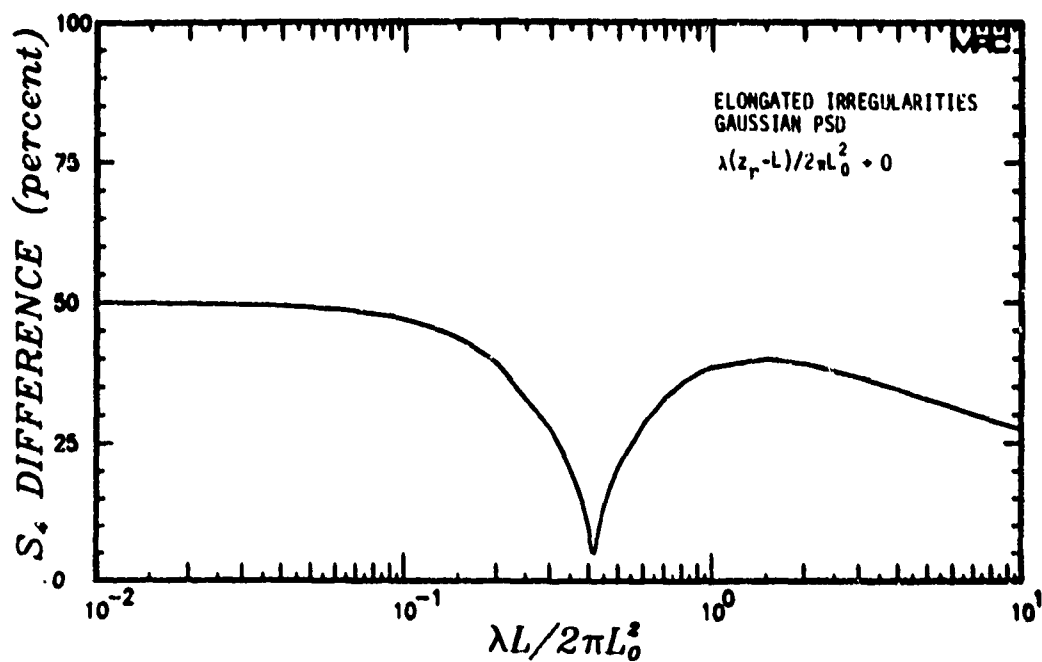


Figure 4-10. Maximum percent difference in  $S_4$  for elongated irregularities.

percent. This difference reflects the worst case accuracy of the thin phase-screen approximation in the weak scattering regime. Note that the difference has a minimum in both figures corresponding to points where the thin phase-screen approximation gives a result identical to the Rytov approximation.

In Section 3 of this report the thin phase-screen approximation is used to determine the onset of severe scintillation defined as the point at which the scintillation index has a value of 0.5. For this purpose, a maximum difference of fifty percent, when compared to the more complicated Rytov approximation, is considered acceptable.

These brief results illustrate the following points regarding the use of the thin phase-screen approximation for weak scattering. First, the accuracy of the thin phase-screen approximation for a thick layer is dependent on the relative lengths of the free-space propagation path and of the propagation path through the turbulent ionized layer. Second, for a free-space propagation distance ten or more times larger than the layer thickness, the thin phase-screen approximation is an accurate model of a thick layer with five percent or less error for  $S_4$ . Third, for equal propagation distances in free-space and through the thick layer, the error in the thin phase-screen approximation is small. Fourth, for a thin phase-screen centrally located to replace a thick layer, the accuracy of the thin phase-screen approximation is a function of the normalized layer thickness  $\xi_L$ . The maximum error in  $S_4$  is fifty percent.

Therefore the thin phase-screen approximation is a useful, accurate tool to use to determine the onset of severe Rayleigh scintillation for the purposes of statistical signal generation.

#### 4.5.4 $\langle \tau \rangle$ and $\sigma_\tau$ - Thick Layer Versus Thin Screen

In this section the simplified results for  $\langle \tau \rangle$ , the mean time delay, and  $\sigma_\tau$ , the time delay jitter, both in the thin phase-screen approximation, are compared to exact results in the strong scatter approximation obtained from Equations 4-117 and 4-118 by integrating the exact power impulse response function. For the exact calculation the power impulse response function is obtained by numerically taking the

Fourier transform of the two-frequency mutual coherence function as specified by Equation 4-13. The required two-frequency mutual coherence function is evaluated numerically in the general case of a thick scattering layer from Equations 4-71 and 4-72 for isotropic and elongated irregularities, respectively. Then  $\langle \tau \rangle$  and  $\sigma_\tau$  are obtained by numerically integrating according to Equations 4-117 and 4-118.

In all cases in this subsection the geometry under consideration is shown in Figure 3-1. For convenience the transmitter distance  $z_t$  is taken as infinity so that the incident wave is plane. The layer thickness is  $L$  and the free-space propagation distance outside the layer is  $z_r - L$ . A  $K^{-4}$  three-dimensional irregularity spectrum is used with a ratio of outer scale to inner scale of 100.

In the thin phase-screen approximation the important parameters  $\sigma_\phi$ ,  $\omega_{\text{coh}}$  and  $\alpha$  have simple expressions for the geometry of interest,

$$\sigma_\phi^2 = 2(\lambda r_e)^2 L L_0 \sigma_{N_e}^2 \quad (4-53)$$

$$\omega_{\text{coh}} = \frac{2\pi\omega_0 L_0^2}{\ln(L_0/\ell_i) \lambda z_r \sigma_\phi^2} \quad (4-162)$$

$$\alpha = \frac{\ln(L_0/\ell_i) \lambda z_r \sigma_\phi}{2\pi L_0^2} \quad (4-163)$$

Equations 4-162 and 4-163 are obtained directly from Equations 4-74 and 4-106. For steeper spectra the constants in these expressions take on different values but the basic algebraic dependence on the important quantities  $\lambda z_r/L_0^2$  and  $\sigma_\phi$  remains unchanged. The expression for  $\omega_{\text{coh}}$  may be substituted into Equations 4-132 and 4-134 to obtain for the thin phase-screen case and isotropic irregularities

$$\frac{\langle \tau_I \rangle \omega_0}{\sigma_\phi^2} = \frac{\ln(L_0/\xi_i) \lambda z_{\text{reff}}}{2\pi L_0^2} \quad (4-164)$$

$$\frac{\sigma_{\tau_I} \omega_0}{\sigma_\phi^2} \left(1 + \frac{1}{\alpha^2}\right)^{-1/2} = \frac{\ln(L_0/\xi_i) \lambda z_{\text{reff}}}{2\pi L_0^2} \quad (4-165)$$

For elongated irregularities, Equations 4-133, 4-134, and 4-162 yield

$$\frac{\langle \tau_E \rangle \omega_0}{\sigma_\phi^2} = \frac{1}{2} \frac{\ln(L_0/\xi_i) \lambda z_{\text{reff}}}{2\pi L_0^2} \quad (4-166)$$

$$\frac{\sigma_{\tau_E} \omega_0}{\sigma_\phi^2} \left(\frac{1}{2} + \frac{1}{\alpha^2}\right)^{-1/2} = \frac{\ln(L_0/\xi_i) \lambda z_{\text{reff}}}{2\pi L_0^2} \quad (4-167)$$

To model a layer of thickness  $L$  with transmitter at infinity and receiver located a distance  $z_r$  from the entrance to the layer, a thin phase-screen located at the layer center has

$$z_{\text{reff}} = z_r - L/2 \quad (4-168)$$

in Equations 4-164 to 4-167.

Therefore, based on the thin phase-screen results of Equations 4-164 to 4-167, it is convenient to plot the expressions on the left-hand side of the four equations.

Figure 4-11 shows the normalized mean time delay for isotropic irregularities

$$\langle \tau_I \rangle \omega_0 / \sigma_\phi^2$$

as a function of the normalized free-space propagation distance  $\xi_z - \xi_L$  for values of the normalized layer thickness  $\xi_L$  ranging from  $10^{-6}$  to 10. As defined previously

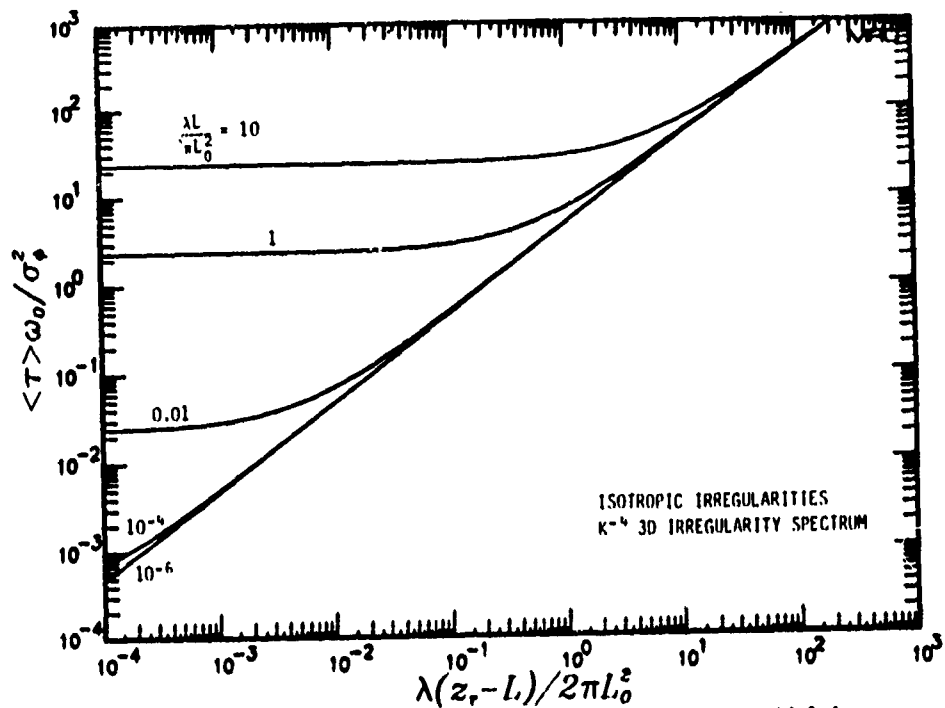


Figure 4-11. Mean time delay as a function of layer thickness and free-space propagation distance.

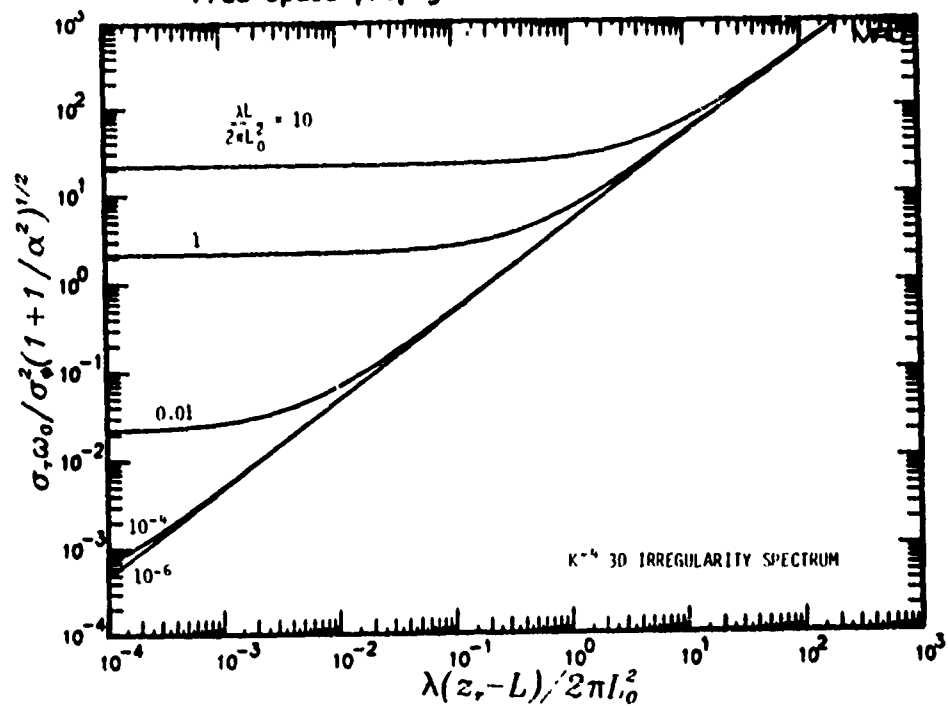


Figure 4-12. Normalized time delay jitter as a function of layer thickness and free-space propagation distance.

$$\xi_z = \lambda z_r / 2\pi L_0^2$$

$$\xi_L = \lambda L / 2\pi L_0^2$$

Results applicable to the case of elongated irregularities may be obtained by dividing the ordinate by two. It is apparent from the figures that for any given free-space propagation distance, the value of the normalized mean time delay converges to the thin phase-screen result as  $\xi_L$  decreases.

For a constant value of the normalized layer thickness,  $\xi_L$ , the normalized mean time delay becomes a constant function of  $\xi_z - \xi_L$  for values of the normalized free-space propagation distance less than about one-tenth of the normalized layer thickness. This situation corresponds to a thick scattering layer with very small free-space propagation distance so that changes in the free-space propagation distance are unimportant and do not affect the geometry.

Figure 4-12 shows the normalized time delay jitter

$$\sigma_{\tau I \omega_0} / \sigma_{\phi}^2 \left( 1 + \frac{1}{\alpha^2} \right)^{1/2}$$

as a function of the normalized free-space propagation distance,  $\xi_z - \xi_L$ . Values of the normalized layer thickness  $\xi_L$  ranging from  $10^{-6}$  to  $10$  are shown. The general appearance of this figure is similar to that of the previous figure. The limiting behavior described above for decreasing layer thickness at a constant free-space propagation distance and for decreasing free-space propagation distance at a constant layer thickness also occurs in Figure 4-12. That is, for a given normalized free-space propagation distance, the normalized time delay jitter converges to the thin phase-screen result as the normalized layer thickness decreases. For a constant value of normalized layer thickness, the normalized time delay jitter reaches a constant value for normalized free-space propagation distance values less than about one-tenth of the normalized layer thickness.



Figure 4-12 is also valid for the case of infinitely elongated irregularities where the ordinate in this case is

$$\sigma_{\tau} E \omega_0 / \sigma_{\phi}^2 \left( \frac{1}{2} + \frac{1}{\alpha^2} \right)^{1/2}$$

At this point consider the calculation of the difference between the exact thick layer results and the thin phase-screen results for values of the mean time delay and time delay jitter. It was shown previously in Section 4.4.1 that both calculations yield the same value of the mean time delay. It is also apparent that this comparison is also available for the time delay jitter for a few values of normalized layer thickness from the curves of Figure 4-12. To make such a comparison it is important to modify the effective free-space propagation distance shown on the abscissa so that the thin phase-screen is located at the center of the original thick scattering layer.

Figure 4-13 shows values of the difference between the exact strong scatter calculation and the thin phase-screen approximation

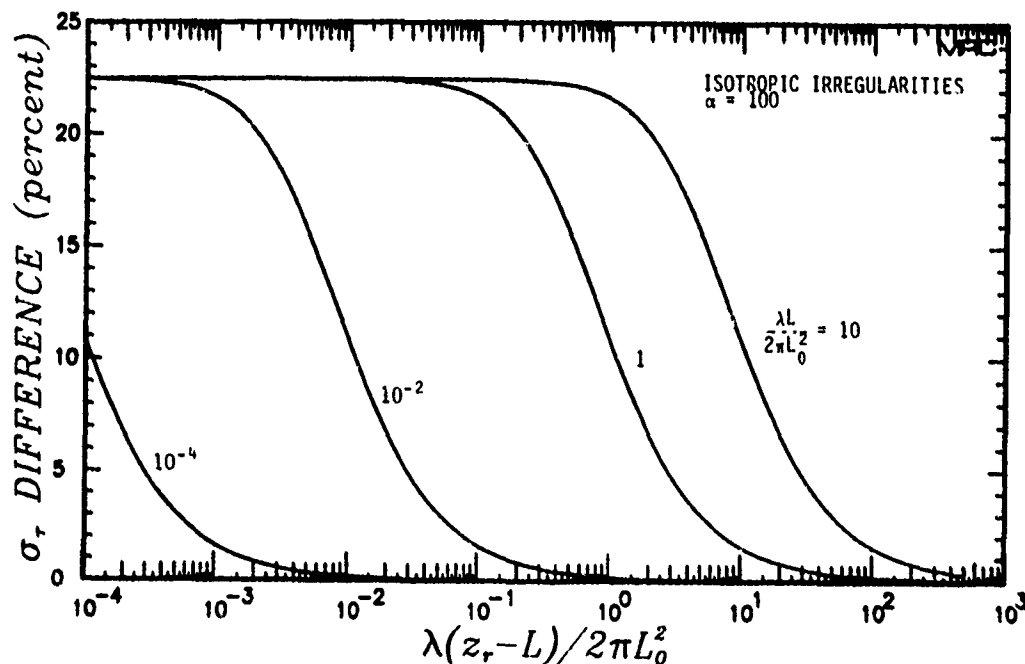


Figure 4-13. Relative time delay jitter accuracy of the thin phase-screen approximation, isotropic irregularities,  $\alpha = 100$ .

$$\frac{|\sigma_{\tau I}(\text{exact}) - \sigma_{\tau I}(\text{phase-screen})|}{\sigma_{\tau I}(\text{exact})}$$

plotted in percent as a function of normalized layer thickness and normalized free-space propagation distance. Figure 4-13 applies to the case of isotropic irregularities and is restricted to a value of  $\alpha$  of 100. Values of the normalized layer thickness  $\xi_L$  range from  $10^{-4}$  to 10. It can be seen that for values of the normalized layer thickness less than or equal to the normalized free-space propagation distance, the difference is at most about 10 percent. The maximum difference is independent of layer thickness and is 22.5 percent. This maximum difference corresponds to the case of a receiver located at the exit of the thick layer with zero free-space propagation distance. As in the preceding calculation of the thin phase-screen approximation to the scintillation index, this geometry is the most difficult to model with a centrally located phase-screen.

Figure 4-14 shows another comparison of the accuracy of the time delay jitter calculation in the thin phase-screen approximation. The calculations presented in this figure differ from the previous calculations only in that the value of the parameter  $\alpha$  is unity for Figure 4-14. It is apparent that the thin phase-screen approximation is more accurate for this decreased value of the parameter  $\alpha$  with a maximum difference of about 9.5 percent for unity  $\alpha$ .

Figure 4-15 shows the difference between the exact strong scatter results and the thin phase-screen results for the time delay jitter for elongated irregularities and unity  $\alpha$ . The general behavior noted in the two previous figures is again observed here. The maximum time delay jitter difference is now decreased to about 6 percent for this elongated irregularity case.

The previous three figures show that the maximum difference in the time delay jitter calculation, caused by modeling a thick scattering layer as a thin phase-screen located at the center of the layer, is a function of the parameter  $\alpha$ .

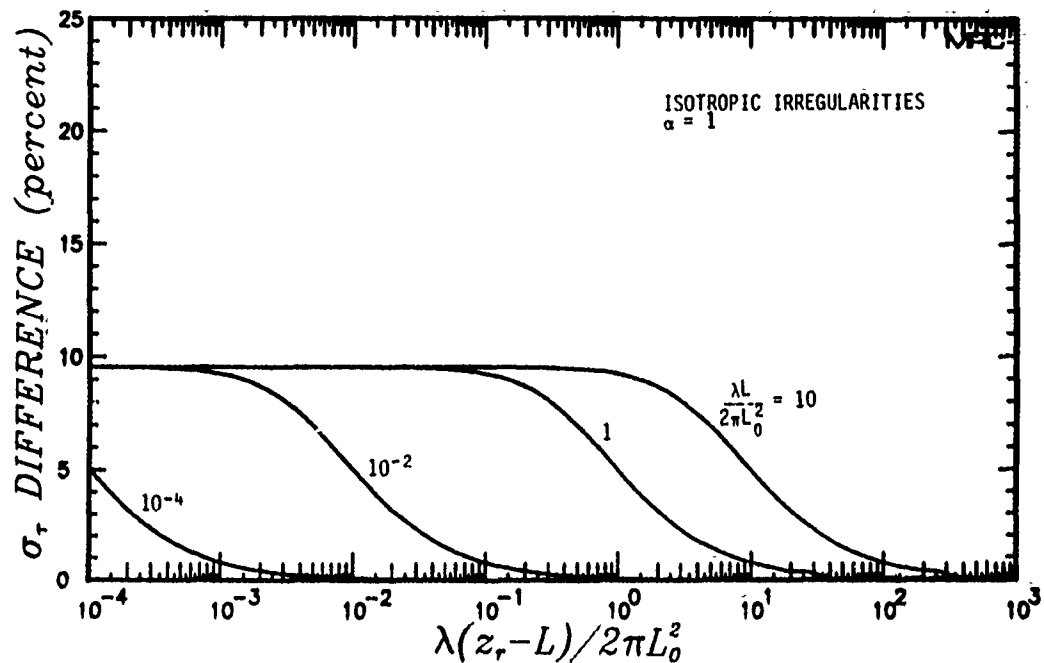


Figure 4-14. Relative time delay jitter accuracy of the thin phase-screen approximation, isotropic irregularities,  $\alpha = 1$ .

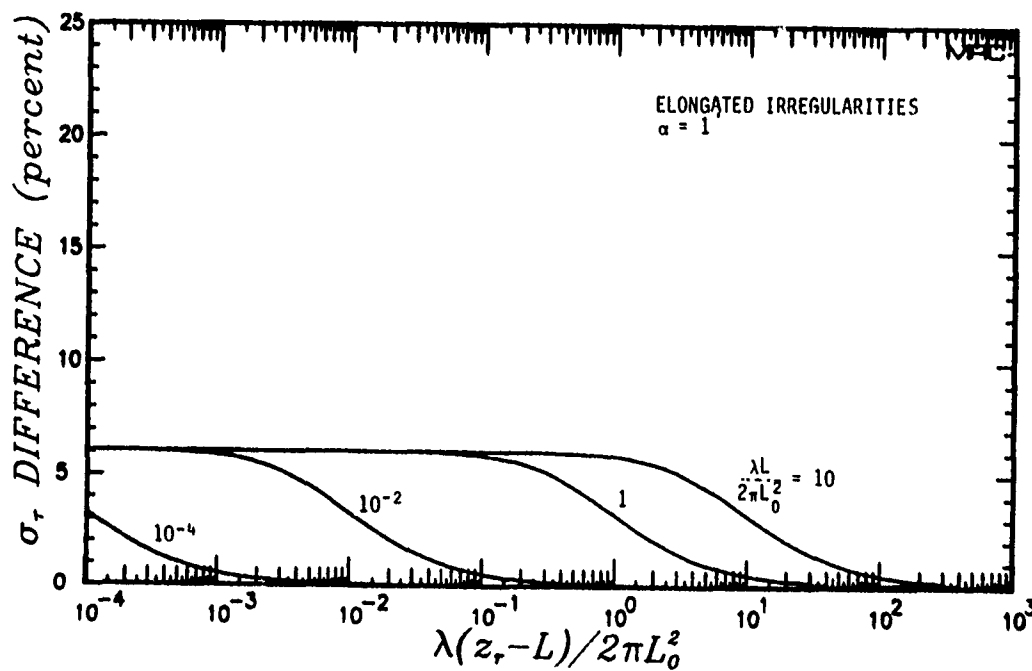


Figure 4-15. Relative time delay jitter accuracy of the thin phase-screen approximation, elongated irregularities,  $\alpha = 1$ .

Figures 4-16 and 4-17 show the maximum error

$$\frac{|\sigma_T(\text{thick layer}) - \sigma_T(\text{phase-screen})|}{\sigma_T(\text{thick layer})}$$

in percent for the isotropic and elongated irregularity cases, respectively. These curves were obtained by taking a value of the normalized layer thickness,  $\xi_L$ , of 10 and a very small value of the free-space propagation distance,  $\xi_Z - \xi_L$ , of  $10^{-6}$ . This case yields the desired maximum difference. It can be seen in both figures that the error decreases to zero for values of  $\alpha$  less than unity and reaches the maximum value of 22.5 percent for values of  $\alpha$  of about 10 and greater. It was noted in Section 4.3.1 that  $\alpha$  is proportional to the quantity  $z_r/F$  where  $z_r$  is the propagation distance and  $F$  is the focal distance. Hence for  $\alpha$  small, the receiver is "close to" the phase-screen and dispersive effects dominate diffractive effects. In this case the time delay fluctuations are caused by large-scale phase fluctuations and are well modeled by a thin phase-screen. For  $\alpha$  large, diffraction is more important than dispersion and a single phase-screen model of a thick layer is relatively less accurate.

It should be emphasized that the maximum error in  $\sigma_T$  caused by modeling a thick layer by a thin phase-screen is 22.5 percent. This error appears to be modest relative to uncertainties in the knowledge of the propagation environment in the case of strong scattering.

As a final comparison of the accuracy of the thin phase-screen approximation to calculate the time domain properties of a wide bandwidth waveform subject to strong scattering, consider the effects of the approximation on the power impulse response function  $G_I(z_r, \tau)$ . Figures 4-18 to 4-20 show the power impulse response function for isotropic irregularities for a thick layer and its thin phase-screen equivalent. The abscissa and ordinate are normalized by multiplying and dividing by  $\omega_{coh}$ . In all three figures the results correspond to a value of  $\alpha$  of 3 where scattering effects slightly dominate dispersive effects. In all three figures the normalized free-space propagation distance,  $\xi_Z - \xi_L$ , is unity; the normalized layer thickness,  $\xi_L$ , takes on values of 0.1, 1.0, and 10 in the three figures. The thin phase-screen equivalents thus

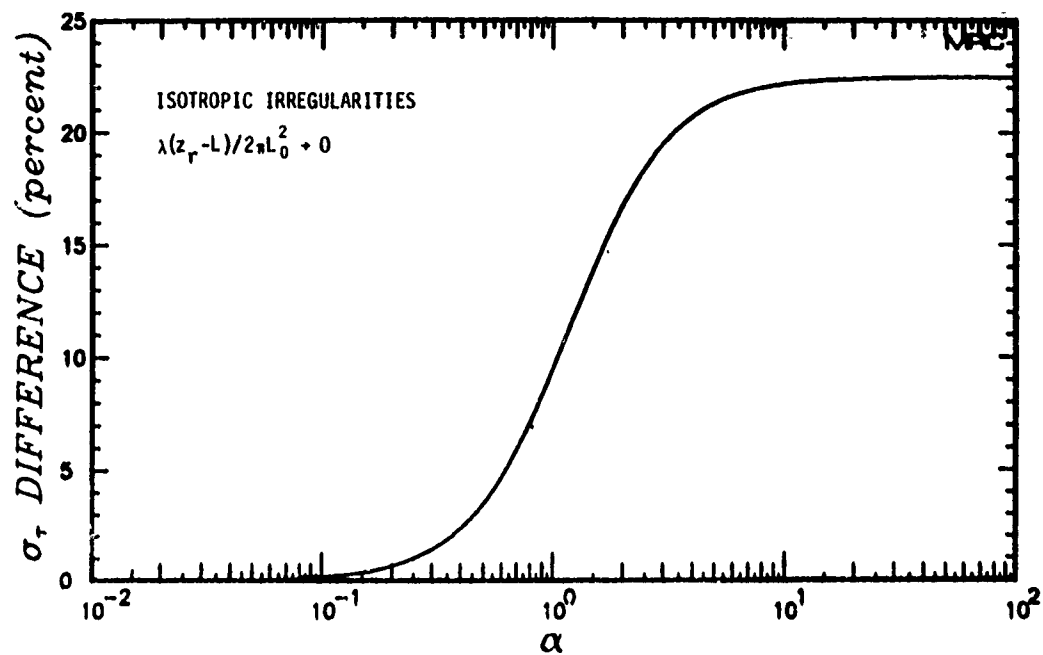


Figure 4-16. Maximum percent difference in  $\sigma_\tau$ , isotropic irregularities.

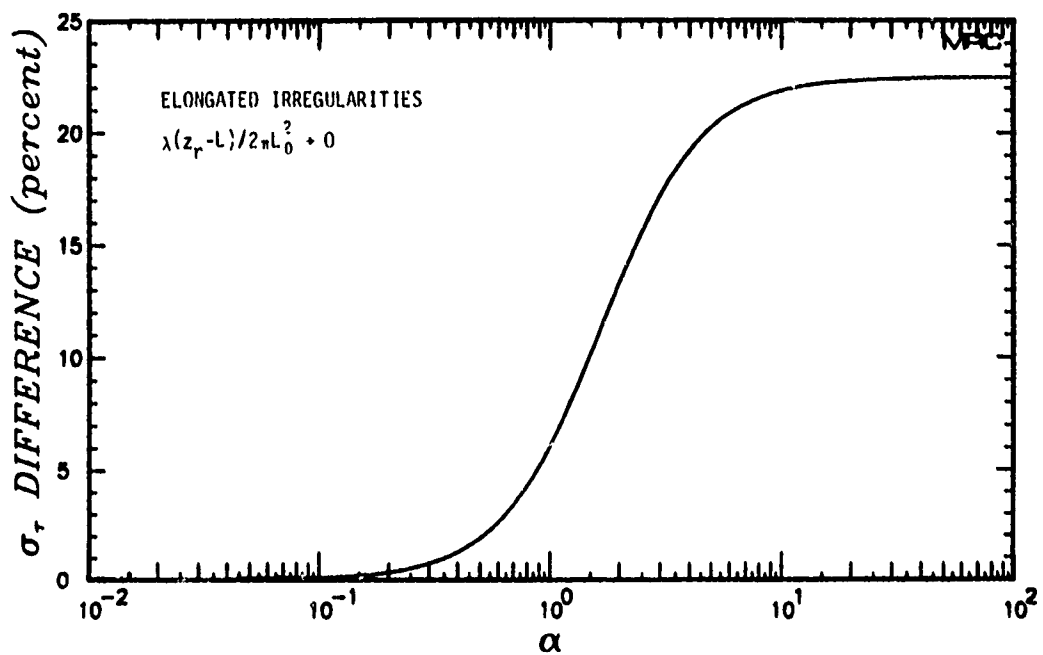


Figure 4-17. Maximum percent difference in  $\sigma_\tau$ , elongated irregularities.

have zero layer thickness and values of the effective normalized propagation distance between phase-screen and receiver of 1.005, 1.5, and 6 respectively. These values are computed directly from Equation 4-168.

In Figure 4-18 the layer thickness is small relative to the free-space propagation distance and the impulse response function is exact for the thin phase-screen approximation to this layer.

In Figure 4-19 the layer thickness and the free-space propagation distance are identical. The power impulse response function for the thick layer is quite similar to that of the thin phase-screen approximation in this case with no difference in the mean time delay and a 9.6 percent difference in the time delay jitter.

In Figure 4-20 the layer thickness is ten times the free-space propagation distance with a resulting 19 percent error in the result for  $\sigma_T$  obtained in the thin phase-screen approximation.

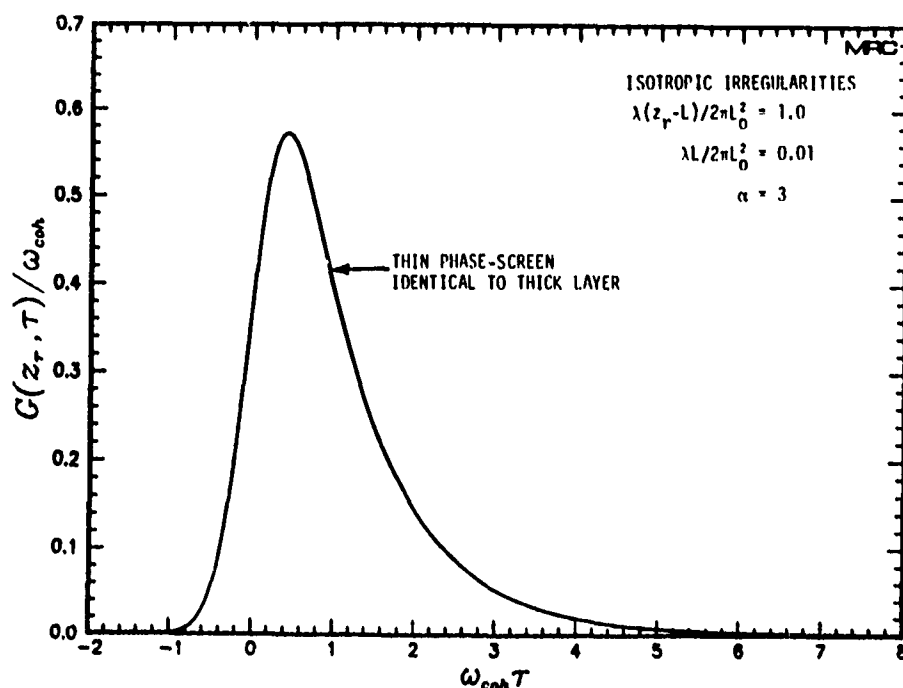


Figure 4-18. Comparison of power impulse response function, thin phase-screen versus thick layer.

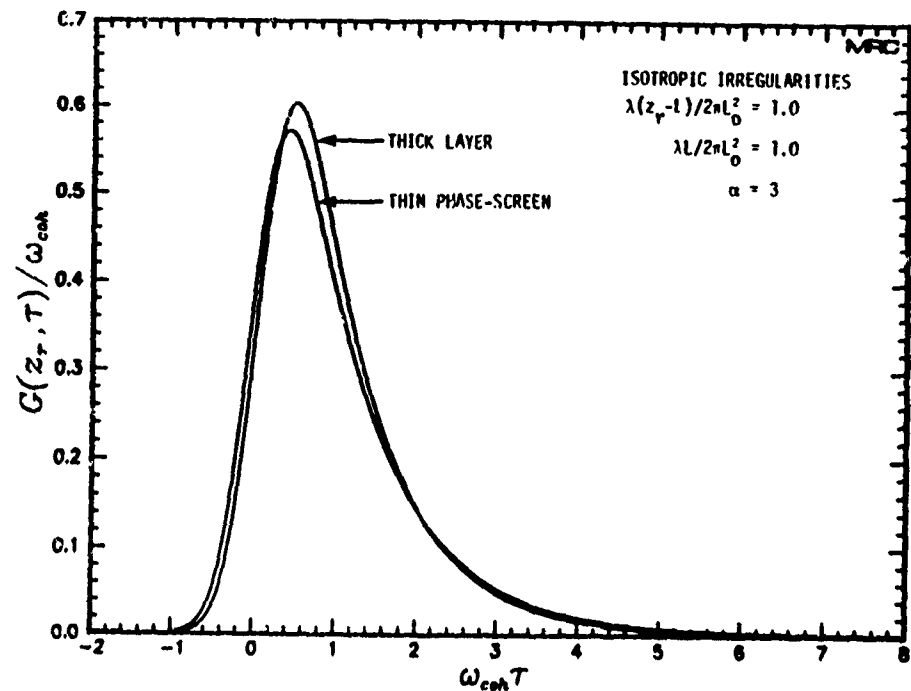


Figure 4-19. Comparison of power impulse response function, thin phase-screen versus thick layer.

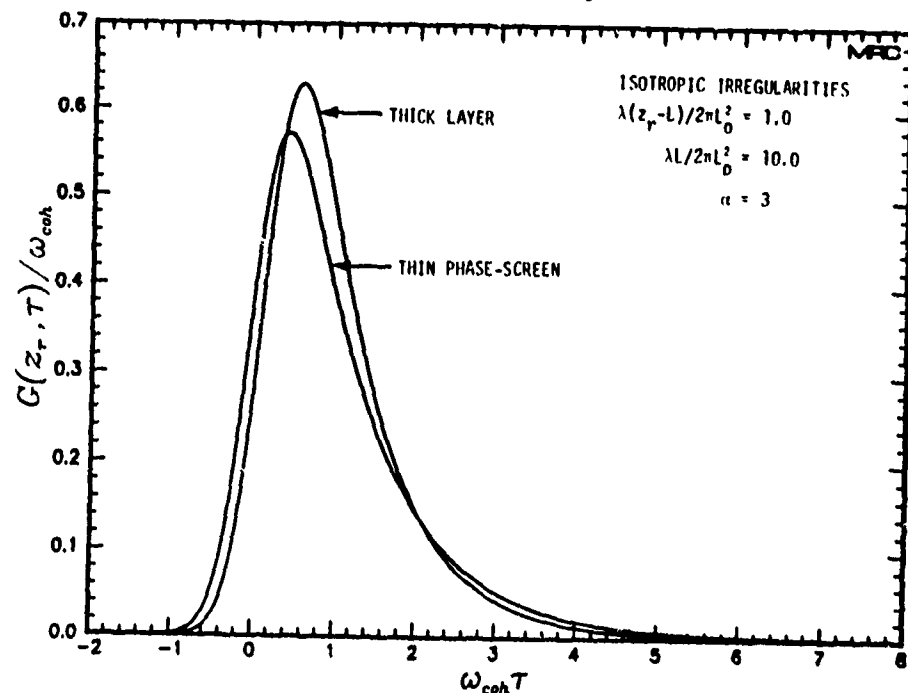


Figure 4-20. Comparison of power impulse response function, thin phase-screen versus thick layer.

Results of this subsection show that the thin phase-screen approximation gives an adequate approximation to the exact, strong scatter result for time delay jitter. It has also been shown that the thin-phase screen approximation provides an accurate approximation to the power impulse response function and thus may be used as the basis for the statistical generation of signals as discussed in Section 3 of this report.



## REFERENCES

Abramowitz, M., and I. A. Stegun, Handbook of Mathematical Functions, Dover: New York, 1965.

Arendt, P. R., and H. Soicher, "Effects of Arctic Nuclear Explosions on Satellite Radio Communication," Proc. IEEE, Vol. 52, No. 6, pp. 672-676, June 1964.

Basu, S., and M. C. Kelley, "A Review of Recent Studies of Equatorial F-Region Irregularities and Their Impact on Scintillation Modeling," Effect of the Ionosphere on Space and Terrestrial Systems, J. M. Goodman, Ed., U.S. Government Printing Office, pp. 90-106, 1978.

Bogusch, R. L., F. W. Guigliano, D. L. Knepp and A. H., Michelet, "Frequency Selective Propagation Effects on Spread-Spectrum Receiver Tracking," Proc. IEEE, Vol. 69, No. 7, pp. 787-796, July 1981.

Boquist, W. P., and J. W. Snyder, "Conjugate Auroral Measurements from the 1962 U.S. High Altitude Nuclear Test Series," Aurora and Airglow, B. M. McCormac, Ed., New York: Reinhold, pp. 325-339, 1967.

Bramley, E. N., "The Accuracy of Computing Ionospheric Radio-wave Scintillation by the Thin-phase-screen Approximation," J. Atmos. Terr. Phys., Vol. 39, pp. 367-373, 1977.

Bramley, E. N., "The Diffraction of Waves by an Irregular Refracting Medium," Proc. Roy. Soc. A, Vol. 225, pp. 515-518, 1954.

Brown, W. P., Computer Simulation of Adaptive Optical Systems, Hughes Research Laboratory, September 1975.

Buckley, R., "Diffraction by a Random Phase-changing Screen: A Numerical Experiment," J. Atmos. Terr. Phys., Vol. 37, pp. 1431-1446, 1975.

Crane, R. K., "Ionospheric Scintillation," Proc. IEEE, Vol. 65, No. 2, pp. 180-199, February 1977.

Dyson, P. L., J. P. McClure, and W. B. Hanson, "In Situ Measurements of the Spectral Characteristics of F Region Ionospheric Irregularities," J. Geophys. Res., Vol. 79, No. 10, pp. 1497-1502, 1 April 1974.

Fante, R. L., "Some New Results on Propagation of Electromagnetic Waves in Strongly Turbulent Media," IEEE Trans. Antennas Propagat., Vol. AP-23, pp. 382-385, May 1975.

Fante, R. L., "Electromagnetic Beam Propagation in Turbulent Media," Proc. IEEE, Vol. 63, No. 12, pp. 1669-1692, December 1975.

Fante, R. L., "Some Physical Insights into Beam Propagation in Strong Turbulence," Radio Science, Vol. 15, No. 4, pp. 757-762, July-August 1980.

Fante, R. L., "Two-position, Two-frequency Mutual-coherence Function in Turbulence," J. Opt. Soc. Am., Vol. 71, No. 12, pp. 1446-1451, December 1981.

Fleck, J. A., J. R. Morris, and M. D. Feit, "Time-Dependent Propagation of High Energy Laser Beams Through the Atmosphere," J. Appl. Phys., Vol. 10, pp. 129-160, 1976.

Fremouw, E. J., R. L. Leadabrand, R. C. Livingston, M. D. Cousins, C. L. Rino, B. C. Fair and R. A. Long, "Early Results from the DNA Wideband Satellite Experiment-Complex Signal Scintillation," Radio Science, Vol. 13, No. 1, pp. 167-187, January-February 1978.

Glasstone, S., and P. J. Dolan, The Effects of Nuclear Weapons, 3rd ed., U.S. Department of Defense and the U.S. Department of Energy, 1977.

Gradshteyn, I. S., and I. M. Ryzhik, Tables of Integrals, Series and Products, Academic Press: New York, 1965.

Hoerlin, H., United States High-Altitude Test Experiences, LA-6405, Los Alamos Scientific Laboratory, October 1976.

Ishimaru, A., Wave Propagation and Scattering in Random Media, New York: Academic Press, 1978.

Johnson, A. L., and P. K. Lee, "Equatorial Scintillation Tests of LES 8/9," Effect of the Ionosphere on Space and Terrestrial Systems, J. M. Goodman, Ed., pp. 25-30, U.S. Government Printing Office, 1978.

Jokipii, J. R., "On the Thin-screen Model of Interplanetary Scintillations," Astrophys. J., Vol. 161, pp. 1147-1152, September 1970.

Keyes, J. G., and B. A. Tinsley, "Optical Observations from Western Samoa of the Artificial Auroral Display, 9 July 1962," New Zealand J. Geol. Geophys., Vol. 5, No. 6, pp. 925-932, December 1962.

King, M. A., and P. B. Fleming, "An Overview of the Effects of Nuclear Weapons on Communications Capabilities," Signal, pp. 59-66, January 1980.

Knepp, D. L., Multiple Phase-Screen Propagation Analysis for Defense Satellite Communications System, DNA 44241, MRC-R-332, Mission Research Corporation, September 1977.

Knepp, D. L., and R. L. Bogusch, Predictions of GPS X-Set Performance During the PLACES Experiment, DNA 50381, MRC-R-514, Mission Research Corporation, July 1979.

Linson, L. M., and J. B. Workman, "Formation of Striations in Ionospheric Plasma Clouds," J. Geophys. Res., Vol. 75, No. 16, pp. 3211-3219, June 1970.

Maeda, H., A. J. Shirgaokar, M. Yasuhara, and S. Matsushita, "On the Geomagnetic Effect of the Starfish High-Altitude Nuclear Explosion," J. Geophys. Res., Vol. 69, No. 5, pp. 917-945, 1 March 1964.

Marshall, J., "PLACES-A Structured Ionospheric Plasma Experiment for Satellite System Effects Simulation," AIAA 20th Aerospace Sciences Meeting, Orlando, Florida, January, 1982.

Matsushita, S., "On Artificial Geomagnetic and Ionospheric Storms Associated With High-Altitude Explosions," J. Geophys. Res., Vol. 64, No. 9, pp. 1149-1161, September 1959.

Mercier, R. P., "Diffraction by a Screen Causing Large Random Phase Fluctuations," Proc. Cambridge Phil. Soc., Vol. 58, pp. 382-400, 1962.

Mullen, J. P., A. Bushby, J. Lanat, and J. Pantoja, "Gigahertz Scintillation at the Magnetic Equator," Effect of the Ionosphere on Space and Terrestrial Systems, J. M. Goodman, Ed., U.S. Government Printing Office, pp. 31-35, 1978.

Papoulis, A., Probability, Random Variables, and Stochastic Processes, McGraw Hill: New York, 1965.

Paulson, M. R., and R. U. Hopkins, "Spaced-Receiver Investigations of Equatorial Scintillation made at Guam during 1971 and 1976," Effect of the Ionosphere on Space and Terrestrial Systems, J. M. Goodman, Ed., pp. 41-47, U.S. Government Printing Office, 1978.

Phelps, A. D. R., and R. C. Sagalyn, "Plasma Density Irregularities in the High-Latitude Top Side Ionosphere," J. Geophys. Res., Vol. 81, No. 4, pp. 515-523, 1 February 1976.

Pope, J. H., and R. B. Fritz, "High Latitude Scintillation Effects on Very High Frequency (VHF) and S-band Satellite Transmissions," Indian J. Pure App. Phys., Vol. 9, pp. 593-600, August 1971.

Prettie, C. W., and J. M. Marshall, "Satellite Link Measurements" in Proceedings of the STRESS Data Review Meeting, 29-30 November 1977, DNA 46201, SRI International, compiled by D. R. McDaniel, June 1978.

Ratcliffe, J. A., "Some Aspects of Diffraction Theory and Their Application to the Ionosphere," Reports on Progress in Physics, Vol. 19, pp. 188-267, The Physical Society, London, 1956.

Rino, C. L., "Iterative Methods for Treating the Multiple Scattering of Radio Waves," J. Atmos. Terr. Phys., Vol. 40, No. 9, pp. 1011-1018, September 1978.

Rino, C. L., "Numerical Computations for a One-dimensional Power Law Phase Screen," Radio Science, Vol. 15, No. 1, pp. 41-47, January-February 1980.

Rino, C. L., V. H. Gonzalez, and A. R. Hessing, "Coherence Bandwidth Loss in Transionospheric Radio Propagation," Radio Science, Vol. 16, No. 2, pp. 245-255, March-April 1981.

Rothwell, P., J. H. Wager, and J. Sayers, "Effect of the Johnston Island High-Altitude Nuclear Explosion on the Ionization Density in the Topside Ionosphere," J. Geophys. Res., Vol. 68, No. 3, pp. 947-949, 1 February 1963.

Rufenach, C. L., "Ionospheric Scintillation by a Random Phase Screen: Spectral Approach," Radio Science, Vol. 10, No. 2, pp. 155-165, February 1975.

Salpeter, E. E., "Interplanetary Scintillations. I. Theory," Astrophys. J., Vol. 147, pp. 433-448, 1967.

Scannapieco, A. J., S. L. Ossakow, S. R. Goldman, and J. M. Pierre, "Plasma Cloud Late-Time Striation Spectra," J. Geophys. Res., Vol. 81, No. 34, pp. 6037-6045, 1 December 1976.

Shkarofsky, I. P., "Generalized Turbulence Space-correlation and Wave-number Spectrum-function Pairs," Canadian J. Phys., Vol. 46, pp. 2133-2153, 1968.

Skinner, N. J., R. F. Kelleher, J. B. Hacking and C. W. Benson, "Scintillation Fading of Signals in the SHF Band," Nature (Phys. Sci.), Vol. 232, pp. 19-21, 5 July 1971.

Sreenivasiah, I., A. Ishimaru, and S. T. Hong, "Two-frequency Mutual Coherence Function and Pulse Propagation in a Random Medium: An Analytic Solution to the Plane Wave Case," Radio Science, Vol. 11, No. 10, pp. 775-758, October 1976.

Sreenivasiah, I., and A. Ishimaru, "Beam Wave Two-frequency Mutual-coherence Function and Pulse Propagation in Random Media: An Analytic Solution," Applied Optics, Vol. 18, No. 10, pp. 1613-1618, May 1979.

Stakgold, I., Boundary Value Problems of Mathematical Physics, Vol. 1, Macmillan: London, 1967.

Tatarskii, V. I., The Effects of the Turbulent Atmosphere on Wave Propagation, translated by Israel Program for Scientific Translations, National Technical Information Service, U.S. Department of Commerce, 1971.

Tatarskii, V. I., Wave Propagation in a Turbulent Medium, Dover: New York, 1967.

Taur, R. R., "Simultaneous 1.5- and 4-GHz Ionospheric Scintillation Measurements," Radio Science, Vol. 11, pp. 1029-1036, December 1976.

Wandzura, S. A., "Meaning of Quadratic Structure Functions," J. Opt. Soc. Am., Vol. 70, No. 6, pp. 745-747, June 1980.

Wernik, A. W., C. H. Liu, M. Y. Youakim and K. C. Yeh, A Theoretical Study of Scintillation of Transionospheric Radio Signals, University of Illinois at Urbana-Champaign, June 1973.

Whitney, H. E., and S. Basu, "The Effect of Ionospheric Scintillation on VHF/UHF Satellite Communications," Radio Science, Vol. 12, No. 1, pp. 123-133, January-February 1977.

Wittwer, L. A., The Propagation of Satellite Signals Through Turbulent Media, AFWL-TR-77-183, Air Force Weapons Laboratory, January 1978.

Wittwer, L. A., Radio Wave Propagation in Structured Ionization for Satellite Applications, DNA 5304D, Defense Nuclear Agency, December 1979.

Wittwer, L. A., A Trans-Ionospheric Signal Specification for Satellite C<sup>3</sup> Applications, DNA 5662D, Defense Nuclear Agency, December 1980.

Yeh, K. C., and G. W. Swenson, Jr., "The Scintillation of Radio Signals from Satellites," J. Geophys. Res., Vol. 64, No. 12, pp. 2281-2286, December 1959.

Yeh, K. C., and C. H. Liu, "An Investigation of Temporal Moments of Stochastic Waves," Radio Science, Vol. 12, No. 5, pp. 671-680, September-October 1977.

Zinn, J., H. Hoerlin, and A. G. Petschek, "The Motion of Bomb Debris Following the Starfish Test," Radiation Trapped in the Earth's Magnetic Field, B. M. McCormac, Ed., Dordrecht, The Netherlands: D. Reidel, pp.671-692, 1966.

## APPENDIX A

### A.1 EVALUATION OF THE GENERALIZED POWER SPECTRUM $S(K, \tau)$

#### A.1.1 Numerical Method

In this appendix the generalized power spectrum, as calculated in Section 4 in the thin phase-screen approximation, is evaluated for a number of interesting conditions. The evaluation of  $S(K, \tau)$  is somewhat tedious as is seen here but is, of course, quite necessary for the calculation of statistical realizations of the impulse response function. In the thin phase-screen approximation the generalized power spectrum is given by Equations 4-97 and 4-99 repeated here for convenience

$$S_E(K, \tau) = \frac{\alpha \omega_{coh} \ell_0}{2^{3/2} \pi} \exp \left\{ -\frac{1}{4} K^2 \ell_0^2 - \frac{1}{2} \alpha^2 \left[ \frac{1}{4} K^2 \ell_0^2 - \omega_{coh} \tau \right]^2 \right\} \quad (A-1)$$

$$S_I(K, \tau) = \frac{\beta^{1/2} \omega_{coh} \ell_0}{4\pi^{3/2}} \exp \left\{ -\frac{1}{4} K^2 \ell_0^2 - \frac{1}{2} \alpha^2 \left[ \frac{1}{4} K^2 \ell_0^2 - \omega_{coh} \tau \right]^2 \right\} \\ \times \exp \left( \beta^2 / 4 \alpha^2 \right) K_{1/4} \left( \beta^2 / 4 \alpha^2 \right) \quad (A-2)$$

where

$$\beta = \alpha^2 \left[ \frac{1}{4} K^2 \ell_0^2 - \omega_{coh} \tau \right] + 1 \quad (A-3)$$

Equation A-1 gives the generalized power spectrum for elongated irregularities and is appropriate for the two-dimensional geometry solved by the MPS propagation simulation. This equation is easy to evaluate numerically.

Equation A-2 gives the generalized power spectrum for the case of isotropic irregularities and is somewhat more difficult to evaluate. It is convenient to consider four cases and use different, efficient evaluation algorithms for each case.

Case 1:  $0 < \beta^2/4\alpha^2 \leq 3.5$

For  $\beta^2/4\alpha^2$  between zero and 3.5,  $S_I(K, \tau)$  is easily evaluated since in this range the  $K_{1/4}$  Bessel function may be directly calculated using the expressions

$$K_\nu(z) = \frac{\pi}{2} \left( \frac{I_{-\nu}(z) - I_\nu(z)}{\sin \nu\pi} \right) \quad (\text{A-4})$$

$$I_\nu(z) = (z/2)^\nu \sum_{k=0}^{\infty} \frac{(z^2/4)^k}{k! \Gamma(\nu+k+1)} \quad (\text{A-5})$$

which are taken directly from Abramowitz and Stegun, 1964. For  $z \leq 3.5$  sufficient accuracy is obtained using at most twelve terms in the convergent series given by A-4. The  $\Gamma$  function required in Equation A-5 is available on most computer systems and is also given in Abramowitz and Stegun.

Case 2:  $\beta^2/4\alpha^2 > 3.5$

For  $\beta^2/4\alpha^2 > 3.5$  it is necessary to use the asymptotic expansion for the factor

$$\exp(\beta^2/4\alpha^2) K_{1/4}(\beta^2/4\alpha^2)$$

which has the form

$$e^z K_\nu(z) \approx (\pi/2z)^{1/2} \left\{ 1 + \frac{\mu-1}{8z} + \frac{(\mu-1)(\mu-9)}{2!(8z)^2} + \frac{(\mu-1)(\mu-9)(\mu-25)}{3!(8z)^3} + \dots \right\} \quad (\text{A-6})$$



where  $\mu = 4\nu^2$ . Equation A-6 is taken directly from 9.7.2 in Abramowitz and Stegun.

Cases 3 and 4:  $\beta$  less than zero

For  $\beta$  negative it is necessary to carefully evaluate the term

$$\beta^{1/2} K_{1/4}(\beta^2/4\alpha^2)$$

This is easily done with the aid of Equation 9.6.31 from Abramowitz and Stegun. The result is found as

$$\begin{aligned} \beta^{1/2} K_{1/4}(\beta^2/4\alpha^2) = \\ |\beta|^{1/2} \{K_{1/4}(\beta^2/4\alpha^2) + \pi\sqrt{2} I_{1/4}(\beta^2/4\alpha^2)\} \quad , \quad \beta < 0 \quad (A-7) \end{aligned}$$

Also one needs the identity

$$\begin{aligned} -\frac{\alpha^2}{2} \left[ \frac{1}{4} K^2 \ell_0^2 - \omega_{\text{coh}} \tau \right]^2 + \frac{\beta^2}{4\alpha^2} = \\ \frac{1}{\alpha^2} \left( \beta - \frac{1}{2} \right) - \frac{\beta^2}{4\alpha^2} \end{aligned} \quad (A-8)$$

Substituting Equation A-7 into the expression for  $S_I(K, \tau)$  and replacing the appropriate factors in the exponent by use of A-8, one obtains for  $\beta < 0$

$$\begin{aligned} S_I(K, \tau) = \frac{\omega_{\text{coh}} \ell_0 |\beta|^{1/2}}{4\pi^{3/2}} \exp \left\{ -\frac{1}{4} K^2 \ell_0^2 \right\} \\ \times \left\{ \exp \left\{ -\frac{1}{2} \alpha^2 \left[ \frac{1}{4} K^2 \ell_0^2 - \omega_{\text{coh}} \tau \right]^2 \right\} \exp(\beta^2/4\alpha^2) K_{1/4}(\beta^2/4\alpha^2) \right. \\ \left. + 2^{1/2} \pi \exp \frac{1}{\alpha^2} \left( \beta - \frac{1}{2} \right) \exp(-\beta^2/4\alpha^2) I_{1/4}(\beta^2/4\alpha^2) \right\} \quad (A-9) \end{aligned}$$

Case 3:  $\beta < 0$ ,  $0 < \beta^2/4\alpha^2 \leq 3.5$

For  $\beta$  negative and  $\beta^2/4\alpha^2 \leq 3.5$  accurate results can be obtained using the convergent series for  $K_{1/4}$  and  $I_{1/4}$  given by Equations A-4 and A-5 to evaluate the expression for the generalized power spectrum given by A-9.

Case 4:  $\beta < 0$ ,  $\beta^2/4\alpha^2 > 3.5$

For  $\beta$  negative and  $\beta^2/4\alpha^2$  greater than 3.5 use of the convergent series expression becomes inefficient and causes inaccurate numerical results. Instead use the asymptotic expansion given by Equation A-6 for the term

$$\exp(\beta^2/4\alpha^2) K_{1/4}(\beta^2/4\alpha^2)$$

to evaluate the term with the K Bessel function. For the remaining term,

$$\exp(-\beta^2/4\alpha^2) I_{1/4}(\beta^2/4\alpha^2)$$

use the asymptotic expression 9.7.1 in Abramowitz and Stegun.

$$e^{-z} I_{\nu}(z) \approx \frac{1}{\sqrt{2\pi z}} \left\{ 1 - \frac{\mu-1}{8z} + \frac{(\mu-1)(\mu-9)}{2!(8z)^2} - \frac{(\mu-1)(\mu-9)(\mu-25)}{3!(8z)^3} + \dots \right\} \quad (\text{A-10})$$

where  $\mu=4\nu^2$ .

The numerical techniques described in this section enable accurate and efficient evaluation of the generalized power spectra. In the following subsection results for these functions are shown for a number of different values of the parameter  $\alpha$ .

### A.1.2 Examples of $S(K, \tau)$

In this section plots of the generalized power spectra  $S_E(K, \tau)$  and  $S_I(K, \tau)$  are shown as a function of the parameter  $\alpha$ . This parameter is described in Section 4 where it is seen that  $\alpha$  much less than unity corresponds to the case where large scale phase effects and dispersion are more important than angular scattering or diffraction.  $\alpha$  greater than unity corresponds to the case where diffraction provides the dominate scattering mechanism.

Figures A-1 to A-20 show plots of the function  $S_E(K, \tau)$  and  $S_I(K, \tau)$  for values of the parameter  $\alpha$  of 10.0, 5.0, 1.0, 0.1, 0.01. In all cases the generalized power spectra are plotted as a function of the normalized variables  $k_0 K$  and  $\omega_{coh} \tau$ . This is a convenient normalization as can be readily seen from Equations A-1 and A-2. Two types of figures are shown here. In one case contours of the generalized power spectra are shown as functions of the two normalized variables  $k_0 K$  and  $\omega_{coh} \tau$ . A second plot of  $S(K, \tau)$  is provided which gives a three-dimensional view of this function to provide better understanding of the functional dependences.

Figures A-1 to A-4 for a value of  $\alpha$  of 10 shows the behavior of the generalized power spectra for large  $\alpha$ . The delta function behavior for the case of elongated irregularities as given by Equation 4-110 is shown in Figures A-1 and A-3. Recalling from Fourier analysis that the variable  $K$  is related to the sine of the scattering angle,  $\theta$  in the parabolic approximation, for small  $\theta$

$$K = \frac{2\pi \sin \theta}{\lambda} \approx \frac{2\pi \theta}{\lambda} \quad (A-11)$$

Since the generalized power spectrum takes on the form

$$\delta \left( \frac{1}{4} K^2 k_0^2 - \omega_{coh} \tau \right)$$

when diffractive or angular scattering effects are dominant, there is a one-to-one correspondence between scattering angle and time delay. That is,

$$K = \pm \frac{2}{\ell_0} \sqrt{\omega_{\text{coh}} \tau} \approx \pm \frac{2\pi\theta}{\lambda}, \quad \alpha \gg 1 \quad (\text{A-12})$$

Of course, the resulting time domain power impulse response function is the integral of the generalized power spectrum over all  $K$  or equivalently, over all scattering angles (e.g., Equation 4-107).

The effect of the difference between isotropic irregularities and infinitely elongated irregularities is also seen from a comparison of Figures A-1 and A-3 versus A-2 and A-4. Notice that for the case of isotropic irregularities, the characteristic horseshoe shape given by the equation

$$\omega_{\text{coh}} \tau = \frac{1}{4} K^2 \ell_0^2 \quad (\text{A-13})$$

has a tendency to be filled in. For elongated irregularities, less energy is present inside the horseshoe.

The reason for this difference is that angular scattering can occur in only one plane for the case of infinitely elongated irregularities. For large  $\alpha$  and elongated irregularities a single time delay can result from scattering at only two angles as specified by Equation A-12. For isotropic irregularities, angular scattering occurs in two planes and a large number of different scattering angles can yield the same time delay even for large  $\alpha$ . It is the angular scattering from the additional plane which causes the horseshoe shaped figure to be filled in for the case of isotropic irregularities.

Figures A-5 through A-16 show the development of the generalized power spectra as the parameter  $\alpha$  decreases from 5.0 to 0.1.

Figures A-17 to A-20 for the case of  $\alpha$  of 0.01 show the generalized power spectra for the case where angular scattering is unimportant and large phase effects and dispersion are the dominant factor. As discussed earlier, the case of small  $\alpha$  corresponds to the basic geometry where the focal length of the irregularities is much larger than the propagation distance to the receiver. Equivalently the receiver is located very close to the scattering medium. In this case, the phase irregularities comprising the scattering layer appear as very large, frequency selective lenses which cause little angular scattering but which may cause different frequency components of a wide bandwidth waveform to propagate at different velocities. These large phase excursions in the medium may also cause large scale changes in the mean time delay. In either case the generalized power spectrum for isotropic or elongated irregularities has the Gaussian form given by Equation 4-112 and shown in Figures A-17 to A-20.

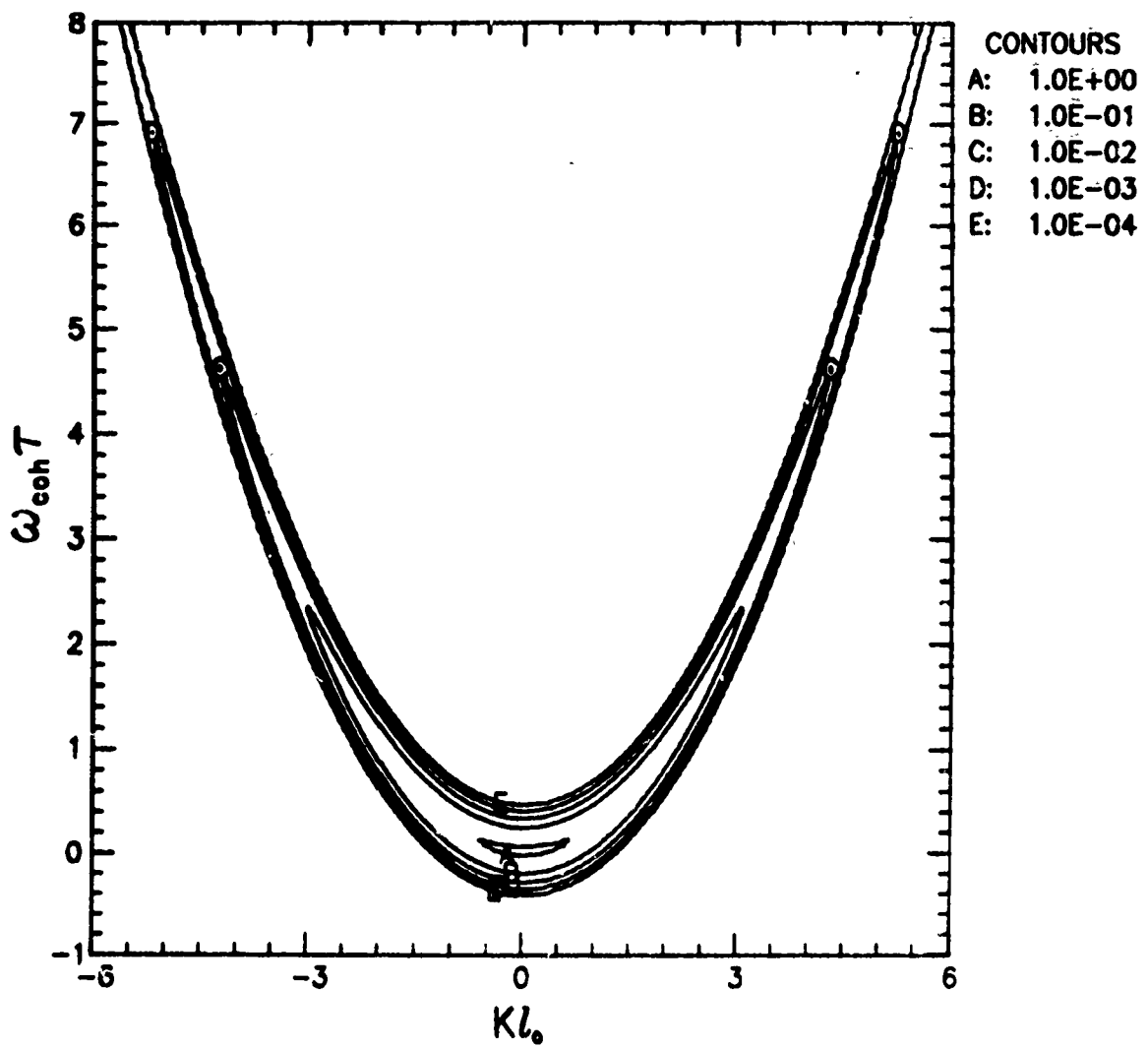


Figure A-1. Generalized power spectrum for elongated irregularities,  $\alpha = 10$ .

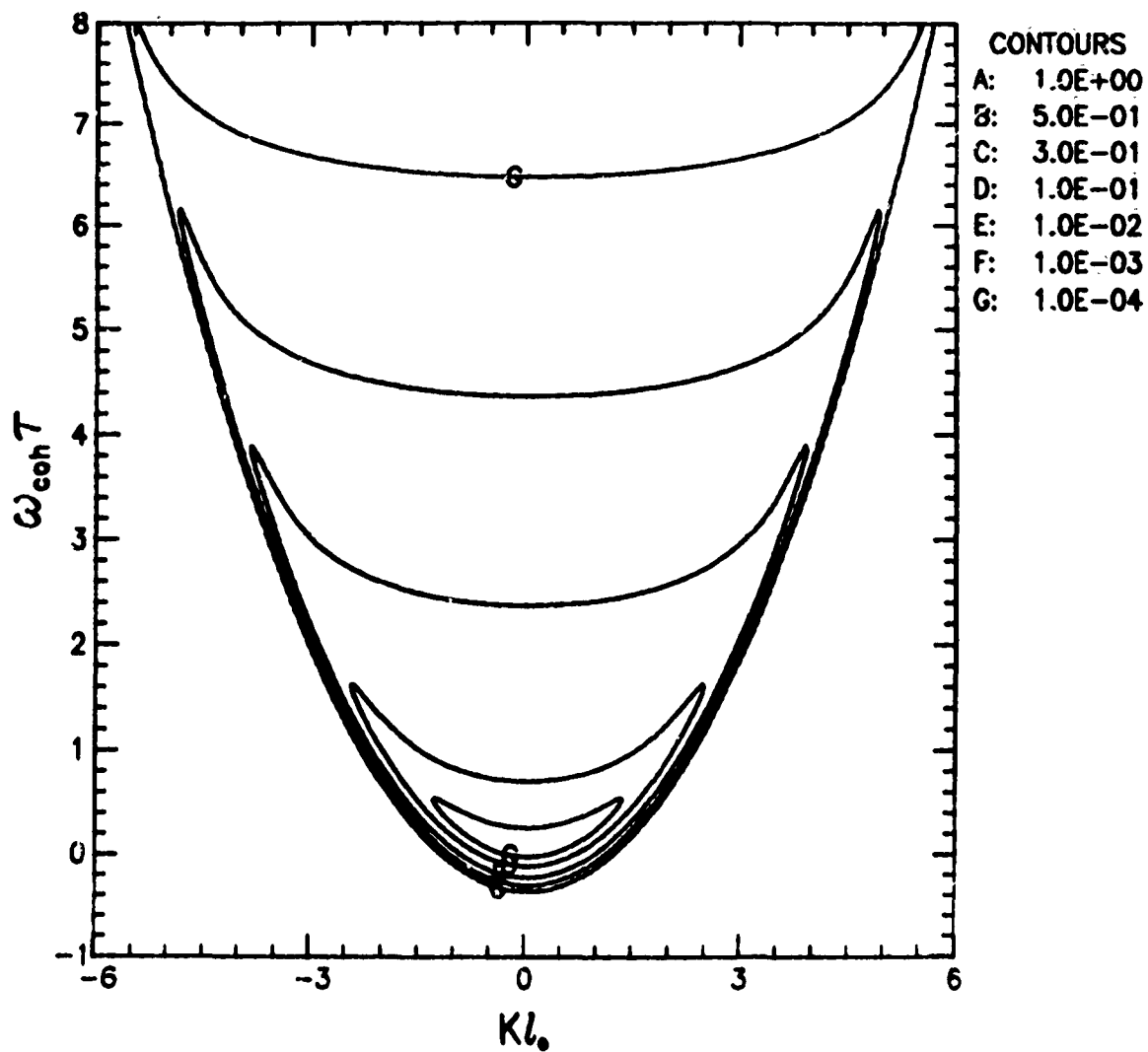


Figure A-2. Generalized power spectrum for isotropic irregularities,  
 $\alpha = 10$ .

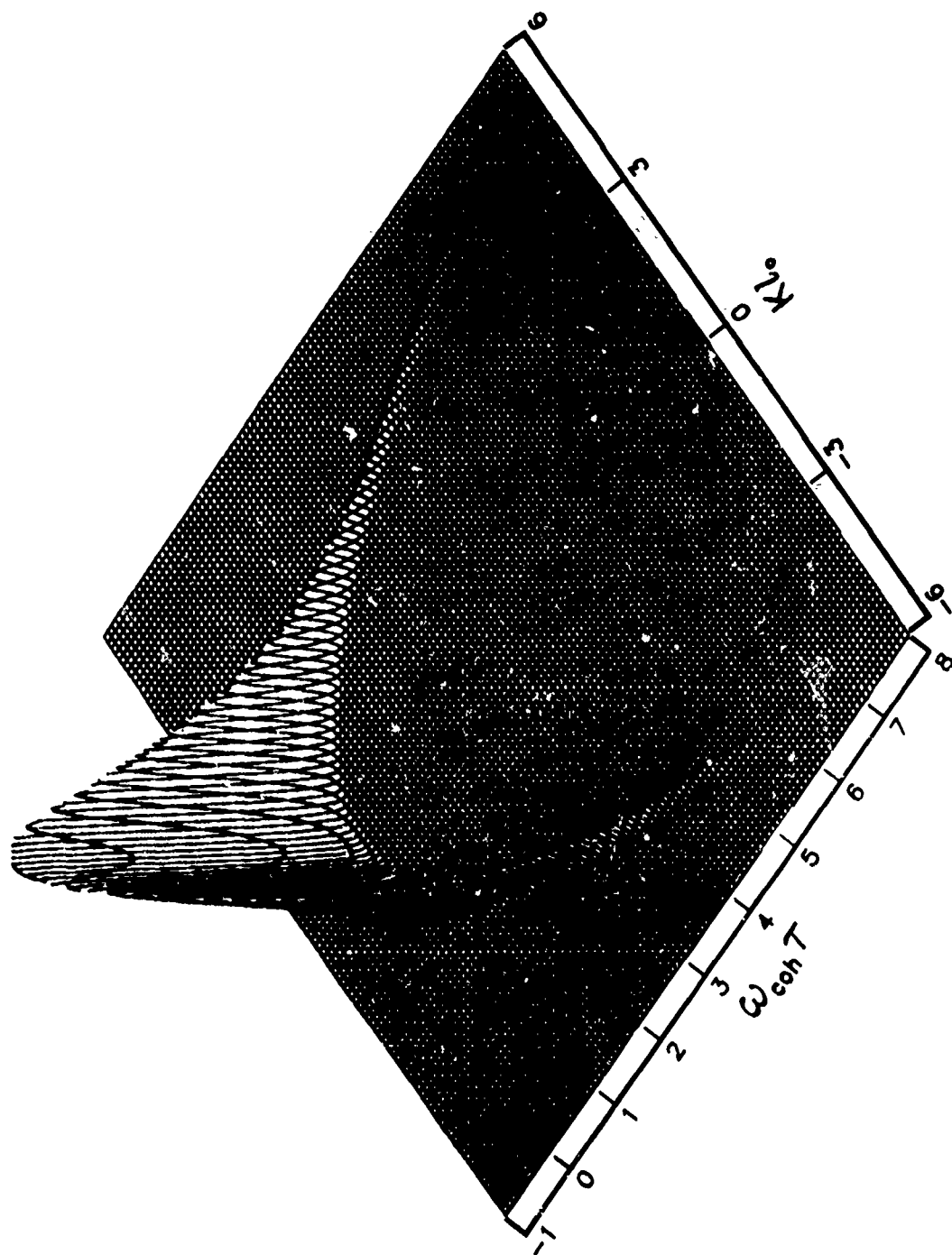


Figure A-3. Generalized power spectrum for elongated irregularities,  $\alpha = 10$ .



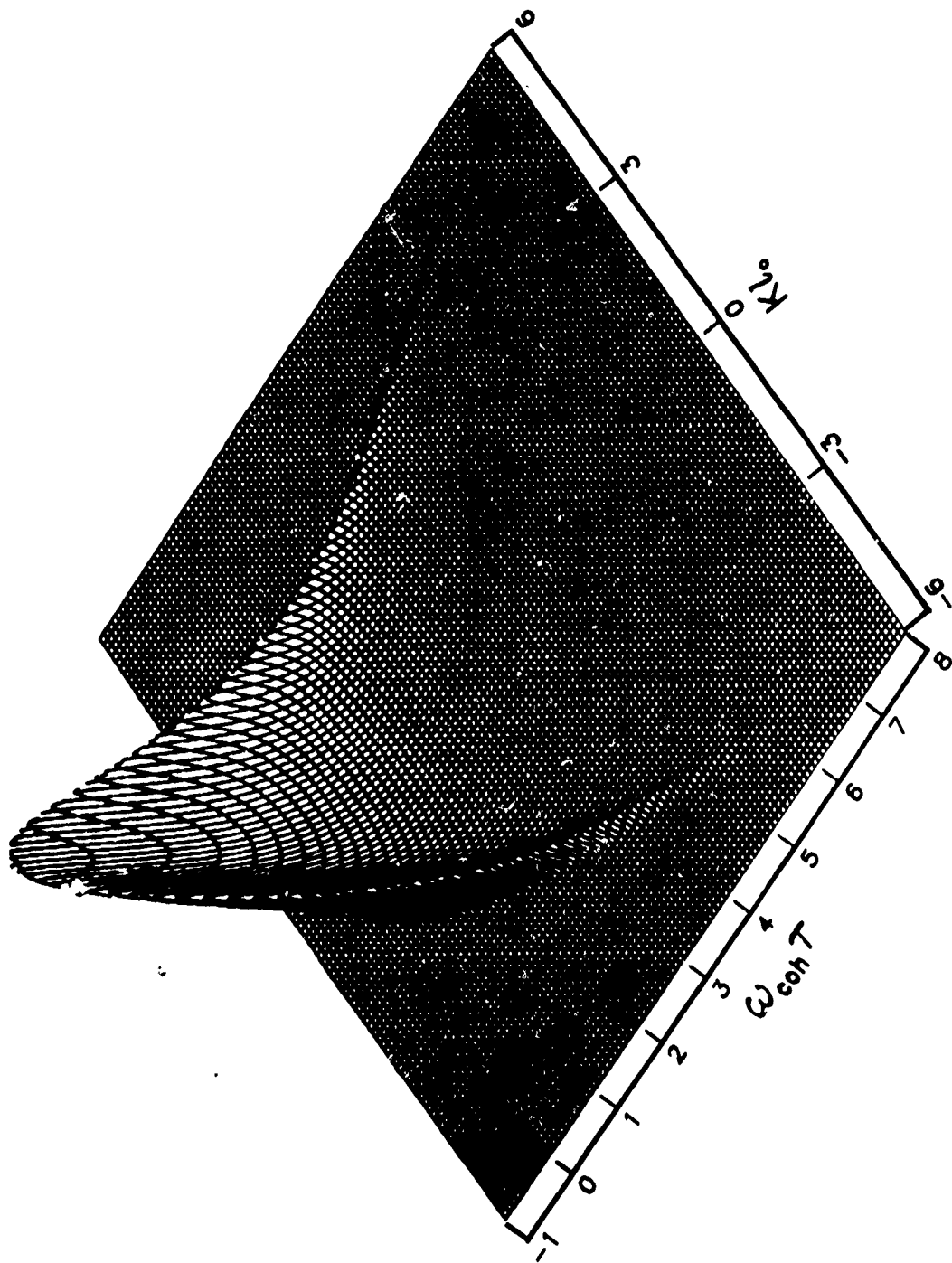


Figure A-4. Generalized power spectrum for isotropic irregularities,  $\alpha = 10$ .

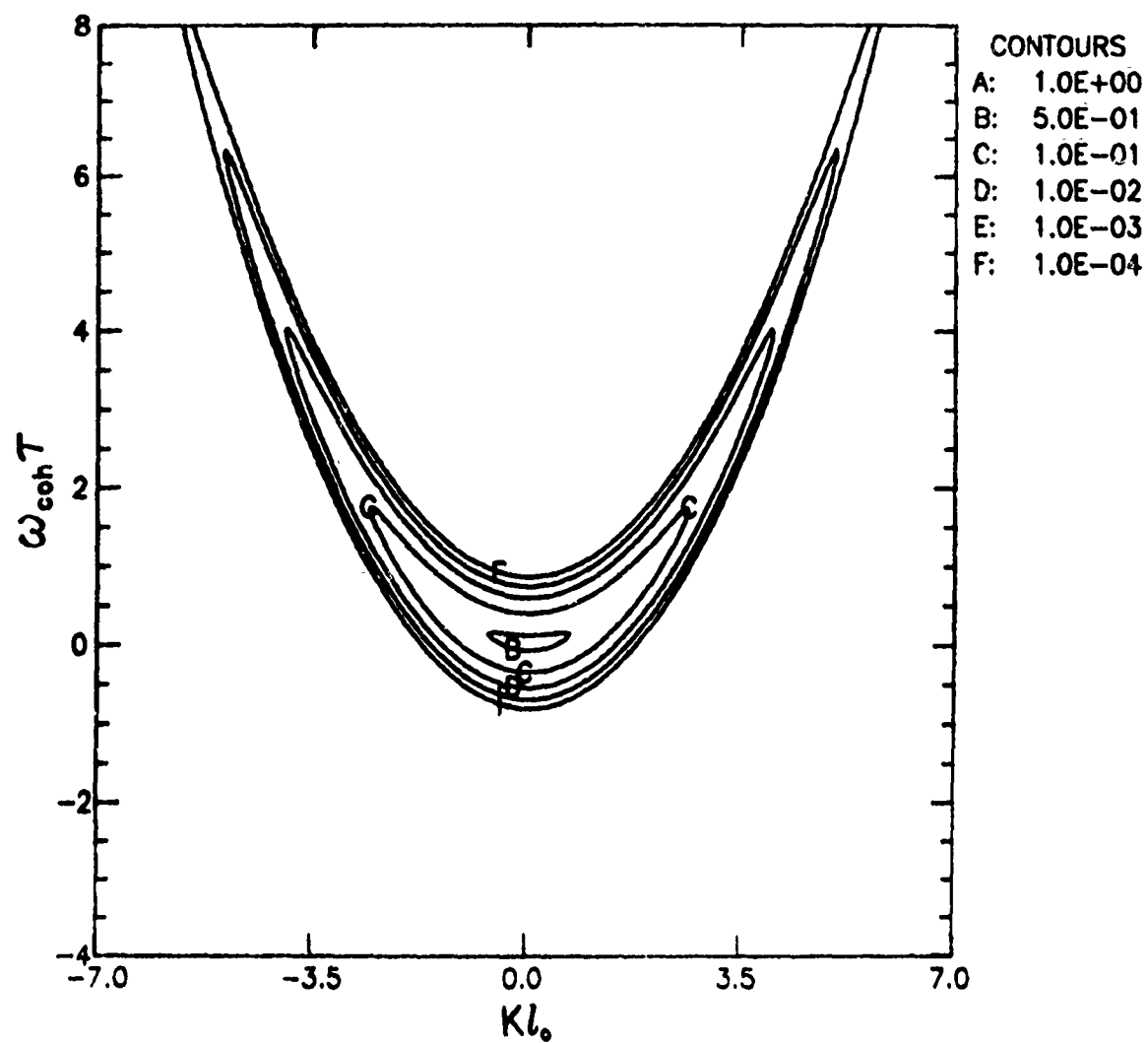


Figure A-5. Generalized power spectrum for elongated irregularities,  
 $\alpha = 5$ .

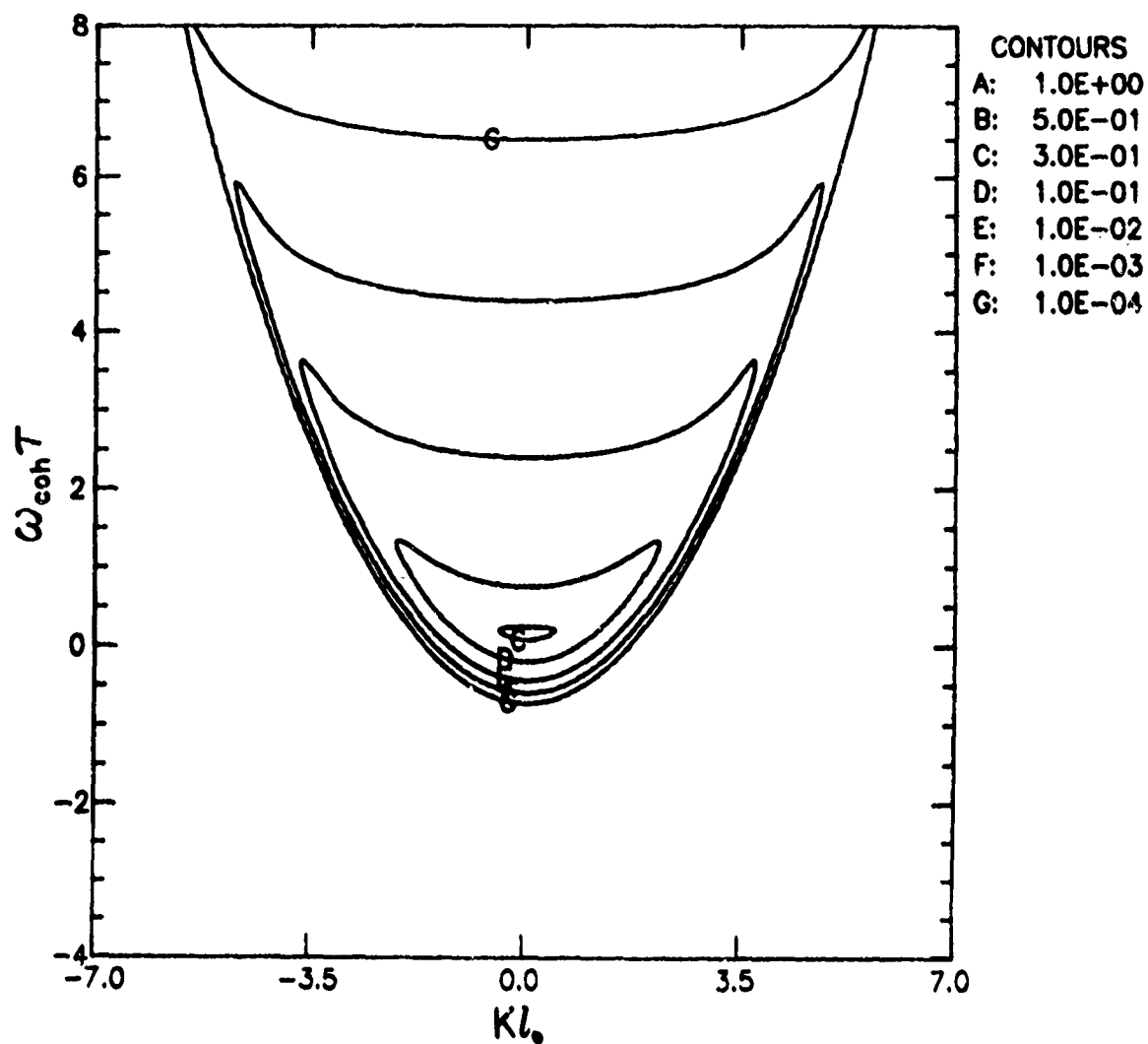


Figure A-6. Generalized power spectrum for isotropic irregularities,  
 $\alpha = 5$ .

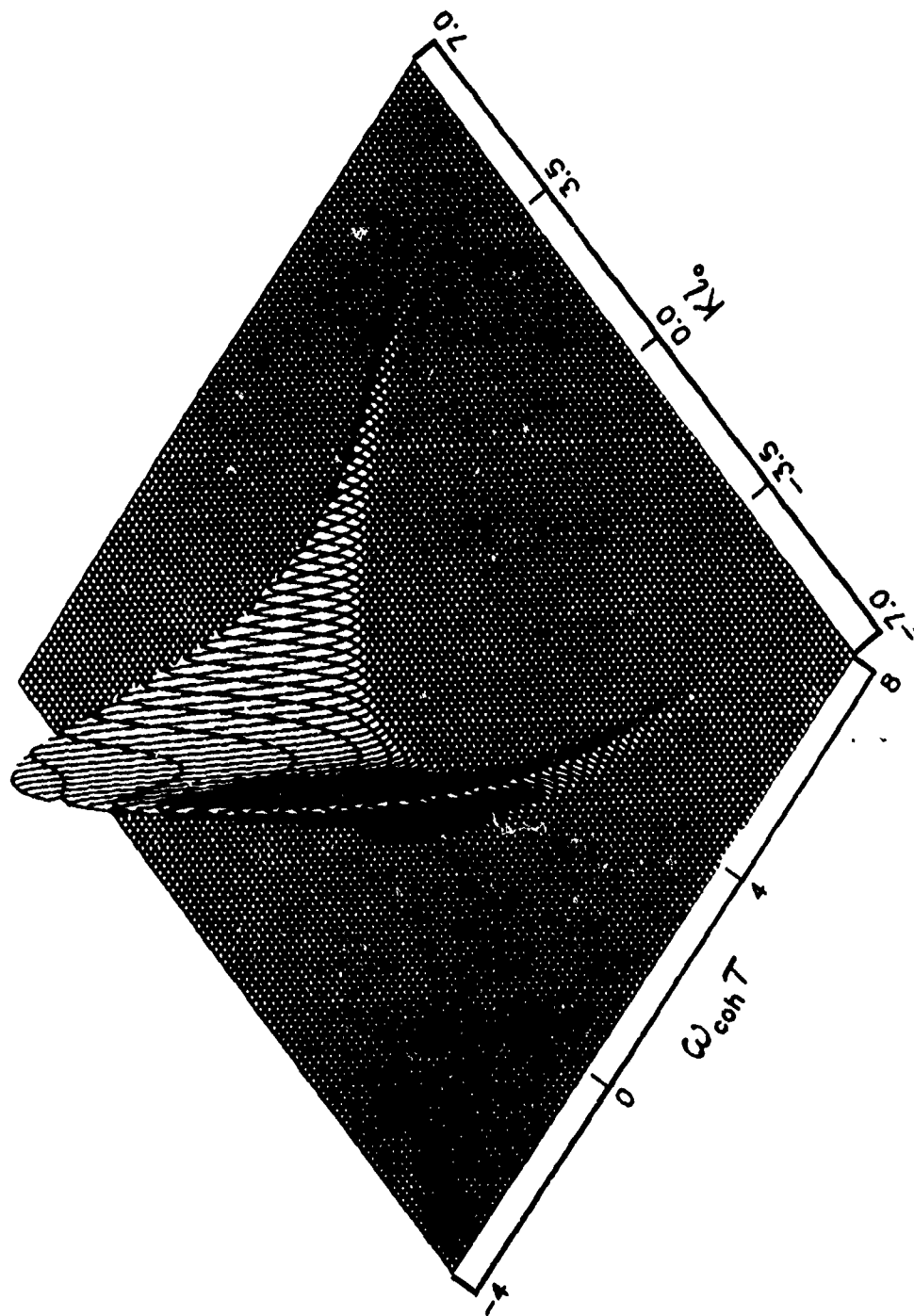


Figure A-7. Generalized power spectrum for elongated irregularities,  $\alpha = 5$ .

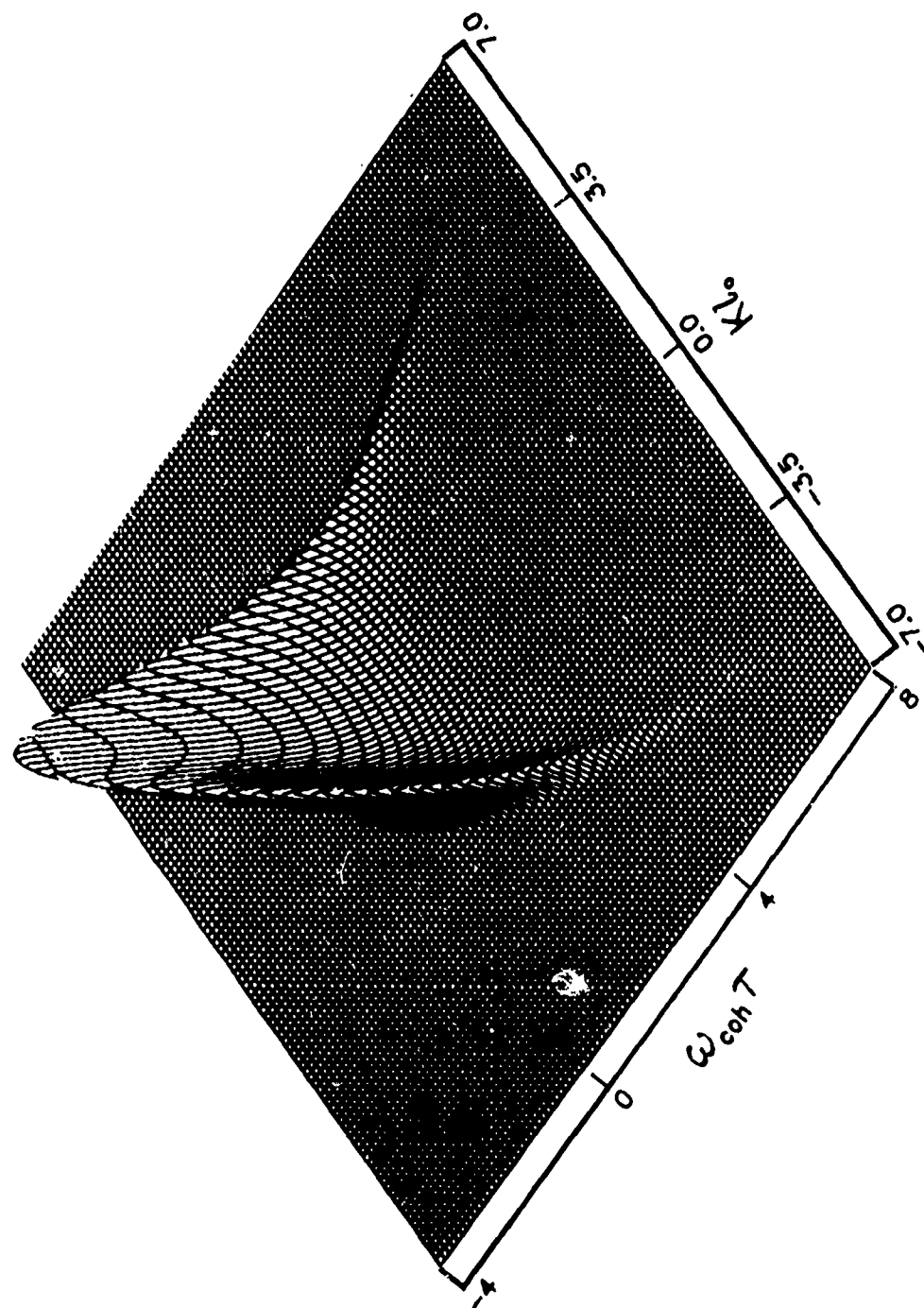


Figure A-8. Generalized power spectrum for isotropic irregularities,  $\alpha = 5$ .

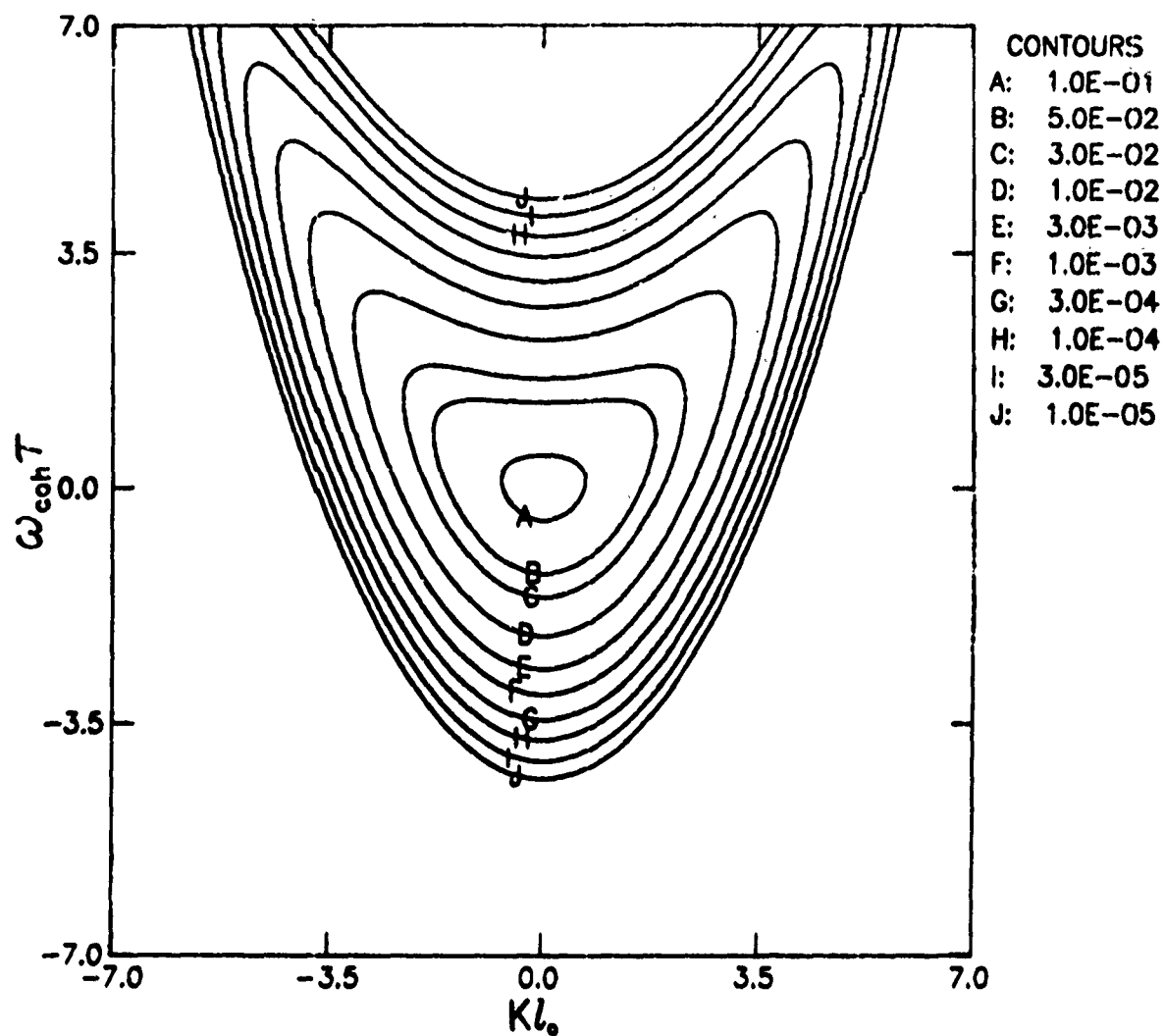


Figure A-9. Generalized power spectrum for elongated irregularities,  $\alpha = 1$ .

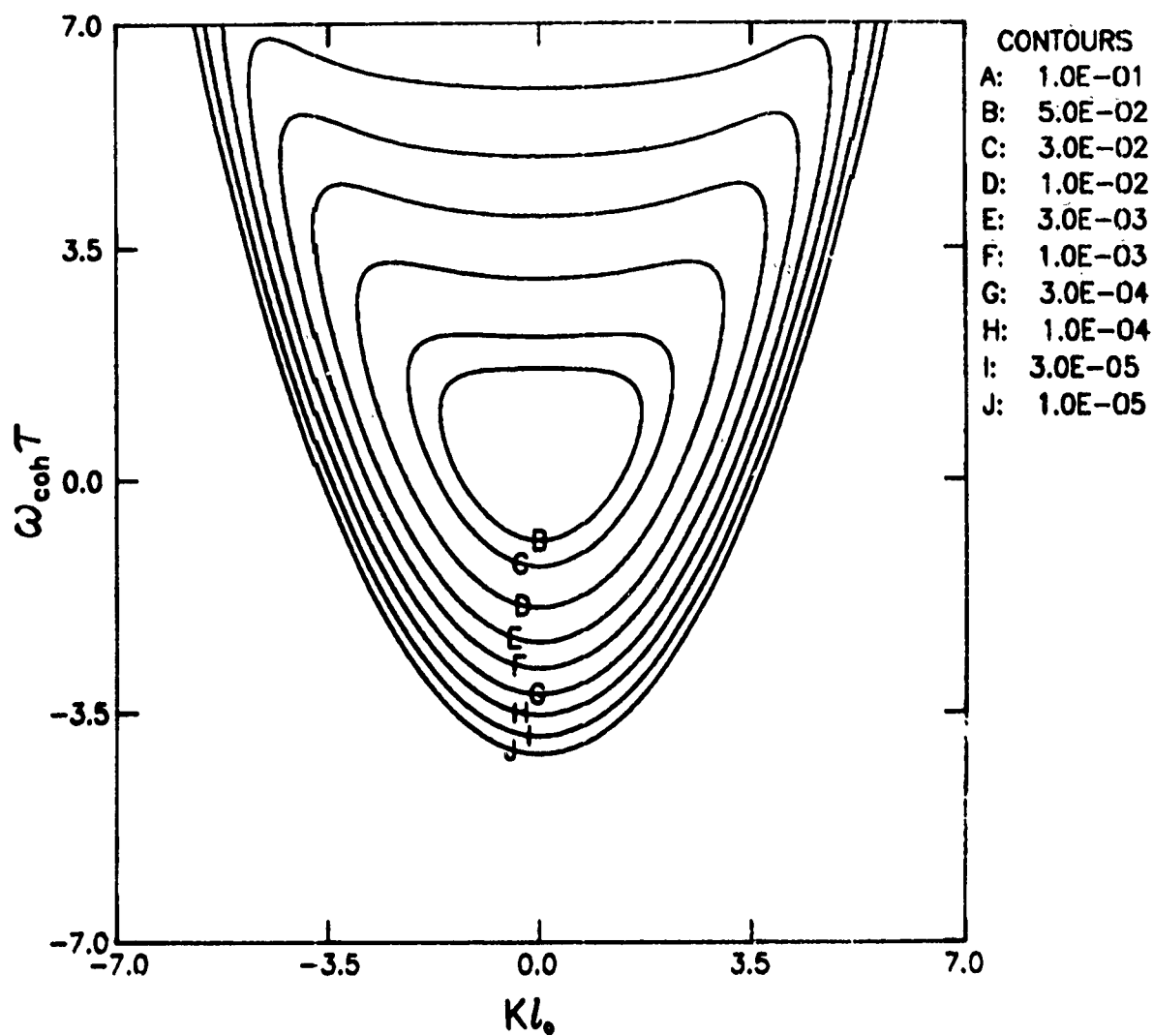


Figure A-10. Generalized power spectrum for isotropic irregularities,  
 $\alpha = 1$ .

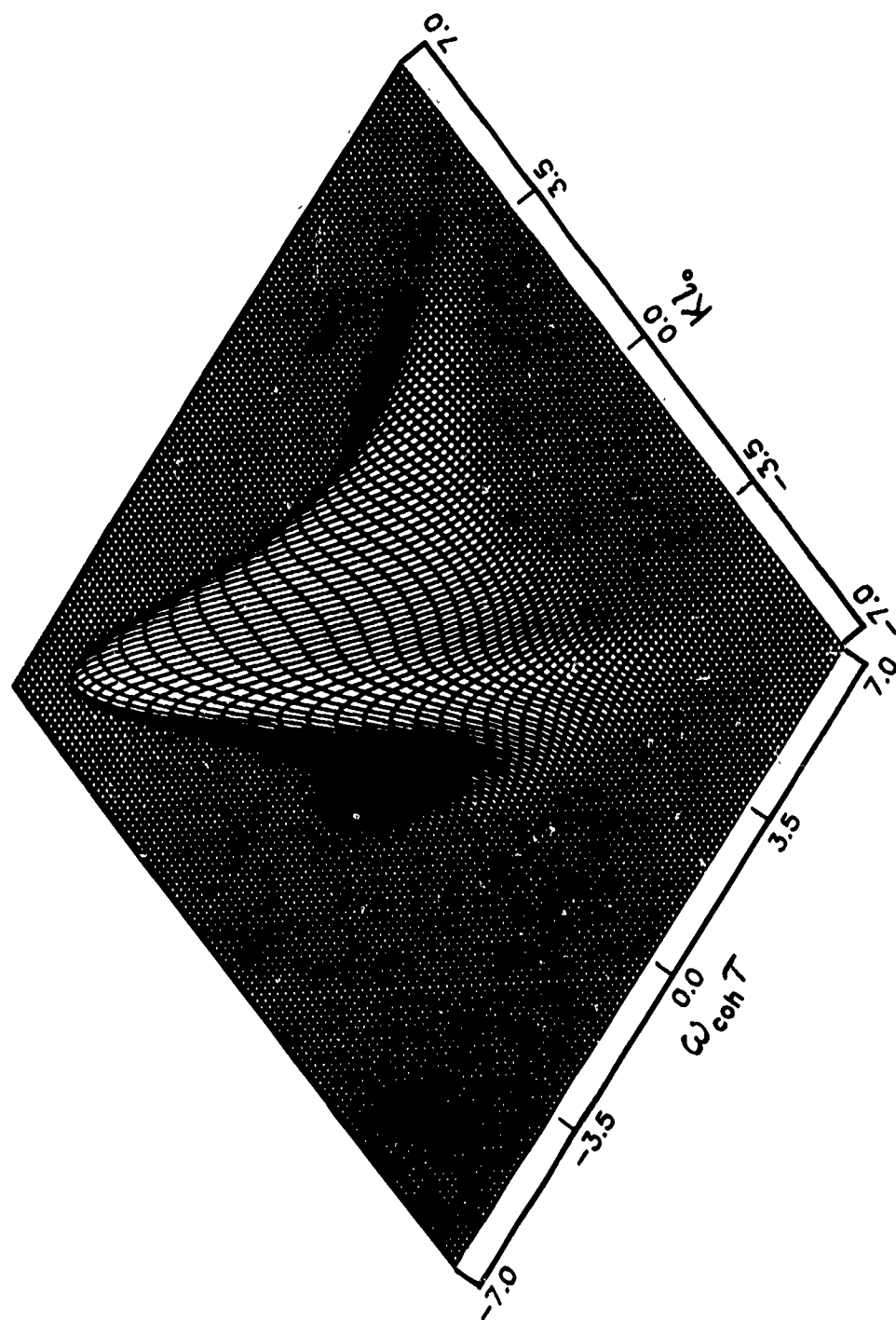


Figure A-11. Generalized power spectrum for elongated irregularities,  $\alpha = 1$ .



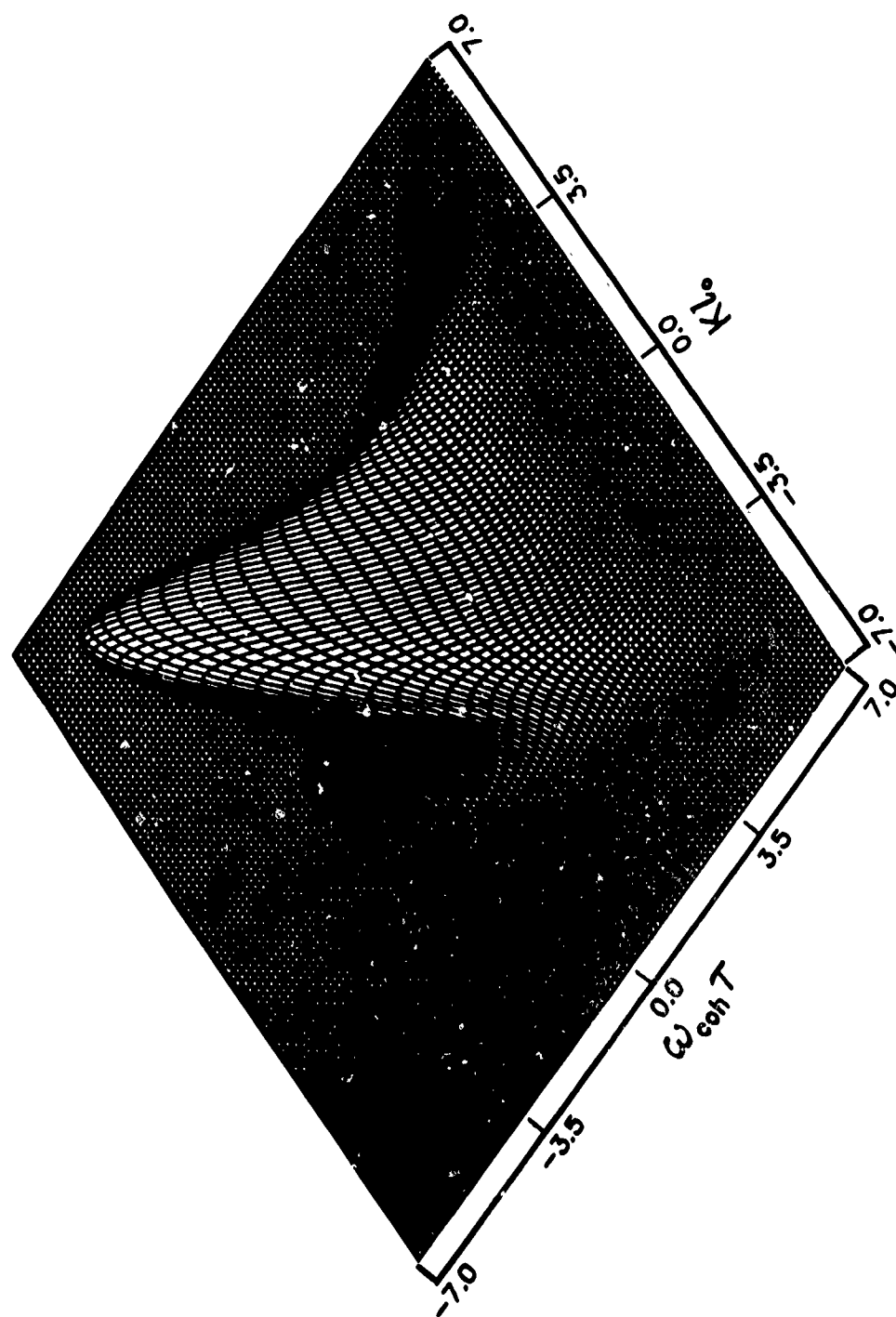


Figure A-12. Generalized power spectrum for isotropic irregularities,  $\alpha = 1$ .

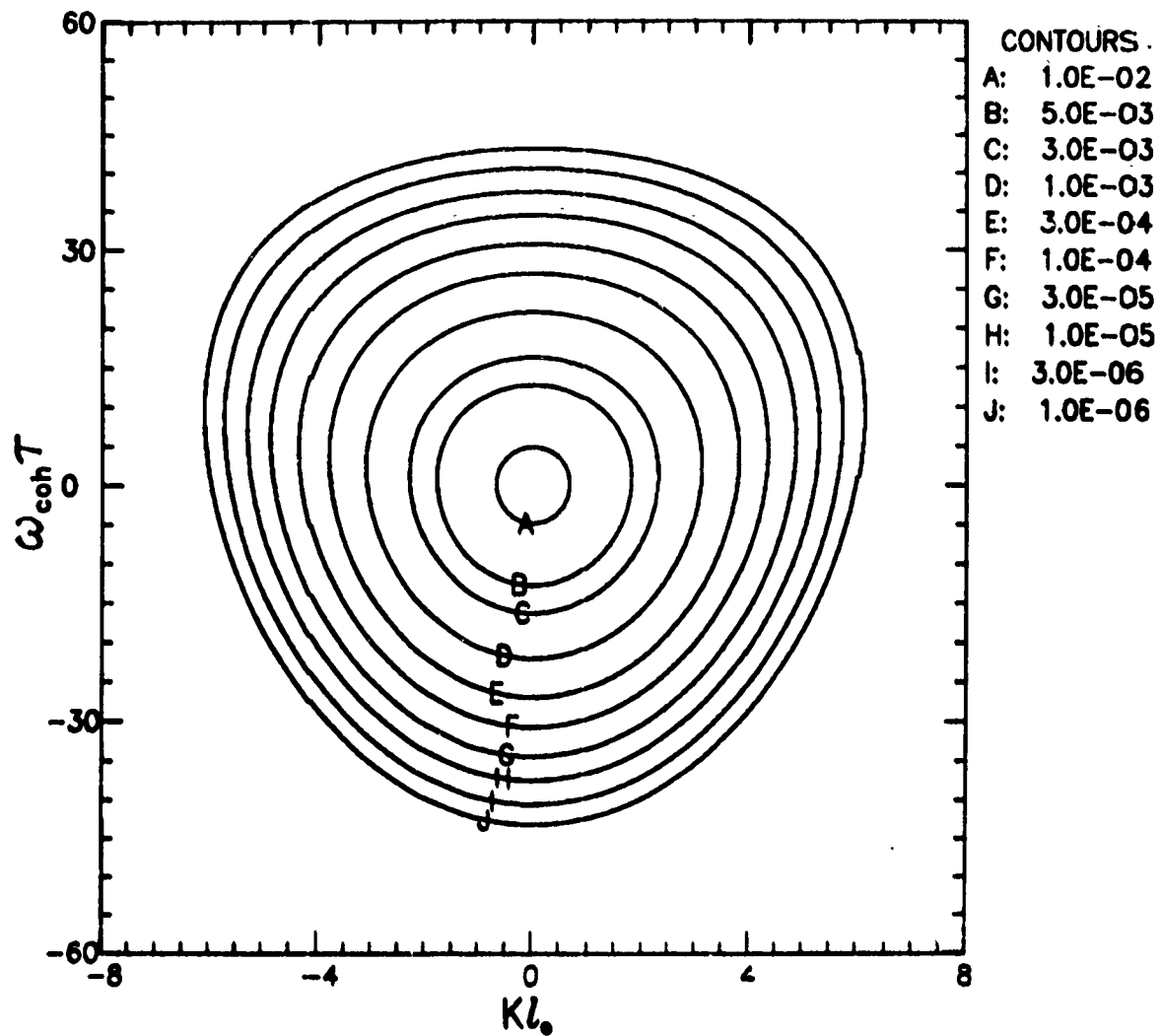


Figure A-13. Generalized power spectrum for elongated irregularities,  
 $\alpha = 0.1$ .

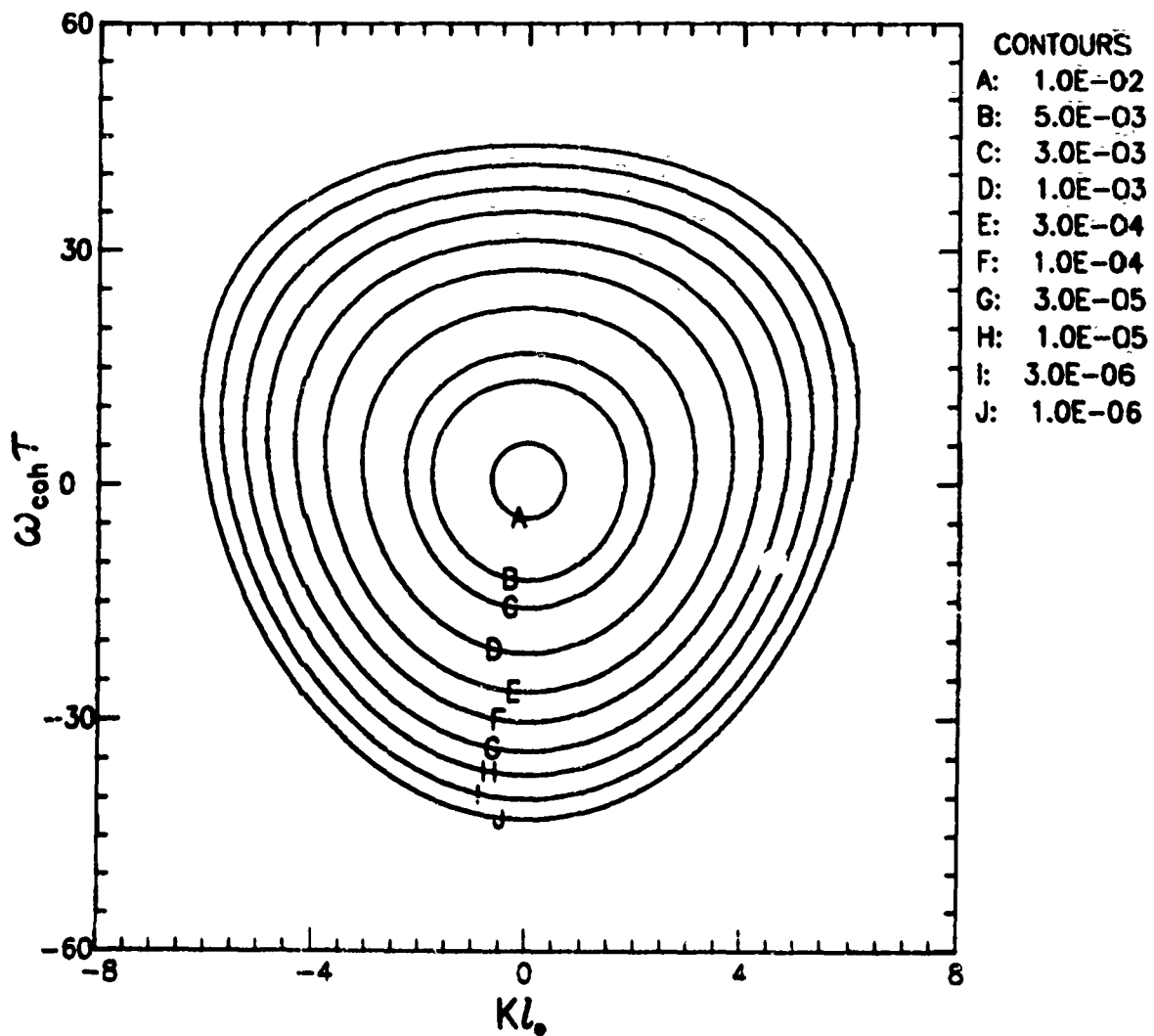


Figure A-14. Generalized power spectrum for isotropic irregularities,  $\alpha = 0.1$ .

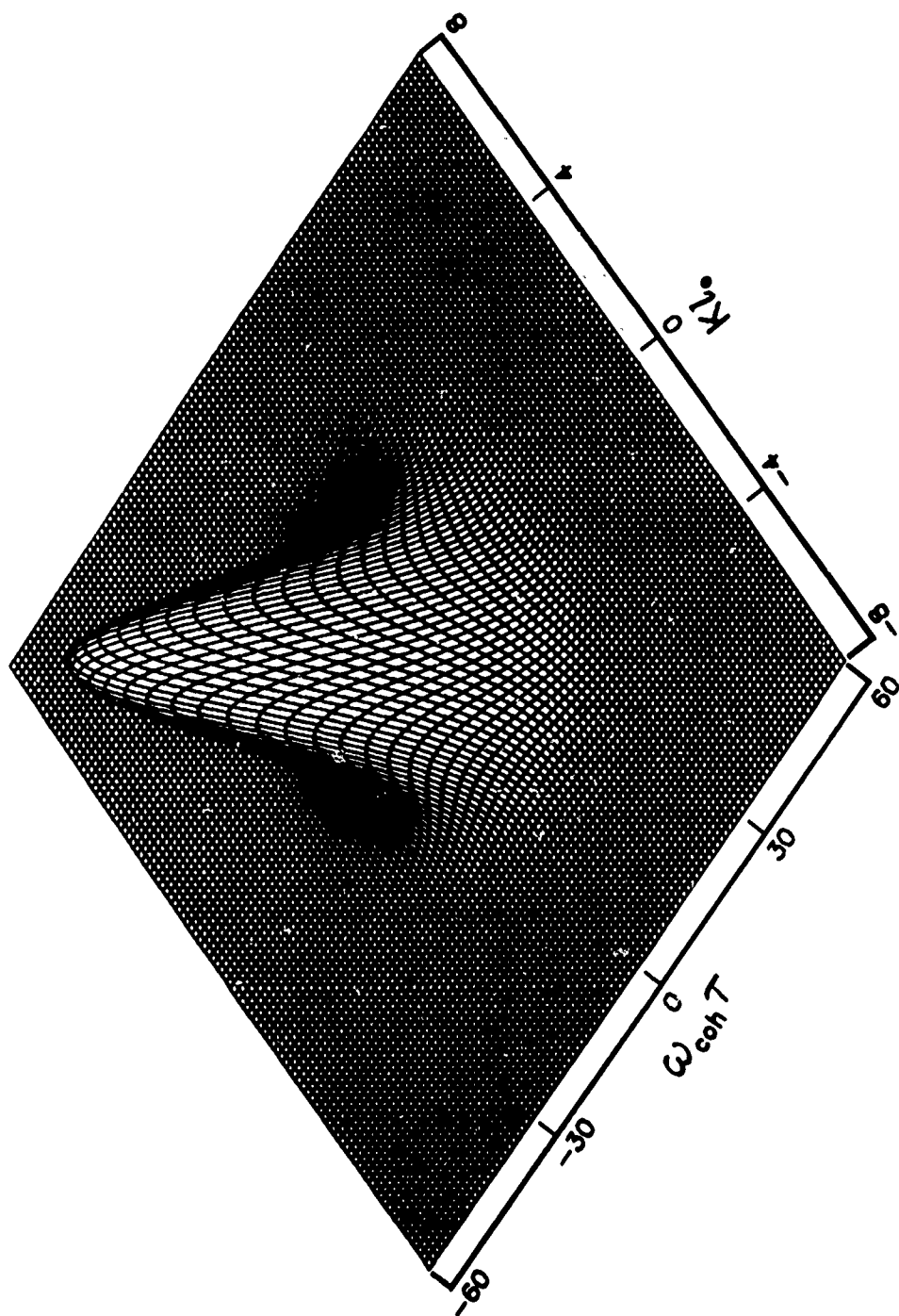


Figure A-15. Generalized power spectrum for elongated irregularities,  $\alpha = 0.1$ .

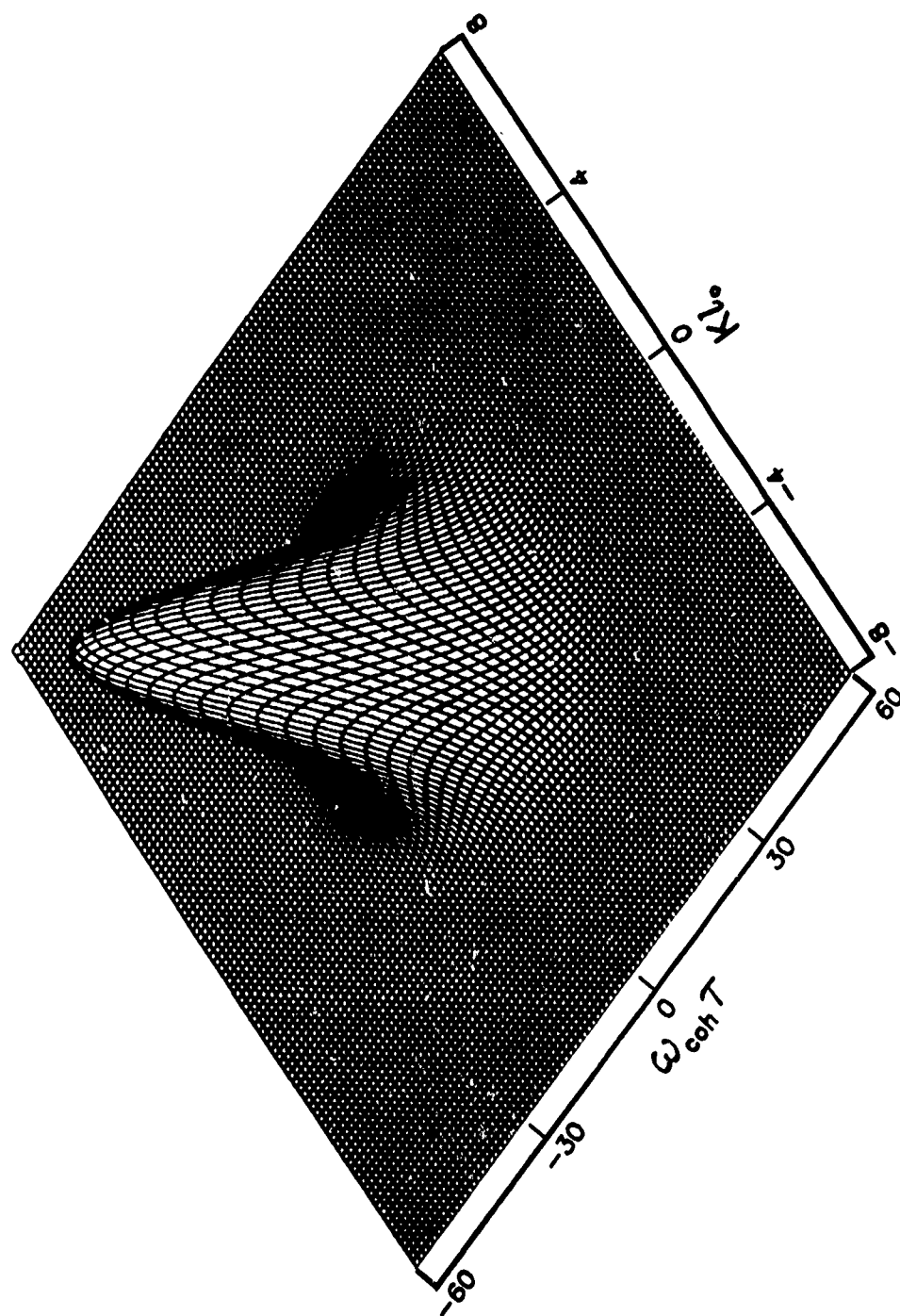


Figure A-16. Generalized power spectrum for isotropic irregularities,  $\alpha = 0.1$ .

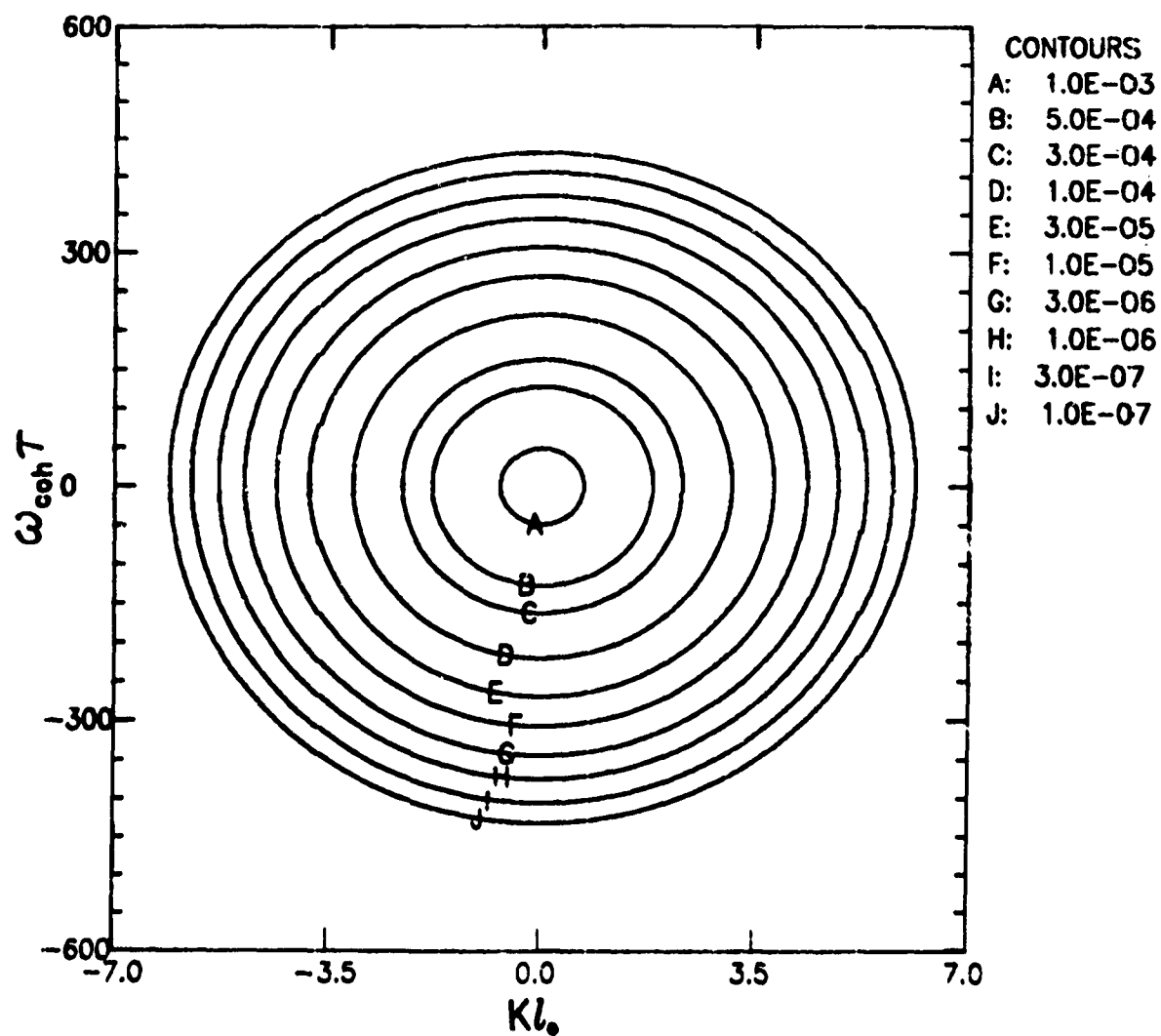


Figure A-17. Generalized power spectrum for elongated irregularities,  
 $\alpha = 0.01$ .

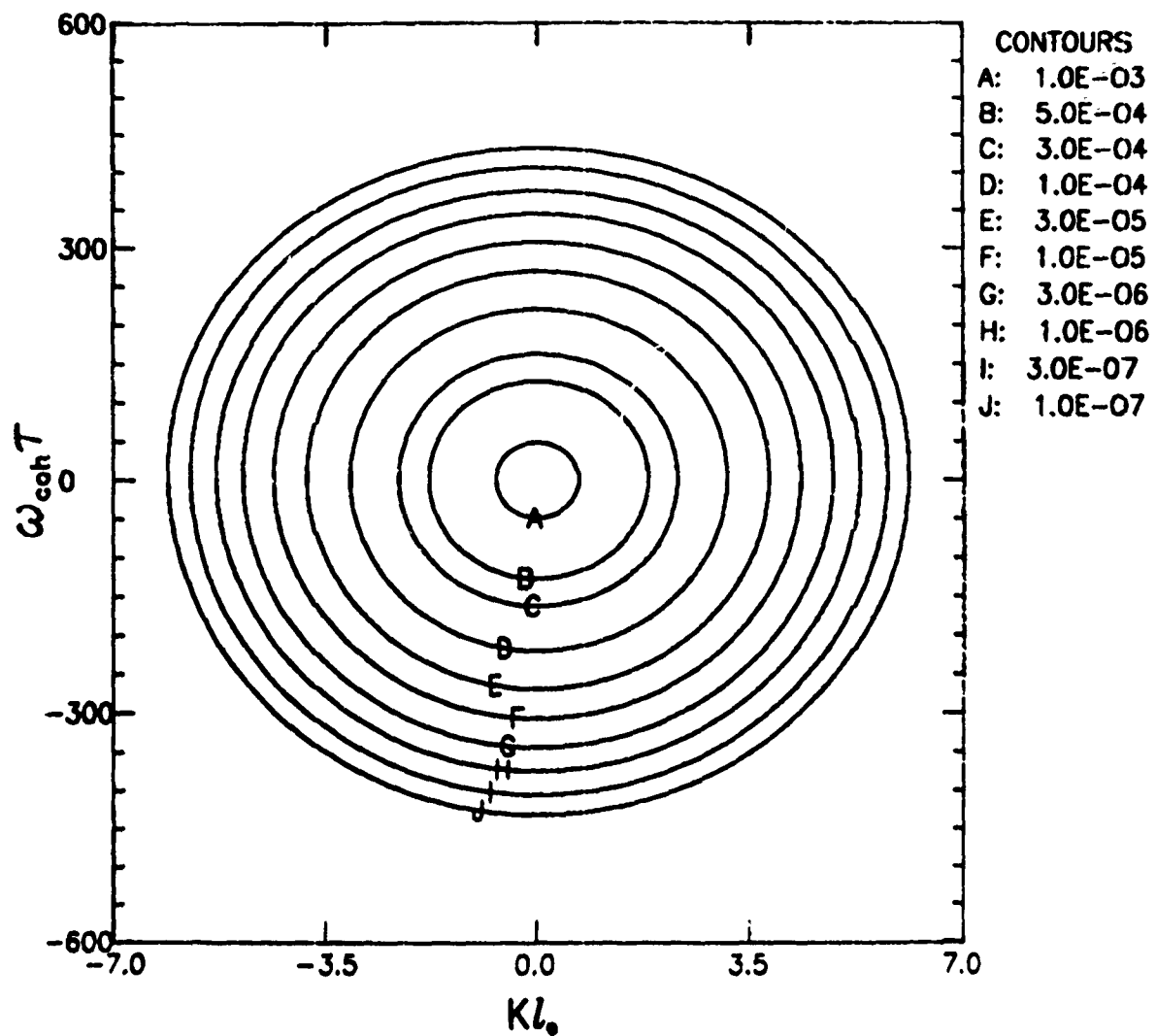


Figure A-18. Generalized power spectrum for isotropic irregularities,  $\alpha = 0.01$ .

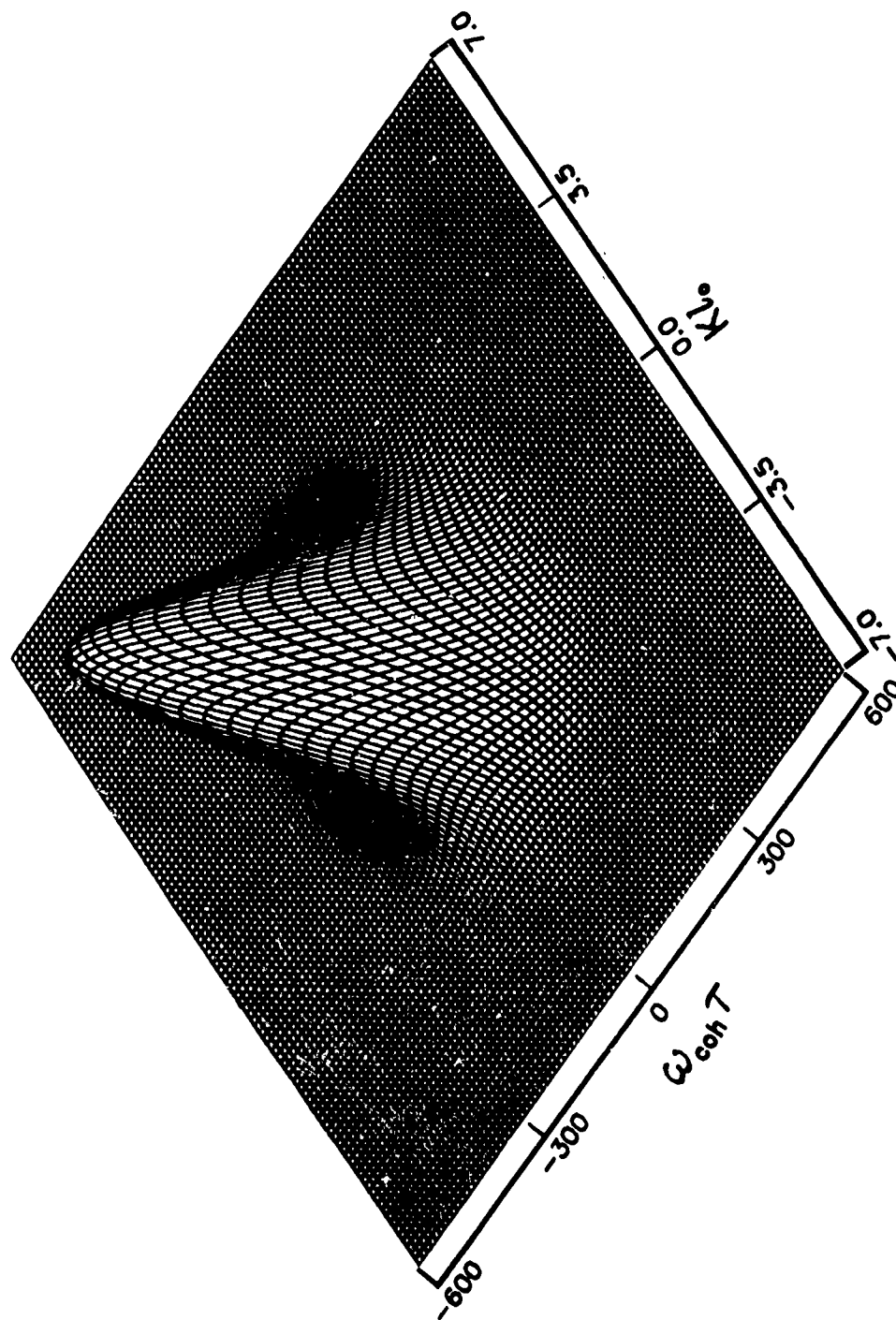


Figure A-19. Generalized power spectrum for elongated irregularities,  $\alpha = 0.01$ .



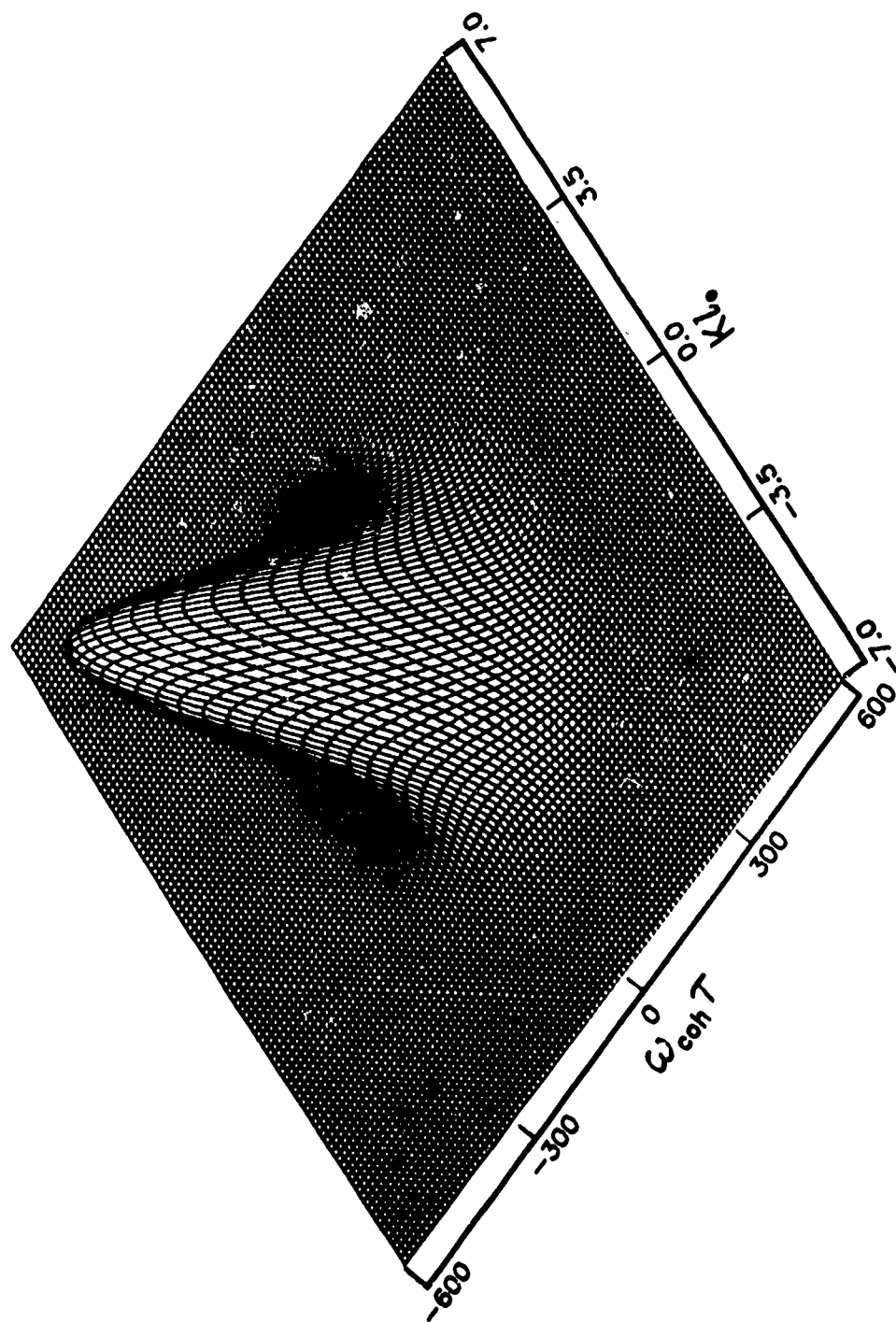


Figure A-20. Generalized power spectrum for isotropic irregularities,  $\alpha = 0.01$ .

Blank

## DISTRIBUTION LIST

### DEPARTMENT OF DEFENSE

#### Command & Control Technical Center

ATTN: C-650  
 ATTN: C-312, R. Mason  
 ATTN: C-650, G. Jones  
 3 cy ATTN: C-650, W. Heidig

#### Defense Communications Engineer Center

ATTN: Code R410, N. Jones  
 ATTN: Code R410  
 ATTN: Code R410, R. Craighill  
 ATTN: Code R123, Tech Lib

#### Defense Nuclear Agency

ATTN: STNA  
 ATTN: NAED  
 ATTN: RAEI  
 ATTN: NATD  
 ATTN: RAAE, P. Lunn  
 3 cy ATTN: RAAE  
 4 cy ATTN: TITL

#### Defense Technical Information Center

12 cy ATTN: DD

#### Det 1 FCDNA

Lawrence Livermore Lab  
 ATTN: FC-1

### DEPARTMENT OF THE ARMY

#### U.S. Army Electronics R & D Command

ATTN: DELAS-EO, F. Niles

#### BMD Advanced Technology Center

ATTN: ATC-R, D. Russ  
 ATTN: ATC-O, W. Davies  
 ATTN: ATC-R, W. Dickinson  
 ATTN: ATC-T, M. Capps

#### BMD Systems Command

ATTN: BMDSC-HLE, R. C. Webb  
 2 cy ATTN: BMDSC-HW

#### Harry Diamond Laboratories

ATTN: DELHD-NW-P (20240)  
 ATTN: DELHD-NW-R, R. Williams (22000)

#### U.S. Army Communications Command

ATTN: CC-OPS-W  
 ATTN: CC-OPS-WR, H. Wilson

#### U.S. Army Communications R&D Command

ATTN: DRDCO-COM-RY, W. Kesselman

#### U.S. Army Foreign Science & Tech Ctr

ATTN: DRXST-SD

#### U.S. Army Nuclear & Chemical Agency

ATTN: Library

#### U.S. Army Satellite Comm Agency

ATTN: Document Control

### DEPARTMENT OF THE NAVY

#### Naval Electronic Systems Command

ATTN: PME 117-211, B. Kruger  
 ATTN: PME 106-13, T. Griffin  
 ATTN: Code 501A  
 ATTN: PME 117-20  
 ATTN: PME-117-2013, G. Burnhart  
 ATTN: Code 3101, T. Hughes  
 ATTN: PME 106-4, S. Kearney

#### Naval Ocean Systems Center

ATTN: Code 5322, M. Paulson  
 ATTN: Code 532  
 ATTN: Code 5323, J. Ferguson

#### Naval Research Laboratory

ATTN: Code 4720, J. Davis  
 ATTN: Code 4780  
 ATTN: Code 7500, B. Wald  
 ATTN: Code 4780, S. Ossakow  
 ATTN: Code 6700  
 ATTN: Code 7950, J. Goodman  
 ATTN: Code 4187  
 ATTN: Code 4700

#### Theater Nuclear Warfare Proj Office

ATTN: PM-23, D. Smith

### DEPARTMENT OF THE AIR FORCE

#### Air Force Geophysics Laboratory

ATTN: OPR, H. Gardiner  
 ATTN: OPR-1  
 ATTN: LKB, K. Champion  
 ATTN: CA, A. Stair  
 ATTN: Phy, J. Buchau  
 ATTN: R. Babcock  
 ATTN: R. O'Neil

#### Air Force Technical Applications Ctr

ATTN: TN

#### Air Force Weapons Laboratory, AFSC

ATTN: SUL  
 ATTN: NTYC  
 ATTN: NTN

#### Air Force Wright Aeronautical Lab/AAAD

ATTN: A. Johnson  
 ATTN: W. Hunt

#### Air University Library

ATTN: AUL-LSE

#### Assistant Chief of Staff

##### Studies & Analyses

ATTN: AF/SASC, C. Rightmeyer  
 ATTN: AF/SASC, W. Kraus

#### Electronic Systems Div

ATTN: SCT-2, J. Clark  
 ATTN: SCS-1E  
 ATTN: SCS-2, LTC Vinkejs

DEPARTMENT OF THE AIR FORCE (Continued)

Foreign Technology Division, AFSC  
ATTN: NIIS, Library  
ATTN: TQTD, B. Ballard

Rome Air Development Center, AFSC  
ATTN: OCS, V. Coyne  
ATTN: TSLD

Rome Air Development Center, AFSC  
ATTN: EEP, J. Rasmussen

OTHER GOVERNMENT AGENCY

National Telecommunications & Info Admin  
ATTN: L. Berry  
ATTN: A. Jean  
ATTN: W. Utlaut

DEPARTMENT OF ENERGY CONTRACTORS

EG&G, Inc  
Los Alamos Division  
ATTN: D. Wright  
ATTN: J. Colvin

University of California  
Lawrence Livermore National Lab  
ATTN: Technical Info Dept, Library  
ATTN: L-389, R. Ott  
ATTN: L-31, R. Hager

Los Alamos National Laboratory  
ATTN: MS 664, J. Zinn  
ATTN: P. Keaton  
ATTN: D. Simons  
ATTN: MS 670, J. Hopkins  
ATTN: T. Kunkle, ESS-5  
ATTN: R. Jeffries  
ATTN: J. Wolcott  
ATTN: C. Westervelt

Sandia National Lab  
ATTN: D. Dahlgren  
ATTN: Tech Lib 3141  
ATTN: Space Project Div  
ATTN: D. Thornbrough  
ATTN: Org 1250, W. Brown  
ATTN: Org 4231, T. Wright

DEPARTMENT OF DEFENSE CONTRACTORS

Aerospace Corp  
ATTN: V. Josephson  
ATTN: T. Salmi  
ATTN: R. Slaughter  
ATTN: I. Garfunkel  
ATTN: J. Straus  
ATTN: D. Olsen

Analytical Systems Engineering Corp  
ATTN: Radio Sciences

Analytical Systems Engineering Corp  
ATTN: Security

BDM Corp  
ATTN: L. Jacobs  
ATTN: T. Neighbors

DEPARTMENT OF DEFENSE CONTRACTORS (Continued)

Berkeley Research Associates, Inc  
ATTN: J. Workman  
ATTN: S. Brecht  
ATTN: C. Prettie

Booz-Allen & Hamilton, Inc  
ATTN: B. Wilkinson

University of California at San Diego  
ATTN: H. Booker

Charles Stark Draper Lab, Inc  
ATTN: A. Tetewski  
ATTN: J. Gilmore  
ATTN: D. Cox

Cornell University  
ATTN: D. Farley, Jr  
ATTN: M. Kelly

EOS Technologies, Inc  
ATTN: B. Gabbard

ESL, Inc  
ATTN: R. Ibaraki  
ATTN: R. Heckman  
ATTN: J. Lehman  
ATTN: E. Tsui  
ATTN: J. Marshall

General Electric Co  
ATTN: C. Zierdt  
ATTN: A. Steinmayer

General Research Corp  
ATTN: B. Bennett

Geo-Centers, Inc  
ATTN: E. Marram

Honeywell, Inc  
ATTN: G. Collyer, Avionics Dept  
ATTN: G. Terry, Avionics Dept

IBM Corp  
ATTN: H. Ulander

Institute for Defense Analyses  
ATTN: E. Bauer  
ATTN: H. Wolfhard  
ATTN: J. Aein  
ATTN: H. Gates

International Tel & Telegraph Corp  
ATTN: Technical Library

International Tel & Telegraph Corp  
ATTN: G. Wetmore

JAYCOR  
ATTN: J. Sperling

Johns Hopkins University  
ATTN: J. Newland  
ATTN: T. Evans  
ATTN: P. Komiske  
ATTN: J. D. Phillips

DEPARTMENT OF DEFENSE CONTRACTORS (Continued)

Kaman Sciences Corp  
ATTN: T. Stephens

Kaman Tempo  
ATTN: B. Gambill  
ATTN: DASIAC  
2 cy ATTN: J. Devore  
ATTN: W. Knapp  
ATTN: K. Schwartz  
ATTN: W. McNamara

Lockheed Missiles & Space Co, Inc  
ATTN: C. Old, Dept 68-21  
ATTN: D. Churchill, Dept 81-11  
ATTN: Dept 60-12

M.I.T. Lincoln Lab  
ATTN: D. Towle

MA/COM Linkabit Inc  
ATTN: H. Van Trees  
ATTN: A. Viterbi  
ATTN: I. Jacobs

Mission Research Corp  
ATTN: R. Hendrick  
ATTN: C. Lauer  
ATTN: R. Kilb  
ATTN: F. Fajen  
ATTN: R. Bigoni  
ATTN: G. McCartor  
ATTN: F. Guigliano  
6 cy ATTN: Tech Library/Doc Control  
ATTN: S. Gutsche  
ATTN: R. Bogusch  
4 cy ATTN: D. L. Knepp

Mitre Corp  
ATTN: A. Kymmel  
ATTN: B. Adams  
ATTN: G. Harding  
ATTN: C. Callahan  
ATTN: MS J104/M, R. Dresp

Physical Dynamics, Inc  
ATTN: E. Fremouw

Physical Research, Inc  
ATTN: R. Deliberis

R & D Associates  
ATTN: B. Yoon

DEPARTMENT OF DEFENSE CONTRACTORS (Continued)

R & D Associates  
ATTN: R. Lelevier  
ATTN: C. Greifinger  
ATTN: R. Turco  
ATTN: H. Ory  
ATTN: W. Wright  
ATTN: M. Gantsweg  
ATTN: W. Karzas  
ATTN: F. Gilmore

Rand Corp  
ATTN: E. Bedrozian  
ATTN: C. Crain

Science Applications, Inc  
ATTN: L. Linson  
ATTN: C. Smith  
ATTN: E. Straker  
ATTN: D. Hamlin

Science Applications, Inc  
ATTN: J. Cockayne

SRI International  
ATTN: G. Price  
ATTN: R. Tsunoda  
ATTN: J. Vickrey  
ATTN: W. Chesnut  
ATTN: R. Livingston  
ATTN: D. Neilson  
ATTN: J. Petrickes  
ATTN: D. McDaniel  
ATTN: R. Leadabrand  
ATTN: M. Baron  
ATTN: A. Burns  
ATTN: C. Rino  
ATTN: G. Smith  
ATTN: V. Gonzales  
ATTN: W. Jaye

Stewart Radiance Laboratory  
ATTN: J. Ulwch

Strategic Systems Div  
ATTN: J. J. Concordia  
ATTN: I. Kohlberg

Visidyne, Inc  
ATTN: C. Humphrey  
ATTN: O. Shepard  
ATTN: W. Reidy  
ATTN: J. Carpenter

Blank